Alma Mater Studiorum · Università di Bologna

DOTTORATO DI RICERCA IN FISICA

Ciclo XXX
Settore Concorsuale di afferenza: 02/A1
Settore Scientifico displinare: FIS/01

Study of multi-lepton final states with the ATLAS experiment: from Standard Model to Beyond Standard Model Higgs.

Presentata da: Giulia Ucchielli

Coordinatore Dottorato:
Prof. Silvia Arcelli

Supervisore:
Prof. Maximiliano Sioli

Relatore:
Dott. Antonio Sidoti

Esame Finale Anno 2018

Sommario

Questa tesi sfrutta le caratteristiche peculiari degli stati finali contenenti leptoni con stessa carica elettrica, prodotti in collisioni protone-protone da LHC a $\sqrt{s}$ =13 TeV, analizzate dal rivelatore ATLAS con dati raccolti nel 2015 e nel 2016. Eventi contenenti leptoni di stesso segno permettono di rigettare gran parte dei fondi dovuti a processi del Modello Standard. La ricerca di nuova fisica viene effettuata in modo indiretto e diretto attraverso due specifici processi: la produzione associata di un bosone di Higgs a coppie di quark top ($t\bar{t}H$) e la produzione di nuovi bosoni di Higgs con doppia carica elettrica ($H^{\pm\pm}$). La misura della *signal strength* (μ) del processo $t\bar{t}H$ in stati finali leptonici fornisce $\mu = 2.5^{+1.3}_{-1.1}$, compatible con le previsioni del Modello Standard $\mu_{t\bar{t}H} = 1$, con un livello di confidenza del 95%. Nessuna evidenza di nuova fisica è osservata, in modo diretto, tramite la produzione di $H^{\pm\pm}$. Vengono posti limiti inferiori alla sua massa, variabili tra 770 GeV e 870 GeV, con un livello di confidenza del 95%.

Abstract

This thesis exploits the features of final states containing light leptons with same electric charge, produced in LHC proton-proton collisions at $\sqrt{s}$ =13 TeV and collected by the ATLAS detector during the 2015 and 2016 data-taking. Events containing leptons with same electric charge allow to reject a substantial fraction of the background from the Standard Model processes. New physics is searched both indirectly and directly through two processes: the production of a Higgs boson in association with a pair of top quarks ($t\bar{t}H$) and the production of new doubly charged Higgs bosons ($H^{\pm\pm}$). The measurement of the $t\bar{t}H$ signal strength (μ) into leptonic final states provides $\mu = 2.5^{+1.3}_{-1.1}$, compatible at 95% confidence level with the Standard Model prediction $\mu_{t\bar{t}H} = 1$. Regarding direct searches, no evidence for new physics is found in the search for $H^{\pm\pm}$ boson production: lower limits on its mass are set and vary from 770 GeV to 870 GeV at 95% confidence level.

"Good morning!
..and in case I don't see ya:
good afternoon,
good evening
and good night!"

The Truman Show (1998)

Contents

Introduction

The Standard Model of particle physics is the most advanced and predictive theory, up to present day, describing the behaviour of fundamental constituents of matter and their interactions. Although the Standard Model was finalized in ∼1970s, its foundations can be traced back to the first decades of the XXth century.

In order to be considered reliable, a theory has to be supported by experimental evidence. Particle physics is one of the greatest examples of how theory works in synergy with experiments. The Large Hadron Collider (LHC) reached the unprecedented center-of-mass energies of $\sqrt{s}$ =13 TeV and now, for the very first time, allows scientists to explore phase space corners that had never been looked at before.

Particle physics is approaching a crossroad: either signatures for new physics are found or the Standard Model predictions are proved with increasing precision. Both paths allow us to gain information on Nature: complete our theory knowledge or exclude a number of beyond Standard Model theories.

Beyond Standard Model physics is more than a formal desire, it is a necessary completion of the theory required to describe what in Nature cannot be explained by the Standard Model. However, the energy scale for new physics remains unknown although, in many beyond Standard Model scenarios, it is assumed $\mathcal{O}$(1 TeV), within the reach of the LHC. New physics can be searched both indirectly and directly.

Indirect searches are aimed at finding deviations of the Standard Model parameters from theory expectations, such as the Higgs boson couplings, particularly sensitive to new physics. The most important one is the top-Higgs Yukawa coupling, directly measurable through $t\bar{t}H$ production, connected to universe vacuum stability and thus to the energy scale foreseen for new physics phenomena. The value of the coupling is expected to be close to unity, due to the very large mass of the top quark, therefore its high precision measurement is of fundamental importance.

Direct searches for new physics usually involve the production of new mass

resonances. Many beyond Standard Model theories enlarge the Standard Model scalar sector, adding new Higgs bosons, or assume that the Higgs is a composite particle. Left-right symmetric models are particularly appealing: they enlarge the Standard Model symmetry group to restore parity symmetry in weak interactions at higher energy scales and explain light neutrino masses through See-Saw mechanisms. New particles appear in this model, such as doubly charged Higgs bosons $H^{\pm\pm}$, right-handed gauge bosons Z_R, W_R and heavy right-handed neutrinos N_R. Their masses are unknown parameters of the theory and need to be constrained by experiments.

An indirect and a direct search for new physics at the LHC, using final states containing light leptons with same electric charge, are presented in this work. Indeed, most of the Standard Model processes produce leptons with opposite charge and thus the charge requirement helps to reject most of the background from well-known processes. The challenging background for this type of search mainly arises from mis-reconstructed objects: tracks with incorrect charge assignment or mis-identified leptons. Ad hoc techniques are implemented for the estimation of the magnitude of these background sources into the regions where the signal is expected to appear. Lepton final states provide key signatures for many new physics scenarios and have the advantage of carrying low systematic uncertainties associated with their reconstruction.

The aim of this work is the search for $t\bar{t}H$, $H^{\pm\pm}$, W_R and N_R production using same charge leptons using the ATLAS detector during 2015 and 2016, in LHC pp collisions at a center-of-mass energy of $\sqrt{s} = 13$ TeV. All the processes previously described share a common feature: the decays into same charge leptons. Each process has well defined characteristics; for example $t\bar{t}H$ production leads to final states with large number of jets. However, several features connect these channels, especially in the techniques used to estimate background from mis-reconstructed objects. New physics might manifest here as an excess of events in the search for $t\bar{t}H$ production or as a resonant peak hinting to the production of particles predicted by left-right symmetric models. It is clear that a natural evolution for such searches is a model independent search into same charge lepton final states.

The first chapter of this work presents the theoretical framework: the Standard Model, its limitations and left-right symmetric models. The second chapter focuses on their respective phenomenology, their production at the LHC and their decays inside ATLAS. The third and fourth chapters describe the LHC collider and the ATLAS detector, their performance, the challenging environment of Run 2 collisions and how particle reconstruction is performed in ATLAS. Since many aspects of the analyses share the same methodologies (i.e. Monte Carlo simulation, data processing, background

estimation and statistical treatment), they are presented in a common way in the fifth chapter. The sixth chapter illustrates the search for the Standard Model $t\bar{t}H$ production into multi-lepton final states, with particular attention to the final state containing exactly two same charge leptons. The last chapter presents the search for $H^{\pm\pm}$, W_R and N_R production under the assumption of left-right symmetric models. Finally, the work performed on the LUCID detector is shown in an Appendix.

Chapter 1

The Standard Model of particle physics and beyond

Quantum mechanics, gauge theory, statistical behaviour of particles (according to their spin) and special relativity are the ingredients of the Standard Model (SM) [1]. Out of the four fundamental forces of physics, the SM deals with the electromagnetic, strong and weak interactions. The fourth fundamental interaction, gravity, does not find place inside the SM since, up to now, it cannot be explained in terms of quantum field theories upon which the model is built. A variety of experiments, from accelerator machines, underground or space-based observatories, conducted over many years led to the confirmation of the SM. This chapter provides an overview of the SM, through gauge theories and the Higgs mechanism, and shows how open questions call for models beyond the SM (BSM).

1.1 The Standard Model

The SM is presented in terms of its fundamental constituents. According to their spin values, all particles are divided into *fermions* and *bosons*: fermions are 1/2 spin particles obeying Fermi-Dirac statistics while bosons have integer spin and follow Bose-Einstein statistics.
Spin is a *quantum number*, a property describing the value of conserved quantities under transformations of quantum systems, namely rotations. Fermions are divided into *leptons* and *quarks*, whose properties are described in terms of the following quantum numbers:

- *electric charge* carried by all particles except neutrinos. All other leptons have electric charge $Q=\pm 1$. Quarks carry a fraction of the electron

charge: u,c and t have $Q{=}\pm 2/3$ while d,s and b have $Q{=}\mp 1/3$. Hadrons always carry integer charge.

- *colour charge* carried only by quarks and responsible for *confinement*, which makes impossible to observe free quarks. They need to be confined in colour charge singlets, namely *hadrons*, such as the proton.
- *leptonic number* associated to each lepton and globally conserved by all the interactions.
- *flavour number* also associated to each lepton. In the quark sector, flavour is different for each quark and it is not conserved by weak interactions.

Quarks and leptons are further divided into three families, or generations:

$$\begin{pmatrix} e^- \\ \nu_e \end{pmatrix} \quad \begin{pmatrix} \mu^- \\ \nu_\mu \end{pmatrix} \quad \begin{pmatrix} \tau^- \\ \nu_\tau \end{pmatrix}$$

$$\begin{pmatrix} u \\ d \end{pmatrix} \quad \begin{pmatrix} c \\ s \end{pmatrix} \quad \begin{pmatrix} t \\ b \end{pmatrix}$$

with increasing mass ordering, and categorized by lepton number and flavour. In the SM, fermions interact through the exchange of field quanta, which are the photon γ for the electromagnetic interaction, the Z^0 and $W^\pm$ bosons for the weak force and the *gluon* for the strong force. The last experimentally observed particle of the SM is the *Higgs boson*, responsible for the mass of SM particles as we will see in Sec. 1.2.

1.1.1 Basics of gauge theory

The simplest example of *gauge theory* is provided by the theory of quantum electrodynamics, where the electromagnetic potential, generating the fields in Maxwell's equations, is not uniquely defined. *Gauge invariance* lays, in fact, in the possibility to arbitrarily choose the potential to describe the same electromagnetic field. This property of the electromagnetic potential translates into the invariance of the system lagrangian under the transformation of a certain group of symmetry.
Symmetries can be divided in two groups:

- *global symmetries* for which, under certain transformations, lagrangians change in every point of the space-time by the same amount;

- *local symmetries* when lagrangians are invariant under transformation of parameters different from point to point.

According to Noether's theorem, the continuous symmetry of the lagrangian leads to conserved quantities. We are interested in a theory whose equations transform under parameters depending on the space-time coordinates: local symmetries are the ones on top of which the SM is defined. The SM group structure is:

$$SU(3)_C \otimes SU(2)_L \otimes U(1)_Y \tag{1.1}$$

where $SU(3)_C$ is the non-abelian group associated with the strong force, while $SU(2)_L \otimes U(1)_Y$ is associated to the electroweak interaction. We start by describing the basis of the electromagnetic interactions and quantum chromodynamics.

1.1.2 Quantum Electrodynamics and Chromodynamics

Quantum Electrodynamics (QED) describes how interactions between electrically charged particles occur. A relativistically covariant formulation of Maxwell's theory can be obtained by expressing the electric and magnetic field strengths $\vec{E}$ and $\vec{B}$ in terms of the four-vector potential $A^\mu(x)$. The Lorentz-invariant lagrangian describing the free propagation of an electromagnetic field is written in terms of the tensor $F^{\mu\nu} = \partial^\mu A^\nu - \partial^\nu A^\mu$ and, adding a free fermion ψ propagation term, gives the following:

$$\mathcal{L}_{QED} = \bar{\psi}(i\gamma^\mu \partial_\mu - m)\psi - \frac{1}{4} F^{\mu\nu} F_{\mu\nu} \tag{1.2}$$

where the first term is kinetic term for free fermion propagation, the second one the kinetic term for photon propagation and γ^μ are the Dirac matrices [1]. Equation 1.2 still contains no interaction terms. We want to make this equation invariant under local transformations of the $U(1)$ symmetry group of the type:

$$\psi \rightarrow \psi' = e^{iq\alpha(x)}\psi \tag{1.3}$$

where $\alpha(x)$ is a real parameter function of the space-time coordinate x. It can be shown that we need to replace the derivative operator ∂_μ with the *covariant derivative* defined as $D_\mu = \partial_\mu + iqA_\mu$, to keep the invariance of the lagrangian under local transformation of the $U(1)$ symmetry group. Writing again the lagrangian with the replacement $\partial_\mu \rightarrow D_\mu$ gives the following result:

$$\mathcal{L}_{QED} = \bar{\psi}(i\gamma^\mu \partial_\mu - m)\psi - \frac{1}{4} F^{\mu\nu} F_{\mu\nu} - q\bar{\psi}\gamma^\mu A_\mu \psi \tag{1.4}$$

where the main difference from Eq. 1.2 is the last term. It follows that the requirement of local gauge invariance in our gauge choice, transforming the A_μ field as:

$$A_\mu(x) \rightarrow A'_\mu(x) \equiv A_\mu(x) - \partial_\mu \alpha(x), \tag{1.5}$$

originates the interaction term between the charged fermion and the potential of the electromagnetic field A_μ, which is related to the *gauge boson* γ, carrier of the electromagnetic field and generator of the $U(1)$ symmetry group. The interaction is described, at the fundamental level, by the Feynman diagram in Fig.1.1.

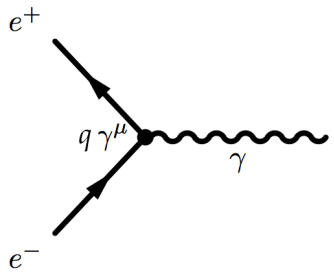

Figure 1.1: Feynman diagram for the simplest QED vertex, showing electron-positron annihilation.

Similarly to charged particles that interact through the exchange of a photon, quarks interact via exchange of the mediator of the strong interaction: the *gluons*. **Quantum Chromodynamics (QCD)**, based on the same gauge principles as QED, describes strong interactions. Differently from the electromagnetic charge, the colour charge presents three possible states so quarks are represented as three component spinors ψ transforming under the $SU(3)$ symmetry group. The $SU(3)$ group has 8 generators, usually defined by the Gell-Mann matrices λ^a [1], and each element of the group can be defined in terms of 3×3 unitary matrices in the form $U = e^{-i\alpha_a \frac{\lambda^a}{2}}$. The non-abelian feature of the $SU(3)$ QCD group arises from the fact that, in contrast with QED where photons, being neutral, do not interact among themselves, gluons also carry colour charge and interact with each other. The definition of the covariant derivative for $SU(3)$ is the following

$$D_\mu = \partial_\mu + i g_s A_{\mu a} T^a \tag{1.6}$$

where T^a is a generator of the group, g_s the coupling constant of QCD and A_μ the gluonic propagator of the strong interaction. The covariant derivative

in Eq. 1.6 changes the representation of the tensor field:

$$F^a_{\mu\nu} = \partial_\mu A^a_\nu - \partial_\nu A^a_\mu + g_s f^{abc} A^b_\mu A^c_\nu \tag{1.7}$$

where f^{abc} are the fine structure constants of the group, in such a way that the last term in Eq. 1.7 differs from zero, reflecting the non-commutative feature of QCD generators. This last term describes the *self-interaction* of gluons and is a direct consequence of the requirement of local gauge invariance of the theory. Self-interaction terms between gluons are shown in the second and third diagram of Fig. 1.2.

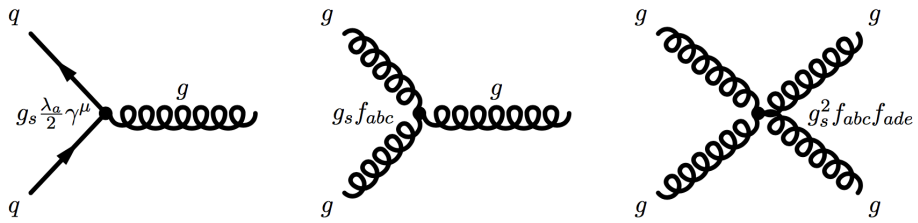

Figure 1.2: Feynman diagram for QCD vertices: in order, quark-gluon interaction, three-gluon vertex and four-gluon vertex.

Finally, the QCD lagrangian is written as:

$$\mathcal{L}_{QCD} = \sum_f \bar{q}_f (i\gamma^\mu \partial_\mu - m_f) q_f - g_s \sum_f (\bar{q}_f \gamma^\mu \frac{\lambda_a}{2} F^a_\mu q_f) - \frac{1}{4} F^a_{\mu\nu} F^{\mu\nu}_a \tag{1.8}$$

where the index $f = (u, d, c, s, t, b)$ identifies quark flavour.

Coupling Constants

As shown in Eq. 1.2 and 1.8, QED and QCD interactions have different *coupling constants*, i.e. different relative strengths when compared to each other. Usually the couplings are defined as follows:

$$\alpha_{QED} = \frac{e^2}{4\pi\epsilon_0 \hbar c} \qquad \alpha_{QCD} = \frac{g_s^2}{4\pi} \tag{1.9}$$

where e is the electron charge, $\hbar$ the Planck constant, ϵ_0 the free space permittivity and c the speed of light. Numerically, in the low energy limit, $\alpha_{QED} \sim 1/137$ and $\alpha_{QCD} \sim 1$. Although we refer to them as *constants*, the couplings themselves depend both on the energy scale $\mathcal{Q}$ at which a given process happens and on the definition of what we call *vacuum*. Let us now

imagine to send a probe particle towards a free propagating charged fermion, quark or gluon. The vacuum surrounding, for instance, a free electron can be described as a cloud of virtual electron-positron pairs appearing and annihilating from and into photons. Virtual e^+ and e^- pairs tend to arrange themselves accordingly to their charge, in such a way that the resulting effect is a *screening* of the electron bare charge. This is known as *vacuum polarization* and shows how the effective charge of a particle gets smaller at higher distances (or lower energies). We can similarly translate the vacuum interpretation in terms of QCD. In this case, however, besides quark-antiquark creation and annihilation which act in a similar way to electron-positron virtual loops in QED, we also need to take into account gluon self-interaction. As we know, gluons carry colour charge causing an *anti-screening* effect of the bare colour charge, which appears higher at higher distances.
As an effective result, α_{QED} and α_{QCD} are **running couplings** since their value depend on the energy of the processes. Moreover, this dependence on energy does not follow the same behaviour for α_{QED} and α_{QCD}. The running coupling QCD has an important effect on quarks behaviour known as **confinement**: given that α_{QCD} becomes stronger at higher distances, it is impossible to separate quarks from a combined state, such as a hadron, and we cannot observe free quarks. On the contrary, quarks, inside hadrons, behave as free particles, because their coupling is weaker, allowing to use perturbation theory to provide quantitative predictions for hadronic interactions; this is the so-called **asymptotic freedom**.

Let us suppose we want to calculate the cross-section for a given process, e.g. $pp \to t\bar{t}H$. To perform such calculation we use perturbative QCD. At the simplest level of theory calculation (called *Leading-Order* (LO) or *tree-level*), to evaluate the cross-section for a given process, one could in principle only take into account the QED and QCD vertices shown in Fig. 1.1 and 1.2. However, LO predictions for a process are not always accurate enough to describe experimental data. Like the expansion terms in a series, perturbative QCD expands a series in powers of α_{QCD}.

We can push theory predictions to higher order correction terms: *Next-to-Leading-Order* (NLO) or *Next-to-Next-to-Leading-Order* (NNLO) corrections, as shown in Fig. 1.3. NNLO calculations are in general much more complicate and, up to now, we have a prediction beyond α^2_{QCD} precision only for very few processes, e.g. $gg \to H$.

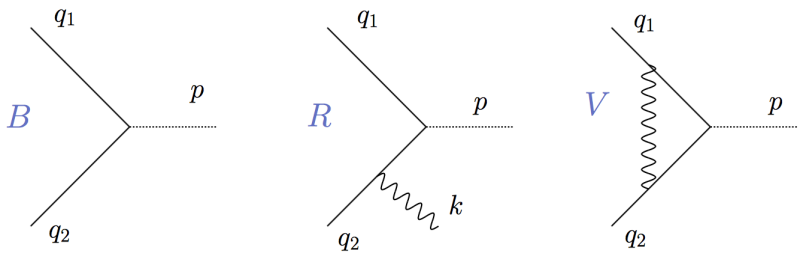

Figure 1.3: Feynman diagrams accounted for when performing a QCD calculation in powers of α_{QCD}. The three terms are respectively proportional to $\sim$1, $\sim \alpha_{QCD}$ and $\sim \alpha^2_{QCD}$. They represent, respectively, the "born" Matrix Element (ME) for a two-quark interaction, the real initial state gluon emission from one of the interacting partons and a virtual loop gluon exchange between the two interacting partons in the initial state.

1.1.3 Weak interactions and unified electroweak model

Each SM fermion experiences weak interactions which, at low energy, present a much smaller relative intensity compared to the electromagnetic and to the strong interactions. The *weakness* of this force can be quantified by measuring the lifetime of particles decaying via this interaction, such as the pion or the muon, which are typically of the order of 10^{-8} s. These lifetimes are extremely long compared to the lifetimes of particles decaying via strong interactions ($\sim 10^{-23}$ s) or through electromagnetic interactions ($\sim 10^{-16}$ s).

The first attempt to give a theoretical explanation to the *β-decay* which, at a nuclear level, is described by the process:

$$n \rightarrow p + e^- + \bar{\nu}_e \tag{1.10}$$

was given by Enrico Fermi in 1932. Fermi initially built his theory on the basis of the electromagnetic interaction and described weak interactions as a point-like vectorial (V) current interaction of four fermions. Driven by the observation that weak interactions violate parity[1], Fermi's theory was extended introducing to the model an axial (A) term which conserved its

[1] Particles exists in two helicity states: left-handed or right-handed. Weak interactions are found to involve only left-handed particles or right-handed anti-particles, which are defined by the chirality projector operators as:

$$\psi^L(x) = \frac{1-\gamma_5}{2}\psi(x), \qquad \psi^R(x) = \frac{1+\gamma_5}{2}\psi(x) \tag{1.11}$$

respectively identifying left-handed and right-handed particles.

sign under parity transformations. The final structure of the theory became a V-A current of the type [1]:

$$J_\mu(x) = \sum_l \bar{\psi}_l(x)\gamma_\mu(1-\gamma_5)\psi_{\nu l}(x) \tag{1.12}$$

where $l = \{e, \mu, \tau\}$ and $\nu l = \{\nu_e, \nu_\mu, \nu_\tau\}$. Writing separately the V and A terms

$$J^V_\mu = \sum_l \bar{\psi}_l(x)\gamma_\mu\psi_{\nu l}(x) \tag{1.13}$$

$$J^A_\mu = \sum_l \bar{\psi}_l(x)\gamma_\mu\gamma_5\psi_{\nu l}(x) \tag{1.14}$$

it can be shown, thanks to the properties of Dirac matrices, that only the V term changes its sign under parity transformation so that in weak interactions, where products of the V·A terms appear, parity is violated.
We now want to make the weak interaction a gauge theory and, in analogy to what we did for the QED and QCD, we require it to be invariant for local gauge symmetries.

During the 60's, Glashow, Salam and Weinberg started to work on a possible unification of the electromagnetic and weak interactions. Glashow [2] first pointed out that, in analogy with QED, weak interactions could also be mediated by vector gauge bosons. Weinberg in 1967 [3] and Salam in 1968 [4], reached independently the same result which led to the construction of the unified electroweak (EW) theory.
To develop the unified theory we need to identify a symmetry group. We already know that QED is invariant for local gauge transformations of the $U(1)$ symmetry group. We can extend this concept by introducing a new quantum number, called *weak isospin* T, generating a $SU(2)$ algebra as well as the *hypercharge* Y, generating a $U(1)$ algebra. Hypercharge and the third component of the weak isospin T^3 are connected to the electric charge by the relation:

$$Q = T^3 + \frac{Y}{2} \tag{1.15}$$

known as the Gell-Mann–Nishijima formula. From now on we will identify the electroweak symmetry group as $SU(2)_L \times U(1)_Y$. Under the $SU(2)_L$ symmetry group, fermion fields are divided into left-handed isospin doublets and right-handed isospin singlets, such as:

$$\psi_1(x) = \begin{pmatrix} u_L \\ d_L \end{pmatrix}, \quad \psi_2(x) = u_R, \quad \psi_3(x) = d_R \tag{1.16}$$

where the same notation stands for leptons. The local gauge transformation for the $U(1)_Y$ group is of the type:

$$\psi(x) \rightarrow e^{i\frac{Y}{2}\beta(x)}\psi(x) \tag{1.17}$$

where β identifies an arbitrary space-time dependent parameter. $SU(2)_L$ transformations only act on left-handed fermion fields and are of the type:

$$U_L = e^{i\frac{\sigma_a}{2}\alpha_a(x)} \tag{1.18}$$

where U_L are 2×2 unitary matrices, σ_a are the $SU(2)$ generators know as Pauli matrices and α_a free parameters. To construct the theory, we introduce the $B_\mu(x)$ field for the $U(1)_Y$ symmetry group and three $W^a_\mu(x)$ fields for the $SU(2)_L$ group. The covariant derivative for the electroweak interaction is written as:

$$D_\mu = \partial_\mu + ig^{'}\frac{Y}{2}B_\mu(x) + ig\frac{\sigma_a}{2}W^a_\mu(x) \tag{1.19}$$

where $g^{'}$ and g are the coupling constants for $U(1)_Y$ and $SU(2)_L$. The Lagrangian for the EW interaction is:

$$\mathcal{L}_{EW} = \sum_{j=1}^{3} i\bar{\psi}_j(x)\gamma^\mu D_\mu\psi_j(x) - \frac{1}{4}B_{\mu\nu}B^{\mu\nu} - \frac{1}{4}W^a_{\mu\nu}W^{\mu\nu}_a \tag{1.20}$$

where the first term describes lepton propagation and also contains the interaction term, while the last two terms describe EW free field propagation. The $\vec{W}^a_\mu(x) = (W^1_\mu, W^2_\mu, W^3_\mu)$ field is composed by two charged and one neutral components; the two charged fields combine as follows:

$$W^\pm_\mu = \sqrt{\frac{1}{2}}(W^1_\mu \mp iW^2_\mu) \tag{1.21}$$

representing the two charged $W^\pm_\mu$ bosons involved in charged weak currents. Furthermore, the B_μ and W^3_μ fields also mix and generate the neutral physical states:

$$A_\mu = B_\mu\cos\theta_W + W^3_\mu\sin\theta_W \tag{1.22}$$

$$Z_\mu = -B_\mu\sin\theta_W + W^3_\mu\cos\theta_W \tag{1.23}$$

where A_μ is the electromagnetic field, Z_μ the mediator of neutral weak interactions and θ_W the Weinberg angle. It can be proved that, if we write the neutral electroweak current, to obtain back the term for the pure electromagnetic interaction we need to require:

$$g\sin\theta_W = g^{'}\cos\theta_W = e \tag{1.24}$$

and that, as a consequence, the *mixing angle* θ_W can be expressed in terms of the two independent coupling constants: $\tan\theta_W = g'/g$.

The mixing relation points out an important feature of the weak interaction: when a first attempt of unification between weak and electromagnetic interaction was made, it was argued that weak interactions might have been a *manifestation* of the electromagnetic interaction [5]. On the contrary, the relation between coupling constants shows that the physical interpretation of weak interactions is more complicated: the electromagnetic interaction seems to "sit across" weak isospin and weak hypercharge, modulated by the Weinberg angle. The value of the Weinberg angle is obtained by parity violation experiments, and its value corresponds to $\sim 30°$ [6].
At this level we have to note that in Eq. 1.20, SM gauge bosons appear to be massless[2]. Indeed, introducing mass terms into those equations, would spoil the local gauge invariance of the theory, destroying therefore theory renormalizability. As a consequence, mass terms cannot be introduced *by hand* into the lagrangian. On the other hand the need for massive gauge bosons comes from the evidence that weak force is a short-range interaction. This must imply a quite massive gauge boson exchange. From the effective lagrangian of the weak interaction at low energy (which has to reduce to Fermi's model), the W propagator can be related to Fermi's constant G_F through the relation:

$$\frac{G_F}{\sqrt{2}} = \frac{g^2}{8M_W^2} \tag{1.25}$$

hinting to a weak charged massive boson of mass $\sim$100 GeV. This hypothesis was later confirmed by the discovery of the two massive weak vector bosons by the UA1 [7, 8] and UA2 [9, 10] Collaborations at CERN in 1983. We will now go through the mechanism able to naturally introduce mass terms in the SM lagrangian.

1.2 Spontaneous Symmetry Breaking and mass generation

Before getting into the details of the spontaneous symmetry breaking (SSB) of the $U(1)_Y \times SU(2)_L$ group, we start with a simple scalar and real case. Let us take into account the following lagrangian for scalar particles:

$$\mathcal{L} \equiv T - V = \frac{1}{2}\left(\partial_\mu \phi\right)^2 - \left(\frac{1}{2}\mu^2\phi^2 + \frac{1}{4}\lambda\phi^4\right) \tag{1.26}$$

[2] Only kinematic terms for free boson fields propagation appear in the lagrangian.

where $\lambda > 0$, symmetric for the replacement of $\phi \to -\phi$. The potential has two possible forms depending on the sign of μ^2, as shown in Fig. 1.4.

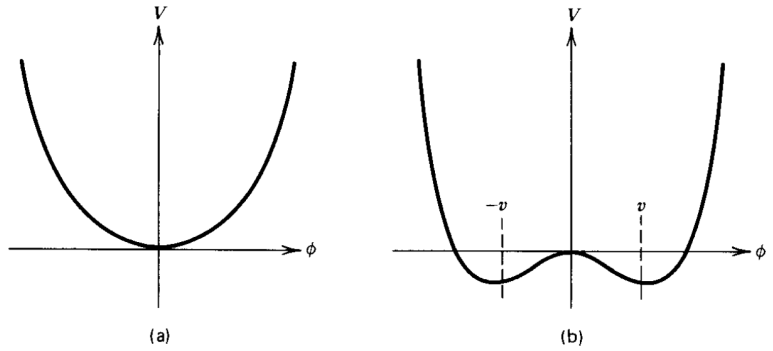

Figure 1.4: Functional behaviour of the $V(\phi)$ scalar potential as a function of the sign of μ^2: (a) $\mu^2 > 0$ and (b) $\mu^2 < 0$. In both cases $\lambda > 0$.

The first case ($\mu^2 > 0$) describes a scalar field with mass μ and four-particles self-interactions terms have coupling λ. We have a uniquely-defined *ground state*, identified by $\phi = 0$. The second case ($\mu^2 < 0$) has two minima:

$$\phi = \pm v, \quad \text{with} \quad v = \sqrt{-\mu^2/\lambda} \tag{1.27}$$

which we can expand by a perturbation $\eta(x)$ in the following way:

$$\phi = v + \eta(x). \tag{1.28}$$

where we choose the positive v vacuum state. If we substitute Eq. 1.28 into 1.26, we find:

$$\mathcal{L} = \frac{1}{2}(\partial_\mu \eta)^2 - \lambda v^2 \eta^2 - \lambda v \eta^3 - \frac{1}{4}\lambda \eta^4 + \text{ const} \tag{1.29}$$

in which appears a field η with mass:

$$m_\eta = \sqrt{2\lambda v^2} = \sqrt{-2\mu^2} \tag{1.30}$$

and the higher-order expansion terms in η correspond to the field self-interactions. The two lagrangians 1.26 and 1.29 are equivalent, meaning that a transformation of the type 1.28 cannot change the physics. If the two langrangians describe the same physical state, an exact solution for Eq. 1.26 or 1.29 would lead to the same physics. It is however impossible to perform such a calculation and for this reason we must use perturbation theory and calculate the fluctuations around the minimum energy state. Expanding 1.26 around the

minimum energy state $\phi = 0$ leads to a non-converging perturbation series because the minimum is unstable. Using instead 1.29, and expanding in η around the stable vacuum state $\phi = +v$, gives the correct picture of physics. Using this procedure, we reached two important physical results: we generated a massive field η and we broke the lagrangian symmetry by choosing a specific vacuum state to perform our perturbative calculations on.

1.2.1 The Higgs mechanism

To explain how masses are generated in the SM, we extend the previous case to the spontaneous breaking of a local $U(1)$ symmetry. Assuming a scalar and complex field whose lagrangian stays invariant under the transformation of the type $\phi \to e^{i\alpha(x)}\phi$ and defining the following covariant derivative:

$$D_\mu = \partial_\mu - ieA_\mu \tag{1.31}$$

we can write the lagrangian as:

$$\mathcal{L} = (\partial_\mu + ieA^\mu)\phi^*(\partial_\mu - ieA_\mu)\phi - \mu^2\phi^*\phi - \lambda(\phi^*\phi)^2 - \frac{1}{4}F_{\mu\nu}F^{\mu\nu}. \tag{1.32}$$

We write the vacuum states as:

$$\phi_1^2 + \phi_2^2 = v^2 \quad \text{with} \quad v^2 = -\frac{\mu^2}{\lambda} \tag{1.33}$$

and visualize them as in Fig. 1.5.

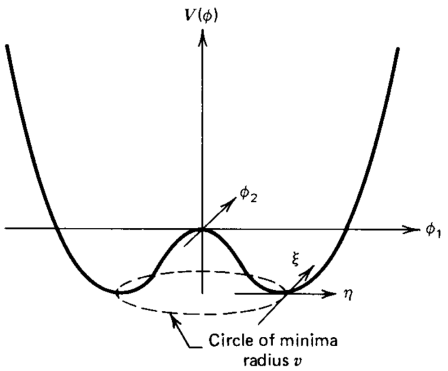

Figure 1.5: Functional behaviour of the $V(\phi)$ for a complex scalar field where μ^2 <0 and $\lambda >0$.

We now choose again our minimum energy state to be $\phi_1 = v$, $\phi_2 = 0$ and perform the vacuum perturbation:

$$\phi(x) = \sqrt{\frac{1}{2}}(v + \eta(x) + i\xi(x)) \tag{1.34}$$

to obtain the following lagrangian:

$$\mathcal{L} = \frac{1}{2}(\partial_\mu \xi)^2 + \frac{1}{2}(\partial_\mu \eta)^2 - v^2\lambda\eta^2 + \\ + \frac{1}{2}e^2v^2A_\mu A^\mu - evA_\mu\partial^\mu\xi - \frac{1}{4}F_{\mu\nu}F^{\mu\nu} + \text{interaction terms.} \tag{1.35}$$

We see appearing a massless Goldstone boson ξ[3], a massive scalar field η and a massive vector A_μ, for which:

$$m_\xi = 0, \tag{1.36}$$
$$m_\eta = \sqrt{2\lambda v^2}, \tag{1.37}$$
$$m_A = ev. \tag{1.38}$$

To get rid of the unphysical Goldstone boson we generated in this procedure, we can use a simple gauge transformation of fields as follows:

$$\phi \rightarrow \sqrt{\frac{1}{2}}(v + h(x))e^{i\theta(x)/v}, \tag{1.39}$$
$$A_\mu \rightarrow A_\mu + \frac{1}{ev}\partial_\mu\theta, \tag{1.40}$$

where we choose $\theta(x)$ so that h is real. Substituting the new fields into 1.35, we obtain:

$$\mathcal{L} = \frac{1}{2}(\partial_\mu h)^2 - v^2\lambda h^2 + \frac{1}{2}e^2v^2A_\mu^2 - \lambda v h^3 - \frac{1}{4}\lambda h^4 \\ + \frac{1}{2}e^2A_\mu^2h^2 + ve^2A_\mu^2h - \frac{1}{4}F_{\mu\nu}F^{\mu\nu} \tag{1.41}$$

where the Goldstone boson disappeared[4]. Equation 1.41 shows how we generated two interacting massive particles (the A_μ vector gauge bosons) and a new massive scalar field h, through the **Higgs mechanism**.

1.2.2 Spontaneous Breaking of a local SU(2) symmetry

The final step is to extend the Higgs mechanism to break a local $SU(2)$ symmetry. Choosing a $SU(2)$ doublet of complex scalar fields of the type:

$$\phi = \begin{pmatrix} \phi_\alpha \\ \phi_\beta \end{pmatrix} = \sqrt{\frac{1}{2}}\begin{pmatrix} \phi_1 + i\phi_2 \\ \phi_3 + i\phi_4 \end{pmatrix} \tag{1.42}$$

[3] The Goldstone theorem says that whenever we encounter a continuous symmetry breaking a massless scalar has to appear.

[4] The Goldstone boson was indeed an unnecessary degree of freedom of the theory, since we were able to eliminate it by simply using a gauge transformation.

invariant under local $SU(2)$ transformations $\phi \rightarrow e^{i\alpha_a \tau(x)_a/2}\phi$, requires the definition of a new covariant derivative:

$$D_\mu = \partial_\mu + ig\frac{\tau_a}{2}W_\mu^a \tag{1.43}$$

letting us write the lagrangian:

$$\mathcal{L} = \left(\partial_\mu\phi + ig\frac{1}{2}\tau W_\mu\phi\right)^\dagger \left(\partial^\mu\phi + ig\frac{1}{2}\tau W^\mu\phi\right) - V(\phi) - \frac{1}{4}W_{\mu\nu}W^{\mu\nu} \tag{1.44}$$

where the Higgs potential is:

$$V(\phi) = \mu^2\phi^\dagger\phi + \lambda(\phi^\dagger\phi)^2. \tag{1.45}$$

Making the vacuum choice to be $\phi_1 = \phi_2 = \phi_4 = 0$ and $\phi_3^2 = -\mu^2/\lambda \equiv v^2$ leads to the following expression for the field:

$$\phi(x) = \frac{1}{2}\begin{pmatrix} 0 \\ v + h(x) \end{pmatrix}. \tag{1.46}$$

The *vacuum expectation value* (vev) associated to the ground state is written as:

$$|\phi_0|^2 = -\frac{\mu^2}{2\lambda} \equiv \frac{v^2}{2}. \tag{1.47}$$

As a summary, we extended the Higgs mechanism to a $SU(2) \times U(1)$ symmetry, and our choice of a vacuum state leaves one scalar Higgs field ϕ_3 with $T_3 = -1/2$.
By using a similar approach to the previous section, we write the Higgs lagrangian as:

$$\mathcal{L}_{Higgs} = \frac{1}{2}\partial_\mu h\partial^\mu h + (v+h)^2\left(\frac{g^2}{4}W_\mu^\dagger W^\mu + \frac{g^2}{8\cos^2\theta_W}Z_\mu Z^\mu\right) - \lambda v^2h^2 - \lambda v h^3 - \frac{\lambda}{4}h^4. \tag{1.48}$$

Equation 1.48 shows how we eventually obtained, from a SSB mechanism, mass terms for the $W^\pm$ and Z^0 bosons, while leaving a massless photon. This procedure also generates a new scalar boson h, the so-called Higgs boson. The Higgs mechanism solves the problem of mass generation although, at the same time, introduces several new free parameters to the theory. The vev of the Higgs field v, for instance, is directly connected to the Fermi's constant by the relation:

$$v^2 = \frac{1}{\sqrt{2}G_F} \simeq 246\ \text{GeV}^2 \tag{1.49}$$

while λ remains a free parameter of the theory as well as the mass of the Higgs boson. The way weak bosons get their masses, through their coupling to the Higgs boson, also allows us to measure the values for these couplings, using the relations:

$$g_{HVV} = \frac{2m_V^2}{v}, \quad g_{HHVV} = \frac{2m_V^2}{v^2}, \quad g_{HHH} = \frac{3m_H^2}{v}, \quad g_{HHHH} = \frac{3m_H^2}{v^2}, \quad (1.50)$$

where, however, we need to know the value of the Higgs boson mass. From a purely aesthetic point of view, the more free parameters are added to a theory, the more it hints to a more complete theory laying beyond. This fact is one of the reasons to look for theories BSM.

1.2.3 Yukawa couplings to fermions

So far, EW symmetry breaking generates gauge boson masses leaving SM fermions massless. Mass terms for fermions can be added to the lagrangian through the so-called *Yukawa couplings* to the Higgs boson, without spoiling the local gauge-invariance.
We write the following Yukawa lagrangian for leptons:

$$\mathcal{L}_{Yukawa}^{Leptons} = -G_l \left[(\bar{\nu}_l, \bar{l})_L \begin{pmatrix} \phi^+ \\ \phi^0 \end{pmatrix} l_R + \bar{l}_R (\phi^-, \bar{\phi^0}) \begin{pmatrix} \nu_l \\ l \end{pmatrix}_L \right] \quad (1.51)$$

which, after SSB becomes:

$$\mathcal{L}_{Yukawa}^{Leptons} = -\frac{G_l}{\sqrt{2}} v(\bar{l}_L l_R + \bar{l}_R l_L) - \frac{G_l}{\sqrt{2}} (\bar{l}_L l_R + \bar{l}_R l_L) h \quad (1.52)$$

generating lepton masses of value $m_l = \frac{G_l v}{\sqrt{2}}$. Here it is important to note that, given the unknown value for G_l, also lepton masses are in principle free parameters of the theory. It also must be noted that neutrinos, which do not have right-handed states, remain massless.
In the same way, we describe Higgs interaction with quarks obtaining the lagrangian:

$$\mathcal{L}_{Yukawa}^{Quarks} = -m_d^i \bar{d}_i d_i \left(1 + \frac{h}{v}\right) - m_u^i \bar{u}_i u_i \left(1 + \frac{h}{v}\right) \quad (1.53)$$

where i is the number of quark doublets. In analogy to the lepton case, quark masses are also a free parameter of the theory. The $SU(3)_C$ color symmetry of QCD in untouched by the Higgs mechanism.
Both from Eq. 1.52 and 1.53 it is clear that Higgs coupling to leptons and

quarks is proportional to the particle mass.
The final SM lagrangian can be eventually written as the sum of different contributions:

$$\mathcal{L}_{SM} = \mathcal{L}_{EW} + \mathcal{L}_{Higgs} + \mathcal{L}_{Yukawa}^{Leptons} + \mathcal{L}_{Yukawa}^{Quarks} + \mathcal{L}_{QCD}. \tag{1.54}$$

1.3 The Standard Model: successes and open questions

The discovery of the Higgs boson in 2012 by the ATLAS [11] and CMS [12] Collaborations at CERN, is often regarded as the biggest success in the confirmation of the SM. We referred to the *Higgs mechanism*, although the existence of a new scalar boson responsible for SM particle masses was theorized more than 50 years ago by Higgs [13], Brout and Englert [14] independently. The discovery of the Higgs boson is, however, only the last step reached by particle physics experiments in confirming the predictive power of the SM.

Precision measurements of θ_W, m_Z, m_W, branching ratios etc. allow to validate theory predictions and to put constraints on new physics (NP) processes. Table 1.1 shows the agreement between experimental data and theory predictions.

Quantity	Measured Value [GeV]	Standard Model best-fit	
m_t	173.34 ± 0.81	173.76 ± 0.76	
m_W	80.387 ± 0.016 (Tevatron) 80.376 ± 0.033 (LEP 2) 80.370 ± 0.019 (ATLAS) [15]	80.361 ± 0.006	
Γ_W	2.046 ± 0.049 (Tevatron) 2.195 ± 0.083 (LEP 2)	2.089 ± 0.001	-0.9 1.3
m_Z	91.1876 ± 0.0021	91.1880 ± 0.0020	-0.2
Γ_Z	2.4952 ± 0.0023	2.4943 ± 0.0008	0.4

Table 1.1: Comparison between some of the SM best-fit predictions and the corresponding values from experiments [6]. The top mass as well as the W and Z boson masses, and decay widths, are presented.

1.3.1 What's left: the need for theories beyond

The agreement between theory predictions and the measurements performed in experiments is extremely satisfying. Nevertheless, several hints from Nature, as will be shown in the next sections, do not find explanation inside the existing model.

Grand Unification Theory (GUT)

From an aesthetic point of view, the main motivation to look for a unified theory may be related to the number of free parameters present in the SM [1]. The structure of the symmetry group $SU(3)_C \times SU(2)_L \times U(1)_Y$ reflects in different coupling constants and raises the question weather it is possible to reduce the couplings to a single one. The three coupling constants are not the only free parameters in the theory: we need to add 6 mass parameters for quarks, 3 mixing angles, 1 CP-violating phase, 2 parameters for the Higgs potential and other 3 mass parameters for leptons (neglecting neutrino masses and mixing). In total, there are 18 free parameters in the SM. Moreover, quarks and leptons, although being spin $1/2$ structureless particles, seem to have different behaviour under certain types of interactions. Last, but not least, gravitation is absent into the picture and at some energy scale has to enter into the scheme.
The strength of the electromagnetic and weak interactions becomes comparable at energies $\gg M_W^2$ and the strong coupling approaches α_{QED} at very high energy. This observation points to a higher level symmetry which, in the GUT framework, might be identified with only one group of symmetry, reducing in the low energy limit to the SM group. In this picture, if we use the *Minimal Supersymmetric Standard Model* (MSSM) the evolution of the coupling constants is shown in Fig. 1.6. Assuming no further interactions appear up to unification (*desert hypothesis*), the energy scale for GUT theory is $\sim 10^{16}$ TeV.

CP violation

CP transformation is the product of charge conjugation and parity inversion. CP symmetry assumes Nature to be invariant when replacing the particle with its antiparticle and left-handed with right-handed fields. Experimentally, CP symmetry is preserved by electromagnetic and strong interactions but it is violated by weak ones. CP violation in weak interactions was first observed by Cronin and Fitch [16] in K^0 oscillations and more recently confirmed by $B-$mesons experiments. Despite the phenomenological success of the CKM mechanism [6], it fails to accommodate the baryon asymmetry

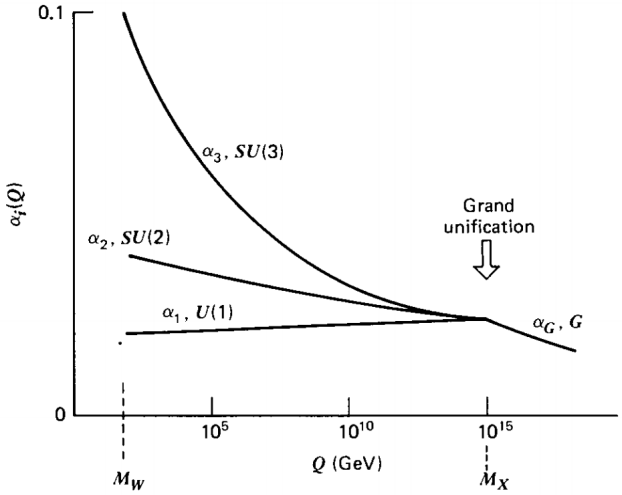

Figure 1.6: Evolution of the running coupling constants α_i with $\mathcal{Q}$ in the MSSM, showing the grand unification behaviour of the strong $SU(3)_C$ and electroweak $SU(2)_L \times U(1)_Y$ interactions at very short distances or at very high energies ($1/\mathcal{Q} \approx 1/M_X$).

observed in nature by several orders of magnitude.
Besides weak interactions, the QCD lagrangian also contains a term which could be responsible for CP violation in strong interactions of the type:

$$\mathcal{L}_{\text{strongCP}} = \theta \frac{\alpha_s}{8\pi} F_{a\mu\nu} F_a^{\mu\nu} \tag{1.55}$$

which leads to an enormous neutron electric dipole moment, unless θ is tiny ($\theta < 10^{-9}$) [17]. Since CP violation is not observed in strong interactions, the CP phase is set to zero. Therefore we have two possibilities: θ is exactly zero, requiring a new symmetry to be spontaneously broken by the introduction of a new gauge field (the *axion* as suggested by Peccei-Quinn [17]), or θ is unnaturally small. This *fine-tuning* is considered unnatural and it is known as the *strong CP problem*. This is one of the strongest motivations to search for an extended symmetry of Nature which would set to zero the strong CP phase.

Dark matter

Historically, the first strong indication for the existence of dark matter came from astrophysical observations. Galaxies are astrophysical objects presenting a higher matter density in proximity of their center, and their visible density of matter, mainly due to stars, decreases getting away from

the central point. Objects which are closer to the center of the galaxy are expected to move, following a Keplerian motion, at higher speeds when compared to the peripheral objects. On the contrary, the rotation velocity curves of galaxies appear to be flat at increasing distances, suggesting the existence of non-visible and gravitationally interacting matter. This latter is referred to as *dark matter* since it does not seem to interact electromagnetically.
Apart from galaxy motion, further proofs in favour of dark matter come from *Cosmic Microwave Background* (CMB) [18] patterns as well as from *gravitational lensing* [19].
So far we know that approximately 5% of the mass-energy in the Universe is formed of ordinary baryonic matter, 23% of dark matter and the rest in the form of an unknown type of *dark energy*. Dark matter is usually divided into *hot* (relativistic), *warm* (semi-relativistic) and *cold* (non-relativistic) components [20]. The only SM particles that are non-baryonic, weakly interacting and neutral dark matter candidates are neutrinos. SM neutrinos have masses in the sub-eV range and can only constitute hot dark matter. The analysis of Universe structure formation, however, indicates that most of dark matter should be cold or warm at the onset of galaxy formation, when the Universe temperature was about 1 keV. There might also be new types of neutrinos, the so called *sterile* neutrinos, which could be responsible for dark matter. A very active experimental research program is dedicated to carefully check for the existence of sterile neutrinos [21–24].
Dark matter candidates can also arise in left-right symmetric models, which will be discussed in details in Sec. 1.4.1, whose group structure eases the building of many dark matter models [25]. The production of W_R or N_R (right-handed W bosons and neutrinos) provides the most interesting collider signature for these dark matter candidates. Its phenomenology will be discussed in Chapter 2 and the search for W_R and N_R production will be the subject of Chapter 7.
If dark matter is of non-baryonic type it could be made of axions and WIMPs (*weakly interacting massive particles*). These are massive particles predicted by, for instance, *supersymmetry* (SUSY) or *extra dimensions*. They could be identified with *neutralinos* or *gravitinos*. SUSY theories are particularly appealing because they solve other SM issues such as the *hierarchy problem*.

The hierarchy problem

The hierarchy problem is strictly linked to the concept of *naturalness*. Any macroscopic behaviour of a physical system is expected to follow from a microscopic theory. In other words, we do not want a microscopic theory having a number of free parameters *fine-tuned* to reproduce the features of

the macroscopic world. We report here the definition that 't Hooft [26] gave in 1979 to naturalness: *"at any energy scale μ, a physical parameter or set of parameters $\alpha_i(\mu)$ is allowed to be very small only if the replacement $\alpha_i(\mu)=0$ would increase the symmetry of the system."*
We know from Eq. 1.52 that lepton masses are originated from the couplings to the Higgs boson, and their expression is of the type $G_l v/\sqrt{2}$. This calculation, however, is only valid at the *tree-level*. When we compute high order corrections to the fermion masses, we need to include one-loop contributions to the fermion propagator due to the coupling with scalar particles which, in the SM, are only represented by the Higgs boson. The one-loop correction to fermion propagator is shown in Fig. 1.7(a).

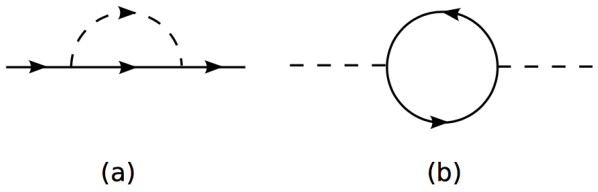

Figure 1.7: (a): Correction to the fermion propagator due to a scalar field loop. (b): Correction to a scalar propagator due to a fermionic loop.

The real mass of the fermion can be re-written as:

$$m_f = \frac{G_l v}{\sqrt{2}} - \frac{3G_l^2 m_f}{64\pi^2} \log \frac{\Lambda^2}{m_f^2} + ... \tag{1.56}$$

where Λ is the cutoff to the theory (the energy scale beyond which the theory is not valid anymore). We can similarly compute the mass corrections for a scalar particle in which, this time, we need to consider fermion loops to scalar propagators (Fig. 1.56(b)). The correction takes the form:

$$\delta m_s^2 = -\frac{G_l^2}{8\pi} \left[\Lambda^2 - 6m_f^2 \log \frac{\Lambda}{m_f} + 2m_f^2 + ... \right] \tag{1.57}$$

and, differently from Eq. 1.56, it is quadratically divergent in the cutoff Λ. This brings up the following problem: the radiative corrections to a scalar particle mass can be extremely high, especially if we assume our theory to be valid up to the Planck scale. Unless the mass of the particle and its correction are at most of the same order, the theory is said to have a naturalness problem.
The Higgs boson mass has corrections of the type in Eq. 1.57, where the biggest contribution comes from the top quark loops (since it is the heavier

quark and δm_s^2 depends on the square of the fermion mass). There are two ways to solve divergences: we could introduce a counter term to cure and cancel divergences, but this would be highly unnatural, or set a different cutoff to the theory. Assuming the theory valid up to $\mathcal{O}(1\text{ TeV})$ would cure the divergences but, on the other hand, requires the introduction of new phenomena at $\mathcal{O}(1\text{ TeV})$. The hierarchy problem is the biggest motivation to search for NP at the TeV scale.

Neutrino masses

If we look back at Eq. 1.52, we see that to generate lepton masses we both need a left-handed and a right-handed fermion field, coupling to the Higgs boson. We stated that, given that right-handed neutrinos were not observed so far, they cannot acquire mass through the Higgs mechanism.
If ν_R do exists, from a theory point of view we could simply add the lagrangian terms for neutrino masses without any symmetry modification. Since 1998 [27, 28], we know that neutrinos oscillate, i.e. convert from one flavour ν to another. Bruno Pontecorvo in 1958 was the pioneer of the theoretical frame for neutrino oscillations. He suggested that, if neutrinos do oscillate, their masses must be different from zero and not degenerate.
The experimental evidence of neutrino oscillations, requiring them to be massive, does not fit then into the mass mechanism through the Higgs boson, for which we need right-handed neutrinos. Moreover, even if we introduce the neutrino mass term into the lagrangian, the naturalness of the theory would be spoiled by the huge difference between other fermion and neutrino masses.

In this last section we went through the main problems of the SM as we know it today. We pointed out the key points suggesting us that new theories are needed to explain observations that cannot be fitted into SM. We now examine a type of SM extension able to solve the neutrino mass problem.

1.4 Extension of the Higgs scalar sector

The models presented in this section try to solve neutrino mass generation and parity symmetry breaking by the SM electroweak interaction. We focus on *left-right symmetric models* (LRSM), through which an extension of the Higgs sector is realized. These models introduce new particles, such as the **doubly-charged Higgs bosons** and **right-handed W bosons and neutrinos**. The search for the production of these new particles is presented in Chapter 7.

1.4.1 The Left-Right Symmetric Models

We start from the observation that weak interaction is not invariant under parity transformations, because weak gauge bosons only couple to left-handed fermions. From a very qualitative point of view, the idea, first suggested by Salam, Mohapatra, Pati and Senjanovic in the 1970s [29–32], is the following: parity can be broken at low energy scales but we want it to be restored at higher energies. The way to restore the symmetry is to extend the SM gauge group.
It is clear that, to restore LR symmetry, any extension of the SM group requires the addition of right-handed counterparts for the W and Z weak bosons. LRSM are also appealing because they offer the possibility to generate both Dirac and Majorana[5] neutrino mass terms. We enlarge the Higgs sector by the addition of a Higgs triplet field both in left- and right-handed states:

$$\Delta_{L,R} = (\Delta^0_{L,R}, \Delta^+_{L,R}, \Delta^{++}_{L,R}) \tag{1.58}$$

whose neutral right-handed component, acquiring a non-vanishing vev, breaks the symmetry at higher energy.
Equation 1.58 shows that the model introduces a new neutral Higgs fields as well as a *singly* and *doubly-charged Higgs bosons.*

LR symmetry group and gauge structure

Let us assume a higher level gauge group of symmetry, namely [29]:

$$SU(2)_L \otimes SU(2)_R \otimes U(1)_{B-L}, \tag{1.59}$$

B and L being the baryon and lepton number. The unification of the left and right gauge couplings is achieved by requiring the lagrangian to be invariant for $SU(2)_L \to SU(2)_R$, except for the Higgs boson mass term.

We can assign quarks and leptons to doublets of the gauge groups $SU(2)_L$ and $SU(2)_R$ according to their chirality:

$$\psi_L = \begin{pmatrix} \nu_l \\ l^- \end{pmatrix}_L, \quad \psi_R = \begin{pmatrix} \nu_l \\ l^- \end{pmatrix}_R, \tag{1.60}$$

$$Q_L = \begin{pmatrix} u \\ d \end{pmatrix}_L, \quad Q_R = \begin{pmatrix} u \\ d \end{pmatrix}_R, \tag{1.61}$$

[5] Particles are turned into anti-particles under the action of charge conjugation. If the particle is identical to its anti-particle it is said to be of Majorana type, otherwise of Dirac type.

so that under parity transformations $\psi_L \leftrightarrow \psi_R$ and $Q_L \leftrightarrow Q_R$.
The new symmetry group has seven generators: three for each $SU(2)_{L,R}$ group, $T_{iL,R}$, and one for the $U(1)_{B-L}$ group. The generators $T_{iL,R}$ follow the Lie algebra:

$$[T_{iL,R}, T_{jL,R}] = i\epsilon_{ijk}T_{kL,R} \tag{1.62}$$

where ϵ_{ijk} is the Levi Civita tensor. The seven group generators correspond to seven gauge bosons $W^{\mu}_{iL,R}$ and B^{μ}. Not all of them correspond to physical states and, indeed, the effect of the LRSM is to duplicate the weak bosons with their right-handed counterparts. We can write the Gell-Mann formula for the charge operator in the following way:

$$Q = T_{3L} + T_{3R} + \frac{B-L}{2}. \tag{1.63}$$

The covariant derivative for the group is the following:

$$D_{\mu} = \partial_{\mu} - ig\sum_{j=1}^{3}(W_{Lj\mu}T_{Lj\mu} + W_{Rj\mu}T_{Rj\mu}) - ig^{'}B_{\mu}Y \tag{1.64}$$

where $Y = (B-L)/2$, $g^{'}$ is the $U(1)_{B-L}$ coupling constant and we set the couplings for left (g_L) and right (g_R) weak interactions of equal strength $g_R = g_L = g$ to make the lagrangian invariant for parity transformations. Under the action of the derivative in 1.64, the gauge bosons transform as:

$$W^{i}_{\mu L,R} \rightarrow W^{'i}_{\mu L,R} = W^{i}_{\mu L,R} + \epsilon^{ijk}W^{k}_{\mu L,R} - \frac{1}{g}\partial_{\mu}\theta^{i}_{L,R}(x)$$
$$B_{\mu} \rightarrow B^{'}_{\mu} = B_{\mu} - \frac{1}{g^{'}}f(x)$$

where $f(x)$ and $\theta^{i}_{L,R}(x)$ are respectively the gauge parameters of the $U(1)_{B-L}$ and $SU(2)_{L,R}$ symmetry groups. Fermions transform as:

$$\psi(x) \rightarrow \psi^{'}(x) = e^{-i\theta_i(x)T_{iL,R}}\psi(x) \tag{1.65}$$
$$\psi(x) \rightarrow \psi^{'}(x) = e^{-i\alpha f(x)\psi(x)} \tag{1.66}$$

respectively under $SU(2)_{L,R}$ and $U(1)_{B-L}$ and ψ here can represent either quarks or leptons.
Using the strength of g and $g^{'}$, an analogous of the Weinberg angle can be also defined in the model [33]:

$$\sin\theta_W = -\frac{g^{'}}{\sqrt{g^2 + 2g^{'2}}}. \tag{1.67}$$

We obtain the total LRSM lagrangian by writing the following field propagation terms:

$$F_{\mu\nu} = \partial_\mu B_\nu - \partial_\nu B_\mu \tag{1.68}$$

$$G^i_{L,R\mu\nu} = \partial_\mu W^i_{L,R\nu} - \partial_\nu W^i_{L,R\mu} + g\epsilon^{i,j,k} W^j_{L,R\mu} W^k_{L,R,\nu}. \tag{1.69}$$

which, after the addition of the fermion propagation term, results in:

$$\mathcal{L}_{\text{gauge}} = i[\bar{\psi}_L \gamma D^\mu \psi_L + \bar{\psi}_R \gamma D^\mu \psi_R] - \frac{1}{4} F_{\mu\nu} F^{\mu\nu} - \frac{1}{4} G^i_{L\mu\nu} G^{i\mu\nu}_L - \frac{1}{4} G^i_{R\mu\nu} G^{i\mu\nu}_R. \tag{1.70}$$

The lagrangian in Eq. 1.70 is written in terms of the unphysical gauge bosons $W_{iL,R}$ and B. We obtain the physical charged gauge boson states W by a combination of the $W_{1,2}$ fields:

$$W^+_{L,R} = \frac{W_{1L,R} - iW_{2L,R}}{\sqrt{2}} \tag{1.71}$$

$$W^-_{L,R} = \frac{W_{1L,R} + iW_{2L,R}}{\sqrt{2}} \tag{1.72}$$

where $W^\pm_L$ is identifiable with the SM W. In a similar way, the rotation relating the fields $W_{3L,R}$ and B with A and $Z_{L,R}$, through the angles $\cos\theta_W$ and $\sin\theta_W$ returns the SM Z^0 (from here on indicated as Z_L) and a right-handed Z_R.
The LRSM realizes the electromagnetic and weak unification duplicating the weak bosons with right-handed partners.

Higgs sector and SSB

We need to extend the Higgs scalar sector to get a mechanism for breaking the new group of symmetry to the SM group. The SSB happens in two steps. First, at high energy the $SU(2)_L \otimes SU(2)_R \otimes U(1)_{B-L}$ group is broken into $SU(2)_L \otimes U(1)_Y$. Then, the Higgs mechanism explained in Sec. 1.2.2 occurs. In the *minimal left-right symmetric models* we need the following Higgs multiplets:

$$\Phi = \begin{pmatrix} \phi^0_1 & \phi^+_2 \\ \phi^-_1 & \phi^0_2 \end{pmatrix}, \quad \Delta_{L,R} = \begin{pmatrix} \Delta^+/\sqrt{2} & \Delta^{++} \\ \Delta^0 & -\Delta^+\sqrt{2} \end{pmatrix}_{L,R}. \tag{1.73}$$

The form for the Higgs potential is in general quite complicated and we will not go into details[6]. All the neutral components of the Higgs fields acquire

[6] The details of the potential can be found here [33].

a vev of the type:

$$\langle\Phi\rangle = \frac{1}{\sqrt{2}}\begin{pmatrix} v_1 e^{i\alpha_1} & 0 \\ 0 & v_2 e^{i\alpha_2} \end{pmatrix}, \tag{1.74}$$

while for the triplet:

$$\langle\Delta_{L,R}\rangle = \frac{1}{\sqrt{2}}\begin{pmatrix} 0 & 0 \\ v_{L,R} e^{i\theta_{1,2}} & 0 \end{pmatrix} \tag{1.75}$$

four phases appear. Let us recall that the generators of $SU(2)_L \times SU(2)_R \times U(1)_{B-L}$ are three (T_{3L}, T_{3R} and $B-L$), commuting with the charge operator Q. Associating the three operators with the following transformation parameters θ_L, θ_R and θ_{B-L}, the Higgs fields transform as follows:

$$\langle\Phi\rangle \rightarrow e^{iT_{3L}\theta_L}\langle\Phi\rangle e^{-iT_{3R}\theta_R}, \tag{1.76}$$
$$\langle\Delta_L\rangle \rightarrow e^{iT_{3L}\theta_L}\langle\Delta_L\rangle e^{-iT_{3L}\theta_L} e^{i\theta_{B-L}}, \tag{1.77}$$
$$\langle\Delta_R\rangle \rightarrow e^{iT_{3R}\theta_R}\langle\Delta_R\rangle e^{-iT_{3R}\theta_R} e^{i\theta_{B-L}}, \tag{1.78}$$

implying the following transformations for the phases:

$$\alpha_1 \rightarrow \alpha_1 + \frac{1}{2}\theta_L - \frac{1}{2}\theta_R \tag{1.79}$$
$$\alpha_2 \rightarrow \alpha_2 - \frac{1}{2}\theta_L + \frac{1}{2}\theta_R \tag{1.80}$$
$$\theta_{1,2} \rightarrow \theta_{1,2} - \theta_{L,R} + \theta_{B-L}. \tag{1.81}$$

We see that only two phases can be removed and conventionally we set the phases of v_1 and v_R to zero, so that the vev become:

$$\langle\Phi\rangle = \begin{pmatrix} v_1 & 0 \\ 0 & v_2 e^{i\alpha} \end{pmatrix}, \langle\Delta_L\rangle = \begin{pmatrix} 0 & 0 \\ v_L e^{i\theta_L} & 0 \end{pmatrix}, \langle\Delta_R\rangle = \begin{pmatrix} 0 & 0 \\ v_R & 0 \end{pmatrix} \tag{1.82}$$

where $v_{1,2}$ and $v_{L,R}$ are real and positive. The symmetry is thus broken in two steps, first at high energy scales by the vev acquired by the $\langle\Delta_R\rangle$ field and then, at the electroweak energy scale, by the vev acquired by $\langle\Phi\rangle$.
The minimization of the Higgs scalar potential actually leads to two possible vev choices: $v_L = v_R$, $v_L = 0$ or $v_R = 0$. The first choice is rejected because we need spontaneous violation of parity and consequently v_L and v_R cannot have same magnitude, so the case $v_L = 0$ or $v_R = 0$ is the one we are interested in. The SSB parameters are connected by the following relation:

$$v_L \propto \frac{v^2}{v_R}. \tag{1.83}$$

which, as we will see now, leads to a specific hierarchy choice. The v_L of the left-handed triplet enters the mass value for both the W_L, Z_L bosons, modifying the relation (assuming $v^2 = v_1^2 + v_2^2$):

$$\rho = \frac{M_{W_L}^2}{\cos^2\theta_W M_{Z_L}^2} \sim \frac{1 + 2v_L^2/v^2}{1 + 4v_L^2/v^2}. \tag{1.84}$$

Precision measurements indicate that $\rho = 1.0004 \pm 0.0003$. Given that the relation between W_L and Z_L masses has to be respected, v_L must be < 9 GeV, leading to the parameter hierarchy: $v_R \gg v_{1,2} \gg v_L$.
The SSB mechanism gives mass to the gauge bosons through the vev as:

$$M_{W_R}^2 \simeq g^2\left(\frac{v_1^2 + v_2^2}{4} + v_R^2\right) \simeq g^2 v_R^2 \tag{1.85}$$

$$M_{W_L}^2 \simeq g^2\left(\frac{v_1^2 + v_2^2}{4}\right) \tag{1.86}$$

$$M_{Z_R}^2 \simeq \frac{g^2}{c^2}\left(\frac{(v_1^2 + v_2^2)\,(c^2 - s^2)}{4} + \frac{c^4 v_R^2}{c^2 - s^2}\right) \tag{1.87}$$

$$M_{Z_L}^2 \simeq \frac{g^2}{c^2}\left(\frac{v_1^2 + v_2^2}{4}\right) \tag{1.88}$$

where $c \equiv \cos\theta_W$ and $s \equiv \sin\theta_W$. It is important to underline here that the masses of the SM W_L and Z_L bosons are recovered ($M_{W_L}/M_{Z_L} \simeq \cos\theta_W$).

1.4.2 Neutrino masses: Yukawa lagrangian

As we saw in the previous sections, the LRSM introduces a right-handed neutrino for each lepton flavour ν_e, ν_μ and ν_τ. The Yukawa lagrangian for leptons presents couplings both to the Φ and the Δ fields:

$$\mathcal{L}_{lep} = [\bar{\psi}_{Li}(F_{ij}\Phi + \tilde{F}_{ij}\tilde{\Phi})\psi_{Ri}] + [\bar{\psi}_{Li}\Gamma_{1ij}\Delta_L^\dagger\sigma_2\psi_{Lj}^c + \bar{\psi}_{Ri}\Gamma_{2ij}\Delta_R^\dagger\sigma_2\psi_{Rj}^c] + \text{h.c.} \tag{1.89}$$

where Y_{ij},$\tilde{Y}_{ij}, F_{ij}, \tilde{F}_{ij}, \Gamma_{1ij}, \Gamma_{2ij}$ are 3×3 matrices in the families spaces of Yukawa couplings and $\tilde{\Phi} = \sigma_2\Phi\sigma_2$. The generic spinor ψ transforms under the charge-conjugation operator C as $\psi_{L,R}^c = C\gamma_0\psi_{L,R}^*$. It is clear that the Higgs triplet does not participate in the Dirac masses generation for fermions but contributes to Majorana mass terms. Moreover, the two last terms in Eq. 1.89 show that the lagrangian allows lepton flavour violating interactions.

Let us now focus on neutrino mass terms. The lagrangian 1.89 provides the following Dirac

$$\bar{\nu_L} m_\nu \nu_R + \text{h.c.} \tag{1.90}$$

and Majorana

$$\bar{\nu}_{L,R} M_{L,R} \nu^c_{L,R} + \text{h.c.} \tag{1.91}$$

neutrino mass terms. It is convenient to write the lagrangian mass term in matrix notation as follows:

$$\begin{pmatrix} \bar{\nu}_L & \bar{\nu}^c_R \end{pmatrix} \begin{pmatrix} M_L & m \\ m^T & M_R \end{pmatrix} \begin{pmatrix} \nu^c_L \\ \nu_R \end{pmatrix}. \tag{1.92}$$

The matrix in 1.92 is symmetric and, under the hypothesis $M_R \gg m \gg M_L$, can be diagonalized as follows:

$$\begin{pmatrix} M_L - m M_R^{-1} m^T & 0 \\ 0 & M_R \end{pmatrix} \tag{1.93}$$

where $M_{light} \simeq M_L - m M_R^{-1} m^T$ and $M_{heavy} \simeq M_R$ indicate the light and heavy neutrinos respectively. In this way we generated a right-handed heavy neutrino M_R with large mass due to its proportionality to v_R. At the same time, the light left-handed neutrino m is light because of two reasons: the term M_L is light because it depends on v_L which, as we already concluded, is found to be small; the term $m M_R^{-1} m^T$ depends on $1/v_R$ and, consequently is also light. This process of mass generation for neutrinos is known as a combined type I (mediated by the heavy right-handed neutrino) and type II See-Saw mechanisms (mediated by the interaction of the Higgs triplet field). By using the Majorana mass term for the left-handed neutrino in Eq. 1.93 ($m_\nu = M_L - m M_R^{-1} m^T$) and the two following relations [34]:

$$M_L = \frac{v_L}{v_R} M_R \tag{1.94}$$

$$m = m^T \tag{1.95}$$

one finds

$$m = M_R \sqrt{\frac{v_L}{v_R} - \frac{1}{M_R} m_\nu} \tag{1.96}$$

which enlightens the mixing between light and heavy neutrinos. In this way, at LHC we can directly probe the Majorana nature of the right-handed neutrino through its equal branching ratios into charged leptons and anti-leptons.

We reviewed the SM theoretical framework where the Higgs boson is introduced. We highlighted the demand for new physics following the difficulty

for the SM to explain neutrino masses, dark matter, etc. We also provided an overview of the minimal LRSM, which adds new particles to the frame such as the doubly-charged Higgs boson and the right-handed neutrinos and W gauge bosons.
A phenomenological overview of $t\bar{t}H$ and LRSM particles production and decay is provided in the following chapter.

Chapter 2

Same-Sign lepton signatures: from $t\bar{t}H$ to $H^{\pm\pm}$

Same-sign (SS) lepton final states provide a very powerful signature for BSM searches. This chapter discusses the models looking at final states with SS leptons in ATLAS, with particular attention to the processes which will be analyzed in this work, i.e. $t\bar{t}H$, $H^{\pm\pm}$, W_R and N_R production.

2.1 SM sources of same-sign leptons

Events from SM processes rarely produce two SS leptons. Indeed, SM processes with relatively large cross-section, such as $Z/\gamma*$ or $t\bar{t}$ production, produce two opposite-sign (OS) leptons. SS leptons mainly appear in three ways: events from diboson production where at least one of the leptons is lost, events containing electrons with mis-reconstructed charge (see Section 5.3) or events with leptons from jet secondary decays (see Section 5.4). Diboson processes, in particular WZ and ZZ production, are indeed the only background to SS signatures without mis-reconstructed objects in the final state. To distinguish these events from NP signatures one has to rely on the topology of both the NP signal and the diboson production.
Regarding final states with mis-reconstructed objects, Z+jets and $t\bar{t}$ are the most significant processes which can either lead to electrons with wrong electric charge or non-prompt leptons. The production cross-sections for these processes, measured by ATLAS at $\sqrt{s}$ =13 TeV, are $\sigma(pp \to Z) = 58.43 \pm 0.03 \pm 1.66$ nb, $\sigma(pp \to t\bar{t}) = 818 \pm 8 \pm 35$ pb and $\sigma(pp \to W^{\pm}Z) = 50.6 \pm 2.6 \pm 2.5$ pb [35] and allow to conclude that, besides diboson production, the contribution from Z+jets and $t\bar{t}$ to the SS final states is significant.

2.2 BSM sources of same-sign leptons

A plenty of BSM models involve final states with two SS leptons:

- **SUSY** models, presented in Chapter 1, predict bosonic (fermionic) superpartners for each SM fermion (boson). The LHC could observe SUSY particles such as *gluinos* or *squarks* by looking at their decays into SM particles. We can consider, for instance, the processes depicted in Fig. 2.1 for gluino, stop and sbottom production [36]. All the processes involve a SUSY particle cascade leading to the lightest stable SUSY particle $\tilde{\chi}_1^0$ and SS $W^{\pm}$ bosons eventually decaying to SS leptons.

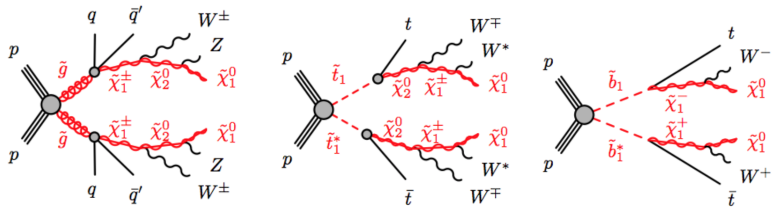

Figure 2.1: Feynman diagrams for gluino (a) and third generation stop (b) and sbottom (c) production.

- **Little Higgs models** [37] (LH) assume that the SM Higgs boson is a composite particle, a bound state of more fundamental particles held together by a new type of force. The composite nature of the Higgs boson should manifest at the cutoff energy scale of the one-loop radiative corrections to the μ parameter of the Higgs field Λ, $\sim$2 TeV. Due to the precise constraints from electroweak measurements, the new interaction should appear at $\mathcal{O}$(10 TeV) and this requires an additional mechanism to stabilize the *little hierarchy* between the Higgs mass and the new interaction scale. LH models provide an alternative to SUSY regarding the hierarchy problem, absorbing the quadratically divergent contributions to the Higgs mass into a *collective* pattern in which the gauge and Yukawa couplings break a global symmetry. All the LH models predict new particles with masses around 1 TeV, including $H^{\pm\pm}$ bosons.

- **Higgs triplet models** [38] add a $SU(2)$ triplet of scalar particles with $Y = 2$ to the SM Lagrangian. Neutrinos acquire their mass through the vev of the neutral Higgs boson. These models also predict the existence of $H^{\pm\pm}$ bosons.

- **Left-right symmetric models** discussed in Section 1.4.1, complete the Higgs triplet models solving the weak interactions parity breaking. LRSM introduce a set of scalar bosons, including $H^{\pm\pm}$, right-handed counterparts for weak bosons ($W_R^{\pm}$, Z_R) and three heavy neutrinos $N_{R,e}$, $N_{R,\mu}$ and $N_{R,\tau}$. These models, after the SSB of $SU(2)_L \otimes SU(2)_R \otimes U(1)_{B-L}$, return the SM Lagrangian.

All these models share several features. From a theoretical point of view, apart from SUSY, they extend the Higgs scalar sector by adding new Higgs bosons, mainly responsible for neutrino masses. From a phenomenological point of view, the final signatures of new particle decays involve SS leptons. However, SS lepton signatures often occur in other BSM models, such as universal extra dimensions [39], vector-like quarks [40], the Zee-Babu neutrino mass model [41, 42] and the coloured Zee-Babu model [43]. It naturally follows that, in principle, one could span over all the possible final states combinations, including additional jet presence, missing transverse energy, or various lepton multiplicities aiming to a model independent search for NP discovery. So far, a model independent search using SS lepton final states was performed by the ATLAS Collaboration at $\sqrt{s} = 7$ TeV and 8 TeV and not yet updated at $\sqrt{s}=$ 13 TeV. Upper limits at 95% CL on the fiducial cross-section for NP are performed in each flavour channel ee, $e\mu$ and $\mu\mu$ under a SM background only hypothesis and found to be in the range $\sigma_{95}^{\text{fid}} \in$ [0.15,0.28] pb and $\sigma_{95}^{\text{fid}} \in$ [0.48,32] fb respectively at $\sqrt{s} = 7$ TeV and 8 TeV [44, 45].
In the following, we highlight channels which can, either indirectly or directly, lead to the discovery of NP, namely the $t\bar{t}H$ production and the LRSM doubly-charged Higgs bosons ($H^{\pm\pm}$), W_R and N_R production.

2.3 The Higgs and associated $t\bar{t}H$ production

The associated production of a Higgs boson with a top-quark pair is one of the possible Higgs production mechanisms at LHC energies. The main Higgs production modes are the *gluon-gluon* fusion (ggF), vector-boson fusion (VBF), associated production with a weak boson (VH) and the associated production with a $t\bar{t}$ pair, as shown in Fig. 2.2.

Each of these processes is used to measure the Higgs boson coupling either to fermions or to gauge bosons. The cross-section for the different production modes is illustrated in Fig. 2.3 and summarized in Table 2.1.

Despite the lower cross-section compared to other production mechanisms,

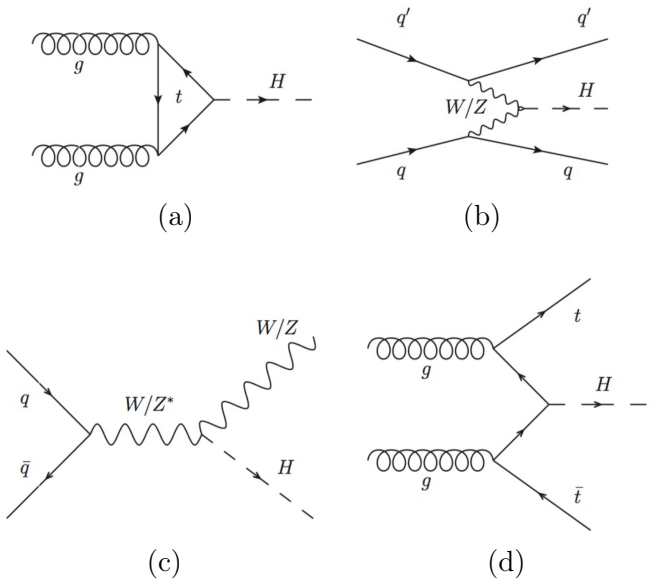

Figure 2.2: LO Feynman diagrams for the Higgs boson production mechanisms at LHC: the ggF (a), VBF (b), VH (c) and $t\bar{t}H$ (d) production.

$\sqrt{s}$ (TeV)	ggF	VBF	WH	ZH	$t\bar{t}H$	total (pb)
7	$15.1 \pm 15\%$	$1.22^{+3\%}_{-2\%}$	$0.58 \pm 4\%$	$0.33 \pm 6\%$	$0.09^{+12\%}_{-18\%}$	17
8	$19.3 \pm 15\%$	$1.58^{+3\%}_{-2\%}$	$0.70^{+4\%}_{-5\%}$	$0.41 \pm 6\%$	$0.13^{+12\%}_{-18\%}$	22
13	$43.9^{+15\%}_{-14\%}$	$3.75 \pm 4\%$	$1.38^{+3\%}_{-4\%}$	$0.87 \pm 6\%$	$0.51^{+15\%}_{-18\%}$	50
14	$49.5^{+15\%}_{-14\%}$	$4.23 \pm 3\%$	$1.52 \pm 3\%$	$0.97 \pm 6\%$	$0.61^{+15\%}_{-18\%}$	57

Table 2.1: Theoretical Higgs boson production cross-section in pp collisions as a function of the center-of-mass energy $\sqrt{s}$. The leading theoretical uncertainties derive from the choice of the renormalization (μ_R) and factorization (μ_F) scales and from the uncertainties on the PDF and strong coupling constant α_s [46, 47].

$t\bar{t}H$ production receives the highest boost from the LHC center-of-mass energy increase (almost a factor 6 raising the energy from 7 to 13 TeV).

The ***gg*F** production accounts for the ∼87% of the Higgs production, at each center-of-mass energy. It is mediated by a virtual loop of t or b quarks, where the t quark is favoured due to its higher mass and thus higher Yukawa coupling to the Higgs boson. The theoretical calculation for this process is computed at the NNLO [48]. Among the NLO corrections for the ggF process, *virtual* loops and legs are considered: the former do not affect the initial or final state while the latter involve corrections due to

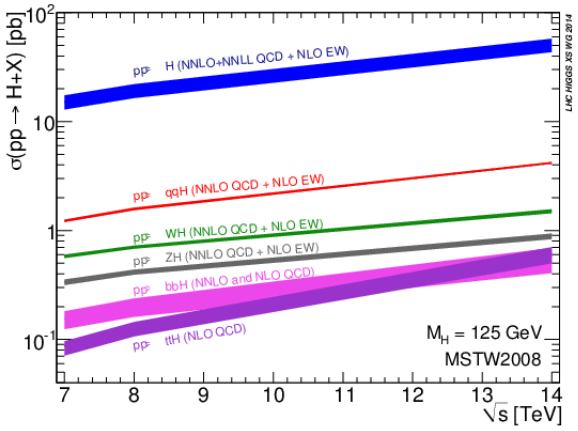

Figure 2.3: Higgs boson production cross-section split by production mechanism as a function of the collisions center-of-mass energy $\sqrt{s}$ [46]. The bands correspond to the total theoretical uncertainties.

additional partons in the final state ($gg \to Hg$, $qg \to Hq$ and $q\bar{q} \to Hg$). The uncertainty on ggF production mainly depends on the energy scale and on the parton distribution function (PDF) uncertainty.

The **VBF** mechanism is the second leading production mode for the Higgs boson at the LHC (∼8% of the total cross-section). The peculiar topology of the VBF process, which presents two hard jets in the forward-backward directions of the ATLAS detector, allows an easier separation of the signal from background. The production cross-section is calculated with full NLO QCD and EW corrections and approximate NNLO QCD corrections [49].

In the **Higgs-Strahlung** (**VH**) process the Higgs boson is radiated through an *off-shell* W, Z boson. This process dominates at e^+e^- colliders and is the third one, in order of relevance, at the LHC. NNLO QCD corrections range between 25% and 40% [50] and a typical NLO process involves a quartic loop of virtual top quarks.

Although the Higgs-top Yukawa coupling can be indirectly constrained through the ggF process where top appears in the virtual loop, it can be directly measured only using the $\boldsymbol{t\bar{t}H}$ production mode. Indeed, the top quark is heavier than the Higgs boson, which cannot decay into pairs of top quarks, leaving the $t\bar{t}H$ production the only mechanism to experimentally constrain the Yukawa parameter. Due to the top large mass, the coupling is expected to be very close to one, differently from other quarks for which couplings are around $\sim 10^{-2}$. This unique feature of the $t\bar{t}H$ channel, together with the production cross-section increase, make it a challenging and the most interesting channel for Higgs searches in Run 2. To disentangle the SM $t\bar{t}H$

production from new physics signals, a precise prediction of the $t\bar{t}H$ process is needed, namely as inclusive or differential cross-section. QCD correction to $t\bar{t}H$ production are important to reduce the dependence of the cross-section on the arbitrary renormalization and factorization scales[1].

2.4 $t\bar{t}H$ decay

The final states of the $t\bar{t}H$ process are determined by the decay of two different systems: the Higgs boson and the $t\bar{t}$ pair [6]. The top quark always decays into a $W^{\pm}b$ pair, with the following possible decays:

$$45.7\% \text{ (all hadronic)} : t\bar{t} \to W^+bW^-\bar{b} \to q\bar{q}bq\bar{q}\bar{b}$$
$$43.8\% \text{ (semileptonic)} : t\bar{t} \to W^+bW^-\bar{b} \to q\bar{q}b\ell^-\bar{\nu}_\ell\bar{b} + \ell^+\nu_\ell bq\bar{q}\bar{b}$$
$$10.5\% \text{ (all leptonic)} : t\bar{t} \to W^+bW^-\bar{b} \to \ell^+\nu_\ell b\ell^-\bar{\nu}_\ell\bar{b}$$

leading to various topologies. The SM prediction for the decay of a Higgs boson with mass 125 GeV gives the following branching ratios:

$$57\% : H \to b\bar{b}$$
$$21\% : H \to WW^*$$
$$9\% : H \to gg$$
$$6\% : H \to \tau\bar{\tau}$$
$$3\% : H \to c\bar{c}$$
$$3\% : H \to ZZ^*$$
$$0.2\% : H \to \gamma\gamma$$
$$0.8\% : H \to \text{others}.$$

Besides the different lepton multiplicities which arise from the possible combinations of Higgs and $t\bar{t}$ decays, the final state is characterized by a high jet multiplicity.
Figure 2.4 provides the Feynman diagrams for the tree-level $t\bar{t}H$ production in which the Higgs boson decays to WW^*, ZZ^* or $\tau\bar{\tau}$.

2.4.1 $t\bar{t}H$ and new physics

One of the most important quantities which can give us hints of the scale of NP is the top-Higgs Yukawa coupling y_t.
In fact, the SM is a renormalizable quantum field theory and problems arise

[1] More details on the $t\bar{t}H$ cross-section calculation are provided in Section 6.2.2.

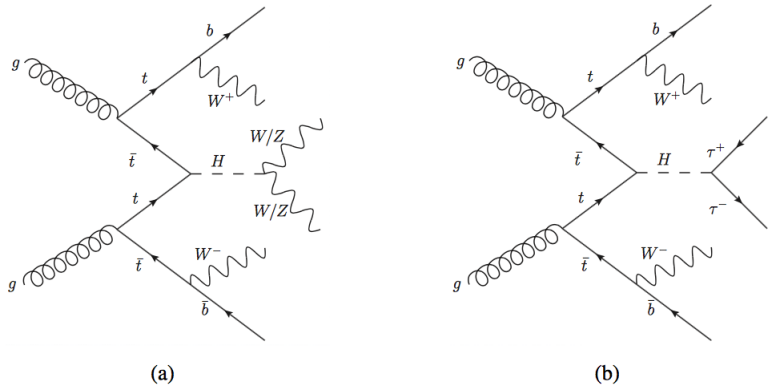

Figure 2.4: Tree-level production mode for the $t\bar{t}H$ process with consequent decays into WW^*, ZZ^* (left) or $\tau\bar{\tau}$ (right).

when the renormalization evolution of some of the coupling constants becomes large or additional minima of the effective potential appear, changing the vacuum structure. The most sensitive parameter in this sense is the Higgs boson self coupling constant λ [51]:

$$\frac{d\lambda}{d\ln\mu} \propto \lambda y_t^2 - y_t^4 \tag{2.1}$$

which receives both positive and negative contributions from y_t. The very special value of the Higgs boson mass, as measured from the LHC experiments, guarantees a vacuum life-time longer than the Universe life-time.
To evaluate where NP might appear we consider the Higgs field effective potential, which also strongly depends on y_t. The negative term is responsible for an extra minima in the potential at large values of the Higgs field. The *critical value* of y_t can be defined as the one where the effective Higgs potential presents two degenerate minima, resulting in:

$$y_t^{\text{crit}} = 0.9244 \pm 0.0012 \times \frac{m_H/\text{GeV} - 125.7}{0.4} + 0.0012 \times \frac{\alpha_s(m_Z) - 0.1184}{0.0007} \tag{2.2}$$

where α_s is the strong coupling constant at the Z-boson mass. We can now see how the effective Higgs field potential changes with different values of y_t very close to y_t^{crit}, as shown in Fig. 2.5.

Depending on the value of y_t:

- if $y_t < y_t^{\text{crit}} - 1.2 \times 10^{-6}$, V_{eff} increases as the fields increases. In this case the vacuum state is unique and our universe is cosmologically safe;

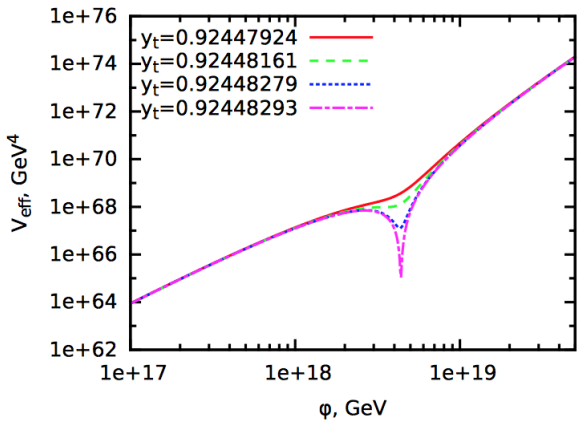

Figure 2.5: Effective Higgs field potential as a function of the Higgs field φ, computed for different values of the top-Higgs Yukawa coupling [51].

- if $y_t > y_t^{\text{crit}} - 1.2 \times 10^{-6}$, a new minimum of the potential appears at large values of φ. The evolution of the universe should lead the system to our vacuum state as far as our vacuum is the global minimum;
- if $y_t = y_t^{\text{crit}}$ the electroweak vacuum state is degenerate with a new one;
- if $y_t > y_t^{\text{crit}}$ the new minimum is deeper than the one in which our Universe is, meaning that the vacuum state is metastable;
- if $y_t > y_t^{\text{crit}} + 0.04$ the life-time of the vacuum is smaller than the age of the Universe.

Let us say that the actual value of y_t can move from the critical value y_t^{crit} by a small ($\sim 10^{-5}$) amount δy_t. The case $y_t < y_t^{\text{crit}} + \delta y_t$ does not allow to derive any information on the scale of NP. In the case $y_t > y_t^{\text{crit}} + \delta y_t$, we can consider the value of the scalar field for which the effective potential crosses zero or the normalization point μ_{new} where the scalar self-coupling λ crosses zero, indicating an instability at that energy. To ensure the scalar potential or self-coupling to be positive at all energies, NP should appear at the energy scale $E \simeq \mu_{\text{new}}$.

Figure 2.6 illustrates the dependence of the new energy scale μ_{new} from the distance between the measured y_t and its critical value y_t^{crit}. We can see that, especially in the range where y_t gets really close to y_t^{crit}, a tiny variation of the difference $y_t - y_t^{\text{crit}}$ leads to a change in μ_{new} by many orders of magnitude. From this follows that a precise experimental measurement of y_t is needed.

The measurement of y_t with high precision brings information on the energy

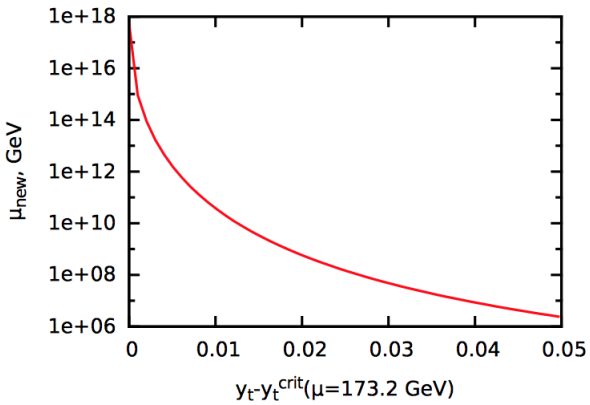

Figure 2.6: Energy scale at which the Higgs self-coupling λ becomes negative as a function of the top-quark Yukawa coupling [51].

scale of our theory validity which can reach the 10^{17} GeV scale. It is extremely important to derive and complement our physics knowledge of what should happen between the Fermi and the Planck scales.

First searches for $t\bar{t}H$ production were performed by the CDF [52] and DØ [53] collaborations at the Tevatron collider, which only put limits to this Higgs production mode. At the LHC, the first search for $t\bar{t}H$ production was performed by the ATLAS Collaboration in Run 1 and continued with Run 2 data, targeting the measurement of the signal strength μ[2] (see Section 5.6).

In the multi-lepton final state [54], where $t\bar{t}H$ ($H \to WW^*/\tau\tau/ZZ^*$), a $\mu = 2.1^{+1.4}_{-1.2}$ was observed resulting in an upper limit of $\mu < 4.7$ at 95% CL. In the di-photon final states [55], where $t\bar{t}H$ ($H \to \gamma\gamma$) and inclusive in Higgs production mechanism, a $\mu = 1.4^{+2.1(\text{stat.})+0.6(\text{syst.})}_{-1.4(\text{stat.})-0.3(\text{syst})}$ was observed with a limit of $\mu < 6.7$ at 95% CL. In the $t\bar{t}H$ ($H \to b\bar{b}$) channel [56] a $\mu = 1.5^{+1.1}_{-1.1}$ was observed, resulting in an upper limit of $\mu < 3.4$ at 95% CL.
The same measurement was performed by the CMS Collaboration which, combining the multi-lepton, di-photon and hadronic channels, obtained a $\mu = 2.8^{+1.0}_{-0.9}$ resulting to an upper limit of μ <4.5 at 95% CL [57]. The measurement of the signal strength of the $t\bar{t}H$ process into multi-lepton final states performed by ATLAS in Run 1 is provided in Fig. 2.7. The Run 2 analysis will be discussed in details in Chapter 6.

[2] The signal strength is defined as $\mu = \sigma^{t\bar{t}H}_{\text{obs}}/\sigma^{t\bar{t}H}_{\text{SM}}$.

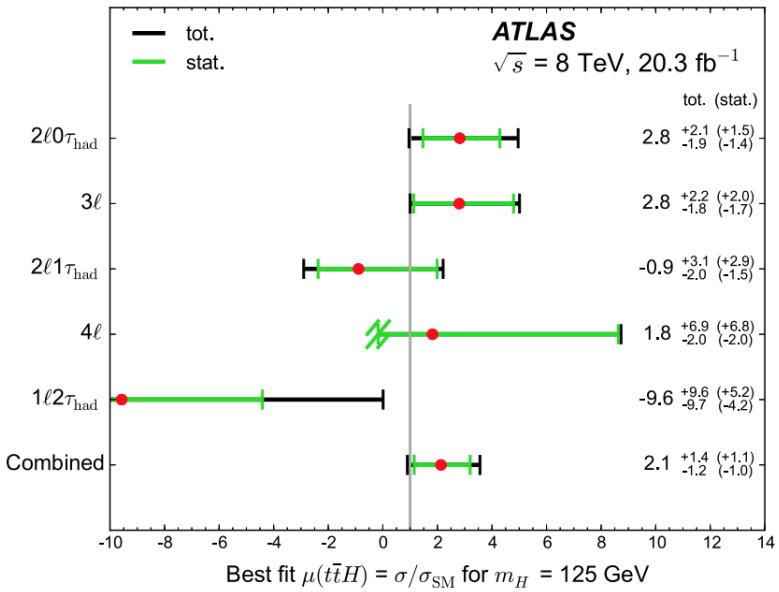

Figure 2.7: Best-fit value of the signal strength and related statistical (green line) and total (black line) uncertainties for the individual multi-lepton channels and their combinations. The results are obtained by the measurement performed at $\sqrt{s} = 8$ TeV with a total integrated luminosity of $\mathcal{L} = 20.3$ fb^{-1} [54].

2.5 Phenomenology of LRSM

As presented in Section 1.4.1, LRSM introduce a new set of particles. We are here interested in the $H^{\pm\pm}$, right-handed neutrinos and W bosons phenomenology at the LHC.

2.5.1 $H^{\pm\pm}$ production and decay

The $H^{\pm\pm}_{L,R}$ cannot be produced in quark interactions because of charge conservation but can be produced via interactions with electroweak gauge bosons, through Drell-Yan pair production or VBF (see Fig. 2.8).

The main production mechanism for $H^{\pm\pm}_{L,R}$ is the **Drell-Yan pair production**

$$q\bar{q} \rightarrow \gamma^*/Z^*_R \rightarrow H^{++}_R H^{--}_R \tag{2.3}$$
$$q\bar{q} \rightarrow \gamma^*/Z^*_L \rightarrow H^{++}_L H^{--}_L \tag{2.4}$$

through an s-channel photon or a Z boson exchange. Here the couplings of $H^{\pm\pm}_{L,R}$ to photon and Z are fixed by the gauge structure. The cross-section

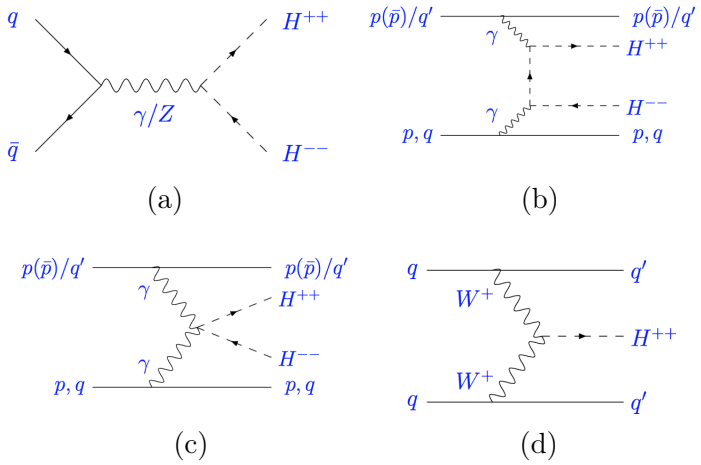

Figure 2.8: LO Feynman diagrams for $H^{\pm\pm}_{L,R}$ production at LHC, via Drell-Yan pair production (a), photon-photon fusion (b),(c) and WW fusion (d).

for this process, computed at LO, only depends on the mass of $H^{\pm\pm}_{L,R}$. NLO QCD effects were studied and resulted in k-factors of approximately ∼1.2-1.3 at $\sqrt{s}$= 14 TeV with renormalization and factorization scales set to be $\mu_F^2 = \mu_R^2 = \mathcal{Q}^2$, which is the natural scale choice for Drell-Yan like processes. These $k-$factors show a slight dependence on the $H^{\pm\pm}_{L,R}$ mass, varying from 1.19 for $m_{H^{\pm\pm}} = 50$ GeV to 1.24 at $m_{H^{\pm\pm}}$= 1 TeV, with a peak at 1.26 for $m_{H^{\pm\pm}} = 300$ GeV.

The **photon-photon fusion** also produces pairs of $H^{\pm\pm}_{L,R}$, with the additional presence of two partons in the final state. The exchange of a Z instead of a γ is suppressed and is not considered here. The initial photon can be originated from the proton (elastic processes) or from a single parton (inelastic processes). The total cross-section combines both processes and represents ∼10% of the Drell-Yan production cross-section. In this sense, the $\gamma\gamma$ fusion can be considered as a simple enhancement of the dominant Drell-Yan cross-section.

The $H^{\pm\pm}_{L,R}$ coupling to the gauge bosons

$$h_{WW} \propto g^2_{L,R} v_{L,R} W^{\pm}_{L,R} W^{\pm}_{L,R} H^{\mp\mp}_{L,R} \tag{2.5}$$

allows it to be produced also through **vector-boson-fusion**, proportional either to the $SU(2)_R$ symmetry breaking scale v_R or to v_L. However, from the bounds on v_L, the VBF mechanism is suppressed for $H^{\pm\pm}_L$ but can still be relevant for $H^{\pm\pm}_R$, since v_R is essentially unconstrained by the SM. Even in such cases the predicted cross-sections are generically $\lesssim$10 fb, making the VBF dominant only in cases of very heavy $H^{\pm\pm}_R$ when the pair production

cross-section is small due to the parton distribution function suppression, at large Q^2 values.

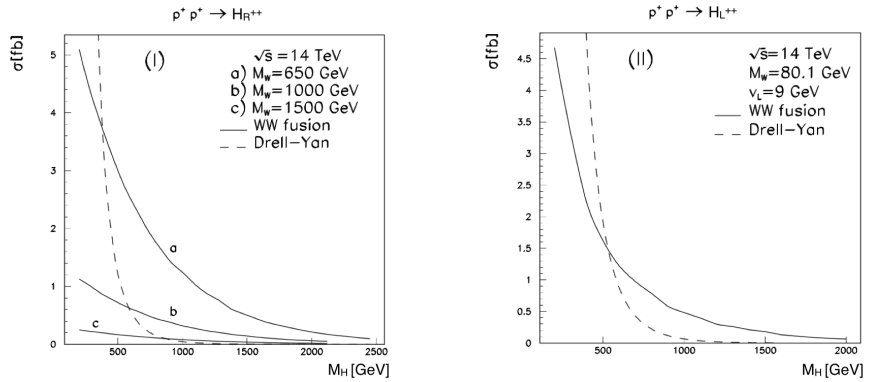

(a) (b)

Figure 2.9: Cross-section for doubly-charged Higgs boson production as a function of the $H^{\pm\pm}$ invariant mass for the right-handed (a) and left-handed (b) particles at $\sqrt{s} = 14$ TeV [58]. Curves are given for different values of $M_{W_R} = \{650, 1000, 1500\}$ GeV and production mechanisms.

The production cross-section calculation is shown in Fig. 2.9. For the right-handed case it is evaluated for three different values of the W_R mass. For low values of M_{W_R} it is a rapidly falling function of the $H^{\pm\pm}$ mass and, going from 650 GeV to 1.5 TeV, the cross-section for $m_{H^{\pm\pm}}$ decreases by more than an order of magnitude. If a light $H_R^{\pm\pm}$ is detected, its cross-section can be used to extract indirect information on the W_R mass. For heavier $H_R^{\pm\pm}$ the cross-section has a lower dependence on M_{W_R}. Figure 2.9a also shows a comparison with the Drell-Yan production mode for the right-handed $H^{\pm\pm}$. The left-handed case is computed using the highest allowed value for $v_L = 9$ GeV. For the chosen value of v_L the production cross-section is comparable with the one for $H_R^{\pm\pm}$ but falling faster with the Higgs mass (Fig. 2.9b).

Besides the two main production mechanisms just illustrated, the $H^{\pm\pm}$ boson can also be **produced in association with a *singly-charged Higgs boson*** $H^{\pm}_{L,R}$ which also appears in the LRSM Higgs triplet. The production process is the following [59]:

$$q\bar{q}^{'} \rightarrow W^{*\pm}_{L,R} \rightarrow H^{\pm\pm}H^{\mp}$$

and its cross-section depends on the relative magnitude of the $H^{\pm\pm}$ and $H^{\pm}$ masses. The overall effect of this additional production mode is a cross-section enhancement to pair-production, as in the photon-photon fusion case.

In the best case scenario, when $m(H^{\pm}) \gg m(H^{\pm\pm})$, the contribution from associated production almost doubles the pair production cross-section. In the worst case scenario, $m(H^{\pm}) \ll m(H^{\pm\pm})$, the additional contribution is $\sim$50%. Being extremely dependent on the mass hypothesis for $H^{\pm}$, this production mechanism is not taken into account in this work.

The highest $H^{\pm\pm}_{L,R}$ branching ratios are the ones either into pairs of SS leptons or pairs of SS W bosons.
The decay width into SS leptons is [60]:

$$\Gamma(H^{\pm\pm} \to \ell^{\pm}\ell'^{\pm}) = \frac{1}{1+\delta_{\ell\ell'}} \frac{|\tilde{h}_{\ell\ell'}|^2 m_{H^{\pm\pm}}}{16\pi}, \qquad \tilde{h}_{\ell\ell'} = \begin{cases} 2h_{\ell\ell'} & \ell = \ell', \\ h_{\ell\ell'} & \ell \neq \ell' \end{cases} \tag{2.6}$$

where the factor $1/(1+\delta_{\ell\ell'})$ accounts for the phase space factor of $1/2$ for identical final state leptons and $\tilde{h}_{\ell\ell'}$ for the symmetry factor in the Feynman rule. The Yukawa couplings to leptons are related to the Dirac neutrino masses and the vev according to

$$m_{\nu_{ij}} = h_{\ell_i\ell_j} v \tag{2.7}$$

and, assuming $m_\nu \sim 0.1$ eV and a very small value for v, the leptonic decay mode dominates.
In the case of non-vanishing vev, the decay rate into $W^{\pm}W^{\pm}$ can be written as:

$$\begin{aligned} \Gamma(H^{\pm\pm} \to W^{\pm}W'^{\pm}) &= \frac{g^4 v^2}{32\pi m_{H^{\pm\pm}}} \left[8 + \frac{m^4_{H^{\pm\pm}}}{m^4_W} \left(1 - \frac{4m^2_W}{m^2_{H^{\pm\pm}}} \right)^2 \right] \sqrt{1 - \frac{4m^2_W}{m^2_{H^{\pm\pm}}}} \\ &\approx \frac{g^4 v^2}{32\pi} \left(\frac{8}{m_{H^{\pm\pm}}} + \frac{m^3_{H^{\pm\pm}}}{m^4_W} \right) \end{aligned} \tag{2.8}$$

where the second line is derived in the approximation $m_{H^{\pm\pm}} \gg m_W$. The first term in Eq. 2.8 corresponds to the W transverse component, proportional to $1/m_{H^{\pm\pm}}$, while the second component to the longitudinal one, proportional to $m^3_{H^{\pm\pm}}$. If the vev of the triplet is different from zero, it follows that the possible decay modes for the $H^{\pm\pm}$ can be a mixture of both leptonic and bosonic states.

The branching ratios are shown in Fig. 2.10a as a function of the vev for $m_{H^{\pm\pm}}$= 300 GeV and in Fig. 2.10b as a function of the $m_{H^{\pm\pm}}$ setting $v = 10^{-4}$ GeV. We can also notice that for a $m_\nu \sim 1$ eV and $m_{H^{\pm\pm}} \sim 1$ TeV the two decay modes are comparable, when $v \sim 10^{-4}$ GeV. Besides the two dominant decay modes, decays of the type $H^{\pm\pm} \to H^{\pm(*)}W^{\pm(*)}$ and $H^{\pm\pm} \to H^{\pm(*)}H^{\pm(*)}$

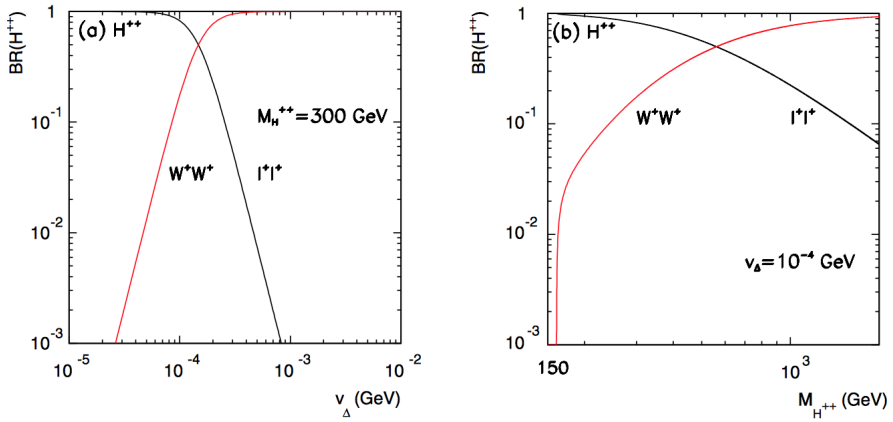

(a) (b)

Figure 2.10: $BR(H^{\pm\pm})$ as a function of the vev for $m_{H^{\pm\pm}}$= 300 GeV (a) and as a function of $m_{H^{\pm\pm}}$ (b) setting v=10^{-4} GeV [61].

are also possible and depend on v and on the scalar self-couplings.

First direct searches for $H^{\pm\pm}$ production were performed at LEP by the L3 Collaboration using 624.1 pb^{-1} of data collected at $\sqrt{s}$ = 189-209 GeV which set lower limits on the $H^{\pm\pm}$ mass varying from > 95.5 GeV to > 100.2 GeV at 95% CL [62]. The Tevatron CDF and DØ Collaborations repeated the measurement at $\sqrt{s}$= 1.96 TeV. The DØ Collaboration set a lower limit of $H^{\pm\pm}$ >130 GeV at 95% CL [63] while for the CDF Collaboration the lower mass limit was varying between 112-114 GeV at 95% CL [64]. All the searches performed by the LEP and the Tevatron Collaborations targeted the benchmark model of the Drell-Yan $H^{\pm\pm}$ pair production with subsequent decay into lepton (e, μ and τ) final states, without any specific tuning of the analysis for $H^{\pm\pm} \to W^{\pm}W^{\pm}$ decays. The decay of the $H^{\pm\pm}$ into $W^{\pm}W^{\pm}$ is searched for the first time in Run 2 by the ATLAS Collaboration and provides the complementary analysis to the one presented in this work. Searches for $H^{\pm\pm}$ production were performed also by the ATLAS and CMS Collaborations in Run 1 with a center-of-mass energy of $\sqrt{s} = 8$ TeV. The ATLAS Collaboration excluded at 95% CL $H^{\pm\pm}_{L,R}$ with masses smaller than 465-550 GeV and 370-435 GeV respectively [45]. The CMS Collaboration also looked at the associated production of a $H^{\pm\pm}$ with a singly charged Higgs boson $H^{\pm}$. The most stringent limits, however, come from the pair-production mode which resulted in a lower limit of ∼560 GeV on $m_{H^{\pm\pm}}$ at 95% CL [65], showing a similar sensitivity to the results provided by the ATLAS Collaboration.

Indirect constraints on $H^{\pm\pm}$ production arise from SM processes in which

virtual exchange of doubly charged Higgs bosons could lead to sizeable deviations from SM predictions. Four main types of processes can be used to place constraints on $H^{\pm\pm}$ couplings and are briefly outlined here:

- the Bhabha scattering (Fig. 2.11a), used to constrain h_{ee}. OPAL [66] and L3 [62] experiments derived limits for h_{ee} ranging from 0.15 to 1.5, for $H^{\pm\pm}$ masses between 80 GeV and 2 TeV.
- lepton flavour violating (LFV) decays of μ and τ leptons (Fig. 2.11b, 2.11c), as $\mu^- \to e^- e^+ e^-$, $\tau \to \ell_j^- \ell_k^+ \ell_l^-$, $\mu \to e\gamma$ and $\tau \to \mu\gamma$. From the upper limits on these LFV decay's branching ratios one can extract upper limits on $\frac{h_{\ell_{i,j,k}} h_{\ell_{i,j,k}} h_{\ell_{i,j,k}} h_{\ell_{i,j,k}}}{m^2_{H^{\pm\pm}}/(100\text{ GeV})^2}$ which are of the order of $< 10^{-7} - 10^{-4}$ [60];
- the muonium-antimuonium conversion (Fig. 2.11d) gives a constraint on $h_{ee} h_{\mu\mu}/(m_{H^{\pm\pm}}/100\text{ GeV})^2 < 1.98 \times 10^{-3}$ [60];
- the muon anomalous magnetic moment $g-2$ (Fig. 2.11e) as measured from experiments is consistent with its SM predicted value within 4σ, and gives an upper limit on the following couplings combination $\frac{|h_{\mu\mu}|^2 + 1/4|h_{e\mu}|^2 + 1/4|h_{\mu\tau}|^2}{m^2_{H^{\pm\pm}}/(100\text{ GeV})^2} < 0.034$ [60].

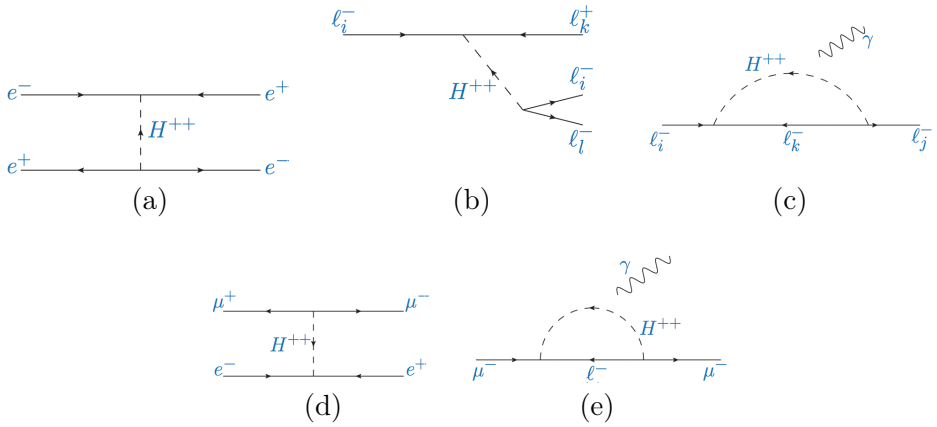

Figure 2.11: Feynman diagrams with $H^{\pm\pm}$ virtual loop contribution to Bhabha scattering (a), anomalous μ and τ decays (b), (c), muonium-anti-muonium conversion (d) and muon $g-2$ (e) [60].

2.5.2 Right-handed W bosons and Majorana neutrinos

LRSM have several free parameters, including the masses of right-handed W bosons and heavy neutrinos. These two particles can be mainly produced through the following processes [67]:

- $pp \to 2\ell^{\pm} + X$ due to W_R fusion,
- $pp \to W_R \to \ell + N_R$,
- $pp \to Z_R \to 2N_R$ with subsequent decay of N_R into charged leptons $\ell^{\pm}$ and jets.

The first process is very similar to the neutrinoless double β-decay violating the lepton number but its cross-section is small compared to the other two processes, which have similar cross-sections. This work focuses on the second production and decay chain, whose Feynman diagram is reported in Fig. 2.12, also known as Keung-Senjanović process [68].

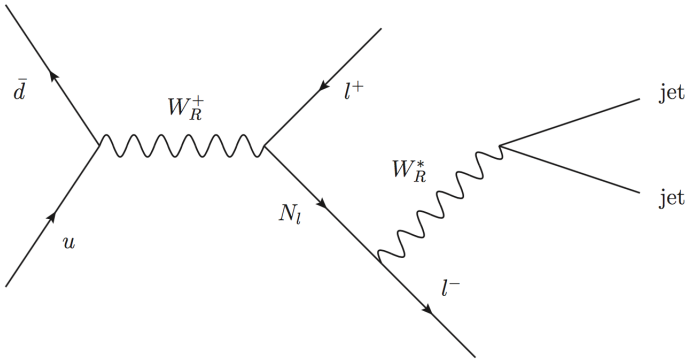

Figure 2.12: Feynman diagram for the production of a W_R with consequent decay into a N_R and a charged lepton under the hierarchy hypothesis $m(W_R) > m(N_R)$. The N_R eventually decays into a W_R and a charged lepton. If the N_R is a Dirac particle, the final state contains two OS leptons and two jets, while in the Majorana case the final state contains two jets and equally divided SS or OS leptons. Under the opposite hierarchy hypothesis, $m(W_R) < m(N_R)$, the first W_R is off-shell while the one originating from the N_R decay is on-shell.

The cross-section computation for this process depends on the value of the coupling constant g_R, the masses of N_R and W_R, the elements of the Cabibbo-Kobayashi-Maskawa (CKM) mixing matrix for the right-handed sector and the $W_R - W_L$ mixing strengths. The following assumptions are made in the cross-section computation [69]:

- the right-handed CKM matrix is identical to the left-handed one,
- the left- and right-handed coupling constants are identical ($g_R = g_L$),
- the mixing between right and left sectors is negligible ($< 10^{-3}$),
- the right-handed neutrino is light enough to be observed at the LHC.

Under these assumptions, the Z_R is about 1.7 times heavier than the W_R and for this reason the corresponding cross-section is smaller. If N_R is a Majorana particle, it could either decay into leptons or anti-leptons, leading to OS or SS signatures. The advantage of the SS signature is the low SM background contribution, providing a very powerful signature for W_R and at the same time proves the Majorana nature of N_R. It is important to stress here that, given the unknown mass hierarchy between the two particles, either the W_R or the N_R can be off/on shell. Consequently, the final state can be reconstructed using both the leptons and the jets in case $m(W_R) > m(N_R)$, while for the opposite mass hierarchy $m(W_R) < m(N_R)$ only two jets and one lepton provide the invariant mass of the N_R. Furthermore, right-handed neutrinos with different flavours are not bounded to have same masses.

The Keung-Senjanović process was searched by both the ATLAS and CMS Collaborations at $\sqrt{s}$=7 TeV [70, 71] and $\sqrt{s}$ = 8 TeV [72, 73]. No evidence for the production of W_R or N_R resulted from these searches. The most stringent limit was set by CMS at 8 TeV, excluding W_R with masses smaller than 3 TeV for $m(N_R) \sim 0.8$ TeV. The highest excluded N_R masses are ∼2 TeV, for $m(N_R) \sim 2.5$ TeV. However, the hierarchy $m(W_R) < m(N_R)$ was not previously explored and it is here presented for the first time (Chapter 7).

Chapter 3

The ATLAS experiment at the LHC

The Large Hadron Collider (LHC [74]) represents the state-of-the-art particle accelerator machine. It is designed to reach the highest energy ever explored in particle physics, and its primary target was the discovery of the last missing piece of the SM: the Higgs boson. However, the Higgs boson discovery was not the only purpose of the accelerator. Indeed, the LHC is a discovery machine and it is designed to explore the unknown. If new particles exist around the TeV scale, the LHC should be able to find them.
Four main experiments are located in underground facilities along the LHC tunnel: ATLAS, CMS, LHCb and ALICE.
This chapter illustrates the LHC machine and the technology beyond particle acceleration, focusing on the ATLAS experiment which detected and recorded the data used in this work.

3.1 The Large Hadron Collider

The Large Hadron Collider is installed in the tunnel previously hosting the Large Electron-Positron Collider (LEP) at CERN. The collider total length is 27 km and the tunnel, through which accelerated particles flow, is located between 50 and 175 m underground. The LHC is designed to accelerate both protons and heavy ions (mainly lead) up to a center of mass energy of $\sqrt{s} = 14$ TeV and $\sqrt{s} = 2.76$ TeV/nucleon respectively.
Regarding heavy ions, LHC can operate both in p-Pb and in Pb-Pb collision modes and, already in 2015, the energy per colliding nucleon pair outperformed the design value, reaching 5.02 TeV/nucleon.

Since the results of this work are obtained from proton-proton collisions, in the following we focus on the *pp* operation mode. Moreover, given that the data used in this work were collected during 2015 and 2016, we concentrate on the data taking performance concerning these two years.
After the 2013-2014 shutdown[1], the LHC was upgraded to reach its design performance and resumed its operations in 2015. Table 3.1 presents an overview of the machine performance in Run 1 and Run 2 and a comparison with the design project.

Parameter	2012	2016	Design
Beam energy (TeV)	4	6.5	7
Bunch spacing (ns)	50	25	25
Max number of bunches	1374	2220	2808
Protons per bunch	1.65×10^{11}	1.1×10^{11}	1.15×10^{11}
Transverse normalized emittance ϵ_n (μm)	2.4	3.4	3.75
Half crossing angle (μrad)	145	185	143
Peak luminosity ($cm^{-2}s^{-1}$)	0.75×10^{34}	1.4×10^{34}	1×10^{34}
Pile-up (μ)	∼35	∼50	∼20

Table 3.1: LHC performance in Run 1 and Run 2 compared to the machine design values [75]. The operations in 2012 and 2016 were taken as reference, providing the years with the highest integrated luminosity collected respectively in Run 1 and in Run 2 (up to the writing of this work).

Almost all the accelerator parameters reached their design values (Tab. 3.1). The last row in the table shows the number of multiple *pp* interactions per bunch crossing (usually called *pile-up* or μ). LHC protons do not flow as a continuous beam inside the machine but are packed into *bunches*, due to the radiofrequency cavities used to accelerate charged particles at high energies (see Section 3.1.1). The number of protons inside a bunch is of the order of 10^{11}. At a bunch-crossing rate of 40 MHz, the pile-up exceeded ∼3 times the design value. Such a high number of multiple interactions per bunch-crossing represents one of the biggest challenges for the ATLAS detector, both for the calorimeter (Sec. 3.2.3) and the trigger (Sec. 3.2.5) systems.
Figure 3.1 shows, on the left, a comparison between the delivered luminosity ($\mathcal{L}$) in Run 1 and in Run 2. The right plot shows the total integrated $\mathcal{L}$ in 2016. The comparison between the luminosity delivered by the LHC (i.e. provided by the accelerator) and the recorded one (i.e. collected by

[1] The period covering the years 2008-2012 is commonly referred to as "LHC Run 1", while the period 2015-ongoing is referred to as "LHC Run 2".

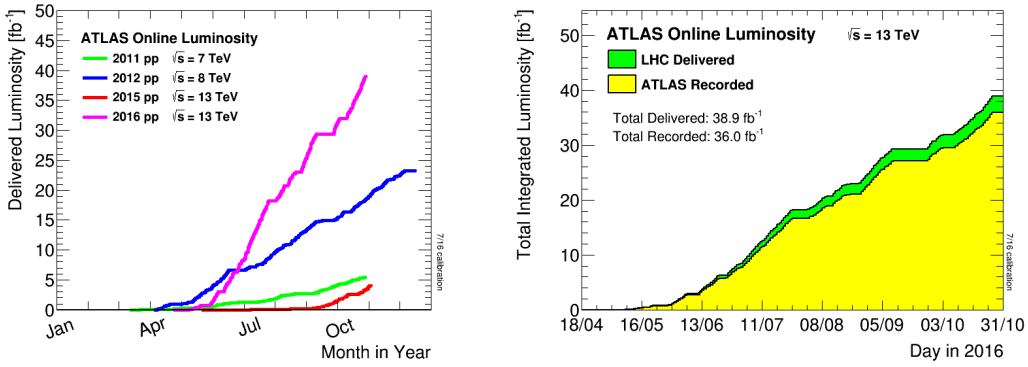

Figure 3.1: Left plot: comparison between ATLAS delivered online luminosity during stable beams for *pp* collisions during 2011 (green), 2012 (blue), 2015 (red) and 2016 (pink) as a function of months in a year. Right plot: total integrated luminosity delivered by LHC (green) and recorded by the ATLAS detector (yellow) in 2016 [76].

the ATLAS detector) achieved a data taking efficiency above 90% in 2016[2]. Data-taking and machine operation, during 2015, were mainly devoted to commissioning towards higher energies. Consequently, to really explore the LHC Run 2 potential, the machine parameters were pushed to reach higher peak luminosities.
The final dataset collected up to end of 2016 by the ATLAS detector almost doubled the total integrated luminosity recorded in Run 1. Indeed, data suitable for physics analysis amount to 20.3 fb^{-1} in Run 1 and to 33.3 fb^{-1}, combining 2015 and 2016 LHC Run 2 data, confirming the excellent performance of both the LHC and ATLAS detector.

3.1.1 Acceleration Chain

A scheme of CERN accelerators is given in Fig. 3.2. The primary proton source is a bottle of Hydrogen gas connected to a *duoplasmatron source* [78]. The source principle is to create plasma from H gas separating protons from electrons. Protons are then injected into the acceleration chain, consisting of:

- **Linac2:** a radiofrequency cavity linear accelerator used to bring protons energy up to 50 MeV. Quadrupole magnets ensure beam focusing. Particles are then transferred to the next accelerating step.

[2] The difference between *delivered* and *recorded* luminosity is given in Sec. 3.1.2.

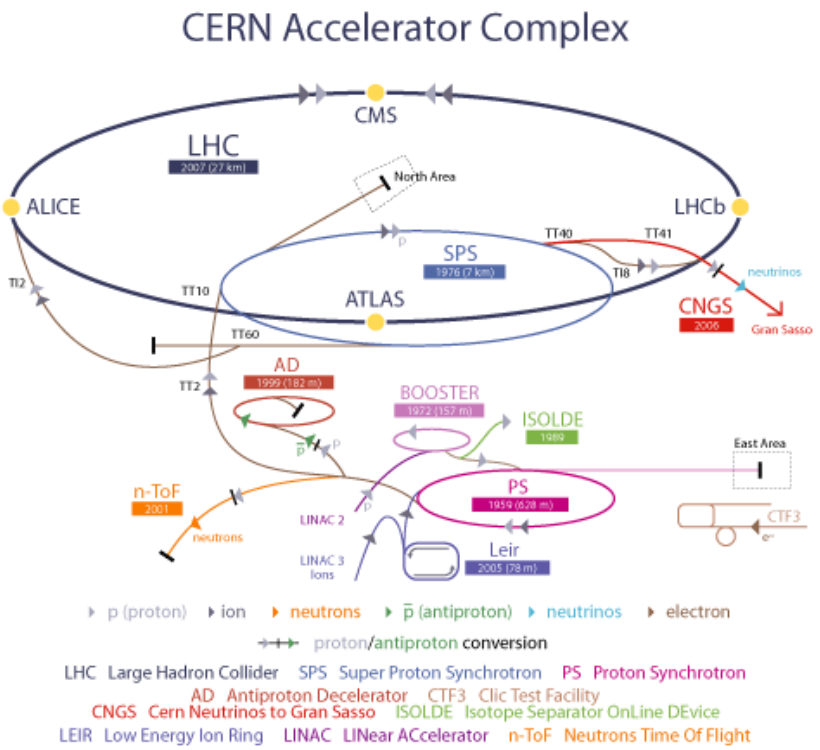

Figure 3.2: CERN accelerator complex: acceleration chain and location of the main LHC experiments [77].

- **Proton Synchrotron Booster (PSB):** is composed by four synchrotrons, accelerating protons up to 1.4 GeV and preparing the injection to the proton synchrotron (PS). The booster was built for LHC to provide ∼100 times more protons to the Proton Synchrotron.
- **Proton Synchrotron (PS):** built in the 1960s, is the oldest circular accelerator of the LHC acceleration chain, with a circumference of 628 m. The PS has 277 electromagnets and 100 dipole magnets to keep the particles on a circular trajectory. The energy reached by the protons is 25 GeV; moreover the PS produces a 25 ns-separated bunch beam.
- **Super Proton Synchrotron (SPS):** is a 7 km circumference circular accelerator. 1317 electromagnets and 744 dipole magnets keep the beam into circular trajectory. The SPS accelerates protons up to 450 GeV.

Particles are eventually transferred into the two beam pipes of the LHC, one beam circulating clockwise and the other one anticlockwise. To keep particles on their trajectories, the accelerator ring is provided with two types of

superconducting magnets, cooled by a system of liquid helium at a temperature of -271.3°C. Bending is performed through 1232 dipole magnets, 15 m long, while 392 quadrupole magnets, each 5-7 m long, are used for focusing. It takes around 20 minutes for each beam to reach its final energy of 6.5 TeV.

Along the LHC ring, the beams are deviated to cross with each other in four interaction points. Four main experiments are hosted in the ring:

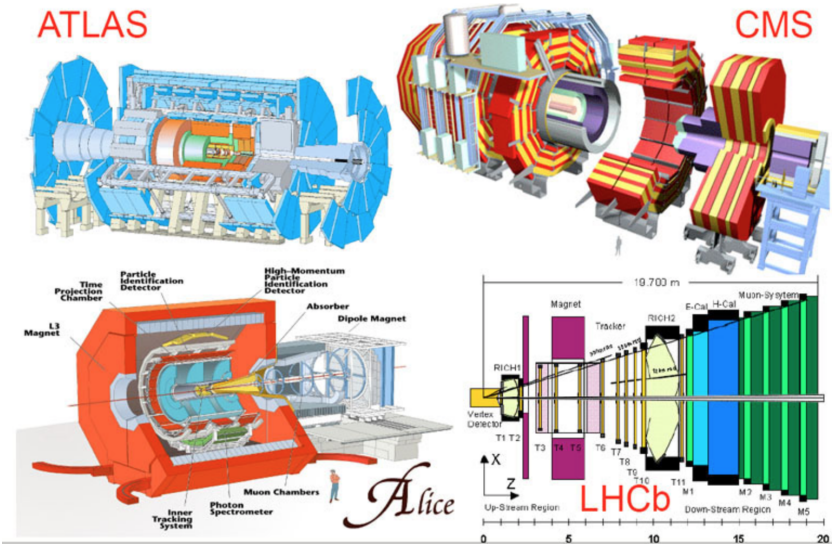

Figure 3.3: Sketches of the detector layouts for the four main LHC experiments: ATLAS, CMS, ALICE and LHCb.

- **A Toroidal LHC Apparatus (ATLAS) and Compact Muon Solenoid (CMS):** they are multi-purpose experiments designed to work at high luminosity. The aims of ATLAS and CMS are the same, allowing cross-checks of each other's results.

- **LHCb:** is devoted to precision measurements in the field of flavour physics, with special attention to the b-quark. Differently from ATLAS and CMS, which try to surround with a 4π angle the interaction point (IP), LHCb has only one arm of the detector in a forward direction, optimizing the b-decay reconstruction.

- **A Large Ion Collider Experiment (ALICE):** is dedicated to the study of the *quark-gluon plasma*, a condensed status of matter produced at high energies, as the ones present in the universe a few moments after the Big Bang. ALICE has to deal with a much higher track density per bunch crossing and it operates at lower instantaneous luminosity, $\mathcal{L}$=10^{27} cm^{-2}s^{-1}

The layouts of the four detectors are shown in Figure 3.3.

3.1.2 LHC Challenges and Beam Luminosity Lifetime

Instantaneous luminosity is a key parameter of a collider and is defined as the ratio between the rate and the cross-section of a given process:

$$\mathcal{L} = \frac{R}{\sigma}. \tag{3.1}$$

The instantaneous luminosity is independent of the process itself, and it is actually defined starting from colliding machine parameters. If the beams are made of identical bunches, Gaussian in shape and perfectly overlapping in the IP, the luminosity is given by:

$$\mathcal{L} = f_r n_b \frac{N_1 N_2}{4\pi\sigma_x\sigma_y} \tag{3.2}$$

where $\sigma_{x,y}$ are the gaussian transverse profiles of the beams, $N_{1,2}$ the number of protons in the two beam bunches, n_b the number of bunches and f_r the beam-revolution frequency. In general, when beams collide with a crossing angle different from zero, $\mathcal{L}$ is expressed as [79]:

$$\mathcal{L} = f_r n_b \frac{N_1 N_2 \gamma}{4\pi\beta^* \epsilon_{xy}} \times F \tag{3.3}$$

where ϵ_{xy} is the geometric emittance[3], γ the relativistic Lorentz factor and F is a geometric reduction factor given by:

$$F = \frac{1}{\sqrt{1 + \frac{(\sigma_s \tan\phi)^2}{\epsilon_{xy}\beta^*}}} \tag{3.4}$$

where σ_s is the bunch length and ϕ half of the crossing angle. From Eq. 3.3 it can be seen that possible ways to increase instantaneous luminosity are related to the increase of n_b and $N_{1,2}$. Increasing the number of protons in a beam results in a higher gain, given the square proportionality in the luminosity equation. Both these two parameters are optimized to take into account their impact on the electron cloud (EC) effect[4] and the heating of

[3] The beam emittance is a measure for the average spread of particles in the beam in a position-momentum coordinate plane and it depends on how the beams are prepared in the accelerator chain.

[4] Relativistic charged particles accelerated radially, as LHC protons, emit synchrotron radiation (i.e. photons) which, interacting with the vacuum chamber walls of the acceleration cavity, creates photoelectrons. Primary electrons, interacting electromagnetically with successive bunches passing in the vacuum chamber, are pulled toward the chamber and hit its walls again, creating secondary electrons. The processes continues into an avalanche effect called *electron cloud* [80].

the cryogenic system. We use Eq. 3.3 with the typical 2016 LHC beam parameters to evaluate the value of the instantaneous luminosity. Considering a number of bunches of n_b= 2220, two beams with 1.1×10^{11} protons, the LHC revolution frequency of f_r=11.25 kHz, a transverse normalized emittance of 2.2 μm, a β^* of 40, a reduction factor $F \sim 0.65$, we obtain

$$\mathcal{L} = \frac{2220 \times (1.1)^2 \times 10^{22} \times 11.25 \times 10^3 \times 0.65 \times 6.9 \times 10^3}{4 \times 3.14 \times 40 \times 2.2 \times 10^{-4}} \sim 1.4 \times 10^{34} \text{cm}^{-2}\text{s}^{-1} \tag{3.5}$$

the peak instantaneous luminosity for 2016.
The instantaneous luminosity is not constant over a physics run but decreases due to the degradation of intensity and emittance of the circulating beam. The law describing luminosity degradation is exponential:

$$\mathcal{L} = \mathcal{L}_0 \times e^{-\frac{t}{\tau}} \tag{3.6}$$

where τ is a time constant of ∼15 h. It follows that certain LHC fills can circulate in the machine for a time of ∼10 h; afterwards the beam needs to be dumped and a new injection chain starts. To evaluate the amount of data collected, we need to distinguish between:

- delivered luminosity, defined as the luminosity made available by the LHC machine,
- recorded luminosity, defined referring to the fraction of time during which both the detector and the data acquisition systems were active.

Delivered luminosity is indeed evaluated independently of the detector or data acquisition systems. To be aware of the actual luminosity available for physics analysis, the delivered luminosity has to be corrected for the detector and data acquisition systems dead-time.

3.1.3 LHC Detectors Requirements

All the LHC detectors were designed to cope with very challenging data taking conditions. To imagine the level of complexity the detectors have to exploit, it is sufficient to think that every 25 ns there can be a pile-up higher than 50. In addition, collisions between protons involve multiple inelastic scatterings of proton constituents (i.e. *partons*), so that there is a non-null probability of multiple interactions even in a single *pp* collision. These latter events are usually referred to as *underlying events* (UE). In addition we have to consider also the initial (ISR) and final state (FSR) gluon radiation. The whole set of particles populating the detector material, sometimes even in

a very restricted portion of space, can totally overwhelm the signature of processes with very low cross-sections, or the ones of NP phenomena.
It follows that all the LHC detectors must satisfy the requirement of high granularity and excellent particle identification. Detectors must provide:

- full calorimetric coverage and high resolution for electron, photon, jets identification and energy measurement, as well as missing transverse energy ($E_{\mathrm{T}}^{\mathrm{miss}}$);
- efficient tracking delivered by the inner detector for particle momentum measurement and charge reconstruction. Identification of τ lepton hadronic decays and b-jets also require to resolve secondary decay vertices' positions, besides the primary ones;
- good muon identification and momentum resolution and in addition the capability to determine without ambiguities the charge of high-p_{T} muons;
- large acceptance in pseudorapidity (η) and good azimuthal angle (ϕ) coverage;
- efficient triggering system with good background rejection;
- radiation-hard electronics and sensor elements to limit the radiation damage due to charged particles from pp collisions and neutrons produced by the interaction of hadrons with the detector material itself;
- fast electronics to limit the dead-time of the data acquisition system.

The combination of all these features allows ATLAS to be able to reconstruct events with high $E_{\mathrm{T}}^{\mathrm{miss}}$, high jet multiplicity or high momentum leptons, which might be connected to the signature of new, or rare, physics phenomena.

In the following section the characteristics of the ATLAS detector are discussed in more details and a summary of the performance goals of the detectors can be found in Table 3.2.

3.2 The ATLAS Experiment

ATLAS [81] is a multi-purpose detector located at Point 1 of the CERN LHC facility, approximately 100 m underground. ATLAS has cylindrical symmetry, it is 44 m long and it has a diameter of 22 m. ATLAS is composed of different sub-detectors, designed to reconstruct particles produced

Detector component	Required resolution	η coverage	
		Measurement	Trigger
Tracking	σ_{p_T}/p_T=0.05%$p_T \oplus$ 1%	$\pm$ 2.5	
EM calorimetry	$\sigma_E/E = 10\%/\sqrt{E} \oplus 0.7\%$	$\pm$ 3.2	$\pm$ 2.5
Hadronic calorimetry			
barrel and end-cap	$\sigma_E/E = 50\%/\sqrt{E} \oplus 3\%$	$\pm$ 3.2	$\pm$ 3.2
forward	$\sigma_E/E = 100\%/\sqrt{E} \oplus 10\%$	3.1< $\lvert\eta\rvert$ <4.9	3.1< $\lvert\eta\rvert$ <4.9
Muon spectrometer	σ_{p_T}/p_T=10% at p_T = 1 TeV	$\pm$ 2.7	$\pm$ 2.4

Table 3.2: General performance requirements of the ATLAS detector. Units for p_{T} and E are in GeV [81].

in pp collisions: electrons, photons, muons, jets and neutrinos (which can only be reconstructed in terms of $E_{\mathrm{T}}^{\mathrm{miss}}$).
Starting from the IP, particles encounter the following sub-detectors: the inner detector, the electromagnetic and hadronic calorimeters and, eventually, the muon spectrometer. The ATLAS magnetic system bends the trajectory of charged particles and allows precise reconstruction of particle momenta. A scheme of the detector can be found in Figure 3.4.

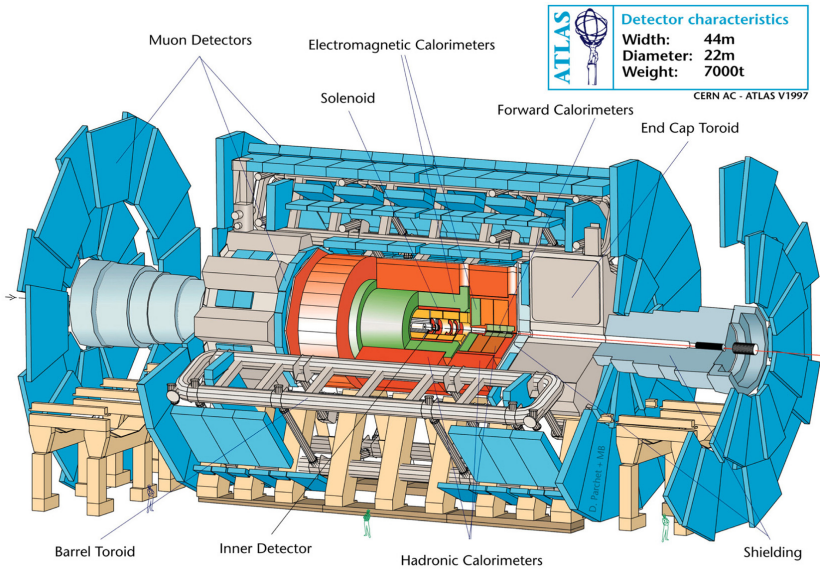

Figure 3.4: Frontal view of the ATLAS detector [81].

To describe particle motion inside the detector, a cylindrical coordinate system is used throughout ATLAS, taking the IP as the origin of the coordinate system (see Fig. 3.5).

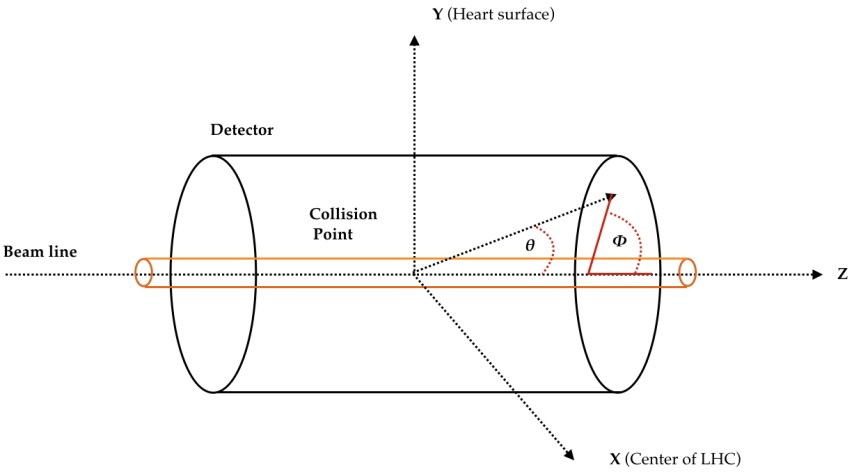

Figure 3.5: ATLAS detector common coordinate system.

The z-axis runs along the beam line, while the xy plane is perpendicular to the beam line and referred to as *transverse plane*, where transverse momenta p_{T} and energies E_{T} are measured. The x-axis points to the center of the LHC ring and the y-axis points up to the earth surface. The detector half at positive z-values is referred to as the *A-side* while the other as the *C-side*. The transverse plane is defined in terms of r-ϕ coordinates, where ϕ is measured from the x-axis, around the beam and r is the distance from the beam line. The polar angle θ is defined as the angle from the positive z-axis. Given that partons interacting in pp collisions carry an initially unknown fraction of the longitudinal proton momentum and assuming the initial transverse momentum (in the xy plane) of the proton beam to be negligibly small, we can assume:

$$\sum p_T \simeq 0\,, \quad p_T = \sqrt{p_x^2 + p_y^2} \tag{3.7}$$

where the sum is extended to all final state particles. It is useful to identify a set of Lorentz-invariant variables, such as the *rapidity*, defined as:

$$y = \frac{1}{2} \ln \left(\frac{E + p_z}{E - p_z} \right) \tag{3.8}$$

where E and p_z are the energy and the z-axis momentum component of the particle. This quantity is invariant under Lorentz transformations along the z-axis, as well as the p_{T} and E_{T}. It is also useful to define the *pseudorapidity*

as:

$$\eta = -\ln\left(\tan\frac{\theta}{2}\right) \tag{3.9}$$

which depends on the particle angular position. For particles whose speed is very close to the speed of light $\eta \simeq y$. Furthermore, a distance measurement in the $\eta - \phi$ plane is introduced:

$$\Delta R = \sqrt{(\Delta\eta)^2 + (\Delta\phi)^2} \tag{3.10}$$

where $\Delta\eta$ and $\Delta\phi$ are the differences in pseudorapidity and azimuthal angles between the particles taken into account.

3.2.1 The ATLAS Magnetic System

ATLAS superconducting magnet systems [82] required pushing the limits of technology and making one of the largest magnets of their type so far. The radius of curvature ρ of a charged particle q, with momentum p entering perpendicularly a magnetic field B, follows from the Lorentz force:

$$\rho = \frac{\vec{p}}{q \cdot \vec{B}} \tag{3.11}$$

increasing with momentum and decreasing at higher magnetic field values. It follows that high-p_{T} particles are less bent by the magnetic field. The minimum detectable bending is limited by the precision of the tracking system and by the perturbations of the particle trajectory due to interactions with the encountered material along the flight-path. The ATLAS magnetic system consists of the following superconducting magnets:

- the **Central Solenoid (CS)** providing a 2 T magnetic field for the inner tracker,
- the **Barrel Toroid (BT)** and two **End-Cap Toroids (ECT)**. The performance of the air-core toroidal system is characterized by the field integral $\int B \cdot dl$, where B is the azimuthal field component and dl is the line trajectory between the inner and the outer radius of the toroids. The provided field integral is 2-6 T·m for the BT and 4-8 T·m for the ECT.

A scheme of the magnetic system is shown in Fig. 3.6.

Given that all coils are superconducting, cooling circuits and cryostats for optimum thermal insulation of the coils are required.
The CS is a single layer aluminum stabilized NbTi/Cu coil wound internally

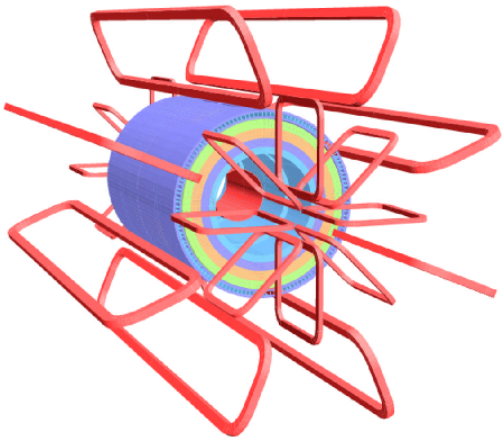

Figure 3.6: 3-Dimensional view of the ATLAS detector magnetic system: the central solenoid, 8 barrel toroid coils and 2×8 coils of the end-cap toroids [82].

in a supporting cylinder. With a radius of 1.2 m and a lenght of 5.3 m, it surrounds the inner detector region providing a 2 T solenoidal magnetic field for precise momentum measurement of charged particles. The coil is placed in front of the liquid-argon electromagnetic calorimeter, thus it was designed to be thin enough to limit the interaction of particles in the coil itself.
The BT consists of a aluminum stabilized NbTi superconductor provided with a current of up to 20.5 kA. The 8 rectangular coils are arranged in a cylindrical configuration. The total length of the BT is 25 m and it has an outer/inner diameters respectively of 20.1 m and 9.4 m, deviating particles in the range $|\eta| \leq 1$.
The ECT is composed of 8 rectangular coils in a single cylindrical vessel, for a total length of 5 m. Its outer diameter is 10.7 m while the inner diameter is 1.65 m. The ECT is arranged to close the magnetic field lines produced by the BT. The field is orthogonal to the beam axis and deviates particles in the region $1.4 < |\eta| < 2.7$. In the transition region ($1.0 < |\eta| < 1.4$) the magnetic field is produced by both the BT and the ECT.
The whole magnetic system is cooled at liquid helium temperature (4.8 K).

3.2.2 The Inner Detector

One of the most important steps in particle identification is non-destructive tracking. Indeed, charged particles only leave a hint of their passage in the innermost part of the ATLAS detector: the **Inner Detector (ID)** [83]. The ID is crucial for the reconstruction of charged particles tracks and their production vertex and, by the information on track multiplicity, allows to

distinguish between electrons, photons or charged hadrons.
Given the very large track occupancy produced by LHC collisions, the granularity of the detector must be very fine to make high precision measurements. The ID has cylindrical symmetry, an outer radius of 105 cm and covers the region up to $|\eta|$ <2.5. The detector is composed of three sub-systems, the **Pixel Detector (PD)**, the **Semiconductor Tracker (SCT)** and the **Transition Radiation Tracker (TRT)**. All sub-system are divided into a barrel region with cylindrical symmetry layers and two end-caps made from disks of silicon sensors or TRT wheels.

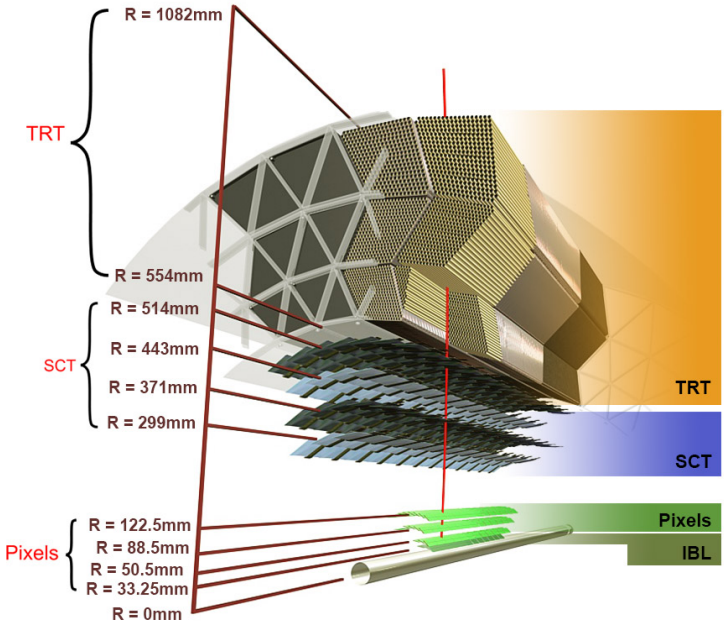

Figure 3.7: Image of the ATLAS barrel Inner Detector: the IBL, Pixels, SCT and TRT components are visible [84].

The performance of the innermost layer of the PD is critical to the full realization of the physics capabilities of the ATLAS experiment. To enhance good vertex reconstruction and *b-tagging*, an **Insertable B-Layer [84]** was designed and installed during 2013-2015 shut-down. It is located between the pixel detector and the beam pipe as shown in Figure 3.7.
The IBL detector had to be fitted in a free space of 12.5 mm (between the already existing part of the PD and the reduced-diameter beam pipe). The IBL consists of 14 staves equipped with both planar and 3D silicon pixels along 332 mm on each side of the ATLAS detector. IBL ensures full ϕ coverage for high p_T tracks. The silicon pixel size is 50 μm in the ϕ direction

and 250 μm in the z direction. The insertion of IBL into the ID significantly improved the quality of the impact parameter and vertex reconstruction, consequently increasing the b-tagging performance. As an example, the IBL reduces the probability for b-jet mistagging (see Section 4.4.2) by a factor $\sim$2 [84], while providing the same tagging efficiency.

The rest of the **PD** [85] is composed by three layers of silicon pixels, placed at 50.5, 88.5 and 122.5 mm from the detector center, for a total of 46080 modules made of 50×400 μm^2 pixels. Five additional rings on each side, with an inner radius of 11 cm and an outer radius of 30 cm, complete the angular coverage of the detector. The read-out system hosts almost 80 million channels.

The **Semi Conductor Tracker (SCT)** [86] is designed to provide precision measurements of momentum, impact parameter and vertex position in the intermediate radial range of the ID. The barrel section of the SCT is composed of four layers of silicon microstrip modules placed at 300, 373, 447 and 520 mm from the beam axis. It provides precise measurements in the $r-\phi$ coordinates and uses an angle stereo to obtain the measurement in the z coordinate. Each silicon detector is 6.36×6.40 cm^2 large, with 768 readout strips of 80 μm pitch in the barrel and variable pitch size in the end-caps. Each module consists of four single-sided p-n silicon detectors. On each side of the module, two detectors are wire-bonded together to form 12.8 cm long strips. The end-cap detector modules have a similar structure. While pixels, because of their geometry have good 2-dimension coverage, microstrips have a better resolution along one coordinate. The spatial resolution of the SCT is 16 μm ($r-\phi$) and 580 μm (z) in the barrel and 16 μm ($r-\phi$) and 580 μm (r) in the end-caps, providing the pseudorapidity coverage $|\eta| \leq 2.5$.

The outer part of the ID is the **Transition Radiation Tracker (TRT)** [87] based on the use of straw detectors. The detector is built with 4 mm diameter tubes, arranged in 36 layers, filled with a Xe or Ar gas mixtures. Each layer is interspersed with a polypropylene fiber. Gas inside the tube ionizes when charged particles pass through it and the low energy ionization signals are collected by a gold-plated 30 μm tungsten wire located at the middle of the tube. The passage through the polypropylene fiber stimulates transition radiation emission from ultrarelativistic charged particles, proportional to their Lorentz γ factor. The process causes the emission of X-rays, which contributes to ionization as a high energy signal. Only electrons and positrons are characterized by this double contribution to ionization, while this is not the case for heavier particles such as protons or pions which, being heavier, have a lower Lorentz γ factor. It follows that the TRT is fundamen-

tal for $e^{\pm}$ identification. The spatial resolution of the TRT is of 130 μm.

The resolution of the ID is parametrized in terms of the transverse impact parameter d_0, defined as the distance of closest approach to the beam-line, and z_0, being the longitudinal impact parameter, in the following way:

$$\sigma(d_0) = 12 \oplus \frac{88}{p_{\mathrm{T}}\sqrt{\sin\theta}}\ \mu\mathrm{m} \tag{3.12}$$

$$\sigma(z_0) = 95 \oplus \frac{160}{p_{\mathrm{T}}\sqrt{\sin^3\theta}}\ \mu\mathrm{m} \tag{3.13}$$

where the track p_{T} is in units of GeV/c [88].

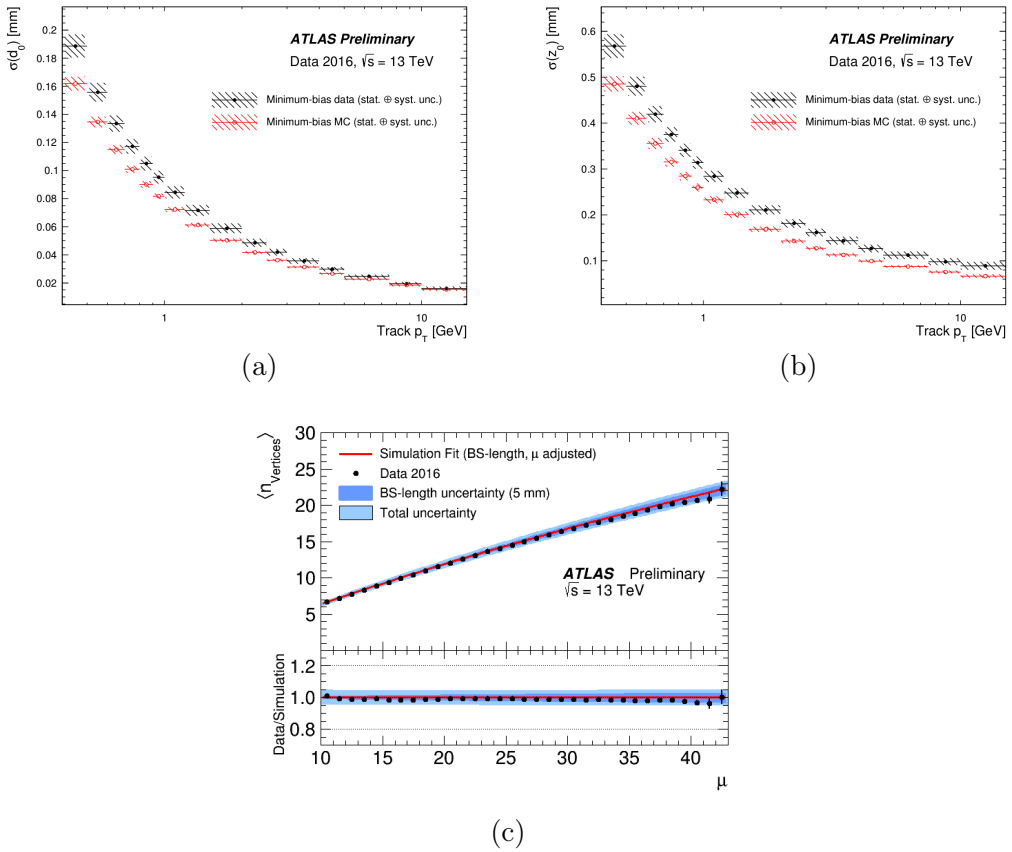

Figure 3.8: ID performance in 2016 [89]: transverse (a) and longitudinal (b) impact parameters resolutions as a function of track p_{T}. Number of reconstructed vertices (c) as a function of pile-up.

The resolution on the transverse and longitudinal impact parameters of tracks is measured using 2016 *minimum-bias* data [89]. Results are shown in Fig. 3.8a and 3.8b respectively for the transverse and longitudinal impact parameters. Differences between the measured resolutions from data and prediction depend both on the exact description of the material of the IBL detector in the simulation (effect dominating at low p_{T}) and on a simplified model for energy deposit which predicts better resolution in MC than in data. Figure 3.8c shows the distribution of the average number of reconstructed vertices as a function of the mean number of multiple pp inelastic interactions per bunch-crossing. Besides the primary vertex (PV) associated to the hard-scattering, pile-up from soft-QCD interactions produces additional PVs. As a consequence, a single physics event can present many PVs. Tracks are selected if satisfying several requirement based on the information collected by the IBL, the PD and the SCT, which are tight enough to reduce the contribution from fake tracks. The vertex is than matched to tracks using a fitting procedure. The presence of significant pile-up makes it more difficult to correctly identify the hard-scatter PV among the pile-up vertices. For this reason, it is effective to identify the hard-scatter PV as the PV with the highest sum of the squared transverse momenta of contributing tracks: $\sum p_{\mathrm{T}}^2$. This choice is based on the assumption that charged particles produced in hard-scatter interactions have higher transverse momentum than those produced in pile-up collisions.
The curve in Fig. 3.8c represents the result of a fit to the simulation of minimum-bias events, while dots are a representative subset of zero-bias[5] data collected in 2016. It is interesting to note the almost linear dependence between the number of PVs and pile-up: $n_{\mathrm{vertices}} \simeq \mu/2$[6].

3.2.3 The ATLAS Calorimeters

Calorimeters are used in ATLAS to measure destructively the energy of electrons, photons and hadrons passing through them. ATLAS is equipped with two systems of sampling calorimeters, an **Electromagnetic Calorimeter (EM)** and a **Hadronic Calorimeter (HC)**.
The structure of a sampling calorimeter is the following: depending on the type of particle we want to detect, a material with high interaction cross-section, for that particle, is chosen as *passive medium*; once the interaction

[5] Zero-bias events are collected by triggering on crossing of filled bunches.
[6] The measurement of n_{vertices} is sensitive to the inelastic pp cross-section, which corresponds to ∼80% of the total pp cross-section described by μ. Taking into account vertex reconstruction efficiency, the expected number of n_{vertices} corresponds to ∼half of the measured μ (see Section 3.2.6).

occurs inside the detector, *electromagnetic* or *hadronic* showers are created and read-out in the *active medium*. The electromagnetic calorimeter covers the $|\eta| < 3.2$ region. The hadronic calorimeters are divided into a barrel region ($|\eta|$ <1.7), two end-caps (1.5< $|\eta|$ <3.2) and a the forward region, covering 3.1< $|\eta|$ <4.9. A view of the ATLAS calorimetric system is given in Fig. 3.9.

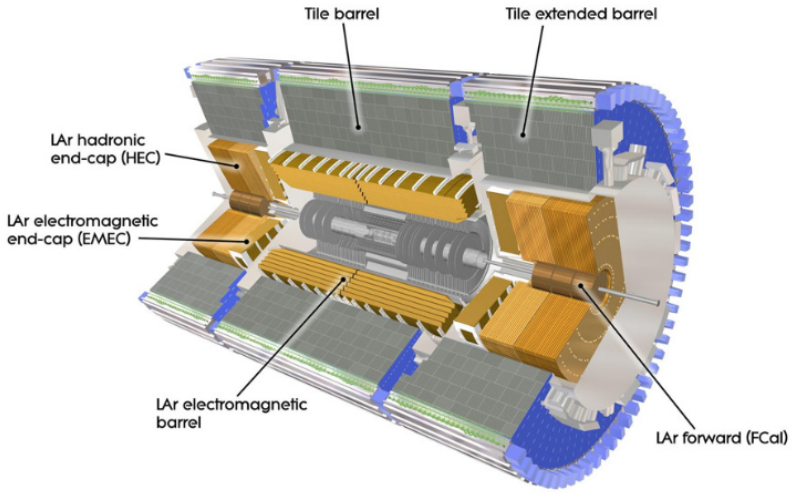

Figure 3.9: View of the ATLAS electromagnetic and hadronic calorimeters [81].

The Electromagnetic Calorimeter

The electromagnetic calorimeter [81] is made of lead absorbing plates as passive medium and liquid-argon (LAr) as active material, following an accordion geometry. Lead plates were chosen due to their large electromagnetic cross-section: high energy electrons and photons mainly interact via *bremsstrahlung* or pair production. Secondary particles produce other particles by the same mechanism generating a cascade. The longitudinal size of an electromagnetic cascade is described in terms of the *radiation length*, X_0, depending on the material itself, representing the average path the particle needs to travel to reduce its initial energy by a factor $1/e$. For calorimeters with 25 X_0 thickness, the shower leakage beyond the end of the detector was proved to be less than 1%, up to electron energies ∼300 GeV [90].
ATLAS EM calorimeter is divided into a barrel ($|\eta|$ <1.475) part and two end-cap elements (1.375< $|\eta|$ <3.2).
The two half-barrel parts are separated by a 6 mm gap at $z = 0$ while each end-cap is divided into two coaxial wheels: an outer one covering the region

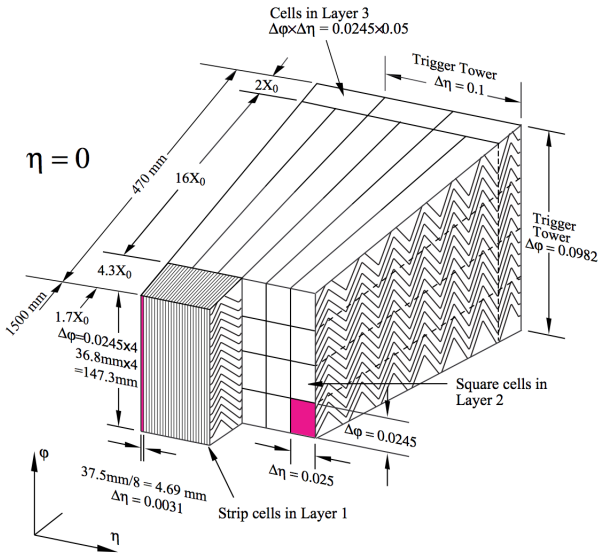

Figure 3.10: Sketch of a barrel module with accordion geometry; the η and ϕ granularity of the cells of each of the three layers and of the trigger towers is shown [81].

$1.375< |\eta| <2.5$ and an inner wheel covering $2.5< |\eta| <3.2$.
The accordion geometry of the EM detector allows complete ϕ symmetry without azimuthal crack regions. The total thickness of the EM calorimeter is larger than 24 X_0 in the barrel and larger than 26 X_0 in the end-caps.
In many physics analysis, objects (electrons, muons, jets) are required to be within the $|\eta| <2.5$ of the ATLAS detector. Thus, to provide high granularity in that region, the EM calorimeter is further segmented into three longitudinal sections, shown in Fig. 3.10.

The first *pre-shower* section uses narrow ($\sim$5 mm in the η direction) cells enhancing particle identification and providing high precision angular measurement. The middle section (made of $\Delta\eta \times \Delta\phi = 0.025\times0.025$ square towers) measures the released energy. The last compartment, with a granularity of 0.05 in η and a thickness varying between 2 X_0 and 16 X_0, measures the energy of particles which are not stopped in the central compartment and allows to distinguish electromagnetic and hadronic clusters. Indeed, the majority of electrons and photons is stopped within the central region of the electromagnetic calorimeter. The transition region between the barrel and the end-caps, within $1.375 < |\eta| < 1.52$, contains inactive material providing necessary services to the ID. This results in a significant energy loss and reduced performance in that region which, in turn, is discarded by most of the analysis selecting photons or electrons.

Energy resolution of the EM calorimeter was studied with electron beams of energies ranging from 10 to 245 GeV [91]. The fit result for the detector resolution led to the expression:

$$\frac{\sigma_E}{E} = \frac{9.4\%}{\sqrt{E[\text{GeV}]}} \oplus 0.1\% \tag{3.14}$$

in agreement with MC simulations.

The Hadronic Calorimeter

The hadronic calorimeter [81] is designed to provide good containment for hadronic showers, to measure hadron energy as well as missing transverse energy and to avoid strong-interacting particles to reach the muon system. Hadronic interactions produce secondary hadrons and can undergo other nuclear processes such as excitation or spallatation. The result of these interactions gives a hadronic cascade composed of secondary particles with energy from the GeV to the MeV scale. In analogy with the electromagnetic case, hadronic calorimeters are described in terms of the *interaction length* $\lambda \sim 35\ A^{1/3}\text{g cm}^{-2}$, defined as the mean free path between interactions. Good resolution for high energy jets is ensured for $\sim$10 λ calorimeter thickness.
ATLAS hadronic calorimeter total thickness is of 11 λ at η=0, sufficient to reduce leakage to the muon spectrometer and to guarantee a good $E_{\text{T}}^{\text{miss}}$ measurement, which is an important signature especially for NP searches.
The hadronic calorimeter covers the range $|\eta|$ <4.9 and various techniques are chosen to suit the widely varying requirements and the high radiation environment.

The **Hadronic Tile Calorimeter (HTC)** is a sampling calorimeter using iron as passive material and scintillating tiles as active material. Signal produced in the scintillators is proportional to the number of secondary particles produced in the interaction and, hence, to the particle energy deposit. The HTC covers the region $|\eta|$ <1.7. The detector was calibrated with pions in test beams, which led to the measured energy resolution [92]:

$$\frac{\sigma_E}{E_\pi} = \frac{(52.7 \pm 0.9)\%\sqrt{\text{GeV}}}{\sqrt{E[\text{GeV}]}} \oplus (5.7 \pm 0.2)\%. \tag{3.15}$$

in agreement with Monte Carlo simulation.
The **Hadronic End-Cap Calorimeters (HEC)**, covering the range 1.5< $|\eta|$ <3.2, uses LAr as active medium. The resolution, in this case, was measured in several test beams with electrons, pions and muons with energies

up to 200 GeV. The analysis of data collected with electrons gives the energy resolution of [93]:

$$\frac{\sigma_E}{E_e} = \frac{(21.4 \pm 0.1)\%\sqrt{\text{GeV}}}{\sqrt{E[\text{GeV}]}} \tag{3.16}$$

while from pion test beams:

$$\frac{\sigma_E}{E_\pi} = \frac{(70.6 \pm 1.5)\%\sqrt{\text{GeV}}}{\sqrt{E[\text{GeV}]}} \oplus (5.8 \pm 0.2)\%. \tag{3.17}$$

again, in agreement with MC simulation.
The **Forward Calorimeter (FCAL)** is placed very close to the beam pipe, and covers the region $|\eta|$ <4.9. It is made of LAr, iron and tungsten. The FCAL was also calibrated with electrons and pions and the following resolutions were measured [94]:

$$\frac{\sigma_E}{E_e} = \frac{(28.5 \pm 0.1)\%\sqrt{\text{GeV}}}{\sqrt{E[\text{GeV}]}} \oplus (3.5 \pm 0.1)\% \tag{3.18}$$

$$\frac{\sigma_E}{E_\pi} = \frac{(94.2 \pm 1.6)\%\sqrt{\text{GeV}}}{\sqrt{E[\text{GeV}]}} \oplus (7.5 \pm 0.4)\%. \tag{3.19}$$

A nice feature of calorimeter detectors with respect to other detectors is the fact that resolution improves with particle energy. Both the electromagnetic and the hadronic calorimeters were performing very well during the 2015 and 2016 data taking.

3.2.4 The Muon Spectrometer

Because of their larger mass with respect to electrons and photons, muon electromagnetic interactions with the calorimeters results in a energy loss of the order of a few MeV/mm. The choice for the **Muon Spectrometer (MS)** [95] to be the outer part of the detector is mainly due to the fact that we expect all the other particles, neutrinos excepted, to not escape the hadronic calorimeter.
In this way, muons are reconstructed by exploiting the combination of information obtained both from the ID and from the MS, whose layout is presented in Fig. 3.11.

The toroidal magnets surrounding the calorimeters generate a magnetic field perpendicular to the beam. Muons traversing the magnetic field change their trajectory allowing an independent measurement of their momentum with respect to the one provided by the ID. The spectrometer has an outer

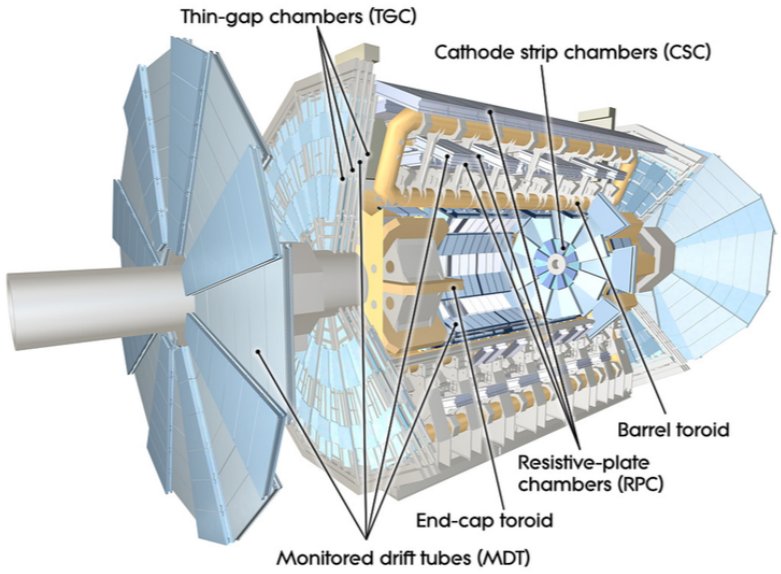

Figure 3.11: View of the ATLAS muon spectrometer [95].

diameter of 22 m and it is composed by *trigger chambers* and *precision chambers*. The chambers in the barrel are arranged in three concentric cylindrical shells around the beam axis at radii of ∼5m (inner station), 7.5 m (middle station) and 10 m (outer station). In the two end-cap regions, large muon wheels are placed perpendicular to the z-axis and located at distances of $|z|$ ∼7.4 m, 10.8 m, 14 m and 21.5 m from the IP.

The Trigger Chambers

Trigger chambers are fast muon momentum measurement detectors consisting of **Resistive Plate Chambers (RPC)**, covering the range $|\eta| < 1.05$, and **Thin Gap Chambers (TGC)**, covering the range $1.05 < |\eta| < 2.4$.
The RPC are filled with a gax mixture of 97% tetrafluoroethane ($C_2H_2F_4$) and 3% isobutane (C_4H_{10}). Muons traversing the chamber produce primary ionization electrons which are multiplied into avalanches by a 4.5 kV/mm electric field. The detecting units are three rectangular layers, two placed in the middle and one in the outer barrel stations, read out by two orthogonal series of pick-up strips, providing information on both the η and ϕ coordinates.
The end-cap region of the trigger chamber is equipped with a very thin multiwire chambers, the TGC. The chambers are filled with a highly quenching gas

mixture of 55% CO_2 and 45% n-pentane (n-C_5H_12) operating in saturation mode. The anode-cathode spacing is smaller than the anode-anode spacing allowing very short drift time, less than 20 ns. The spatial resolution of the TGC is 4 mm in the radial direction and 5 mm in the ϕ coordinate. RPC and TGC are also used to improve the measurements along the ϕ coordinate obtained from the precision chambers.

The Precision Chambers

Precision chambers are used to reconstruct the trajectory of the muons. They are composed by the **Monitored Drift Tubes (MDT)** and the **Cathod Strip Chambers (CSC)**.
The MDT chambers measure only the z coordinate in the barrel region and in the end-cap region up to $|\eta|$ <2. The MDT are drift chambers of two multi-layer (3 or 4 layers) drift tubes, with diameter of 30 mm and aluminum walls, filled with gaseous mixture of argon and carbon dioxide, at a pressure of 3 bar. By measuring the drift time in a single tube, it reconstructs the full particle trajectory, with a single wire spatial resolution of 80 μm.
The CSC are multi-wire chambers with strip cathodes measuring muon momentum in the region 2< $|\eta|$ <2.7. Wires are composed of parallel anodes perpendicular to 1 mm large strips of opposite polarity. The anode-cathode distance equals the distance between the anode wires, typically of 2.5 mm. The time resolution is about 7 ns. Spatial resolution is of 60 μm in the ϕ direction and of the order of one cm in η.

3.2.5 ATLAS Trigger and Data Acquisition System

The ATLAS trigger system underwent major upgrades for Run 2 with respect to Run 1 implementation [81]. The reason for the upgrade is due to the new challenging data-taking conditions resulting in ∼five times higher trigger rates with respect to LHC Run 1 [96].
The aim of the trigger and acquisition system (TDAQ) is to perform an online event selection allowing precision measurements for well known SM processes and enhance sensitivity to NP. It is necessary to find a good compromise between the data acquisition rates and maintaining high efficiency for physics data. The main limitations from Run 2 running conditions come from both the increasing center of mass energy to $\sqrt{s}$= 13 TeV and from the higher peak-luminosity of 1-2×10^{34} $cm^{-2}s^{-1}$. Moreover, the pile-up is now up to 50 multiple collisions per bunch crossing leading to an increased combinatorial

background and the beam-induced fake trigger rates[7]. Figure 3.12 shows an overview of the trigger system and data acquisition systems for Run 2.

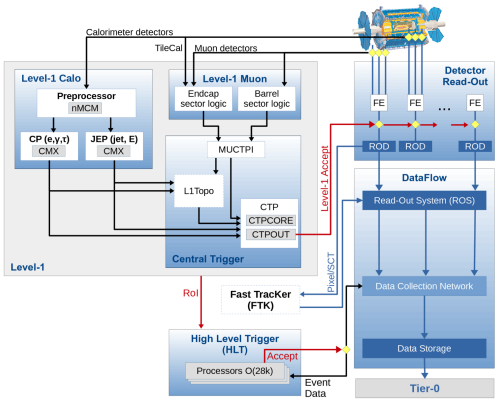

Figure 3.12: The ATLAS TDAQ system in LHC Run 2 [97]. From the top level of the figure, information collected by the calorimeter and muon systems (L1 trigger) are used to build RoI passed to the HLT which eventually accepts events for permanent storage.

The ATLAS trigger system can be divided into a hardware Level-1 (L1) and a software-based high-level trigger (HLT).

Level-1 trigger [99] (in Fig. 3.13) collects information both from the calorimeters (L1 Calo) and the muon detector (L1 Muon). L1 Calo provides information about clusters with measured energy above a given threshold, transverse energy, missing transverse energy and τ-like objects. L1 Muon processes information from trigger chambers, such as p_{T}. L1 Muon also underwent updates for Run 2: additional muon chambers installed in the "feet"[8] of the barrel region give a 4% larger acceptance for L1 muons.
A new topological processor (L1 Topo) was installed in Run 2. As the name says, L1 Topo implements global event-related variables such as the angular distance between objects in the event, the H_{T}, the invariant mass of pairs of objects.
Information is eventually transmitted to the Central Trigger Processor (CTP), elaborating all input signals and producing L1 trigger decision. Besides the

[7] Beam-induced background originates, for instance, from beam-gas scattering taking place all around the accelerator. Some of the particles resulting from these interactions, such as high energy muons, can leave energy deposits in the calorimeters, being reconstructed as a jet.

[8] The feet system is the main support of the ATLAS detector for the two bottom coils of the barrel toroid magnet. The region corresponds to $-2.16 < \phi < -1.77$ and $-1.37 < \phi < -0.98$.

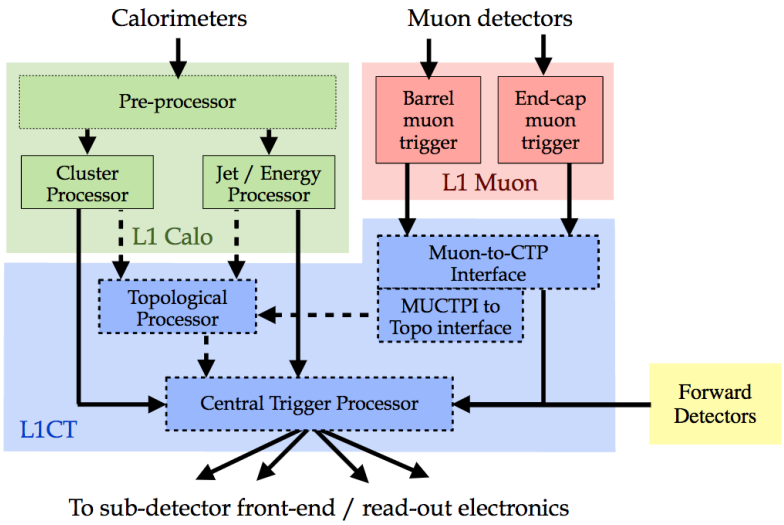

Figure 3.13: Schematic overview of the ATLAS L1 trigger system [98].

event rejection/selection decision, the CTP is also responsible for transmitting timing signals (clock) and synchronizations to all ATLAS sub-detectors. The L1 trigger is implemented with custom-made electronics with a 2.5 μs latency. The event-rate is reduced at L1 from 40 MHz to 100 kHz.

The Run 1 Level-2 trigger, the Event Builder and the Event Filter farms were merged in Run 2 into a unique HLT farm. The reasons for this choice lay in the simplification of the architecture, reducing memory and resource utilization and allowing running more HLT processing unit instances per node [100]. Data are eventually recorded to permanent storage at ~1500 MB/s. A *prescale* factor N can be applied to each trigger item and in those cases only 1 event in N is recorded. Usually, to exploit an optimal bandwidth usage with changes in luminosity and/or background conditions, the prescale factors are adjustable within an LHC physics run.

An example of trigger efficiency is provided in Fig. 3.14 (a) and (b) for some of the trigger menu items used to select events in this analysis (as in Chapters 6 and 7).

3.2.6 ATLAS Forward Detectors

The total pp interaction cross-section σ_{pp} is the sum of two main contributions: the *elastic* (σ_{el}) and *inelastic* (σ_{inel}) cross-sections. At LHC energies, σ_{el} contributes only to the 20% of the total σ_{pp}. The remaining 80% is covered by inelastic interactions, divided into *Single Diffractive dissociations*

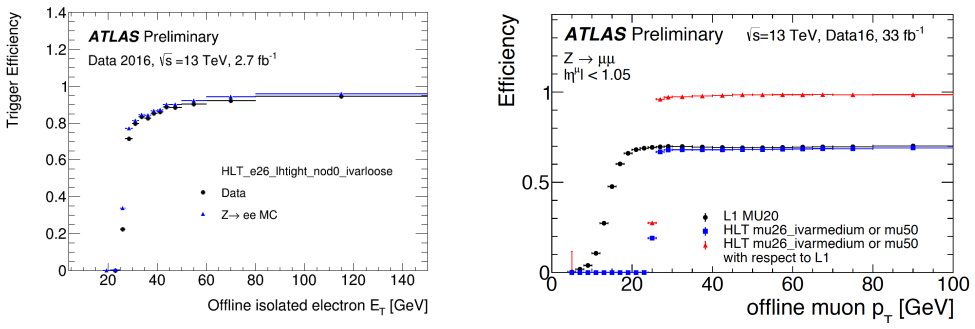

(a) (b)

Figure 3.14: (a) Efficiency of the `HLT_e26_lhtight_nod0_ivarloose` trigger in data (black dots) and simulation (blue triangles) as a function of the offline electron candidate's transverse energy (E_{T}) [101]. (b) Efficiency of L1 MU20 trigger and of the OR of `mu26_ivarmedium` with mu50 High Level triggers (HLT) plotted as a function of p_{T} of offline muon candidates in the barrel detector region [102].

(SD), Double Diffractive dissociations (DD) and *Central Diffractive production (CD)*, plus *non-diffractive* processes.

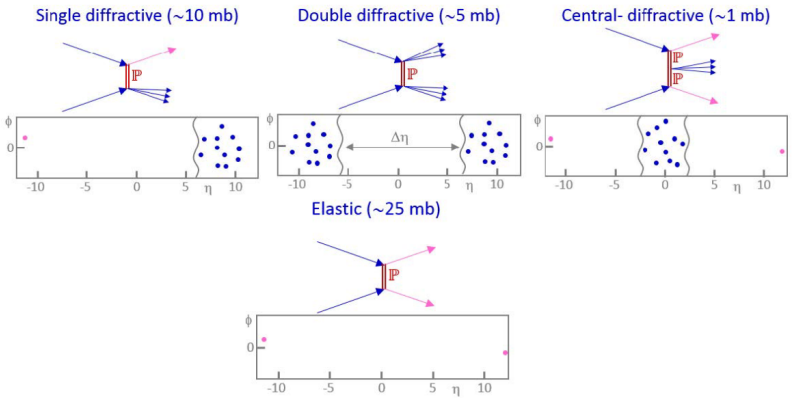

Figure 3.15: Inelastic and elastic process classification: their topology in the central and forward detectors is reported in the lower part of each class (azimuthal angle ϕ versus η). Pink dots represent the diffractively scattered protons, while the blue dots are the products of the diffractive pp interaction [103].

The topology of the events resulting from pp interaction in terms of their elements position in the ATLAS detector is shown in Fig. 3.15. The purpose of ATLAS forward detectors is to extend ATLAS program by also detecting particles in the high rapidity region, which cannot be measured by the central

detectors.
ATLAS Forward Detectors (some of them visible in Fig. 3.16) are divided into [104]:

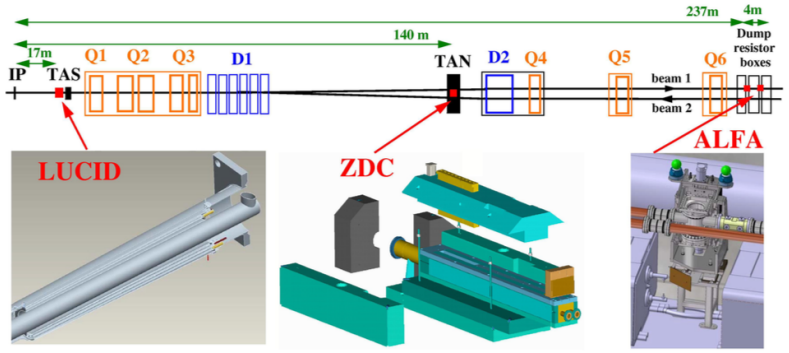

Figure 3.16: View of the ATLAS forward detectors.

- **Minimum Bias Trigger Scintillator (MBTS):** placed at 365 cm from the IP, it covers the region 1.9< $|\eta|$ <3.8. It is made of scintillator plates and used for low luminosity measurements, designed to be sensitive to low momentum particles and to trigger on minimum bias events [105].

- **Beam Conditions Monitor (BCM):** located 1.84 m away from the IP, covers the region 3.9< $|\eta|$ <4.1. The detector consists of a set of diamond sensors revealing the passage of charged particles. The major task of the detector is to provide radiation monitoring for the ID safety. It also provides information about possible beam instabilities and, thanks to its good time resolution, it measures the interaction rate and distinguishes, from the arrival time, true collisions from background events, giving a measurement of the instantaneous relative luminosity [106].

- **Luminosity Measurements Using Cherenkov Integrating Detector (LUCID):** placed at 17 m from the IP, is a Cherenkov detector for relative luminosity measurements in the region 5.6< $|\eta|$ <5.9. A detailed description of the LUCID detector, performance and calibration procedures, is given in Appendix B.

- **Zero Degree Calorimeter (ZDC):** it is a quartz-tungsten calorimeter designed for relative luminosity measurements during heavy ion runs. It is placed at 140 m from the IP, covers the region $|\eta|$ >8.3. It

measures neutral particles (photons and neutrons) close to the beam axis and it is important for the measurements of forward cross-sections.

- **Absolute Luminosity for ATLAS (ALFA):** it lays in the region $10.6 < |\eta| < 13.5$, inside the so-called *Roman Pots* [107], located 240 m away from ATLAS in the LHC tunnel, on both sides of the IP. ALFA is used to detect small-angle scattered protons, giving a measurement of ATLAS absolute luminosity.

- **ATLAS Forward Proton(AFP):** is a two-station spectrometer located at ± 220 m and $\pm$ 420 m from the IP. AFP provides precise measurement of proton position and direction. It was designed to improve the measurement of the SD and DD cross-section and installed for Run 2 data-taking.

The first two years of the LHC Run 2 pushed the performance of both the accelerating machine and of the ATLAS detector beyond expectations. The excellent technical operations as well as the newly designed upgrades for this new stage of the LHC data-taking gave the opportunity to the ATLAS Collaboration to exploit the statistics available from the 2015 and 2016 (~ 36 fb^{-1}) dataset.

Chapter 4

Objects reconstruction

This chapter illustrates how particle reconstruction is performed in ATLAS. Any physics analysis needs to define its objects of interest which typically are electrons, muons, tau leptons, jets (possibly also b-tagged ones) and missing transverse energy. Object definition is further optimized on an analysis-related basis, generally using selections that maximize the sensitivity.
This work selects leptons coming from the IP, from now on referred to as *prompt* leptons. Despite the highly performant lepton reconstruction efficiency provided by the ATLAS detector, the analyses are not background free. Leptons which are not originating from the IP but, for instance, from secondary decays of hadrons are referred to as *non-prompt* leptons. Reconstruction procedures are designed to provide a high efficiency and, at the same time, a reasonable background rejection.

4.1 Electron reconstruction

Inside ATLAS, electrons leave tracks in the ID and, most generally, are stopped within the electromagnetic calorimeter. The information provided by the ID gives the direction with respect to the IP while the EM calorimeter measures electron energy. The reconstruction algorithm for electron identification combines the two sets of information integrated with measurements of the energy leakage in the hadronic calorimeter, good quality criteria from ID objects and finally performs the cluster-track matching [108].
In the EM calorimeter, clusters are built in $\eta \times \phi$ towers using the intermediate section with granularity $\Delta\eta^{tower} \times \Delta\phi^{tower} = 0.025 \times 0.025$. Inside each of these elements, the energy of cells in all longitudinal layers is summed to form the tower energy. A *seed-cluster* algorithm searches for longitudi-

nal electron clusters with tranverse energy above 2.5 GeV. Clusters are then formed around the seeds using a clustering algorithm [109] which removes duplicates and allows a 95% reconstruction efficiency at $E_{\mathrm{T}} = 7$ GeV and more than 99% for $E_{\mathrm{T}} = 15$ GeV.
The track information from the ID is extracted by using both pattern recognition[1] and track fit. First, ID track[2] seeds are searched requiring three hits in different silicon detector layers (IBL, PIX or SCT) with momentum larger than 1 GeV. If the track seed cannot be extended to a full track (with at least 7 hits) using the pion hypothesis for energy loss dE/dx, but it falls within of the EM cluster regions of interest, a new attempt is made using the electron hypothesis allowing up to 30% energy loss for bremsstrahlung. Tracks and calorimeter clusters are matched using the $\eta - \phi$ position of the track. Tracks with at least 4 precision hits and associated to electron clusters are then refitted using an optimized Gaussian Sum Filter (GSF) accounting for non-linear bremsstrahlung effects.
When more than one track satisfies the matching conditions, only one track is chosen as a *primary* track, calculating the cluster-track R distance using the number of pixel hits, the presence of a hit in the first silicon layer and different momentum hypothesis. Electron candidates without associated precision tracks are removed and considered as photons.
To reduce the background from secondary decays or conversions, electron tracks are required to be compatible with the primary interaction vertex of the hard collision.

Electron identification

A large set of observables (track properties, calorimeter shower shapes, variables measuring bremsstrahlung effects, etc.) are used in the electron identification process. Thanks to the introduction of IBL in Run 2, the number of hits in the innermost pixel layer improved the discrimination between electrons and converted photons.
The baseline ID algorithm is the likelihood-based (LH) method, which is a multivariate technique evaluating signal versus background probability density functions (pdfs). These probabilities are combined into a discriminant

[1] The standard pattern recognition uses the pion hypothesis for energy loss in the detector material.
[2] The transverse momentum threshold for tracks reconstructed with the pion hypothesis is 400 MeV based on the pattern recognition.

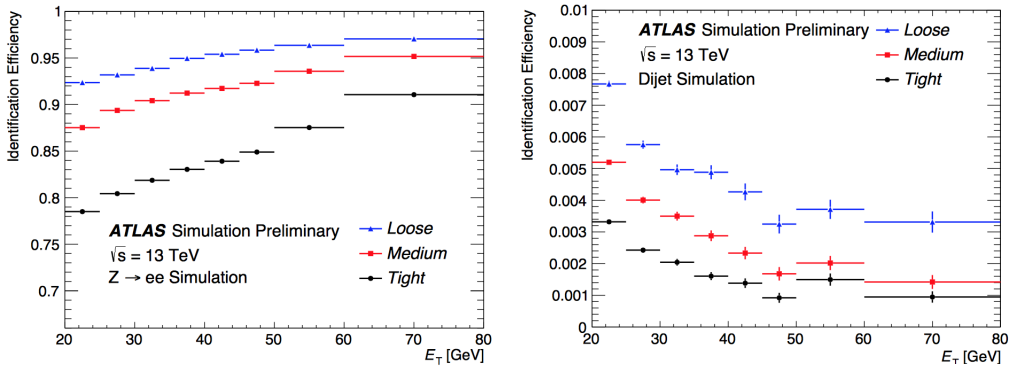

(a) (b)

Figure 4.1: Electron ID efficiency for a simulated $Z \to ee$ sample (a). Background rejection from simulated dijet events (b) [108].

$d_{\mathcal{L}}$ on which a requirement is applied:

$$d_{\mathcal{L}} = \frac{\mathcal{L}_{\mathcal{S}}}{\mathcal{L}_{\mathcal{S}} + \mathcal{L}_{\mathcal{B}}}, \qquad \mathcal{L}_{\mathcal{S}(\mathcal{B})}(\vec{x}) = \prod_{i=1}^{n} P_{s(b),i}(x_i) \tag{4.1}$$

where $\vec{x}$ is the set of discriminating variables, $P_{s(b),i}(x_i)$ the pdfs of the i^{th} variable evaluated at x_i and $\mathcal{L}_{S(B)}(\vec{x})$ are the likelihood functions for signal electrons and background, mostly originating from photon conversions and heavy flavour hadron decays. The set of discriminating variables fed into the MVA are: information on the energy measured in the back and middle layer of the EM calorimeter, the leakage into the hadronic calorimeter, track conditions from the ID measurement and track-cluster matching. Three levels of identification operation points are supported: `Loose`, `Medium` and `Tight`. The same set of variables is used to define each of the LH operating points but the selection on the discriminant is different. The performance of the LH identification algorithms are illustrated in Fig. 4.1 and, depending on the operating point, signal efficiencies for signal (background) electron candidates with $E_{\mathrm{T}} = 25$ GeV are in the range from 78% to 90% (0.3% to 0.8%) and increase (decrease) with E_{T}.

At high E_{T} some of the calorimeter variables used to construct the LH pdfs are different from the typical distributions obtained with $Z \to ee$ events. High energy electrons indeed tend to loose more energy inside the outermost layer of the EM calorimeter or even in the hadronic calorimeter. The `Loose` and `Medium` working points are constructed to be robust enough against these E_{T}-dependent ranges. The tighter requirements used for the `Tight` working point would lead to inefficiencies for electrons with $E_{\mathrm{T}} > 125$ GeV.

To compensate for the efficiency loss, `Tight` selection, on the top of the `Medium` one, adds rectangular cuts on the ratio of cluster energy to track momentum (E/p) and on the calorimeter shower width, which are found to be particularly discriminant between signal and background electrons.

Electron isolation

To further suppress background from non-prompt electrons, isolation on electrons is required in many physics analysis. The isolation variables quantify the energy of particles produced around the electron candidate. The calorimetric isolation energy $E_{\mathrm{T}}^{\mathrm{topocone0.2}}$ is defined as the sum of transverse energy of topological clusters within a cone of ΔR= 0.2 around the electron cluster. An (E_{T},η) dependent correction is then applied to account for energy leakage outside the cluster, removing the energy deposit from the electron itself. The track isolation $p_{\mathrm{T}}^{\mathrm{varcone0.2}}$ is defined as the sum of transverse momenta of all tracks within a cone of $\Delta R = \min(0.2, 10\ \mathrm{GeV}/E_{\mathrm{T}})$ around the candidate electron track. The number of missing hits in the pixel and SCT has to be respectively less than 2 or 1. The track cannot have more than one hit assigned to more than one track in the silicon detector. Finally, a requirement on $|\Delta z_0 \sin\theta| < 3$ mm is applied, where z_0 is the longitudinal impact parameter with respect to the reconstructed PV.
Different cuts on $E_{\mathrm{T}}^{\mathrm{topocone0.2}}/E_{\mathrm{T}}$ and $p_{\mathrm{T}}^{\mathrm{varcone0.2}}/E_{\mathrm{T}}$ identify different electron isolation working points. These operating points can be divided in two classes:

- fixed efficiency operating points: once established the desired isolation efficiency (e.g. 90% or 99%) the requirements on isolation are varied to keep the efficiency constant (see Table 4.1);
- fixed isolation operating points: the upper threshold on the isolation variable is set to a constant value (see Table 4.2). These operating points are optimized by maximizing the sensitivity of $H \to 4\ell$ and multilepton SUSY searches.

Fixed isolation operating working points are usually preferred in analysis using low energy electrons and requiring high background rejection, while in the high energy range looser operating points are preferred to maintain a high signal efficiency.

Electron triggers

Electron candidates are selected by the ATLAS online trigger using both L1 and HLT. At L1, electromagnetic and hadronic calorimeter regions of 4×4

	Efficiency		
Operating point	calorimeter isolation	track isolation	total efficiency
`LooseTrackOnly`	-	99%	99%
`Loose`	99%	99%	∼98%
`Tight`	96%	99%	∼95%
`Gradient`	$0.1143\% \times E_{\mathrm{T}} + 92.14\%$	$0.1143\% \times E_{\mathrm{T}} + 92.14\%$	90/99% at 25/60 GeV
`GradientLoose`	$0.057\% \times E_{\mathrm{T}} + 95.57\%$	$0.057\% \times E_{\mathrm{T}} + 95.57\%$	95/99% at 25/60 GeV

Table 4.1: Electron fixed efficiency isolation working points. In the `Gradient` and `GradientLoose` operating points E_{T} is expressed in GeV.

	Cut value	
Operating point	calorimeter isolation	track isolation
`FixedCutLoose`	0.20	0.15
`FixedCutTightTrackOnly`	-	0.06
`FixedCutTight`	0.06	0.06

Table 4.2: Electrons fixed isolation cut working points. The calorimeter and track isolations refer to the $E_{\mathrm{T}}^{\mathrm{topocone0.2}}/E_{\mathrm{T}}$ and $p_{\mathrm{T}}^{\mathrm{varcone0.2}}/E_{\mathrm{T}}$ isolation variables respectively.

trigger towers are used to calculate electron energy in the inner (core) and surrounding (isolation) regions. A veto on the hadronic leakage is applied by requiring the energy measured by the hadronic calorimeter to be below a given threshold as well as an isolation energy cut on the transverse energy around the core tower. The isolation and the hadronic leakage veto are not applied on electron candidates with $E_{\mathrm{T}} > 50$ GeV.
HLT level electrons are selected using refined information from calorimeter and tracking similarly to the selection which is applied offline. The EM calorimeter clusters identified by the L1 trigger are associated to fast-reconstructed tracks in the ID closer than $\Delta\eta$ <0.2. The second step in the HLT implements the same techniques used for offline reconstruction such as for electron ID. The online likelihood-based identification is similar to the offline one, expect for the momentum loss due to bremsstrahlung ($\Delta p/p$) which is not accounted for in the online identification.

Electron selection efficiency therefore depends on several steps: reconstruction, identification, isolation and trigger selection. Consequently, the total efficiency for a single electron ϵ_{tot} can be factorized as:

$$\epsilon_{tot} = \epsilon_{reco} \times \epsilon_{ID} \times \epsilon_{iso} \times \epsilon_{trig} \tag{4.2}$$

with each single efficiency depending only on each selection step. Since MC simulation does not properly reproduce the measured data efficiencies, a correction factor (*scale factor*) needs to be applied to simulation. Efficiencies are measured both on data and MC and the ratio between data and MC is used as a multiplicative correction factor for MC. The correction factors are rather close to unity and carry a corresponding systematic uncertainty which needs to be propagated into physics analysis.

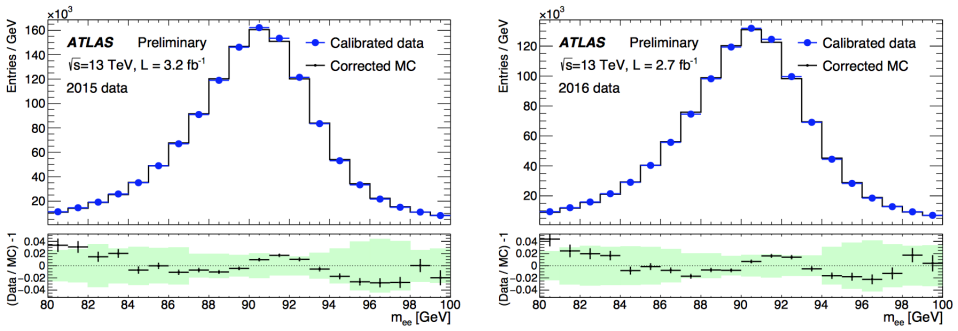

(a) (b)

Figure 4.2: Electron pair invariant mass distributions from $Z \to ee$ events in data and in simulation after applying the full calibration procedure for the full 2015 dataset (a) and part of the 2016 dataset (b). The simulation is normalized to data. The bottom panels show the residuals for the data/MC ratios together with the total uncertainty (green band) [110].

Additional source of systematic uncertainties on electron reconstruction originates from particle calibration procedure [110]. The calibration is divided into subsequent steps and corrections can be applied to data, simulation or both. First, MC simulation is used to model EM cluster properties, including their longitudinal and lateral development, and to calibrate them to the original electron energy. The EM calorimeter material distribution is measured in data using the ratio of the first-layer energy to the second-layer energy in the longitudinally segmented EM calorimeter (E_1 / E_2). This allows a precise measurement of the amount of material in front of the calorimeter. The energy scales measured in the longitudinal segments of the EM calorimeter need to be equalized in data with respect to simulation to ensure the correct extrapolation of the calorimeter response in the full p_{T} range. Afterwards, the MC-based electron response is applied to the cluster energy reconstructed in MC and data. A sample of $Z \to ee$ events is used to calibrate the response in data to match the one from simulation, using a per-

electron scale-factor applied to data. The resolution in data is slightly worse than in simulation, so that additional corrections are derived and applied to simulation to match the data. The calibrated energy scale is validated with electron candidates from $J/\psi \to ee$ events in data and scale factors for p_{T} and η dependencies are derived. Figure 4.2 shows the performance of the full calibration procedure applied to $Z \to ee$ events for 2015 and part of 2016 data, proving for both datasets a good agreement with simulation within the quoted uncertainties [111].

4.2 Muon reconstruction

Muons in ATLAS are reconstructed by combining the information provided by the ID and the MS [112] searching track segments from hits in the muon chambers. In each MDT chamber and in nearby trigger chamber (RPC or TGC) a method for detecting complex pattern of points, known as *Hough transform* [113], is used to search for hits aligned on a trajectory in the bending plane of the detector. Segments in the MDT are thus reconstructed by fitting with a straight line the hits found in each layer. Segments in the CSC are built using a separate combinatorial search in the η and ϕ detector planes. The combined ID and MS information lead to the definition of four types of muons, depending on which subdetectors are used in the reconstruction:

- combined (CB) muon: track reconstruction is performed independently in the ID and MS and eventually combined by a global fit using both ID and MS information, which can add or remove hits from the MS to improve the fit quality. The extrapolation starts from the outer part of the detector (in the MS) and performs an inward matching to the ID track. To complement the measurement, the opposite procedure starting from the ID and proceeding outward to the MS is also performed.

- Segment-tagged (ST) muon: these type of muons are used when they cross only one layer of the MS chambers, either because of low p_{T} or because they fall outside the MS acceptance regions. A track from the ID is classified as a muon if, once extrapolated to the MS, it is associated with at least one local track segment in the MDT or CSC chambers.

- Calorimeter-tagged (CT) muon: reconstructed by matching an ID track to an energy deposit in the calorimeter compatible with a minimum-ionizing particle. Despite the low purity provided by this type of muons, they recover the acceptance in the region where the MS is only partially

instrumented ($|\eta|$ <0.1) and in the momentum range 15 GeV < p_{T} < 100 GeV.

- Extrapolated (ME) or *standalone* muon: reconstruction is performed just using the information provided by the MS track with an additional loose requirement on compatibility with originating from the IP. Muon track parameters are defined at the IP, considering also the energy loss in the calorimeters. The muon is required to traverse at least two layers of the MS and three layers in the forward region. Standalone muons are generally used to recover ATLAS acceptance in the region 2.5 < $|\eta|$ < 2.7 not covered by the ID.

There can be some overlap between the reconstructed muons which need to be resolved before producing the final collection of muons to be used in physics analyses. When two muon types share the same ID track, preference is given to CB muons, then to ST and finally to CT muons. The overlap with standalone muons is solved by analyzing the track hit content and selecting the track with better fit quality and larger number of hits.

Muon identification

Muon identification is performed by applying quality requirements to suppress background from pion and kaon decays and to select prompt muons with high efficiency guaranteeing a robust momentum measurement. Four types of muon identification selections are provided which are `Loose`, `Medium`, `Tight` (where `tight` muons are included in the `loose` category) and `high-`p_{T}.

- `Loose`: designed to maximize reconstruction efficiency while providing good-quality muons. This identification working point is designed for analyses with high lepton multiplicity (i.e. $H \to 4\ell$). All CB and standalone muons satisfying the `Medium` requirements are included in the `Loose` selection. CT and ST muons are restricted to the region $|\eta| < 0.1$. In the region $|\eta|$ <2.5 about the 97.5% of the `Loose` muons are combined muons, ∼1.5% are CT and the last 1% are ST muons.

- `Medium`: is the default working point for muons in ATLAS, minimizing the systematic uncertainties associated to muon reconstruction and calibration and using only CB or standalone tracks. CB muons are required to have at least 3 hits in at least two MDT layers, except for tracks in the $|\eta|$ <0.1 region, where tracks with at least one MDT layer but no more than one MDT hole layer are allowed. Standalone muons

are required to have at least 3 MDT/CSC layers and are used only in the region $2.5 < |\eta| < 2.7$ to extend the acceptance outside the ID geometrical coverage. In the region $|\eta| < 2.5$, ∼0.5% of `Medium` muons originate from the inside-out combined reconstruction strategy.

- `Tight`: this identification working point maximizes muon purity at the cost of some efficiency. `Tight` muons need to satisfy the `Medium` criterium and be CB muons with hits in at least two stations of the MS.

- `High-`p_{T}: is aimed to maximize the momentum resolution for muon tracks with $p_{\mathrm{T}} > 100$ GeV, especially needed in high-mass new physics searches. Muons passing the `Medium` selection, being CB and having at least 3 hits in the three MS stations are selected. The requirement of three MS stations, despite reducing the reconstruction efficiency by ∼20%, improves the p_{T} resolution of muons above 1.5 TeV by 30%.

Reconstruction efficiencies for signal (from W decay) and background (from light-hadron decay) muons are reported in Table 4.3.

	$4 < p_{\mathrm{T}} < 20$ GeV		$20 < p_{\mathrm{T}} < 100$ GeV	
Selection	$\epsilon_{\mu}^{\mathrm{MC}}$[%]	$\epsilon_{hadrons}^{\mathrm{MC}}$[%]	$\epsilon_{\mu}^{\mathrm{MC}}$[%]	$\epsilon_{hadrons}^{\mathrm{MC}}$[%]
`Loose`	96.7	0.53	98.1	0.76
`Medium`	95.5	0.38	96.1	0.17
`Tight`	89.9	0.19	91.8	0.11
`High-`p_{T}	78.1	0.26	80.4	0.13

Table 4.3: Efficiency for prompt muons from W decays and misidentified non-prompt muons from light-hadron decays obtained from a $t\bar{t}$ MC sample. The results are divided into p_{T} ranges for muons candidates with $|\eta| < 2.5$ [112].

No isolation requirements are applied to the selection shown in Table 4.3 and, when applied, misidentification rates are reduced by more than an order of magnitude. The higher misidentification rate observed for `Loose` with respect to `Medium` muons is mainly due to CT muons in the region $|\eta| < 0.1$.

Muon isolation

Muons originating from the decay of heavy particles such as W, Z or Higgs bosons are produced isolated from other particles in the event. On the contrary, muons originating from hadron decays are close to jets and in general surrounded by higher detector activity. As a consequence, isolation is a very

powerful tool to disentangle signal from background muons in many physics analyses. As for the electron case (see Section 4.1), also for muons two type of variables are used to assess isolation. A track-based isolation $p_{\mathrm{T}}^{\mathrm{varcone30}}$ is defined as the scalar sum of the transverse momenta of tracks with p_{T} > 1 GeV in a cone of size ΔR = min(10 GeV /p_{T}^{μ},0.3) around the muon of transverse momentum p_{T}, excluding the muon track itself. The p_{T} dependent cone size helps the isolation performance for high-p_{T} muons. The calorimeter-based isolation $E_{\mathrm{T}}^{\mathrm{topocone20}}$ is defined as the sum of the transverse energy topological clusters in a cone of size ΔR =0.2 around the muon, after muon energy subtraction and corrections due to pile-up effects.
Isolation is assessed as a *relative variable* defined as the ratio of $p_{\mathrm{T}}^{\mathrm{varcone30}}$ or $E_{\mathrm{T}}^{\mathrm{topocone20}}$ to the transverse momentum of the muon.
Several isolation working points are provided in ATLAS (see Table 4.4).

Isolation Working Point	Isolation Variables	Definition
`LooseTrackOnly`	$p_{\mathrm{T}}^{\mathrm{varcone30}}/p_{\mathrm{T}}^{\mu}$	99% efficiency constant in η and p_{T}
`Loose`	$p_{\mathrm{T}}^{\mathrm{varcone30}}/p_{\mathrm{T}}^{\mu}$,$E_{\mathrm{T}}^{\mathrm{topocone20}}/p_{\mathrm{T}}^{\mu}$	99% efficiency constant in η and p_{T}
`Tight`	$p_{\mathrm{T}}^{\mathrm{varcone30}}/p_{\mathrm{T}}^{\mu}$,$E_{\mathrm{T}}^{\mathrm{topocone20}}/p_{\mathrm{T}}^{\mu}$	96% efficiency constant in η and p_{T}
`Gradient`	$p_{\mathrm{T}}^{\mathrm{varcone30}}/p_{\mathrm{T}}^{\mu}$,$E_{\mathrm{T}}^{\mathrm{topocone20}}/p_{\mathrm{T}}^{\mu}$	$\geq$ 90(99)% efficiency at p_{T} = 25 (60) GeV
`GradientLoose`	$p_{\mathrm{T}}^{\mathrm{varcone30}}/p_{\mathrm{T}}^{\mu}$,$E_{\mathrm{T}}^{\mathrm{topocone20}}/p_{\mathrm{T}}^{\mu}$	$\geq$ 95(99)% efficiency at p_{T} = 25 (60) GeV
`FixedCutTightTrackOnly`	$p_{\mathrm{T}}^{\mathrm{varcone30}}/p_{\mathrm{T}}^{\mu}$	$p_{\mathrm{T}}^{\mathrm{varcone30}}/p_{\mathrm{T}}^{\mu} < 0.06$
`FixedCutLoose`	$p_{\mathrm{T}}^{\mathrm{varcone30}}/p_{\mathrm{T}}^{\mu}$, $E_{\mathrm{T}}^{\mathrm{topocone20}}/p_{\mathrm{T}}^{\mu}$	$p_{\mathrm{T}}^{\mathrm{varcone30}}/p_{\mathrm{T}}^{\mu} < 0.06$, $E_{\mathrm{T}}^{\mathrm{topocone20}}/p_{\mathrm{T}}^{\mu}$ <0.30

Table 4.4: Summary and definition of the seven isolation working points provided for muon isolation. Name, discriminating variables and criteria are reported respectively in the first, second and third columns.

The efficiency for the discussed working points were measured in data and simulated $Z \to \mu\mu$ events using a tag-and-probe method. Figure 4.3 shows the measured efficiency for `Medium` muons for the `LooseTrackOnly`, `Loose` and `GradientLoose` isolation working points as a function of the muon p_{T}.

Muon triggers

The L1 Muon trigger decision is based on hits from the RPC in the barrel region and from the TGC in the forward region [114]. The L1 trigger using hits in the RPC requires the coincidence of hits in the three layers for the highest muon trigger p_{T} thresholds while for lower p_{T} thresholds it requires coincidence in two of the three layers. The TGC trigger has two measurement directions: the wire (bending) and strip (non-bending). Coincidence of both type of measurements is required in three layers, except for muons with very low p_{T} threshold.

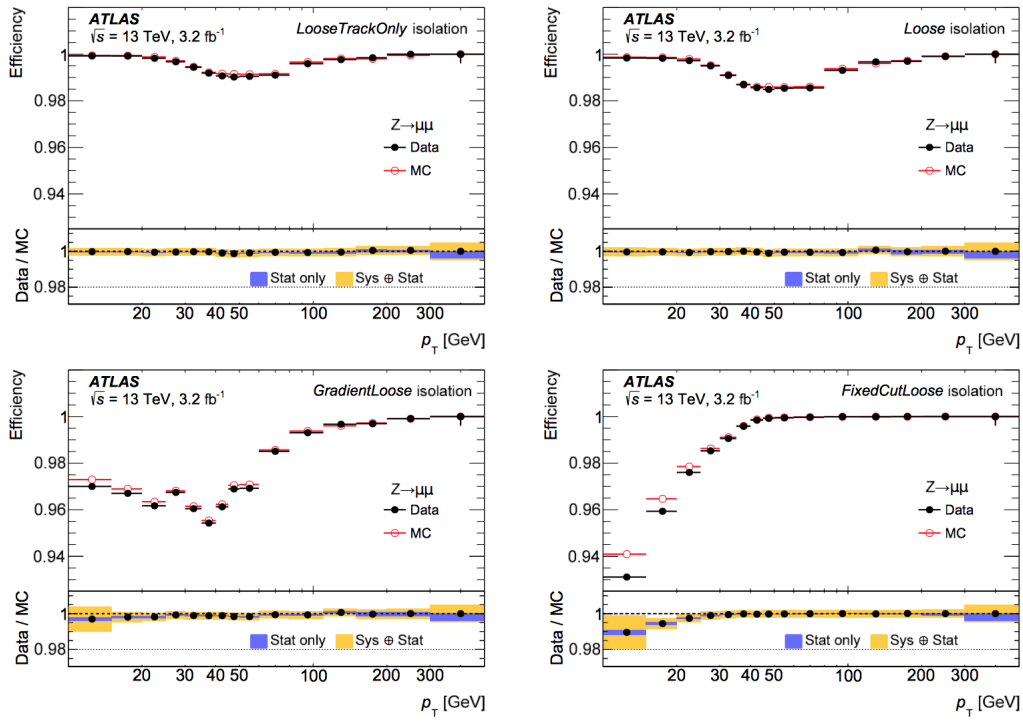

Figure 4.3: Muon isolation efficiency for the `LooseTrackOnly` (top left), `Loose` (top right), `GradientLoose` (bottom left) and `FixedCutLoose` (bottom right) working points shown as a function of the muon p_{T} measured in $Z \to \mu\mu$ events [112].

The HLT muon reconstruction is split into *fast* and *precision* reconstruction stages, the latter being more similar to the offline muon reconstruction. The fast stage refines the L1 muon candidate adding information from the MDT chambers performing a track fit and creating a *MS-only* muons candidate. The MS-only muon is then extrapolated back to the interaction point using the offline track extrapolator combining it with the track reconstructed in the ID. At this stage the muon is a *combined* muon candidate with refined track parameter resolution. In the precision stage, as in the fast one, MS-only muons are combined with ID tracks. If no matching ID track is found, combined muon candidates are searched for by extrapolating ID tracks to the MS. The *inside-out* approach recovers ∼1-5% of the low p_{T} muons, however it is slower and used only if the *outside-in* approach fails.

Muon selection efficiency also depends on several steps and can be factorized as in Equation 4.2, where simulation needs to be properly corrected, using scale factors, to account for differences in the selection efficiency of

simulation with respect to data.

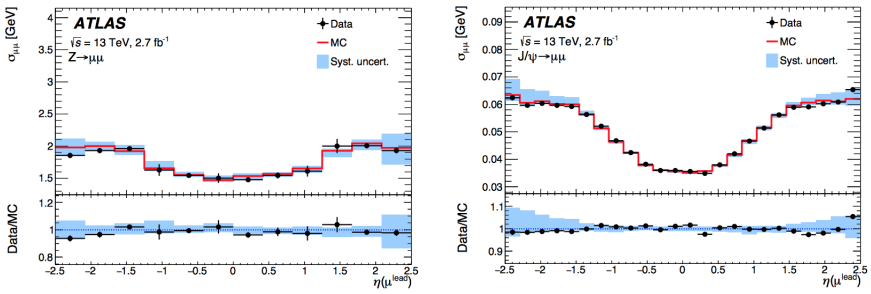

(a) (b)

Figure 4.4: Dimuon invariant mass resolution for CB muons in $Z \to \mu\mu$ (a) and $J/\psi \to \mu\mu$ (b) events for data and corrected simulation as function of the highest-p_{T} muon η. The blue line represents the total systematic uncertainty [112].

Additional systematic uncertainties arise from muon momentum scale and calibration, to correct the simulation to properly match data for the reconstructed momentum in the ID and MS sub-detectors. Corrections are applied as a function of p_{T} and $|\eta|$ to account for inaccuracy in the description of the magnetic fields and for detector mis-alignment in the direction perpendicular to the magnetic field. Additional correction terms model the inaccuracy in the simulation of the energy loss in the calorimeter and other detector materials in the path to the MS. The calibration is performed by using the invariant mass distributions of $J/\psi \to \mu\mu$ and $Z \to \mu\mu$ events. The uncorrected MC simulation shows a narrower signal distribution and a slight shift with respect to data. When two muons have similar momentum resolution, the relative mass resolution $\sigma_{\mu\mu}/m_{\mu\mu}$ is directly proportional to the relative muon momentum resolution σ_{p_μ}/p_μ. Similarly, the total muon momentum scale, defined as $s = \langle (p^{\mathrm{meas}} - p^{\mathrm{true}})/p^{\mathrm{true}} \rangle$, is related to the dimuon mass scale, defined as $s_{\mu\mu} = \langle (m_{\mu\mu}^{\mathrm{meas}} - m_{\mu\mu}^{\mathrm{true}})/m_{\mu\mu}^{\mathrm{true}} \rangle = \sqrt{s_{\mu_1} s_{\mu_2}}$, where s_{μ_1} and s_{μ_2} are the two muons momentum scales. Figure 4.4 shows the dimuon mass resolution which is ∼1.2% (1.6%) at small η values for $J/\psi(Z)$ decays and increases to 1.6% and 1.9% in the end-caps for J/ψ and Z decays respectively.

4.3 Missing transverse energy

The missing transverse energy ($E_{\mathrm{T}}^{\mathrm{miss}}$) in the event accounts for the amount of energy carried by undetected particles, namely neutrinos. However, many

other parameters contribute to the energy balance in ATLAS: the detector is not fully hermetical, the electronic noise in the calorimeters and MS, the presence of devices required for the signal read-out and pile-up. Since all these factors overestimate the effective value of the $E_{\mathrm{T}}^{\mathrm{miss}}$, many algorithms [115] for reconstruction of the $E_{\mathrm{T}}^{\mathrm{miss}}$ are applied, e.g. using the topological calorimetric clusters for noise suppression.
The reconstructed missing transverse energy is characterized by two contributions. The first one, named *hard term*, comprises fully reconstructed and calibrated objects such as electrons, muons, taus, photon and jets. The second one arises from *soft terms*, consisting of signals not associated with any reconstructed object. The missing transverse energy calculated as:

$$\vec{E}_{\mathrm{T}}^{\mathrm{miss}} = -\left(\sum_{i\in e}\vec{p}_{\mathrm{T},i} + \sum_{i\in\mu}\vec{p}_{\mathrm{T},i} + \sum_{i\in\tau}\vec{p}_{\mathrm{T},i} + \sum_{i\in\mathrm{jets}}\vec{p}_{\mathrm{T},i} + \sum_{i\in\gamma}\vec{p}_{\mathrm{T},i} + \sum_{i\in\mathrm{softterm}}\vec{p}_{\mathrm{T},i}\right) \quad (4.3)$$

where the index i identifies the x, y transverse momentum component of the reconstructed objects. The measurement of missing energy is fundamental also for the identification of new neutral particles which do not interact with the detector material such as the ones predicted by SUSY or BSM models.

4.4 Jet reconstruction

In ATLAS, jets are reconstructed using *topological clusters* energy deposits in the calorimeters. Topocluster reconstruction starts with the identification of seed cells with energy significance at least 4σ above their noise level, being the noise defined as the sum in quadrature of electronic and pile-up signals. After the seed identification, the algorithm iteratively clusters nearby cells with energy deposit 2σ higher than the noise. Single clusters are calibrated using local properties such as energy density, calorimeter depth and isolation with respect to close-by clusters. The local cluster weighting (LCW) calibration classifies topological clusters along a continuous scale as being electromagnetic or hadronic, using shower shapes and energy densities. The most important requirements on jet reconstruction algorithms are *infrared* and *collinear* (IRC) safety. Being IRC safe means that modifying an event by a collinear splitting or adding a soft-gluon emission[3] shall not change jet definition. IRC safety is a feature of sequential clustering recombination algorithms such as k_t [116], Cambridge/Aachen [117] and anti-k_t [118]. A priori it

[3] Collinear safety is the property under which one single large-p_{T} particle is divided into two collinear (close-by) particles leading to the same jet definition. If a soft (infrared) emission is added or removed leaving unchanged jet definition the algorithm for jet reconstruction is infrared safe.

is not clear whether it is better to have regular (*soft-resilient*) or less regular (*soft-adaptable*) jets, meaning with regular or irregular shape. On one hand, regularity means a certain rigidity in the jet algorithm's ability to adapt a jet to the branching nature of QCD radiations. On the other hand, a regular jet shape allows easier procedure for jet experimental calibration and helps in decreasing contribution from UE and pile-up to momentum resolution losses.

Among cone algorithms, the one mostly used by ATLAS for jet reconstruction is the anti-k_t, with which the jets in the analyses presented here were reconstructed. The algorithm follows an iterative procedure based on the distance d_{ij} between two clusters or *pseudo-jets* and d_{iB} which indicates the distance between the particle i and the beam (B). For each pseudo-jet i the algorithm evaluates the distance d_{ij} to the other pseudo-jets j defined as:

$$d_{ij} = \min(p_{\mathrm{T},i}^{2p}, p_{\mathrm{T}j}^{2p}) \frac{\Delta R_{ij}^2}{R^2} \tag{4.4}$$

where ΔR_{ij}^2 is the angular distance between i and j defined as

$$\Delta R_{ij}^2 = (\eta_i - \eta_j)^2 + (\phi_i - \phi_j)^2 \tag{4.5}$$

being $p_{\mathrm{T},i(j)}, \eta_{i(j)}$ and $\phi_{i(j)}$ the transverse momentum, the pseudorapidity and the azimuthal angle of the $i(j)$ object. The p parameter in the metrical distance for the anti-k_t algorithm is fixed to p=-1. For each pseudo-jet the distance from the beam is also evaluated as

$$d_{iB} = p_{\mathrm{T},i}^{2p}. \tag{4.6}$$

The two metrical distances d_{ij} and d_{iB} are then compared and, if the minimum value is d_{ij}, then i and j are combined into a single pseudo-jet and the iterative procedure starts from the beginning. If, on the contrary, $d_{ij} > d_{iB}$, the pseudo-jet i is considered as a final state and will not be considered into further iterations.

The difference between the anti-k_t and other sequential clustering algorithms such as k_t and Cambridge/Aachen lies in the value of the p parameter in Eq. 4.4 and can be visualized in Fig. 4.5. For $p = 1$ the formula recovers the k_t algorithm while $p = 0$ is the case for Cambridge/Aachen. In general for $p >0$ the behaviour of the jet algorithm with respect to soft radiation is similar to what observed for the k_t maintaining the ordering between particles for finite values of ΔR. The anti-k_t algorithm sets the p parameter to -1.

To understand how the anti$-k_t$ algorithms operates, let us consider an event with few well-separated hard particles with transverse momentum $p_{\mathrm{T}1}$, $p_{\mathrm{T}2}$, .. and many soft particles. The distance in Eq. 4.4 between the hard

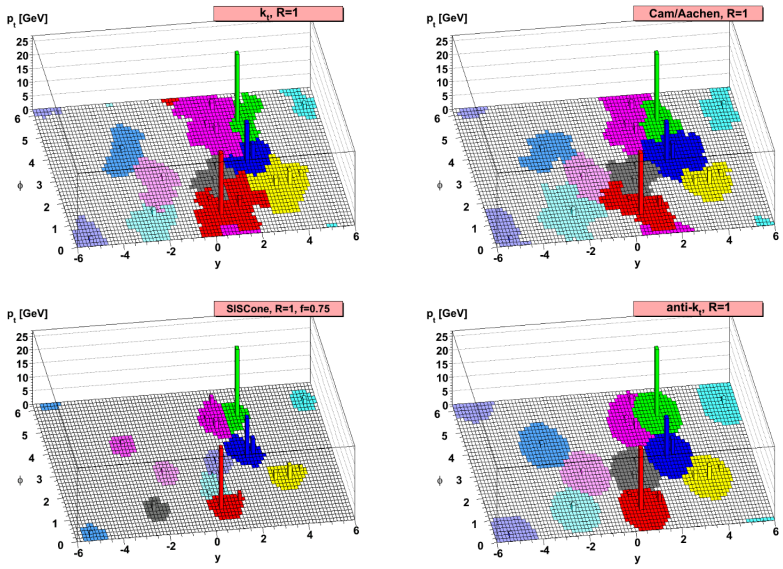

Figure 4.5: Three dimensional (p_{T}, y,ϕ plane) illustration of a parton-level event clustered with different jet algorithms (in order: k_t, Cam/Aachen, SISCone and anti-k_t) showing the catchment areas of the resulting hard jets [118].

particle 1 and the $i-th$ soft particle is determined by the transverse momentum of the hard particle and the ΔR_{1j} separation. The same distance in Eq. 4.4 will instead be much larger if we consider two similarly separated soft particles. Soft particles tend to be clustered with hard ones long before they cluster among themselves. Eventually, a hard particle with no hard close-by particles within a $2R$ distance will accumulate all soft particles in a cone of radius R. The resulting jet will be of conical shape. In a similar way, if another hard particle 2 is in the region $R < \Delta R_{12} < 2R$ then there will be two hard jets and, at most, only one of the two can be perfectly conical, depending on the transverse momentum balance. If $p_{\mathrm{T}1} \gg p_{\mathrm{T}2}$ then jet 1 will be conical and jet 2 will miss the part overlapping with jet 1, resulting partially conical. In the regime $p_{\mathrm{T}1} = p_{\mathrm{T}2}$ none of the resulting jets will be conical and they will be divided by an equal line between the two. When $p_{\mathrm{T}1} \sim p_{\mathrm{T}2}$ both cones will be trimmed with boundary b defined by $\Delta R_{1b}/p_{\mathrm{T}1} = \Delta R_{2b}/p_{\mathrm{T}2}$.
If two particles are closer than $\Delta R_{12} < R$ they will be clustered into a single jet centered on the higher p_{T} particle. For $p_{\mathrm{T}1} \sim p_{\mathrm{T}2}$ the final cone will be the union of cones or radius smaller than R around each particle with a cone of radius R centered on the final jet.
Summarizing, the anti-k_t algorithm is sensitive to hard particles proximity but resilient with respect to soft radiation. The cone distance parameter

used to reconstructed jets in the analyses presented here is $R = 0.4$.

4.4.1 Pile-up corrections

As we saw in Chapter 3, when two pp bunch interact there can be up to ∼50 pile-up collisions. These multiple collisions can interfere with objects coming from a specific interaction vertex modifying, for instance, the jet energy measurement [119]. Indeed, additional interactions and soft energy deposits, independent from the hard-scattering event, need to be properly accounted and subtracted to guarantee precise jet energy measurements. Pile-up can be further divided into *in-time* (inside the same bunch crossing) or *out-of-time* (from collisions originating from previous bunch crossings)[4]. Correction techniques estimate the average energy density deposit due to pile-up using information from the ID, such as the number of reconstructed PVs. Due to the fast response of the silicon tracking detectors, N_{PV} is indeed mostly unaffected by out-of-time pile-up.
The jet energy correction on transverse momentum relies on an average offset correction $\langle f^{\mathrm{jet}} \rangle$:

$$p_{\mathrm{T}}^{\mathrm{corr}} = p_{\mathrm{T}}^{\mathrm{jet}} - \langle f^{\mathrm{jet}}(\langle \mu \rangle, N_{PV}, \eta) \rangle \tag{4.7}$$

where $\langle f^{\mathrm{jet}} \rangle$ is measured with MC simulation or from *in-situ* studies. Being applied as a mean value, the correction does not capture calorimeter energy fluctuations on an event-by-event basis or individual jet information.
Tracking information is crucial to suppress pile-up jet activity because tracks can be precisely associated with specific vertices. The composition of pile-up jets depend both on $\langle \mu \rangle$ and p_{T}: pile-up jets from hard QCD usually present a harder p_{T} spectrum than jets from pile-up fluctuations. Therefore, high p_{T} jets with one associated PV which is not the hard-scatter vertex are more likely to be pile-up QCD jets. On the other hand, the number of QCD jets increases linearly with $\langle \mu \rangle$ while the rate of pile-up jets increases more rapidly. Consequently, at high luminosities the majority of pile-up jets are expected to be low p_{T} ones. Pile-up suppression using track information in ATLAS is done using the **jet vertex fraction (JVF)** and the **jet vertex tagger (JVT)**.

Jet vertex fraction

The JVF is a variable capable of identifying the jet PV; cutting on this variable allows to reject jets not associated to the hard-scattering PV. A

[4] Out-of-time pile-up occurs when the electronics integration time is larger than 25 ns.

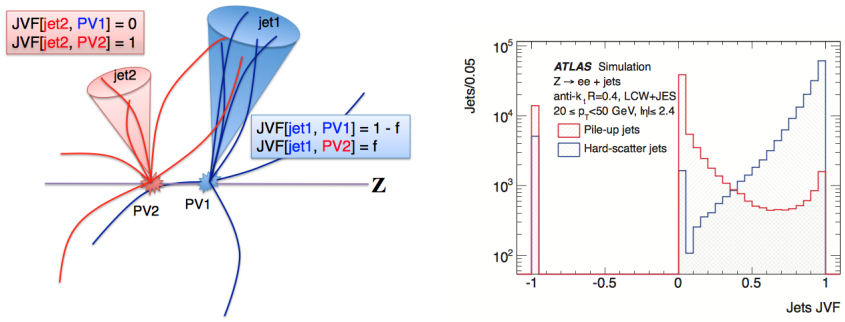

(a) (b)

Figure 4.6: (a) schematic representation of the JVF principle where f is the fraction of track p_{T} due to PV2 but contributing to jet 1. (b) JVF distribution for hard-scatter (blue) and pile-up (red) jets with $20 < p_{\mathrm{T}} < 50$ GeV and $|\eta| < 2.4$ [119].

different JVF can be defined for each jet with respect to each PV in the event, by identifying the PV associated with each charged-particle track pointing towards the given jet. Once the hard-scatter vertex is identified, the JVF can be used to select jets with high likelihood of originating from that vertex. The variable is calculated as the ratio of the scalar sum of the p_{T} of matched tracks that originate from a given PV to the scalar sum of p_{T} of all matched tracks in the jet, independently of their origin. For each jet:

$$\mathrm{JVF}(\mathrm{jet}_i, \mathrm{PV}_j) = \frac{\sum_m p_{\mathrm{T}}(\mathrm{track}_m^{\mathrm{jet}_i}, \mathrm{PV}_j)}{\sum_n \sum_l p_{\mathrm{T}}(\mathrm{track}_l^{\mathrm{jet}_i}, \mathrm{PV}_n)} \tag{4.8}$$

where m runs over all tracks from PV_j matched to jet_i, n over all PVs in the event and l over all tracks originating from PV_n matched to jet_i. Only tracks with $p_{\mathrm{T}} > 500$ MeV are considered in JVF calculation and JVF$\in$[0,1] or with value assigned to -1 when the jet has no associated tracks.

Figure 4.6 schematically shows how the JVF works and its distribution for hard-scatter and pile-up jets. It is important to note that a jet with significant neutral pile-up contribution might receive JVF=1, while JVF=0 might also result from fluctuations in the fragmentation for a hard-scatter jet, causing its constituent charged tracks to all fall below the track p_{T} threshold. Moreover, relying on the assumption that the hard-scattering vertex is well separated from pile-up vertices, a pile-up jet may receive in some cases high values of JVF because its associated PV is close to the hard-scatter primary one. This effect becomes important with increasing $\langle\mu\rangle$.

Jet vertex tagger

Increasing the number of associated PVs in the event shifts the mean JVF for signal jets to smaller values in Eq. 4.8. This results in a JVF intrinsic pile-up dependence which can be addressed in two ways. First, by introducing a pile-up correction in Equation 4.8 denominator (corrJVF) and, secondly, by introducing a new variable uniquely defined on hard-scatter observables ($R_{p_{\mathrm{T}}}$). The first variable is defined as:

$$\mathrm{corrJVF} = \frac{\sum_m p_{\mathrm{T},m}^{\mathrm{track}}(\mathrm{PV}_0)}{\sum_l p_{\mathrm{T},l}^{\mathrm{track}}(\mathrm{PV}_0) + \frac{\sum_{n\geq 1}\sum_l p_{\mathrm{T},l}^{\mathrm{track}}(\mathrm{PV}_n)}{(k\cdot n_{\mathrm{track}}^{\mathrm{PU}})}} \tag{4.9}$$

where $\sum_m p_{\mathrm{T},m}^{\mathrm{track}}(\mathrm{PV}_0)$ is the scalar sum of the p_{T} of the tracks that are associated with the jet and originate from the hard-scatter vertex. The term $\sum_{n\geq 1}\sum_l p_{\mathrm{T},l}^{\mathrm{track}}(\mathrm{PV}_n) = p_{\mathrm{T}}^{PU}$ denotes the scalar sum of the p_{T} of the associated tracks originating from any pile-up vertex and $k = 0.01$. The track-vertex association in corrJVF is done in a different way and aimed to improve efficiency for b-jets. First, if a track is associated to more than a PV, higher priority is given to the vertex with higher $\sum(p_{\mathrm{T}}^{\mathrm{track}})^2$. If this steps returns a track with no associated PV but satisfying $|\Delta z| < 3$ mm with respect to the hard-scatter vertex, it is assigned to it. This step targets tracks from hadrons decay originating from the hard-scatter but not likely to be attached to any vertex.
The variable $R_{p_{\mathrm{T}}}$ is defined as the scalar sum of the p_{T} of tracks associated with the jet and originating from the hard-scatter vertex divided by the fully-calibrated jet p_{T} (including pile-up subtraction):

$$R_{p_{\mathrm{T}}} = \frac{\sum_k p_{\mathrm{T},k}^{\mathrm{track(PV_0)}}}{p_{\mathrm{T}}^{\mathrm{corr}}} \tag{4.10}$$

and it is peaked at 0 and steeply falling for pile-up jets while for hard-scatter jets it has the meaning of a charged p_{T} fraction and its mean value and spread are larger. The relation between $R_{p_{\mathrm{T}}}$ and N_{PV} is a first order dependence.
The jet-vertex-tagger uses corrJVF and $R_{p_{\mathrm{T}}}$ as a two-dimensional likelihood based on a k-nearest neighbour (kNN) algorithm. The training is performed using simulated dijet events and for each point of the corrJVF-$R_{p_{\mathrm{T}}}$ plane the probability for a jet to be of signal type is computed as the ratio of the number of hard-scatter jets to the number of total jets found in a local neighbour around the point. The training sample of signal and pile-up jets requires $20 < p_{\mathrm{T}} < 50$ GeV and $|\eta|$ <2.4.

Figure 4.7a compares the fake rate against the efficiency curves for the four variables JVF, corrJVF, $R_{p_{\mathrm{T}}}$ and JVT. It is clear that JVT provides the

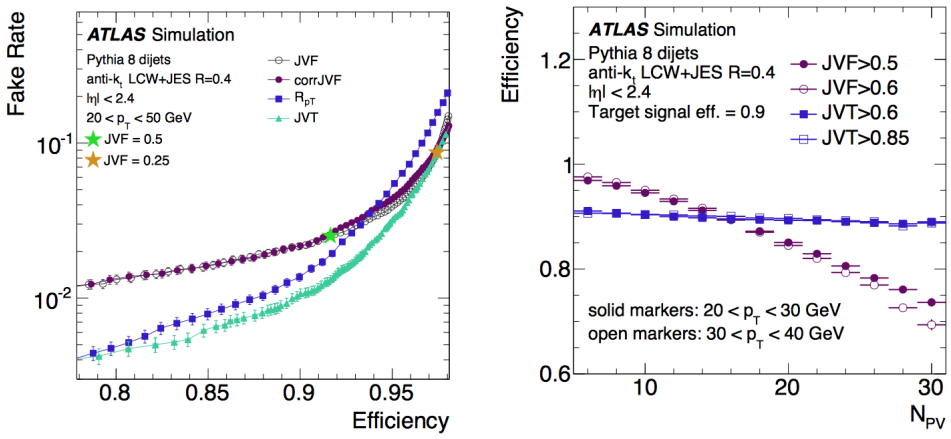

(a) (b)

Figure 4.7: (a) comparison between JVF, corrJVF, $R_{p_{\mathrm{T}}}$ and JVT performance in fake rate versus signal efficiency. Gold and green stars indicate the most common JVF working points at 0.25 and 0.5. (b) PV dependence of signal efficiency divided in p_{T} ranges of 20 $<p_{\mathrm{T}} <$ 30 GeV (solid markers) and 30 $<p_{\mathrm{T}} <$ 40 GeV (open markers) for fixed cuts on JVT (blue square) and JVF (violet circle) with inclusive 90% efficiency [119].

best performance in terms of fake rate on the full range and its performance is driven by the corrJVF in the high signal efficiency region and by the $R_{p_{\mathrm{T}}}$ in the high pile-up rejection region. By using JVT, signal efficiencies of 80%, 90% and 95% are obtained and corresponding, respectively, to 0.4%, 1.0% and 3% fake rates. Imposing the same signal efficiencies requirements on JVF would have resulted in 1.3%, 2.2% and 4% fake rates.
The dependence of signal efficiencies on N_{PV} is shown in Fig. 4.7b. For the full range of considered number of PVs, the signal efficiencies based on JVT selection are stable within 1%. Moreover, the stability of signal efficiency as a function of N_{PV} was proved to be independent on the flavour of the parton initiating the jet.

4.4.2 Algorithms for b-jet tagging

Hadrons containing b-quarks have a relatively long lifetime, of the order of 1.5 ps ($c\tau$ ~450 μm) and travel for few mm inside the ATLAS detector before decaying, so that the resulting event presents at least one displaced vertex from the point where the hard-scatter occurred [120]. The identification of b-tagged jets exploits the use of three basic algorithms: an impact

parameter-based, an inclusive secondary vertex reconstruction and a decay chain multi-vertex reconstruction, eventually combined into a multivariate discriminant which is the default ATLAS algorithm.
Tracks associated to b-hadrons decay vertex usually have large impact parameter which can be separated from the contribution of tracks from the PV. The impact parameter sign depends on the position of the secondary vertex with respect to the primary one. Two taggers are defined using impact parameter information: the first one IP2D uses d_0/σ_{d_0} while the second one IP3D makes use of both the transverse and longitudinal ($z_0 \sin\theta/\sigma_{z_0 \sin\theta}$) impact parameter significance, in a two-dimensional template accounting for their correlation. Different pdfs are implemented for different track hit patterns and for different jet-flavour hypothesis (b, c or light).
The secondary vertex finding (SV) reconstructs the displaced secondary vertex within the jet. All track pairs inside the jets are tested for a two-track vertex hypothesis. Vertices are rejected if they are likely originating from a long-lived particle while, if kept, a new vertex is fitted with all tracks from the accepted two-track vertices. The vertices are required to be significantly displaced from the PV.
The third algorithm is the JetFitter which exploits the topological features of weak b- and c-hadron decays inside the jet and tries to reconstruct the full b-hadron decay chain. A Kalman filter is used to find a common line where both the PV and the b and c vertices lie, approximating the b-hadron flight path and their position. This approach allows to resolve b and c vertices even with a single track attached to them.
The three algorithms are combined into a BDT and the output tagger is called MV2. The training of the BDT is performed using $t\bar{t}$ events with b-jets against c- and light-flavour jets. The kinematic properties of jets, namely p_{T} and $|\eta|$ are included in the training to properly account for correlations with other variables. However, signal jets are re-weighted to match kinematics of background jets during the training and the re-weighting is only removed when the MV2 tagger is applied. There are more than one MV2 taggers, depending on the fraction of c-jets used in the training, with different light versus c-jet rejections. Since the majority of physics analysis are limited by c- rather than light-flavour jet rejection, the c-jet fraction is set in such a way to enhance charm rejection keeping a good light-flavour rejection as well. The MV2c10 tagger background composition is made of 93% light-flavour jets and 7% c-jets, while for the MV2c20 the c- jet fraction is increased to 15%. No c-jet contribution is present in the training used for MV2c00.

The performance of the b-tagging multivariate algorithms is shown in

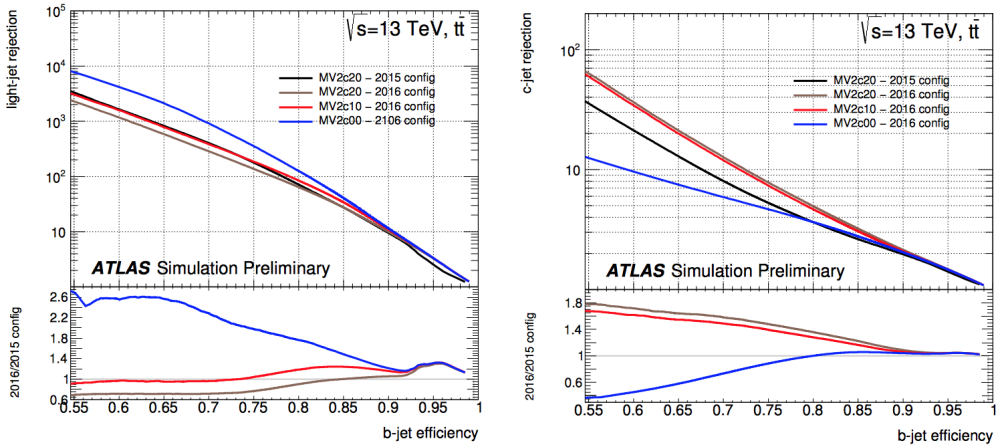

(a) (b)

Figure 4.8: Performance of the MV2 taggers in light-flavour (a) and c-jet (b) rejection versus b-jet efficiency [120].

BDT cut value	b-jet efficiency [%]	c-jet rejection	light-jet rejection	τ rejection
0.9349	60	34	1538	184
0.8244	70	12	381	55
0.6459	77	6	134	22
0.1758	85	3.1	33	8.2

Table 4.5: Operating points for the MV2c10 b-tagger. For a fixed cut on the BDT output, the corresponding b-jet efficiency as well as charm, light and τ rejections are shown. The values are extracted using a $t\bar{t}$ sample of jets with p_{T} >20 GeV.

Fig. 4.8. The light-flavour rejection from the MV2c10 (2016 configuration[5]) is around 4% and 40% for c-jets, at 77% b-jet efficiency. The 2016 MV2c20 provides even better charm but lower light-flavour rejections. The MV2c10 tagger was chosen as the default for 2016 ATLAS analysis. Furthermore, operating points are defined by a single cut value on MV2c10 to provide fixed b-tagging efficiency. The values of the recommended operating points are shown in Table 4.5.

Jet energy scale and resolution

The jet energy calibration is aimed to restore the correct jet energy scale (JES) compensating for the calorimeter response non-linearities, energy losses

[5] Slightly different c-jet fraction configurations were used in 2015 and 2016.

in inactive regions of the detector (passive or dead material), energy from particles outside the detector acceptance (leakage), energy from particles belonging to the truth jet that were not included in the reconstructed jet (out-of-cone particles). The first step in jet calibration is the pile-up subtraction, presented in Section 4.4.1. Afterwards, an origin correction is applied to jets to make them point back to the primary hard-scatter vertex. Consequently, the kinematic properties of each topo-cluster are recalculated using the new jet direction leaving the energy unchanged. The third step of the calibration applies p_{T} and $|\eta|$ dependent corrections derived from the truth particle jet. The final step of the calibration applies a residual correction based on *in-situ* measurements to correct for remaining data-to-MC differences. These corrections exploit the transverse momentum balance between the jet and a well-measured reference object. An additional source of systematic uncertainty arises from the jet flavour tagging and from the knowledge of the jet energy resolution (JER). The simulation describes the jet energy resolution measured in data within ∼10%. Each step of the calibration procedure carries a systematic uncertainty and indeed the uncertainty due to JES and JER plays a leading role in physics analyses looking at final states with high jet multiplicity.

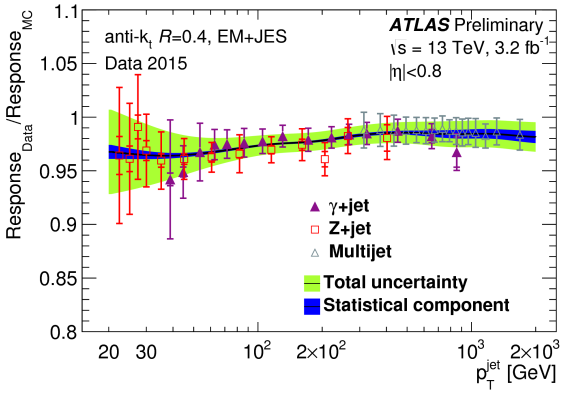

(a)

Figure 4.9: (a) jet response ratio as a function of jet p_{T} [121].

The common figure of merit to measure and characterize jet energy is the *jet response* [122], defined as the ratio between the reconstructed jet energy and the corresponding truth-particle jet energy in the simulation:

$$R(E,\eta) = \left\langle \frac{E^{\mathrm{reco}}}{E^{\mathrm{truth}}} \right\rangle . \tag{4.11}$$

Figure 4.9a shows the jet response ratio of data to MC as a function of jet p_{T} using a Z+jets, a γ+jets and a multijet sample. Jets are reconstructed

using the anti-k_t algorithm R=0.4. The plot shows the compatibility between data and MC as well as the consistency between measurements performed on different physics processes.

4.5 Tau reconstruction

Tau leptons can decay either leptonically ($\tau \to \ell\nu_\ell\nu_\tau, \ell = e, \mu$) or hadronically ($\tau \to$ hadrons $+ \nu_\tau$, named τ_{had}) inside the ATLAS detector. We briefly describe here the reconstruction of hadronic decays which represent 65% of all possible τ decays modes. The hadronic decay products contain one (in the 72% of the cases) or three charged pions (22% of the cases). In 68% of all hadronic decays, at least one associated neutral pion is also produced. Charged and neutral pions provide the visible part of the hadronic tau decay (referred to as $\tau_{had-vis}$). The main background to tau reconstruction arises from jets of energetic hadrons produced by fragmentation of quarks and gluons. To distinguish between signal and background, a multivariate method is adopted, exploiting the feature of the narrow shower in the calorimeter, the distinct number of tracks and the displaced tau decay vertex [123].
Based on jet reconstruction (see Section 4.4), jets from tau are required to have $p_{\mathrm{T}} > 10$ GeV and $|\eta| < 2.5$. Tau candidates in the transition region ($1.37 < |\eta| < 1.52$) are vetoed. In events with pile-up, the PV does not always correspond to the vertex in which the tau lepton is produced. The *Tau Vertex Association algorithm* identifies the PV associated with a tau as the one with the largest fraction of momentum tracks in a cone of $\Delta R < 0.2$ around the seed jet. Tracks satisfying $|d_0| < 1$ mm and $|\Delta z_0 \sin\theta| < 1.5$ mm from the tau vertex are associated to the *core* ($0 < \Delta R < 0.2$) and *isolation* ($0.2 < \Delta R < 0.4$) regions around the tau candidate.
Tau identification uses a BDT separately trained for tau candidates with one or three associated tracks[6]. The training is performed on simulated $Z \to \tau\tau$ for signal and data dijet events for background. Three working points are provided: `Loose`, `Medium` and `Tight`, corresponding to different tau identification efficiency values, designed to be independent of p_{T}. Target efficiencies are 0.6, 0.55 and 0.45 for the one-prong `Loose`, `Medium` and `Tight` working points. For three-prongs taus, target efficiencies are 0.5, 0.4 and 0.3 for `Loose`, `Medium` and `Tight` working points respectively. The output of the BDT for tau identification is provided in Fig. 4.10.

[6] Usually the *associated tracks* are referred to as *prongs* so that in the following these type of events will be named *one-prong* or *three-prongs* events.

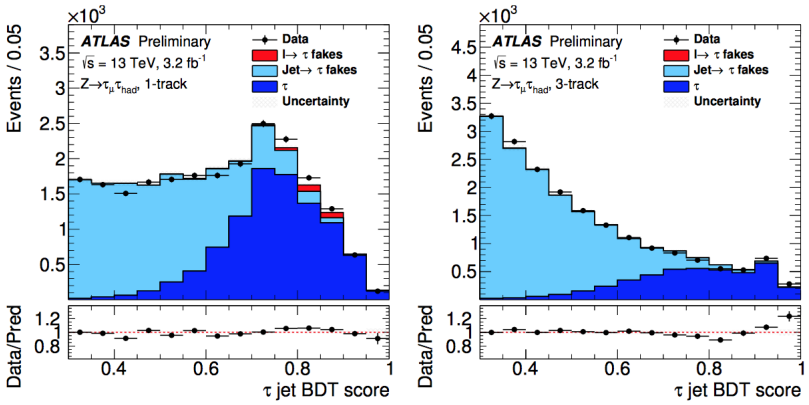

Figure 4.10: Output of the jet BDT discriminant for tau identification for one-prong (left) and three-prongs (right) τ_{had} candidates. The uncertainty band contains only the statistical uncertainty [123].

4.6 Overlap removal

The *overlap removal* (OR) procedure is aimed to further clean objects provided to the analyses [124]. In some cases one physical object can be reconstructed as two different objects (e.g. an electron reconstructed both as an electron and a jet) leading to duplications. Furthermore, the procedure is designed to treat cases in which two separate objects occupy close-by regions of the detector. The OR is composed of several steps and its performance might differ when using different object selections. Recommendations provided by the ATLAS performance group span over many physics analyses providing a common prescription optimized by gathering information by many physics groups.
The discriminating variable used as decision parameter in the OR procedure is the distance between objects in the η-ϕ plane: ΔR.

Electron-jet overlap removal

The goal of this step is to remove either jets identical to reconstructed leptons or to remove one of the two objects when too close to each other, risking to bias each other position or energy measurement. It was proved [124] that the region $\Delta R(e, j)$ <0.2 identifies a population of electrons which are also reconstructed as jets. On the contrary, the region 0.2< $\Delta R(e, j)$ <0.6 consists of events with real jets close to electrons. The proximity between the two objects in this latter region can result in an increase of the jet energy

partially incorporating electron clusters or in a bias in the electron reconstruction. As a summary, removing if $\Delta R(e, j)$ <0.2 allows to reject electron duplicates while the electron, or in some cases the entire event, is removed in the region 0.2< $\Delta R(e, j)$ <0.4.

Muon-jet overlap removal

There are several cases in which a muon overlaps with a jet and these cases are taken into account in the muon-jet OR. Pile-up can produce a jet and a muon in the same detector area from different bunch crossings or same bunch crossing. Light (LF) or heavy (HF) flavour meson decays can lead to close-by muons and for the latter the secondary vertex is closer to the PV and the $\Delta R(\mu, j)$ is generally smaller than for light mesons decays. Bremsstrahlung or FSR produced by muons can lead to a jet very close to a muon track; the ID track is combined with the photon energy deposit in the EM calorimeter and reconstructed both as a muon and a jet.
The most important jet feature in the ID is the number of tracks (usually at least three tracks are required) which allows to discriminate between muons from LF/HF and muons from FSR or bremsstrahlung. Moreover, muons from jet decays generally present lower transverse momentum than the jet itself, while the opposite is true for jets reconstructed from radiating muons. Studies performed on samples containing isolated prompt muons and b- or light-jets [124] showed that removing a jet with a number of associated tracks ≤ 2 when $\Delta R(\mu, j)$ <0.2 effectively reduces muon duplication. In analogy to the electron case, inside a cone of $\Delta R(\mu, j)$ <0.4, if the number of tracks associated to a jet is > 2 and it overlaps with a muon, this latter is removed. In final states containing very high-p_{T} objects, where muons get very close to real hadron jets, a large isolation cone induces significant signal inefficiencies. In these cases, p_{T} variable cone size of $\Delta R(\mu, j)$ <0.04 + 10 GeV/$p_{\mathrm{T}}(\mu)$ is used.

Lepton-lepton overlap removal

Duplication of muons as electrons can happen when the muon radiates a hard photon through FSR or bremsstrahlung. When this happens, the two objects are closer than $\Delta R(\mu, e)$ <0.01 or share the same ID track. The ID track sharing usually provides a better discrimination power against duplications. The choice is to remove the muon, if it has no associated MS signal (CaloTag muons), sharing a track with an electron. Otherwise, the electron is removed.

Tau-X overlap removal

In analyses with tau final states, jets matching to well-identified selected taus are usually removed from the collection of hadronic jets when closer than $\Delta R(j,\tau)$ <0.2. Muons can fake one-prong taus in case of anomalous energy loss in the calorimeter, also leading to worse ID and MS matching, and thus taus are removed when $\Delta R(\mu,\tau)$ <0.2. Electrons can fake one-prong taus and sometimes three-prongs taus. The multivariate discriminant used for tau identification was designed to reject this electron background and is further combined with tau removal when $\Delta R(e,\tau)$ <0.2.

It is important to underline that, changing event object multiplicity, order matters in the OR procedure. For this reason, the recommended hierarchical sequence is the following: removing τ overlapping with e/μ, lepton-lepton overlap removal, lepton-jet and finally τ-jet.

Chapter 5

Data analysis tools

A certain number of general features are shared among the analyses that are going to be presented in the following chapters. They involve MC generators used to model the SM background (see Section 5.1). Besides, given the similarities between the analyses final states, the techniques used to estimate the major backgrounds (see Sections 5.3 and 5.4) are common. The statistical procedure for data analysis is also be presented in this Chapter (see Section 5.6).

5.1 Features of Monte Carlo generators

Monte Carlo simulation is the essential tool of any particle physics analysis allowing a comparison between the data collected by the experiments and the events expected from theoretical predictions. The process we need to simulate is a pp interaction leading to a final state X: $pp \rightarrow X$, whose picture is provided in Fig. 5.1.

The hard scattering of two energetic protons with momentum p_1 and p_2 can be seen as the interaction between two partons of the protons. The probability of finding a parton i or j carrying momentum x_1 or x_2 is described by the PDFs f_i and f_j.
Consequently, we can express the pp deep inelastic cross-section in terms of the parton-parton cross-section. However, we know that QCD suffers from singularities when two daughter partons are collinear or soft. The *QCD factorization theorem* states that the singularities can be removed from the parton cross-section and absorbed into the PDFs of the incoming hadrons and this can be done at all orders in the perturbative expansion. The cross-

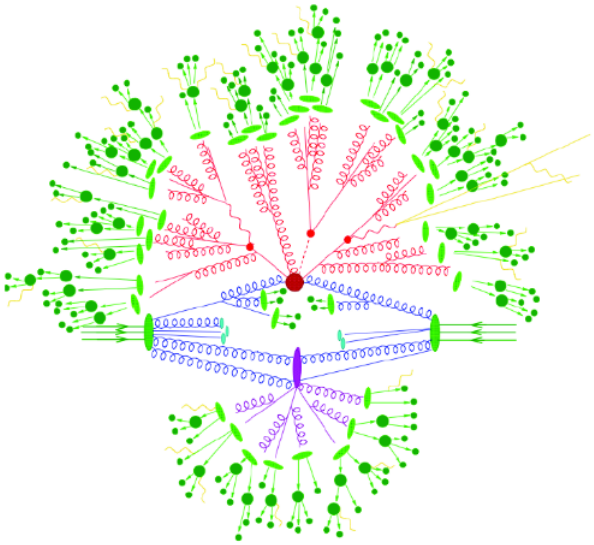

Figure 5.1: Illustration of a hard scattering event: the partonic hard scattering is shown as a red blob while the purple blob represents the additional multi-parton interactions. The initial and final state radiation are depicted by spiral and straight lines. The hadrons generated during the hadronization step are shown in light green while the final stable hadrons are shown in dark green [125].

section for the pp hard-scattering is then written as:

$$\sigma_{pp\to X}(s) = \sum_{i,j} \int dx_i dx_j f_i(x_i, \mu_F^2) f_j(x_j, \mu_F^2) \hat{\sigma}_{ij\to X}(\hat{s}, \mu_F, \mu_R, \alpha_s) \qquad (5.1)$$

where $f_i(x_i, \mu_F^2)$ and $f_j(x_j, \mu_F^2)$ are the PDFs for partons i and j, $\hat{\sigma}_{ij\to X}$ the partonic cross-section, evaluated in perturbative QCD and depending on the center-of-mass energy $\hat{s} \sim x_i x_j s$, the QCD coupling constant α_s, as well as on the *factorization* μ_F and *renormalization* μ_R scales. The factorization scale can be thought as the energy scale separating long- and short-distance physics. A parton with transverse momentum less than μ_F is considered to be part of the hadron structure and absorbed in the PDF. Partons with larger transverse momenta instead participate in the hard scattering process with a short-distance partonic cross-section $\hat{\sigma}$. Therefore, the dependence of the PDFs from the μ_F energy scale is explained. The renormalization energy scale μ_R is an intrinsic parameter arising from the renormalizable nature of QCD theory equations. Indeed, μ_R enters the running α_s calculation and it can be used to extract the value of α_s at any energy scale by using the renormalization group equations.
The hard scattering process, parametrized by the term $\hat{\sigma}_{ij\to X}$ in Eq. 5.1,

is simulated using a ME calculation; numerical integration over the process phase space provides parton level simulated quantities. Hard scattering processes can be calculated at different perturbation levels (LO, NLO, NNLO). Higher orders (NLO) in QED result, for instance, by adding a virtual photon interaction between two charged particles, or emitted and absorbed by the same particle, or by virtual loops of W/Z or Higgs bosons. NLO corrections in QCD result from adding a virtual loops with quarks or gluons, and NNLO correction follow the same principle.
Different set of PDFs ($f_{i,j}(x_i, \mu_F^2)$) are available for today's proton collider experiments, which might differ for the input dataset used, for the LO/NLO/NNLO evolution, for the value of the strong coupling constant α_s or for the parametrization choice. The PDFs used in this work are the CT10 [126] (NLO), CT10NNLO [127] (NNLO), CT10F4 (NLO), CTEQ6L1 [128] (LO), NNPDF2.3LO [129] (LO) and NNPDF3.0LO [130] (LO). The PDFs evolution approximation level should match the hard scattering parturbation level.
After the outcoming partons are generated, their QCD cascade of final state radiation is described by the *parton shower* (PS). The PS describes the splitting of a single parton into two partons, conserving flavour, four momentum and respecting unitarity. The PS usually stops at energy scales of $\mathcal{O}(1\ \text{GeV})$. Different PS implementations depend on the different choice, for instance, for the splitting variable V_i^2, function of the mother and daughter partons momenta. The purpose of the splitting variable is to order splittings within the shower: if the splitting of the parton i comes before the splitting of the parton j then $V_i^2 > V_j^2$. In most cases, V_i^2 is a measure of the hardness of the splitting: when $V_i^2 \to 0$ then the angle between the daughter partons approaches zero or one of the two partons momentum is close to zero. The commonly used splitting variables used for PS are the *virtuality*, i..e the virtual squared mass of the showering parton, the p_{T}^2 of the emitted and remaining partons and $E^2(1 - \cos\theta)$, where E is the energy of the parent parton and θ the angle between the original and emitted partons. In QCD, two types of large logarithms of infrared origin need to be corrected for: collinear (low angle) and soft (low energy and arbitrary angle) emissions. This last effect can be computed inside the PS formalism by using the emission angle as ordering variable and the argument of α_s at the splitting vertex should be the relative parton $p_{\mathcal{T}}$ after the splitting. Therefore HERWIG [131] uses angular ordering as evolution variable. Alternative formulations of QCD cascades focus on soft emission, rather than collinear emissions, as basic splitting mechanism, as in the case of SHERPA [132] and PYTHIA [133].
The PS computations based on collinear and soft approximations are not accurate for hard and large-angle emissions. For such cases the full ME

amplitudes are needed and they need to be properly *matched* to the PS calculation using a *matching scale*, to avoid final state configurations to be double counted. The matching can be done in two ways, using the ME and PS matching (ME+PS) or the matching of the NLO calculation and PS (NLO+PS). The first approach implements the tree-level ME for hard and large angle emissions generating the basic process, and a given number of additional partons, with a minimum separation angle. This can be done by requiring the relative p_{T} in any pair of partons to be above the matching scale cut threshold Q_{cut}. The cut has to be large enough to permit fixed-order perturbation theory, but small enough to allow accurate PS emission. The NLO+PS approach extends the ME accuracy at the NLO, including NLO corrections to the emission of extra radiation, including NLO virtual corrections.
The advantage of the ME+PS approach is the possibility to use existing LO generators, like MadGraph [134], for the ME calculation and then feed the partonic events to Pythia or Herwig. Generators like Sherpa or Herwig++ also include their own ME generators. The NLO+PS process is implemented in aMC@NLO [135] and Powheg [136].
After the PS, hadronization between partons occurs and perturbation theory cannot be used anymore. The two main phenomenological models used to describe hadronization are the Lund string model [137] and the cluster fragmentation model [138, 139]. In the former, when a quark and an anti-quark are separated, the gluon color field lines are stretched until a new $q\bar{q}$ pair is created. The procedure continues until the color field weakens and prevents from further fragmentation. In the cluster fragmentation model gluons are split into $q\bar{q}$ pairs clustered to form color-singlet hadrons. Clusters are fragmented until stable hadrons are formed.
Primary hadrons are unstable and further decay into a set of stable particles (where stable here needs to be intended as with a minimum flight path distance of $c\tau \geq 10$ mm). Consequently, the decay modeling of unstable particles also plays an important role in the description of the physics process. Commonly, MC generators describe the decay process with a Breit-Wigner distribution, truncated at the edge of the physical decay phase space (respecting the branching ratio summation to unity). Additionally, Herwig++ and Sherpa include helicity-dependence in τ decays and provide an improved simulation of hadronic decays, taking into account spin correlations between those decays for which ME are used. CP-violating effects are also included in Sherpa.
The MC tuning changes the model parameters sensitive to MPI and UE modeling, PS modelling and takes into account the dependencies of some of these processes to the PDFs setting. The tuning is performed in this analysis

using the A14 [140], AZNLO [141], Perugia 2012 [142], UE-EE-5 tunes.

To understand how the choice of MC generator for a given process is made, we take as an example one of the physics process involved in the analyses, which is $t\bar{t}$ production.
We compare NLO MC generators, where the prediction of the $t\bar{t}$ inclusive production cross-sections are corrected at NNLO, including NNLL resummation.

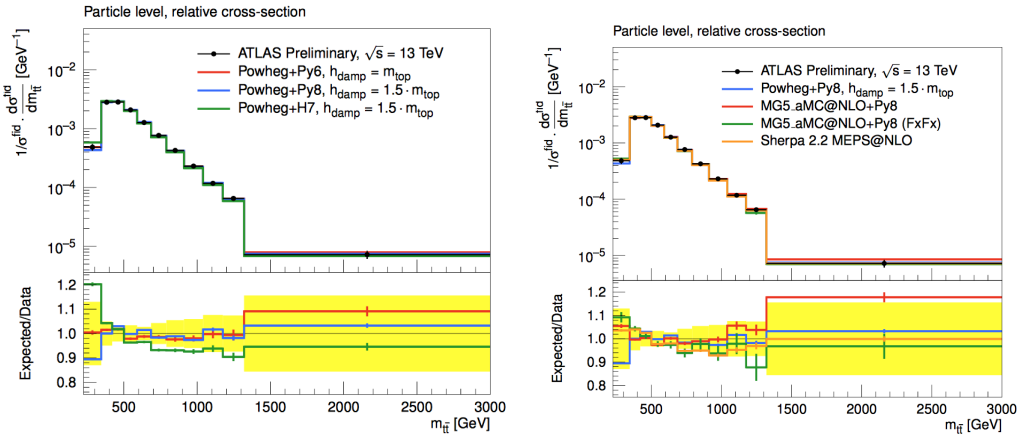

(a) (b)

Figure 5.2: Comparison between different MC generators on $t\bar{t}$ differential cross-section: (a) PS or (b) ME algorithms are compared as a function of the $t\bar{t}$ system invariant mass [143].

To evaluate the effect of different PS or ME generators, different samples are produced [143]. The effect of PS is assessed by using POWHEG interfaced with PYTHIA 6 or 8 and HERWIG. After the optimization of MC generator-specific setting parameters (e.g. h_{damp} which controls the ME/PS matching and regulates high-p_{T} radiation), Fig. 5.2a shows that the better description of the $t\bar{t}$ system invariant mass is provided by POWHEG+PYTHIA8. Regarding the ME calculation, additional samples are produced with MG5_AMC@NLO interfaced with PYTHIA 8 and SHERPA. An inclusive NLO prediction is provided by MG5_AMC@NLO (including also up to two additional partons at NLO accuracy with the FxFx [144] prescription). SHERPA describes up to one additional parton at NLO accuracy and up to four at LO accuracy. The additional samples are compared to POWHEG+PYTHIA8 in Fig. 5.2b which confirms that POWHEG+PYTHIA8 provides the best description of data across the whole $m_{t\bar{t}}$ spectrum. The prediction is also confirmed by the measurements performed at $\sqrt{s}$= 7,8 TeV which are not shown here.

5.2 Derivation framework

Physics analyses in ATLAS perform a huge variety of event selections and need different sets of information out of the data collected by the experiment. ATLAS software framework managing event generation, simulation and reconstruction is named *Athena*. After reconstruction, both data and MC events are eventually stored in the Analysis Object Data (AOD) format. Due to their large size, the AOD files are usually not practical and therefore intermediate-sized data have to be produced satisfying the following main features:

- their size should be a few per mille of the original file size;
- all the information necessary to perform the desired selections, including object calibrations or information necessary to the ATLAS performance groups, need to be present.

To cope with these requirements, a data reduction strategy is implemented in Run 2 [145] using a centralized offline tool, known as *Derivation Framework*. The input to the framework are the Athena processed data and simulation samples in a format called xAOD. The output, called Derived-xAOD or DxAOD, presents the same format of the input but with reduced size. Derivation proceeds in the following steps:

- skimming: removing whole events if not suiting particular derivation requirements;
- thinning: removing reconstructed objects (such as tracks, calorimeter clusters, jets, etc.) from one event, keeping the rest of the event;
- slimming: removing not needed information from objects and keeping the interesting ones;
- augmentation: adding information not found in the input data.

A scheme of data/MC reconstruction is provided in Fig. 5.3.

Derivations are usually grouped as physics groups (e.g. `SM`, `SUSY`, `EXOT`, `HIGG`, etc.). Different sets of derivations are used in the analysis which will be presented in the following chapters.

`HIGG8D1`: events are selected if satisfying one of the following criteria:

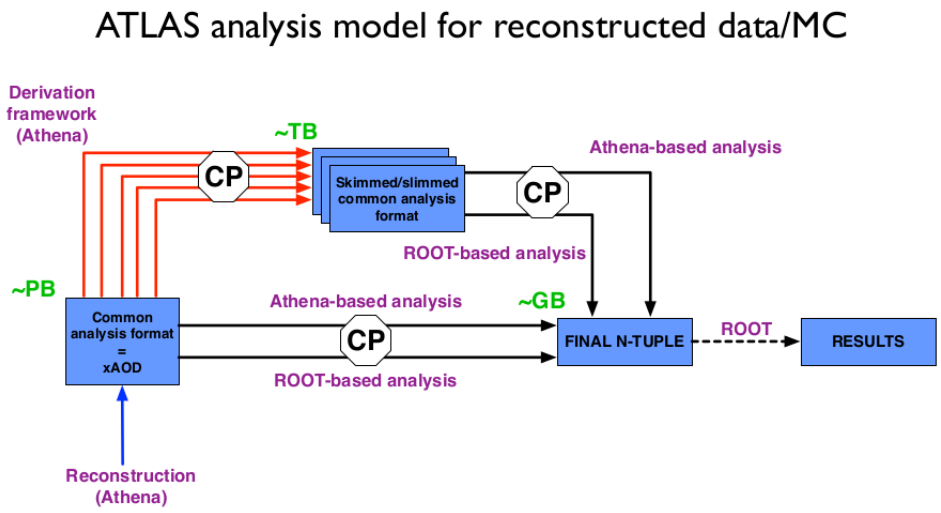

Figure 5.3: The ATLAS analysis model in Run 2.

- at least two light leptons passing loose identification criteria with leading lepton p_{T} >15 GeV and subleading lepton p_{T} >5 GeV, within $|\eta|$ < 2.6;
- at least one light lepton passing loose identification criteria with p_{T} >15 GeV and $|\eta|$ < 2.6 and at least two hadronic τ with p_{T} > 15 GeV, charge ± 1 and three associated tracks.

This derivation will be the one used for the $t\bar{t}H$ analysis illustrated in Chapter 6.

`EXOT12`: events are selected if they contain at least two leptons (in any flavour combination) satisfying the following selection requirements: $p_{\mathrm{T}}^{e} > 20$ GeV and `LHLoose`, $p_{\mathrm{T}}^{\mu} > 20$ GeV being a combined muon. This is the baseline derivation for the $H^{\pm\pm}$ and heavy-neutrino analyses presented in Chapter 7.

`EXOT19`: requires events containing at least one electron with $p_{\mathrm{T}}^{e} > 20$ GeV and passing `LHLoose` identification. This derivation is used for fake estimation in the electron channel in Chapter 7.

`HIGG3D3`: requires events containing at least one electron with $p_{\mathrm{T}}^{e} > 7$ GeV and $|\eta|_{e}$ <2.6 passing the `LHVeryLoose` identification working point or at least one muon with $p_{\mathrm{T}}^{\mu} > 7$ GeV and $|\eta|_{\mu}$ <2.7 being a combined muon. Furthermore, events must contain at least one jet back-to-back (ΔR >2.5)

from the electron or the muon. This derivation is used for fake estimation in the muon channel in Chapter 7.

5.3 Electrons with misidentified charge background

Channels involving two SS electrons ($e^{\pm}e^{\pm}$), and consequently also the ones involving mixed-flavour leptons ($e^{\pm}\mu^{\pm}$), suffer from contamination by OS events where one of the electrons charge is mis-reconstructed (also called *charge-flip* (CF) events). A simplified sketch of the charge mis-identification process is illustrated in Fig. 5.4.

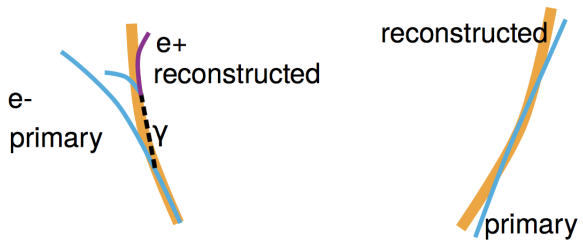

Figure 5.4: Simplified representation of the electron charge mis-identification process due to electron interaction with the detector material.

Charge mis-identification occurs because of the interaction between the electron and the detector material. Different physics processes, mainly divided into two categories, can lead to this type of background:

- Bremsstrahlung followed by photon conversion: this process ($e^{\pm} \rightarrow e^{\pm}\gamma^{*} \rightarrow e^{\pm}e^{+}e^{-}$), called *trident*, can lead to charge mis-reconstruction in the following ways: first, the information from the EM calorimeter can be matched to the wrong electron track (Fig. 5.5a); second, the bremsstrahlung process can originate an electromagnetic shower inside the ID with a loss of information about the initial track (Fig. 5.5b).

- very high-p_{T} electrons (*stiff tracks*) are barely influenced by the momentum curvature induced by the electromagnetic field in the ID. For these type of electrons (Fig. 5.5c), charge reconstruction is also affected by the possibility of a measurement error.

Muon charge reconstruction is performed combining the information collected by the ID and the MS. Charge mis-identification for muons, for which

the probability to undergo bremsstrahlung is significantly smaller than for electrons up to p_{T} of few hundreds of 100 GeV, can only happen as stiff tracks. The error in charge reconstruction for high-p_{T} muons is mainly due to alignment effects of the MS and is measured using a sample of simulated $W' \to \mu\nu$ events [146]. The probability of charge reconstruction errors is in the range 0.2% to 0.9% for W' masses of 1 TeV and still below 4% for W' masses up to 6 TeV. Given the negligible contribution from these type of events to the reducible backgrounds they are usually extracted from MC simulation and negligible.

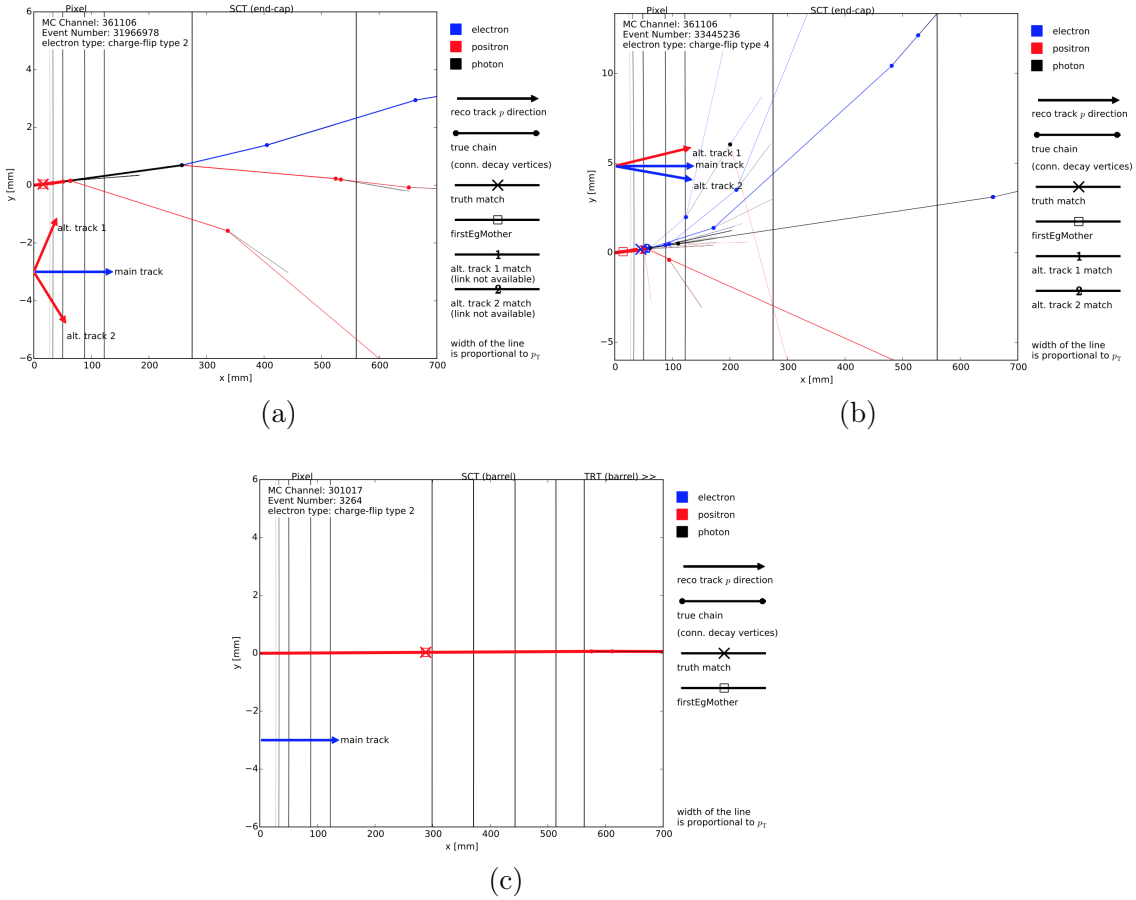

Figure 5.5: Diagrams illustrating different processes responsible for charge misidentification: (a) typical trident process, (b) electromagnetic shower and (c) "stiff" tracks. The plots show on the y axis the distance from the interaction point while on the x axis the distance traversed by the electron inside the first two portions of the ID (Pixel and SCT).

It is clear from the complexity and variety of the different type of pro-

cesses just outlined that MC simulation needs to precisely model both the particle/detector interaction and provide a detailed description of the detector material. Indeed, this is not true and simulation modeling can be off by 10-20% and dedicated procedures based on data need to be applied to correct for simulation mismodeling.
The goal is to measure charge mis-identification probabilities as a function of electron kinematical properties (p_{T}, η). The general idea is to select a very clean sample of prompt electrons, where a relevant fraction of charge-flip might have occurred, such as $Z \to e^+e^-$ events with no requirement on the charge final state. The method is data-driven and relies on a likelihood-fit however the actual charge-flip probabilities measurement and consequent application is analysis dependent.
In the following, the general features of the likelihood-fit will be shown and eventually applied in Chapters 6 and 7. The first quantity to measure is the probability ϵ for one electron to be reconstructed with incorrect charge. If an OS e^+e^- event is produced, the final state can belong to one of the follow categories:

- no charge misidentification, with a probability (1-ϵ)^2;
- charge misidentification for both electrons, with probability ϵ^2;
- only one electron has wrong reconstructed charge, with probability 2ϵ(1-ϵ).

Given an initial number of true OS events, reconstructed events divided by charge are:

$$N^{OS} = (1 - 2\epsilon + 2\epsilon^2)N \simeq (1 - 2\epsilon)N \tag{5.2}$$
$$N^{SS} = 2\epsilon(1 - \epsilon) \simeq 2\epsilon N \tag{5.3}$$

where the last approximations stand when ϵ^2 is negligible. Allowing the probabilities for the two electrons i and j to be different[1], the number of SS events is:

$$N^{ij}_{SS} = N^{ij}(\epsilon_i + \epsilon_j). \tag{5.4}$$

Charge mis-identification probabilities are extracted using events originating from the leptonic decay of the Z boson. If SS events in the Z peak are produced by charge-flip, N^{ij}_{SS} follows a poissonian probability:

$$f(N^{ij}_{SS}; \lambda) = \frac{\lambda^{N^{ij}_{SS} e^{-\lambda}}}{N^{ij}_{SS}!} \tag{5.5}$$

[1] Here i and j bins have to be intended as a region of the electron phase space in the (p_{T},η) plane.

where $\lambda = (\epsilon_i + \epsilon_j)N^{ij}$ is the expected number of SS pairs in bin (i, j). The probability for one electron to produce a charge-flip is expressed by:

$$P(\epsilon_i, \epsilon_j | N_{SS}^{ij}, N^{ij}) = \frac{[N^{ij}(\epsilon_i + \epsilon_j)]^{N_{SS}^{ij}} e^{-N^{ij}(\epsilon_i+\epsilon_j)}}{N_{SS}^{ij}!}. \tag{5.6}$$

The likelihood function $\mathcal{L}$ for all the events can be expressed as:

$$\mathcal{L}(\epsilon | N_{SS}, N) = \prod_{i,j} \frac{[N^{ij}(\epsilon_i + \epsilon_j)]^{N_{SS}^{ij}} e^{-N^{ij}(\epsilon_i+\epsilon_j)}}{N_{SS}^{ij}!} \tag{5.7}$$

and the ϵ_i and ϵ_j parameters, which depend on both electron $|\eta|$ and p_{T}, can be obtained by the minimization of $-\ln \mathcal{L}$, written as:

$$-\ln \mathcal{L}(\epsilon | N_{SS}, N) \approx \sum_{i,j} \ln[N^{ij}(\epsilon_i + \epsilon_j)]^{N_{SS}^{ij}} e^{-N^{ij}(\epsilon_i+\epsilon_j)}. \tag{5.8}$$

As already stated, the likelihood method is performed on a pure Z sample, for which backgrounds need to be subtracted. For this purpose, the Z peak is divided into three regions (A,B and C), where B is the central region and A,C the *side-bands*. The number of events in the side-bands n_A and n_C is subtracted from region B and thus the final number of signal Z events is given by:

$$N_{SS} = n_B - \frac{n_A + n_C}{2}. \tag{5.9}$$

The Z peak for SS pairs is usually shifted to lower ($\sim$2 GeV) values, mainly due to bremsstrahlung energy losses. Consequently, slightly different window ranges for A and C are chosen for OS and SS events.
On top of what is illustrated in this section, which stands for each analysis willing to evaluate the contribution of events with charge mis-identified electrons, different approaches can be adopted both in the fit and in the application of the measured probabilities.
The fit can be performed using a 2D or a 1D$\times$1D parametrization as a function of p_{T} and η. Moreover, the measured rates can be applied to OS data events or on truth-matched MC electrons. The choice is analysis dependent and is discussed in Chapters 6 and 7.

5.4 *Fake* leptons background

One of the main background in channels with SS leptonic final states, besides charge mis-identification for electrons, is due to *fake* and *non-prompt*

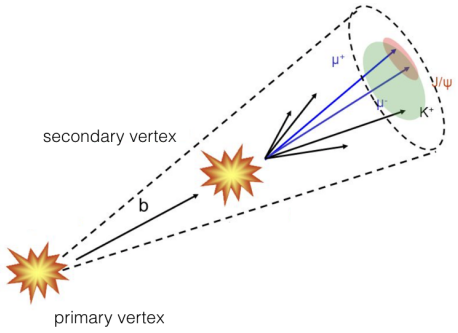

Figure 5.6: Representation of an event containing a non-prompt lepton: a b-hadron is produced in the IP with consequent decay into light quarks jets in secondary displaced vertex. Electrons, or muons, originate from the b-hadron secondary decay and can fake leptons coming directly from the PV.

leptons. As shown in Fig. 5.6, a non-prompt lepton arises from hadron decays inside a jet for which there is non-null probability that such lepton gets reconstructed as originating from the interaction point. Non-prompt leptons are therefore *real* leptons *faking* their actual origin. For instance, inclusive semi-leptonic decays of b-hadrons have a 10% branching ratio for each lepton flavour [6]. However, not only heavy flavour hadrons[2] contribute to non-prompt leptons but also hadrons originating from light (u, d, s) quarks. Besides non-prompt leptons, for the electron case an additional source of background arises from jets produced in the IP (*mis-identified jets*). The electrically charged component of an hadronic jet provides a signal in the ID and a calorimetric energy deposit as electrons do. When some of the jet track information from the ID is lost, a jet can be identified as an electron, and called *fake*.
As already discussed in the case of charge mis-identification, simulation fails in providing a precise description of these types of processes. Moreover, the probability for a jet to fake a lepton is low, thus a very high statistic MC sample would be needed to successfully predict those events.
Data-driven techniques are necessary to provide a satisfactory estimation of events containing both non-prompt leptons and mis-identified jets, which from now on for simplicity will be grouped together under the label of *fakes*.

[2] Here *heavy flavour* indicates hadrons originating from the heavier hadronizing quarks: b, c quarks.

Also in this case, there is not a unique prescription on which method to adopt for fake measurement. Different methods can be applied suiting the different analysis topologies and features. In the following, two of the main methods for fake evaluation are described, namely the *Matrix Method* and the *Fake Factor Method*, applied to the analyses presented in Chapters 6 and 7.

5.4.1 The Matrix Method

The Matrix Method (MM) relies upon loosening some of the identification criteria (named *loose* selection) applied in the analysis standard (*tight*) selection. The selections are:

- tight, defining leptons of the analysis regions,
- loose, defining leptons of the so-called *side-bands* (regions containing at least one loose lepton).

By definition, the set of objects passing the tight selection N_{tight} must be a subset of those passing the loose selection N_{loose}, as schematically portrayed on Fig. 5.7. This can be achieved by loosening, for example, the lepton identification or isolation working points.

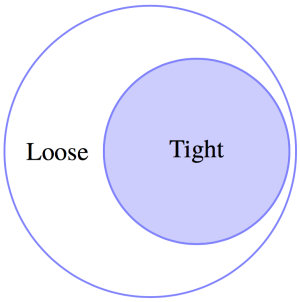

Figure 5.7: The loose and the tight regions in the MM. The tight region must be a subset of the loose region (i.e. tight leptons should also pass all of the loose requirements).

The MM links the number of real (R) and fake (F) objects we want to estimate to the number of tight and loose objects we observe. In a two lepton analysis, all of the possible combinations of lepton candidates are denoted by N_{xy} with $x, y = [R, F]$. The first index represents the first object and the second index the second object (without a particular p_{T} ordering). Both real and fake objects need to pass at least the loose selection criteria to be considered in the MM.

Events are divided into four categories: pairs with two tight objects (TT), pairs with two strictly loose objects ($L'L'$), and pairs with one tight and one strictly loose object ($TL', L'T$). Strictly loose objects are objects that pass the loose criteria but fail the tight ones. To avoid the confusion with the previously defined loose objects, let us symbolize them by L'. The numbers of each of those events are then denoted by N_{xy} with $x, y \in T, L'$. A matrix (M) connects the number of real and fake leptons (right side of Eq. 5.10) and the number of observed tight and strictly loose counted objects (left side of Eq. 5.10):

$$\begin{pmatrix} N_{TT} \\ N_{TL'} \\ N_{L'T} \\ N_{L'L'} \end{pmatrix} = M \times \begin{pmatrix} N_{RR} \\ N_{RF} \\ N_{FR} \\ N_{FF} \end{pmatrix}, \tag{5.10}$$

where M is:

$$\begin{pmatrix} r_1 r_2 & r_1 f_2 & f_1 r_2 & f_1 f_2 \\ r_1(1-r_2) & r_1(1-f_2) & f_1(1-r_2) & f_1(1-f_2) \\ (1-r_1)r_2 & (1-r_1)f_2 & (1-f_1)r_2 & (1-f_1)f_2 \\ (1-r_1)(1-r_2) & (1-r_1)(1-f_2) & (1-f_1)(1-r_2) & (1-f_1)(1-f_2) \end{pmatrix} \tag{5.11}$$

and where r_1 and r_2 are respectively the real rates for the first and the second real lepton and f_1 and f_2 are the fake rates for the first and the second fake lepton. The real (fake) rate is defined as the probability that a real (fake) lepton, that passes the loose selection criteria, also passes the tight selection criteria. They are obtained by measuring the number of loose and the number of tight objects, as shown in Eq. 5.12:

$$r = \frac{N^{\text{real}}_{\text{tight}}}{N^{\text{real}}_{\text{loose}}}, \qquad f = \frac{N^{\text{fake}}_{\text{tight}}}{N^{\text{fake}}_{\text{loose}}}. \tag{5.12}$$

The rates are the crucial part of the MM since, given the rates, it is possible to invert the matrix in Equation 5.11 and deduce the number of events that pass the nominal selection of the analysis (N_{TT}) containing at least a fake lepton. The rates are usually determined in a data-driven approach by measuring them in dedicated control regions dominated by real or fake leptons, and then extrapolating them into the signal region. A typical example of a clean control region for measuring real rates is a $Z \to \ell^+\ell^-$ sample while a good candidate for fake rate measurement is a dijet control region. The contribution of pairs with at least one fake lepton to the tight selection, expressed in the notation of the matrix method is shown in Eq. 5.13.

$$N^{\text{fakes}}_{TT} = rf(N_{RF} + N_{FR}) + f^2 N_{FF} \tag{5.13}$$

Equation 5.13 covers all of the possible sources of fake leptons to the nominal di-lepton selection. However, it depends on inaccessible truth quantities which can not be measured in data. By inverting the matrix in Eq. 5.10 those quantities can be, on the contrary, expressed in terms of the measurable numbers of different kinds of pairs (N_{TT}, $N_{TL'}$, $N_{L'T}$ and $N_{L'L'}$). The inverted matrix is:

$$\begin{pmatrix} N_{RR} \\ N_{RF} \\ N_{FR} \\ N_{FF} \end{pmatrix} = \frac{1}{(r-f)^2} \begin{pmatrix} (1-f)^2 & (f-1)f & f(f-1) & f^2 \\ (f-1)(1-r) & (1-f)r & f(1-r) & -rf \\ (r-1)(1-f) & (1-r)f & r(1-f) & -rf \\ (1-r)^2 & (r-1)r & r(r-1) & r^2 \end{pmatrix} \begin{pmatrix} N_{TT} \\ N_{TL'} \\ N_{L'T} \\ N_{L'L'} \end{pmatrix} \tag{5.14}$$

so that the final contribution from fake leptons to di-lepton tight events is:

$$\begin{aligned} N_{TT}^{\text{fakes}} = \quad & \alpha[2rf(f-1)(1-r) + f^2(1-r)^2]N_{TT} \\ & +\alpha(1-f)fr^2(N_{TL'} + N_{L'T}) \\ & -\alpha r^2 f^2 N_{L'L'}, \end{aligned} \tag{5.15}$$

where $\alpha = 1/(r-f)^2$. One of the method limitation is that, as we see from the definition of the factor α, large MM weights can arise when real and fake efficiencies values get close. To avoid such cases it is usually recommended to define loose leptons as much loose as possible with respect to the tight one. In the analyses performing lepton categorization using loose lepton counting, however, the loose definition also needs to account for potential sensitivity losses (more details in Section 6.2.3). The most problematic region is usually the high-p_{T} one, where the majority of the leptons already tend to be isolated and this causes fake efficiency to reach values close to unity. It is thus preferable, when possible, to remove isolation requirements on loose leptons to enhance the difference between the loose and tight lepton definitions avoiding to spoil the validity of the MM estimation.

5.4.2 The Fake Factor Method

The Fake Factor method (FF) is derived from the MM in the limit where $r \to 1$. To demonstrate this, lets rewrite Eq. 5.15 using A, B, and C:

$$N_{TT}^{\text{fakes}} = AN_{TT} + B(N_{TL'} + N_{L'T}) + CN_{L'L'}, \tag{5.16}$$

where $A = \alpha[2rf(f-1)(1-r)+f^2(1-r)^2]$, $B = \alpha(1-f)fr^2$ and $C = -\alpha r^2 f^2$. By assuming $r = 1$, A becomes equal to 0. If the *fake factor* (F) is defined as:

$$F = \frac{f}{1-f} \tag{5.17}$$

the total contribution of fake leptons to the nominal selection is:

$$N_{TT}^{\text{fakes (FF)}} = F(N_{TL'} + N_{L'T}) - F^2 N_{L'L'}. \tag{5.18}$$

However, the FF formula is just an approximation and does not hold for realistic values of r. Let us compare the results obtained with the FF formula 5.18 to the ones obtained with the MM equations 5.16. By construction, Eq. 5.16 exactly reproduces the fake background from Eq. 5.13. Starting with the FF formula and replacing $N_{TL'}$, $N_{L'T}$, and $N_{L'L'}$ with the exact expressions from Eq. 5.10 we get:

$$\begin{aligned} N_{TT}^{\text{fakes (FF)}} =& \frac{f}{1-f} r(1-r) N_{RR} + \frac{f}{1-f} r(1-f) N_{RF} + \frac{f}{1-f} f(1-r) N_{FR} \\ &+ \frac{f}{1-f} f(1-f) N_{FF} + \frac{f}{1-f} (1-r) r N_{RR} + \frac{f}{1-f} (1-r) f N_{RF} \\ &+ \frac{f}{1-f} (1-f) r N_{FR} + \frac{f}{1-f} (1-f) f N_{FF} - \frac{f^2}{(1-f)^2} (1-r)^2 N_{RR} \\ &- \frac{f^2}{(1-f)^2} (1-r)(1-f) N_{RF} - \frac{f^2}{(1-f)^2} (1-f)(1-r) N_{FR} \\ &- \frac{f^2}{(1-f)^2} (1-f)^2 N_{FF}. \end{aligned} \tag{5.19}$$

Simplifying Eq. 5.4.2 yields to:

$$N_{TT}^{\text{fakes (FF)}} = \frac{f(1-r)}{(1-f)} \frac{2r - fr - f}{1-f} N_{RR} + rf(N_{RF} + N_{FR}) + f^2 N_{FF} \tag{5.20}$$

from which it is clear that the last three terms correspond exactly to the true fake background contribution in Eq. 5.13. The only difference is the contribution from sources with two real leptons, which is wrong as lepton pairs with two real leptons should not contribute to the fake background. This can be fixed using simulation to estimate the number of real leptons (N_{RR}) in all the strictly loose regions ($N_{TL'}$, $N_{L'T}$, and $N_{L'L'}$) and subtracting them, as shown in Eq. 5.21. The final FF formula used in the analysis is:

$$N_{TT}^{\text{fakes}} = (F(N_{TL'} + N_{L'T}) - F^2 N_{L'L'})_{\text{data}} - (F(N_{TL'} + N_{L'T}) - F^2 N_{L'L'})_{N_{\text{RR,MC}}}. \tag{5.21}$$

The equation can be further generalized by separating the FF into two different fake factors F_1 and F_2, respectively for the first and the second lepton candidate. Furthermore, since FF is not constant and should be evaluated for each lepton candidate separately, we rewrite Eq. 5.21 with a sum over all

the lepton pairs:

$$N_{TT}^{\text{fakes}} = \left[\sum_{N_{TL'}} F_2 + \sum_{N_{L'T}} F_1 - \sum_{N_{L'L'}} F_1 F_2\right]_{\text{data}} - \left[\sum_{N_{TL'}} F_2 + \sum_{N_{L'T}} F_1 - \sum_{N_{L'L'}} F_1 F_2\right]_{N_{\text{RR,MC}}} . \tag{5.22}$$

To conclude, in the FF calculation real rates do not have to be obtained from the data, but are effectively evaluated using prompt Monte Carlo. It is important to note that the denominator and numerator regions must be mutually exclusive by construction:

- Denominator $\Leftrightarrow$ strictly loose (pass loose criteria and fail tight criteria)
- Numerator $\Leftrightarrow$ tight

The FF is then measured by observing the ratio of numerator to denominator objects in a fake-enriched sample, similarly to Eq. 5.12.

$$F = \frac{f}{1-f} = \frac{N_{\text{tight}}^{\text{fake}}}{N_{\text{strictly loose}}^{\text{fake}}} \tag{5.23}$$

Since the probability to reconstruct a fake lepton as a real lepton depends on the kinematic of the lepton itself, usually both the real (in the MM) and fake rates (both in the MM and in the FF) are parametrized as a function of lepton p_{T}. Kinematic dependence plays an important role when measuring the real and fake rates. It is therefore recommended to perform their measurement in a phase space as similar as possible to the signal region and with similar background composition. As will be shown in Chapter 6, statistics does not always allow to perform a measurement in bins of p_{T} so the FF can be expressed as a single inclusive numerical value. The MM, or the FF with a kinematic parametrization, are powerful techniques which, besides predicting the total estimate of events containing at least one fake lepton, also successfully predict their shape. They are necessary in analysis using shape information like multivariate techniques.
The methods presented here are applied to the analysis presented in Chapters 6 and 7.

5.5 Overlap between fake and charge misidentification estimates

The methods presented in Section 5.3 and 5.4 for charge mis-identification and fake estimation are based on an extrapolation procedure on data. Moreover, fake leptons are electric charge blind, meaning that they have the same

probability to carry a positive or a negative electric charge. Given that it is not possible to completely disentangle these two type of backgrounds in the data, the two estimations are affected by a potential overlap which needs to be taken into account.
This can be understood considering that:

- when applying the FF or the MM to SS lepton pairs we are blind to the real nature of these leptons in data. Whether we select the sidebands used for fake estimation (namely TL, LT and LL) they present a mixture of prompt, charge-flips and fake leptons. For this reason, similarly to the residual prompt subtraction, we also need to subtract charge-flip events. Indeed, the kinematic properties (e.g. isolation) of the charge-flipped leptons are different from the prompt ones, due to bremsstrahlung and energy loss processes;

- in a similar way, when we apply the charge-flip rates to OS events we should only take into account events with prompt leptons. To avoid the overlap, either we select only OS events from MC and apply the weights to them, or we subtract fakes from the OS region before applying the charge-flip rates.

5.6 Description of statistical analysis

Data are usually statistically interpreted using two hypotheses: they can either be consistent with the SM background only expectation or prove to match the background plus signal hypothesis at a certain *confidence level.*

The main ingredients to build an hypothesis test are a likelihood function, encoding the probability distributions for different regions defined in the analysis, fitted simultaneously, and the hypothesis itself. The likelihood function contains several parameters which are usually divided into *parameters of interest* (POI) and *nuisance parameters* (NPs). The POI is the signal strength μ, which we want to extract, and it is treated as a free parameter in the fit. A μ=0 indicates the background only hypothesis while μ=1 represents the signal plus background hypothesis. The uncertainties enter the likelihood function as nuisance parameters. The true values of both the POI and of the NPs are unknown and are estimated by maximizing the likelihood in the fit, returning their *most likely* values based on the observations from data.

In this section the procedure for data statistical interpretation, performed using the statistical tool HistFitter [147], is presented.

The region of the phase space where a particular signal is expected to produce an excess over the SM expectation identifies the *signal region* (SR). It is clear that a reliable background estimation, either in a data-driven way or using simulation, is necessary to ensure that any observed excess is properly understood. Ideally, after assessing the main background affecting the signal region, each analysis should define a *control region* (CR) specifically used to constrain and study that background by comparing its shape and normalization to data. Once established, the model predicting different background contributions in CRs should be tested in additional regions before being applied to SR. For this purpose, we make use of *validation regions* (VR) which are usually topologically close to SR, still with a negligible signal expected. A sketch illustrating how the fitting strategy operates over analysis regions is provided in Fig. 5.8.

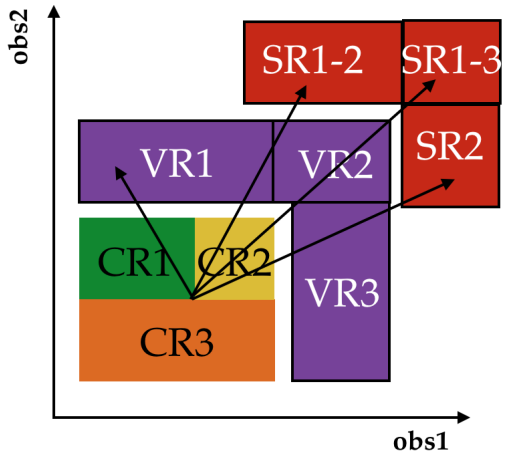

Figure 5.8: Schematic view of a template analysis strategy using multiple control, validation and signal regions. Regions can have single or multiple bins. The extrapolation validity from the CRs to the SRs is previously assessed in the VRs.

Construction of the likelihood function

A *probability density function* (P) is constructed in the fit, containing the POI, the normalization factors for background processes and the NPs. The

likelihood is defined as:

$$\mathcal{L}(\boldsymbol{n}, \boldsymbol{\theta}_0|\mu_{sig}, \boldsymbol{\mu_b}, \boldsymbol{\theta}) = \mathrm{P_{SR}} \times \mathrm{P_{CR}} \times \mathrm{G_{NP}} \tag{5.24}$$

$$= \mathrm{P}\left(n_{\mathrm{SR}}|\mu_{sig} \cdot S(\theta) + \sum_{b}^{bkgs} \mu_b B(\boldsymbol{\theta})\right) \tag{5.25}$$

$$\times \prod_{i \in \mathrm{CR}} \mathrm{P}\left(n_{\mathrm{CR}}|\sum_{b}^{bkgs} \mu_b B(\boldsymbol{\theta})\right) \tag{5.26}$$

$$\times \mathrm{G_{NPs}}(\boldsymbol{\theta}_0|\boldsymbol{\theta}).$$

The first term in Eq. 5.6 describes the poissonian probability to observe n events given the signal plus background hypothesis $\mu_{sig} \cdot S(\boldsymbol{\theta}) + \mu_b \cdot B(\boldsymbol{\theta})$. The number of observed events in the signal region is n_{SR} while $S(\boldsymbol{\theta})$ and $B(\boldsymbol{\theta})$ are the expected signal and background yields, function of the NPs $\boldsymbol{\theta}$. The parameter $\boldsymbol{\mu_b}$ describes the normalization factor for each background and it is constrained using the second term in Eq. 5.6. This latter term is defined similarly to the signal region term, but no reference to signal event appears given that control regions are defined ad hoc to be signal-free. The first two terms in Eq. 5.6 carry an implicit product over the number of bins used to describe the variable entering the fit. Both the signal and the background expected yields depend on nuisance parameters, accounting for the impact of systematic uncertainties on the expected yields. It should be noticed here that not all the NP are common both to CR and SR. When, on the contrary, this is true, nuisance parameters are correlated across the regions.

The third term in Eq. 5.6 describes the parametrization for the nuisance parameters and serves to constrain the value of the *auxiliary measurements* $\boldsymbol{\theta_0}$ to its measured value $\boldsymbol{\theta}$. The function G can be of gaussian or poisson type. Most of the systematic uncertainties are described by gaussian auxiliary measurements, such as luminosity, cross-sections, or experimental systematic uncertainties. Poisson constraints are usually preferred to describe the finite size of the sample used in the analysis. Each systematic uncertainty can either affect the overall normalization of the sample, or its shape, or both. The values of $\boldsymbol{\theta}$ are scaled such that $\boldsymbol{\theta}$ =0 corresponds to the nominal yield expectation, while $\boldsymbol{\theta} = \pm 1$ correspond to the $\pm 1\sigma$ variation of the systematic uncertainty when G is the standard normal distribution.

Hypothesis test

The hypothesis test is performed using the frequentist *profile likelihood ratio* q_μ as test statistic. Given a signal hypothesis with strength μ, the

profile log-likelihood ratio is given by:

$$q_\mu = -2\log\left(\frac{\mathcal{L}(\mu,\hat{\hat{\boldsymbol{\theta}}})}{\mathcal{L}(\hat{\mu},\hat{\boldsymbol{\theta}})}\right) \tag{5.27}$$

where $\hat{\mu}$ and $\hat{\boldsymbol{\theta}}$ maximize the likelihood function and $\hat{\hat{\boldsymbol{\theta}}}$ maximize the likelihood for the specific value of the signal strength μ. The probability value, or *p-value*, assigned to a hypothesis test, is calculated using a distribution of the test statistic $f(q_\mu|\mu,\boldsymbol{\theta})$, which is obtained by throwing multiple pseudo-experiments randomizing the number of observed events and the central values of the auxiliary measurements. According to Wilks' theorem [148] the distribution of $f(q_\mu|\mu,\boldsymbol{\theta})$ is known when the statistics of the data sample is large (also called *asymptotic regime*) and follows a χ^2 distribution with one degree of freedom, independent of the actual values of the auxiliary measurements. This approximation stands from as few as $\mathcal{O}(10)$ data events allowing the use of the asymptotic formula to evaluate the p-value of the hypothesis test. Given that in many cases the total set of auxiliary measurement to consider is large, a most practical solution is adopted: first, a fit of nuisance parameters based on the observed data and the hypothesized μ value is used to set the auxiliary measurement values. This is usually called *profiling* the nuisance parameters on data. Then, pseudo experiments are generated in such a way to maximize the p-value over the auxiliary measurement (*profile construction*). Towards the asymptotic regime, the distribution of $f(q_\mu|\mu,\boldsymbol{\theta})$ becomes independent of the values of the auxiliary measurements used to generate the pseudo experiments and the resulting p-value is robust.

The p-value for a given observation, under the hypothesis μ, is the probability of finding data with an equal or greater incompatibility with the same hypothesis. For an observed value of the test-statistic $q_{\mu,obs}$, the p-value is defined as:

$$p = \int_{q_{\mu,obs}}^{\infty} f(q_\mu|\mu,\boldsymbol{\theta})dq_\mu \tag{5.28}$$

and can be converted into equivalent normal significance Z: by convention a discovery is made when the background-only hypothesis is rejected at 5σ.

To define the confidence level we need to compute both the p-value for the signal plus background hypothesis p_μ and the p-value for the background-only hypothesis p_b. These two quantities are computed using the same test statistic q_μ, which compares the hypothesis of a signal being produced at a rate μ or at a rate smaller than μ. The final confidence level CL_s is computed as the ratio:

$$\mathrm{CL}_s = \frac{p_\mu}{1-p_b}. \tag{5.29}$$

and, if below 5%, allows to exclude a hypothesis at 95% CL.

The uncertainty on the fitted $\hat{\mu}$ depends on the uncertainty Δ_θ on the nuisance parameters. The impact of a single NP θ on $\hat{\mu}$, named $\Delta_{\hat{\mu}}$ is evaluated as:

$$\Delta_{\hat{\mu}} = \hat{\mu}(\hat{\theta} \pm \Delta_\theta) - \hat{\mu}(\hat{\theta}). \tag{5.30}$$

Constraints of the nuisance parameters correspond to such cases when the post-fit Δ_θ is smaller than the pre-fit value and *pulls* to those cases when θ is changed with respect to the pre-fit value. Constraints only affect the post-fit values of the systematic uncertainties while pulls modify the predicted rates of signal and background process and affect their shape.

Extrapolation of background normalization and error propagation

The normalization parameters for background μ_b are estimated, as said, in control regions and extrapolated to validation or signal regions. A unique pdf is constructed using all the nuisance parameters shared between CRs and SRs. This allows to use information from each signal and background component, as well as systematic uncertainties, coherently. The extrapolation proceeds by subsequent steps: the data/MC fit in the CRs is used to extract background normalization further applied to all regions as *normalization factors*. Once the dominant backgrounds are normalized in CRs, the corresponding modifications to the pdf can be extrapolated to the VRs/SRs, even though the VRs/SRs are not used as a constraint in the fit. Based on the normalization factors, the background estimates in the SRs (N_p(SR,est.)) are computed as:

$$\begin{aligned} N_p(\mathrm{SR(VR)}, \mathrm{est.}) &= N_p(\mathrm{CR}, \mathrm{obs.}) \times \left[\frac{\mathrm{MC}_p(\mathrm{SR(VR)}, \mathrm{raw})}{\mathrm{MC}_p(\mathrm{CR}, \mathrm{raw})}\right] \\ &= \mu_p \times \mathrm{MC}_p(\mathrm{SR(VR)}, \mathrm{raw}), \end{aligned} \tag{5.31}$$

where p indicates the physical process, N_p(CR,obs.) the observed number of data events in the CR for the process, and MC_p(SR,raw) and MC_p(CR,raw) the unnormalized estimates of process p obtained from simulation. In this way, the systematic uncertainties on the predicted background processes get canceled in the extrapolation. The total uncertainty on the number of background events in SR is then a combination of the statistical uncertainties in the CRs and the residual systematic uncertainties of the extrapolation.
The uncertainty on the extrapolated background prediction $\sigma_{b,tot}$ is propagated in the following way:

$$\sigma^2_{b,tot} = \sum_i^n \left(\frac{\partial b}{\partial \eta_i}\right)^2 \sigma^2_{\eta_i} + \sum_i^n \sum_{j \neq i}^n \rho_{ij} \left(\frac{\partial b}{\partial \eta_i}\right) \left(\frac{\partial b}{\partial \eta_j}\right) \sigma_{\eta_i} \sigma_{\eta_j} \tag{5.32}$$

where η_i are the floating parameters in the fit, including the normalization factors and the nuisance parameters, ρ_{ij} is the correlation coefficient between the parameter η_i and η_j and σ_{η_i} the standard deviation of η_i.
The *before-fit* correlations are set to zero as well as the errors on the normalization factors of backgrounds, which are unknown prior to the fit.

This chapter, together with Chapter 4, provided a comprehensive overview of the features shared between the $t\bar{t}H$ and $H^{\pm\pm}$ searches. In the following, the two analyses will be presented and the similarities among the analyses techniques will be specifically exploited.

Chapter 6

Search for $t\bar{t}H$ production

The aim of this chapter is the search for $t\bar{t}H$ production in ATLAS. Results are expressed in terms of the $t\bar{t}H$ *signal strength* μ, defined as the ratio between the observed and the SM expected $t\bar{t}H$ cross-section.
The analysis is performed using 2015 and part of 2016 data at $\sqrt{s} = 13$ TeV corresponding to a total integrated luminosity of 13.2 fb^{-1}. This chapter outlines the analysis strategy (Section 6.1) and its final states, the object and event selection (Section 6.2.3), background estimation (Section 6.4), systematic uncertainties and results (Section 6.6).
Here we focus on the final state containing two SS leptons, providing just a brief overview of the other final states, which are eventually combined into the final fit.
The analysis strategy was updated at the end of 2016 to use multivariate techniques and to add new final states. At the end of this chapter, an overview of the analysis performed with the total 2015 + 2016 dataset (corresponding to a total integrated luminosity of $\mathcal{L}$ =36.1 fb^{-1}) is provided.

6.1 Analysis channels

The features and the topology of the $t\bar{t}H$ channel are presented in Sections 2.3 and 2.4, discussing the possible final states arising from both the $t\bar{t}$ pair and the Higgs boson decay modes. This analysis looks into multi-lepton final states, where leptons are divided into "light" ($\ell = e, \mu$) or τ and signal regions are orthogonally defined based on the number of light and τ leptons as follows:

- $2\ell 0\tau_{had}$: exactly two SS leptons and no τ leptons. Given the available statistics, this channel is further divided by flavour into ee, $e\mu$ and $\mu\mu$

events;

- $2\ell 1\tau_{had}$: exactly two SS leptons and one hadronic τ lepton;
- 3ℓ: exactly three leptons;
- 4ℓ: exactly four leptons.

The Higgs signal composition and the signal acceptance (A) multiplied by signal efficiency (ϵ), in the different signal regions (defined in Section 6.3) is presented in Table 6.1. Due to the BR of the $t\bar{t}$ pair and of the Higgs boson, the $2\ell 0\tau_{had}$ provides the highest statistics for this search, followed by the 3ℓ channel. As the $t\bar{t}$ BR in semileptonic final states is around 44% and the Higgs boson decaying to WW^* is 21%, it follows that the majority of signal events belongs to this channel.

Higgs decay mode	4ℓ	3ℓ	$2\ell 1\tau_{had}$	$2\ell 0\tau_{had}$ ee	$2\ell 0\tau_{had}$ $e\mu$	$2\ell 0\tau_{had}$ $\mu\mu$
$H \to WW^*$	72%	74%	46%	76%	77%	79%
$H \to ZZ^*$	9%	4%	2%	2%	3%	3%
$H \to \tau\bar{\tau}$	18%	20%	51%	17%	17%	17%
$H \to b\bar{b}$	$< 1\%$	1%	1%	4%	3%	1%
$H \to \mu\bar{\mu}$	2%	1%	$< 1\%$	$< 1\%$	$< 1\%$	$< 1\%$
$H \to$ other	$< 1\%$	$< 1\%$	$< 1\%$	$< 1\%$	$< 1\%$	$< 1\%$
A$\times\epsilon$ ($\times 10^{-4}$)	0.88	9.2	2.2	14		

Table 6.1: Higgs boson decay composition in each analysis signal region (their event selection is illustrated in Section 6.3) and acceptance times efficiency ($A \times \epsilon$) computed on the $t\bar{t}H$ signal sample (for the features of the MC generator used for $t\bar{t}H$ modeling see Section 6.2.2). The $A \times \epsilon$ includes both Higgs boson and top quark decay branching fractions, detector acceptance, reconstruction and selection efficiency and is computed with respect to the inclusive $t\bar{t}H$ production.

Assuming a 100% lepton reconstruction efficiency and charge identification, only the $H \to WW^*$ channel, with a semileptonic $t\bar{t}$ decay, can produce exactly two SS leptons. In the three and four lepton channels the ∼70% of the events arise from $H \to WW^*$ while the remaining 30% originates from $H \to \tau\tau$ and $H \to ZZ^*$. Finally, channels with hadronic τs are of course mainly sensitive to $H \to \tau\tau$ decays but also to $H \to WW^*$ and $H \to ZZ^*$ where a Z or a W decays into τ.
Regarding jet multiplicity, at generation level, in the $2\ell 0\tau_{had}$ channel the $t\bar{t}H$ final state contains six quarks. In the 3ℓ channel, the $t\bar{t}H$ final state contains four quarks, while in the 4ℓ channel the final state contains zero *light*-quarks in the $H \to WW^*$ case, while two or four in the $H \to ZZ^*$ case. The $2\ell 1\tau_{had}$

channel typically presents four quarks in the final state. As a common feature among all channels, two jets are originated by b-quarks.
The main background to the $2\ell 0\tau_{had}$ channel consists of events containing a non-prompt lepton, mainly originating from $t\bar{t}$ and Z+jets production, or events with a prompt lepton with mis-identified charge. These type of events represent a *reducible* background, while events with exactly the same signature of the signal, such as $t\bar{t}Z$, $t\bar{t}W$, $W^{\pm}Z$, ZZ and $W^{\pm}W^{\pm}$ in association with jets, are called *irreducible* background.

6.2 Data and simulated samples

6.2.1 Data

The data used in this analysis are collected during 2015 and 2016 data-taking periods at $\sqrt{s}$ = 13 TeV with the 25 ns bunch spacing configuration. For the overall 2015 and 2016 data taking, the ratio between recorded and delivered luminosity is ∼93%. The total integrated recorded luminosity collected by the ATLAS detector and satisfying the Good Run List (GRL) requirements, ensuring good data taking conditions of the detectors, is $\int \mathcal{L}dt$ = 13.2 fb^{-1}: 3.2 fb^{-1} from 2015 (periods D-J5) and 10 fb^{-1} from 2016 (periods A-E). The analysis is performed using the `HIGG8D1` ATLAS derivations (see Sec. 5.2).

Periods	$\int \mathcal{L}dt$ (fb^{-1})	Triggers (electrons)	Trigger (muons)

2015	3.2	`HLT_e24_lhmedium_L1EM20VH`
		`HLT_e60_lhmedium`
		`HLTe120_lhloose`
			`HLT_mu20_iloose_L1MU15`
			`HLT_mu50`

2016	10	`HLT_e24_lhtight_nod0_ivarloose`
		`HLT_e60_lhmedium_nod0`
		`HLTe140_lhloose_nod0`
			`HLT_mu24_ivarmedium`
			`HLT_mu50`

Table 6.2: Overview of the single lepton trigger menu used to select interesting events in all the $t\bar{t}H$ channels (see Sections 4.1 and 4.2 for information about the trigger online selections).

Given that all the signal regions are defined by the presence of at least two charged leptons in the final state, data are collected using single electron or single muon triggers. These triggers require at least one lepton to be identified at the first level trigger (L1) and reconstructed at the HLT. The instantaneous luminosity delivered to the ATLAS detector had a peak value of 5×10^{33} cm^{-2}s^{-1} in 2015 and of 13.8×10^{33} cm^{-2}s^{-1} in 2016. For this

reason, the trigger menu changed between the two data taking periods and some of the trigger items, active and not prescaled in 2015, were prescaled in 2016. Slightly higher transverse momentum thresholds were applied in 2016 to single lepton triggers, as shown in Table 6.2 which summarizes the set of triggers used for the two data-taking periods. Moreover, isolation and quality criteria (see Sections 4.1 and 4.2) were also tightened for lower p_{T} threshold triggers. The lower momentum electron trigger for 2016 changed `lhmedium` to `lhtight` quality requirement and an `ivarloose` isolation requirement was added. Regarding muons, the isolation on the lower momentum trigger was also tighten from `iloose` to `ivarmedium`. The trigger choice for 2016 was motivated by a dedicated study to assess the loss of sensitivity related to the higher p_{T} thresholds. Alternative trigger items, such as dilepton triggers, are tested against single lepton triggers. Dilepton triggers indeed have significantly lower online p_{T} thresholds but usually provide lower acceptance compared to single lepton triggers, as will be shown in the following.
Two sets of tests are performed to select the trigger menu for the 2016 data taking:

- a first study to evaluate which single lepton trigger provided the highest acceptance;
- a second MC based study to compare the sensitivity by using single or dilepton triggers.

Choice of single lepton trigger item

The available lowest p_{T} and unprescaled single lepton triggers for those periods, both for electrons and muons, are reported in Table 6.3 while dilepton triggers are reported in Table 6.4. Trigger isolation working points correspond to the following set of cuts, performed at the on-line level:

- `iloose`: $p_{\mathrm{T}}^{\mathrm{cone20}}/p_{\mathrm{T}} < 0.12$;
- `ivarloose`: $p_{\mathrm{T}}^{\mathrm{varcone30}}/p_{\mathrm{T}} < 0.16$;
- `imedium`: $p_{\mathrm{T}}^{\mathrm{cone30}}/p_{\mathrm{T}} < 0.06$;
- `ivarmedium`: $p_{\mathrm{T}}^{\mathrm{varcone30}}/p_{\mathrm{T}}<0.07$.

The online isolation implemented by `ivarmedium` is more similar to the offline `FixedCutTightTrackOnly` isolation requirement on muon and indeed would provide the optimal trigger choice. The `HLT_mu24_iloose` single muon trigger, unprescaled in period A was prescaled in period B.

Periods	e	μ
	single lepton triggers	
A	HLT_e24_lhtight_nod0_ivarloose HLT_e60_lhmedium_nod0 HLT_e140_lhloose_nod0	HLT_mu24_i(var)loose HLT_mu24_i(var)medium HLT_mu50
B	HLT_e24_lhtight_nod0_ivarloose HLT_e60_lhmedium_nod0 HLT_e140_lhloose_nod0	HLT_mu24_i(var)medium HLT_mu50

Table 6.3: Overview of the single lepton trigger menu available in period A and B in 2016.

Periods	ee	$\mu\mu$	$e\mu$
	dilepton lepton triggers		
A	HLT_2e15_lhvloose_nod0_L12EM13VH	HLT_mu20_mu8noL1 HLT_2mu10 HLT_2mu14	HLT_e17_lhloose_nod0_mu14 HLT_e24_lhmedium_nod0_L1EM20VHI_mu8noL1 HLT_e7_lhmedium_nod0_mu24
B	HLT_2e15_lhvloose_nod0_L12EM13VH	HLT_mu20_mu8noL1 HLT_2mu14	HLT_e17_lhloose_nod0_mu14 HLT_e24_lhmedium_nod0_L1EM20VHI_mu8noL1 HLT_e7_lhmedium_nod0_mu24

Table 6.4: Overview of the dilepton lepton trigger menu available for period A and B in 2016.

First, the acceptances of HLT_mu24_iloose, HLT_mu24_ivarloose, HLT_mu24_imedium and HLT_mu24_ivarmedium are compared evaluating event yields from $t\bar{t}H$ and $t\bar{t}$ MC samples in the six signal regions (as defined in Section 6.3). Different trigger combinations resulted in the same signal $A \times \epsilon$ and this was true for all the signal regions, proving a negligible difference between the considered low-p_{T} single muon triggers. Given that no event count difference was observed on either signal or background simulated events we decided to asses the trigger rate difference on the first two periods of the 2016 data taking (period A and period B). The first test is performed on period A data, with a total of 1.26036×10^7 events.

Tables 6.5 and 6.6 show the trigger acceptance using different muon single lepton trigger logical OR combinations. In combination with HLT_mu50, the higher rate fraction is provided by the HLT_mu24_ivarloose trigger, followed by HLT_mu24_iloose ($\sim$ -1.7%), HLT_mu24_ivarmedium ($\sim$ -9.5%) and HLT_mu24_imedium ($\sim$ -10.7%). Considering that i(var)loose triggers were prescaled from period B on and that the i(var)medium trigger items result in an overall $\sim$10% rate decrease, it was decided to select events in the analysis

Trigger combination	HLT_mu24_iloose OR HLT_mu50	HLT_mu24_ivarloose OR HLT_mu50
Data events selected (period A)	3248500	3192510
Fraction of selected events	(25.77 ± 0.01)%	(25.33 ± 0.01)%

Table 6.5: Comparison between trigger acceptance using the logical OR combination of lower p_{T} muon triggers (HLT_mu24_iloose and HLT_mu24_ivarloose) and higher p_{T} trigger HLT_mu50 over a total of 1.26036×10^7 events.

Trigger combination	HLT_mu24_imedium OR HLT_mu50	HLT_mu24_ivarmedium OR HLT_mu50
Data events selected (period A)	2900890	2937530
Fraction of selected events	(23.02 ± 0.01)%	(23.31 ± 0.01)%

Table 6.6: Comparison between trigger acceptance using the logical OR combination of lower p_{T} muon triggers (HLT_mu24_imedium and HLT_mu24_ivarmedium) and higher p_{T} trigger HLT_mu50 over a total of 1.26036×10^7 events.

Trigger	HLT_mu24_ivarmedium	HLT_mu24_imedium
Data events selected (period B)	868586	838032
Fraction of selected events	(17.63 ± 0.01)%	(17.01 ± 0.01)%

Table 6.7: Comparison between trigger acceptance over a period B run containing 4925516 total events for the HLT_mu24_ivarmedium and HLT_mu24_imedium triggers. The number of events selected by HLT_mu24_ivarmedium but not by HLT_mu24_imedium is 30554. The logic AND between the two triggers gives 838032 events.

using the latter. Moreover, the HLT_mu24_ivarmedium trigger provides a slightly higher acceptance with respect to HLT_mu24_imedium.

A similar test was performed on a period B run (i.e. run 300863), as reported in Table 6.7, also showing higher acceptance for HLT_mu24_ivarmedium. Given the very slight difference (∼3%) between the performance of the two trigger isolations and since the ATLAS trigger performance group provided *trigger scale factors* for the HLT_mu24_ivarmedium, this trigger was considered to be optimal for the 2016 data taking, combined with HLT_mu50.

Single versus dilepton trigger acceptance

To assess the acceptance difference by using single, dilepton or a combination of both, a MC based study was performed. The study counts the number of events in the two lepton signal regions (i.e. $2\ell 0\tau_{had}$ and $2\ell 1\tau_{had}$) for $t\bar{t}H$ and the major background, namely $t\bar{t}$. Although we are mainly interested in signal acceptance, $t\bar{t}$ background yields are reported to evaluate the impact of the trigger choice on background acceptance and, as a consequence, on significance. Tables 6.8 and 6.9 show, for the $2\ell 0\tau_{had}$ and $2\ell 1\tau_{had}$ signal regions respectively, a comparison between trigger combination acceptances. The two lepton signal regions are chosen for this test, being the most sensitive to the difference between single or dilepton triggers. In the $2\ell 0\tau_{had}$ channel, the higher significance is obtained when using the logical OR between single and dilepton triggers (which results in a ∼2.5% higher significance and ∼10% acceptance with respect to single triggers only).
For the $2\ell 1\tau_{had}$ channel, moving from single to dilepton triggers results in a ∼9% decrease in signal acceptance and a ∼38% for the $t\bar{t}$ background.

$2\ell 0\tau_{had}$	Single lepton	Dilepton	Combination
$t\bar{t}H$ Events	7.20 ± 0.64	6.56 ± 0.62	7.80 ± 0.67
$t\bar{t}$ Events	20.15 ± 4.34	19.22 ± 4.31	22.52 ± 4.52
$S/\sqrt{S+B}$	1.38 ± 0.34	1.29 ± 0.34	1.42 ± 0.33

Table 6.8: Comparison between trigger acceptance using single, dilepton or the logical OR combination of single and dilepton triggers in the $2\ell 0\tau_{had}$ signal region. Event yields for signal and $t\bar{t}$ backgrounds are provided as well as significance comparisons. The quoted uncertainties are statistical only on the samples normalized to $\mathcal{L}$= 10 fb^{-1}.

$2\ell 1\tau_{had}$	Single lepton	Dilepton	Combination
$t\bar{t}H$ Events	1.08 ± 0.21	0.99 ± 0.19	1.23 ± 0.22
$t\bar{t}$ Events	2.61 ± 1.41	1.62 ± 1.04	2.68 ± 1.41
$S/\sqrt{S+B}$	0.56 ± 0.34	0.62 ± 0.38	0.62 ± 0.35

Table 6.9: Comparison between trigger acceptance using single, dilepton or the logical OR combination of single and dilepton triggers in the $2\ell 1\tau_{had}$ signal region. Event yields for signal and $t\bar{t}$ backgrounds are provided as well as significance comparisons. The quoted uncertainties are statistical only on the samples normalized to $\mathcal{L}$= 10 fb^{-1}.

The improvement using the logic OR of single and dilepton triggers correspond to a $\sim$ 10% and $\sim$15% increase of $t\bar{t}H$ acceptance in the $2\ell 0\tau_{had}$ and $2\ell 1\tau_{had}$ channels respectively. However, given the trigger scale factors computation for the combined configuration is more complicated, we decided to use single lepton triggers.

6.2.2 Monte Carlo samples

The MC generators used in this analysis are listed in Table 6.10.

Physics Process	Event Generator	Parton Shower	PDF set	Tuning	σ (pb)
$t\bar{t}H$	MG5_aMC	Pythia 8	NNPDF 3.0 NLO / NNPDF 2.3 LO	A14	0.509
$tHqb$	MG5_aMC	Pythia 8	CT10 /NNPDF 2.3 LO	A14	0.932
tHW	MG5_aMC	Herwig++	CT10/CTEQ6L1	UE-EE-5	0.241
$t\bar{t}W$	MG5_aMC	Pythia 8	NNPDF 3.0 NLO/2.3 LO	A14	0.566
$t\bar{t}(Z/\gamma^*)$	MG5_aMC	Pythia 8	NNPDF 3.0 NLO/2.3 LO	A14	0.760
$t(Z/\gamma^*)$	MG5_aMC	Pythia 6	CTEQ6L1	Perugia2012	0.250
$tW(Z/\gamma^*)$	MG5_aMC	Pythia 8	NNPDF 2.3 LO	A14	0.016
$t\bar{t}t\bar{t}$	MG5_aMC	Pythia 8	NNPDF 2.3 LO	A14	0.009
$t\bar{t}W^+W^-$	MG5_aMC	Pythia 8	NNPDF 2.3 LO	A14	0.009
$t\bar{t}$	Powheg-Box v2	Pythia 6	CT10/CTEQ6L1	Perugia2012	831
s-, t-channel,	Powheg-Box v2	Pythia 6	CT10/CTEQ6L1	Perugia2012	74
Wt single top					72
VV	Sherpa 2.1.1	Sherpa	CT10	Sherpa default	115
$qqVV$	Sherpa 2.1.1	Sherpa	CT10	Sherpa default	0.934
VVV	Sherpa 2.1.1	Sherpa	CT10	Sherpa default	0.015
$Z \to \ell^+\ell^-$	Sherpa 2.2	Sherpa	NNPDF 3.0 NLO	Sherpa default	6318

Table 6.10: Simulated signal and background event samples used in the search for $t\bar{t}H$ production: the corresponding ME generator, PS, PDF set used for the matrix element, set of tuned parameters and cross-section are shown for each sample. Where two set of PDFs are shown, the first one is used in the ME while the second in the PS calculation. All samples include leading-logarithm photon emission, either modeled by the parton shower generator or by PHOTOS [149].

- **Signal**: the $t\bar{t}H$ signal sample was generated at NLO in QCD with aMC@NLO interfaced with Pythia 8. To have a reasonable MC statistics for each signal channel, specific filters are applied between the generator level and the full simulation on the topology of the $t\bar{t}$ decay: all-hadronic, semi-leptonic and di-lepton decays.
- $\boldsymbol{t\bar{t}+V}$: the $t\bar{t}Z$ and $t\bar{t}W$ processes are simulated at the same QCD accuracy level with aMC@NLO and Pythia 8. The $t\bar{t}Z$ ($Z \to \ell\ell, \ell = e, \mu$ or τ) process was simulated with both an on and off-shell Z boson and γ^* contributions with $m(\ell\ell) > 5$ GeV.

- **$t\bar{t}$ and top**: are simulated using POWHEG-BOX v2.0 with PYTHIA 6 with the same PS, PDF set and tuning configurations. Given that to enter the signal regions selection, events from $t\bar{t}$ production need to have one prompt lepton, a one-lepton filter is applied in event generation.
- ***VV* and *Z*+jets**: diboson and Z+jets events were generated using SHERPA. To validate background modeling, additional Z+jets samples were produced with MADGRAPH+PYTHIA 8 or POWHEG+PYTHIA 8.

All simulated events went through the same processing, reconstruction algorithm and analysis chain as data. Specific corrections are applied to simulated events to account for object and identification efficiencies, energy scale and resolutions differences in simulation with respect to data.

6.2.3 Object Definition

Object reconstruction algorithms are illustrated in Chapter 4. Here we provide a description of analysis specific selection cuts. Objects, namely electrons, muons, taus and jets, selections are optimized to enhance $t\bar{t}H$ signal significance. To use data-driven techniques for background estimation, for each light lepton a *loose* and a more stringent *tight* selection is needed. Lepton multiplicity, used to categorize the events exclusively in each of the analysis regions, is evaluated on loose leptons. After counting, each signal region further tightens its lepton selection and uses tight leptons as a baseline for the analysis. An event with lepton multiplicity N at loose level but N-1 at tight level will consequently be discarded by all analysis region. This procedure ensures complete orthogonality between channels also in the side-bands used for the data-driven fake estimation, for which the difference between the loose and tight *selection working points* is fundamental. The loose lepton definition is then a compromise between sensitivity loss at the categorization stage and being significantly different from the tight lepton definition, not to spoil the data driven background estimation. Table 6.11 and 6.12 show, respectively, the selection criteria applied for loose and tight electrons and muons definition.

It is worth noting that the main differences in loose/tight electron definition are in the identification and isolation working points, as well as the cut on the significance on the impact parameter $|d_0|/\sigma_{d_0}$. In the muon case, tighter isolation requirements and $|d_0|/\sigma_{d_0}$ cuts, as in the electron case, are applied.

Requirement	Signal electrons (tight)	Background electrons (loose)
Identification	`LHTight`	`LHLooseAndBLayer`
Isolation	`FixedCutTight`	`Loose`
p_{T}	$p_{\mathrm{T}} > 10$ GeV	$p_{\mathrm{T}} > 10$ GeV
η	$\lvert\eta\rvert$ <2.47 and veto $1.37 < \lvert\eta\rvert < 2.47$	$\lvert\eta\rvert$ <2.47 and veto $1.37 < \lvert\eta\rvert < 2.47$
$\lvert d_0\rvert/\sigma_{d_0}$	$\lvert d_0\rvert/\sigma_{d_0} < 5$	$\lvert d_0\rvert/\sigma_{d_0} < 5$
$\lvert z_0 \sin\theta\rvert$	$\lvert z_0 \sin\theta\rvert < 0.5$ mm	$\lvert z_0 \sin\theta\rvert$<0.5 mm

Table 6.11: Object definition requirements for definition of tight (left) and loose (right) electrons.

Requirement	Signal muons (tight)	Background muons (loose)
Identification	`Loose`	`Loose`
Isolation	`FixedCutTightTrackOnly`	`Loose`
p_{T}	$p_{\mathrm{T}} > 10$ GeV	$p_{\mathrm{T}} > 10$ GeV
η	$\eta < 2.5$	$\eta < 2.5$
$\lvert d_0\rvert/\sigma_{d_0}$	$\lvert d_0\rvert/\sigma_{d_0} < 3$	$\lvert d_0\rvert/\sigma_{d_0} < 3$
$\lvert z_0 \sin\theta\rvert$	$\lvert z_0 \sin\theta\rvert < 0.5$ mm	$\lvert z_0 \sin\theta\rvert < 0.5$ mm

Table 6.12: Object definition requirements for definition of tight (left) and loose (right) muons.

Hadronic decays of tau leptons are jets reconstructed with the anti-k_t algorithm. They are required to have transverse momentum $p_{\mathrm{T}} > 25$ GeV and $|\eta| < 2.5$, removing the crack region $1.37 < |\eta| < 2.47$. Hadronic τs (see Chapter 4), are defined using a `Medium` working point of a BDT, trained separately for 1 and 3 tracks hadronic decays. Hadronic τs are also required to have charge ± 1 and either one or three prongs.

Jets are reconstructed with an anti-k_t radius of 0.4 and they are accepted if $p_{\mathrm{T}} > 25$ GeV and $|\eta| < 2.5$. *Bad jets*, originated from beam background or from noisy calorimetric cells, are removed. To suppress the contribution from pile-up jets, the JVT cut is applied to jets belonging to the fiducial region $p_{\mathrm{T}} < 60$ GeV and $|\eta| < 2.4$. Jets originating from b-hadron decays are identified by MV2c10 algorithm using the 70% efficiency working point (see Section 4.4).

On top of the baseline[1] selection, an overlap removal procedure (see Sec-

[1] Here the *baseline* selection for leptons means the loose definition.

tion 4.6) is applied to further clean overlapping objects in close-by regions of the detector and summarized in Table 6.13.

Keep	Remove	ΔR cone size or tracks
electron	τ	0.2
muon	τ	0.2
electron	CT muon	sharing an ID track (no muon spectrometer track)
muon	electron	sharing an ID track
electron	jet	0.2
jet	electron	0.4
muon	jet	(0.2 or "ghost-matched" to muon) and (jet tracks $\leq$2)
jet	muon	0.4
τ	jet	0.2

Table 6.13: Summary of the overlap removal steps performed on electrons, muons, τ leptons and jets.

6.3 Analysis signal regions

Each event must have at least two leptons firing one of the single lepton triggers. Given the lowest transverse momentum threshold applied at the trigger level, each light lepton is required to have a $p_{\mathrm{T}} > 25$ GeV in all the channels. The slightly higher momentum selection performed offline with respect to the actual trigger threshold ensures that the trigger efficiency has already reached the *plateau* level.

$2\ell 0\tau_{had}$ channel

Two SS leptons with transverse momentum $p_{\mathrm{T}} > 25$ GeV are selected. The $|\eta|$ cut on electrons is further reduced to 1.37 to suppress the contribution from the charge mis-identification brackground (as shown in Section 6.4.2). There must be no τ lepton in the event and the jet multiplicity has to be $\geq$ 5 jets, with at least one b-tagged jet.
Optimization procedures are carried out to select the optimal selection working points for this channel, such as lepton p_{T} and isolation. The figure of merit chosen for the optimization is the significance, as defined in [150]:

$$Z = \sqrt{2\left[(s+b)\ln\left(1+\frac{s}{b}\right)-s\right]} \tag{6.1}$$

where s is the number of signal events and b the total backgrounds (i.e. mainly $t\bar{t}$, $t\bar{t}W$ and $t\bar{t}Z$). To account for systematic uncertainty Δb on the background yield, b is replaced with $b + \Delta b$. Conservative systematic uncertainties are assigned to the following backgrounds: 20% for $t\bar{t}V$, 30% for $t\bar{t}$ and 50% for diboson. The Z expressed in Eq. 6.1 provides a better alternative to the widely used $Z \sim s/\sqrt{b}$ in the regime $s \ll b$, as in our case. Given that the main background in this channel arises from mis-reconstructed objects mostly originating from $t\bar{t}$ events, object definitions with similar significance but reducing more $t\bar{t}$ background were preferred. Optimization scans over relative isolation variables (see Table 4.1 and 4.2) $E_T^{\text{cone0.2}}/p_{\text{T}}$ and $p_{\text{T}}^{\text{varcone0.2}}/p_{\text{T}}$ for the ee channel and $p_{\text{T}}^{\text{varcone0.3}}/p_{\text{T}}$ for the $\mu\mu$ channel are performed.

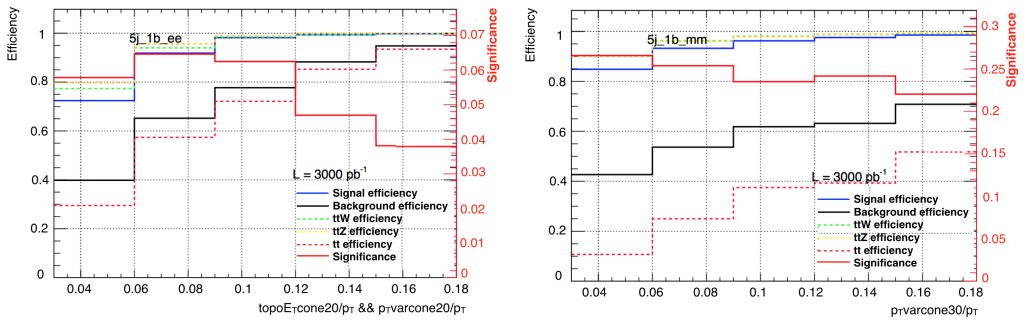

(a) (b)

Figure 6.1: Scan over the relative lepton isolation variables $E_T^{\text{cone0.2}}/p_{\text{T}}$ combined with $p_{\text{T}}^{\text{varcone0.2}}/p_{\text{T}}$ in the ee (a) and $p_{\text{T}}^{\text{varcone0.3}}/p_{\text{T}}$ in the $\mu\mu$ (b) channel. Signal efficiency (blue), background efficiency (black), significance (red), as well as $t\bar{t}W$(green), $t\bar{t}Z$ (yellow) and $t\bar{t}$ (pink) efficiencies are shown.

Figure 6.1 shows the scan over the isolation variable for both electrons and muons. It is clear that the optimal cut (highest significance and good background rejection) for the electron channel would be set at $E_T^{\text{cone0.2}}/p_{\text{T}}$ <0.06 and $p_{\text{T}}^{\text{varcone0.2}}/p_{\text{T}}$ <0.06, corresponding to the `FixedCutTight` (see 4.1) electron isolation working point. For the muon channel, the best cut yields to $p_{\text{T}}^{\text{varcone0.3}}/p_{\text{T}}$ <0.03, which however does not fit to any of the recommended supported isolation. Consequently, in the muon channel also the cut is set at $p_{\text{T}}^{\text{varcone0.3}}/p_{\text{T}}$ <0.06, corresponding to the `FixedCutTightTrackOnly` (see 4.2) isolation working point.
A similar study is performed on the p_{T} of the subleading lepton, after requiring the leading lepton $p_{\text{T}} > 25$ GeV, due to the trigger p_{T} threshold needed for the matching requirement. A 20 GeV threshold on the subleading lepton

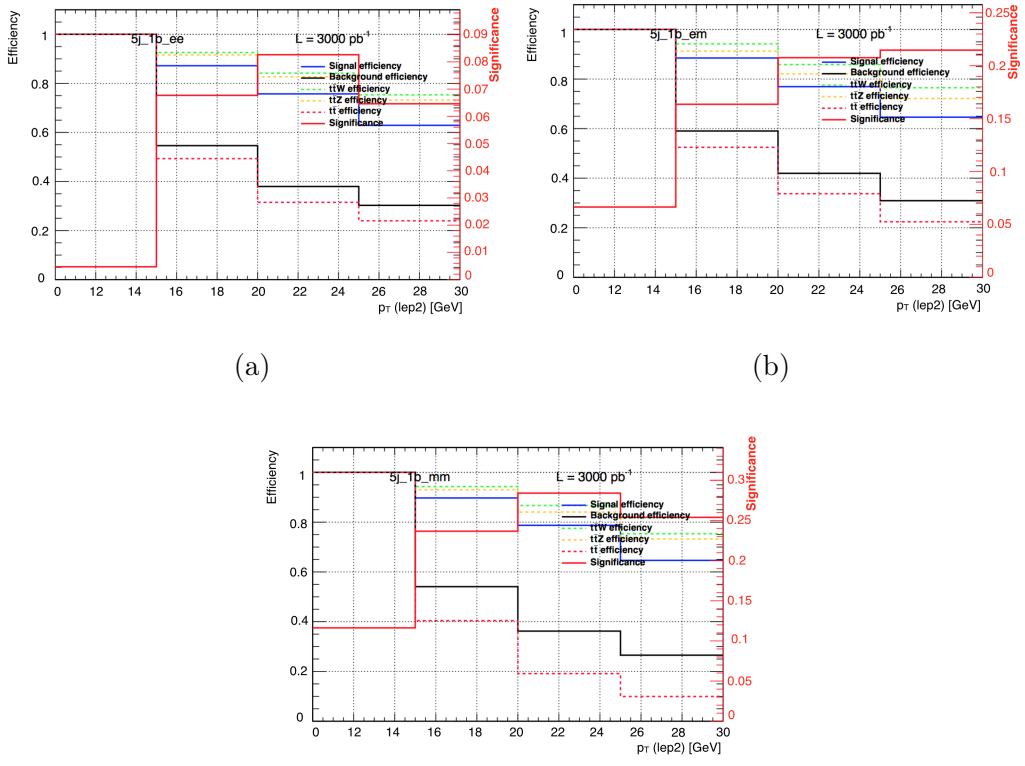

(a) (b)

(c)

Figure 6.2: Scan over the subleading lepton p_{T} ranges after fixing the leading lepton p_{T} at 25 GeV in the ee (a), $e\mu$ (b) and $\mu\mu$ (c) channels. Signal efficiency (blue), background efficiency (black), significance (red), as well as $t\bar{t}W$(green), $t\bar{t}Z$ (yellow) and $t\bar{t}$ (pink) efficiencies are reported.

looks favoured both in the ee and $\mu\mu$ channels while 25 GeV leading leptons maximize the significance in the $e\mu$ channel, as shown in Fig. 6.2. However, considering that simulation underestimates fakes and that the 25 GeV p_{T} cut leads to a higher $t\bar{t}$ rejection, it was decided to require both leptons to have $p_{\mathrm{T}} > 25$ GeV in the signal region.

Similar optimization procedures are carried out for the other channels and the results led to signal region definitions that are provided in the following sections.

$2\ell 1\tau_{had}$ channel

The selection is similar to the one presented for the $2\ell 0\tau_{had}$ channel, but there is no requirement on the electron $|\eta|$. However, to remove events with mis-reconstructed charge from $Z \to e^+e^-$ an invariant mass cut on the $e^{\pm}e^{\pm}$ channel is applied: $|m(e^{\pm}e^{\pm}) - 91.2|$ GeV > 10 GeV. The leading lepton is required to have p_{T} >25 GeV while for the subleading the cut is relaxed to p_{T} > 15 GeV. Additionally, one hadronic τ is required in the event. Regarding jet multiplicity, the event must contain at least 4 jets one of which b-tagged.

3ℓ channel

In this channel, the total charge from leptons must be $\pm$ 1. The *opposite-charge* lepton with respect to other two in the set is designated as *lepton 0*. Between the remaining two, the closest one in $\Delta R(\ell, \ell_0)$ to ℓ_0 is called *lepton 1*, so that the remaining is called *lepton 2*. The main background affecting this channel is $t\bar{t}V$ and $t\bar{t}$ production. Fake leptons from these processes will enter the signal region in different ways. A $t\bar{t}W$ event with a dileptonic decay of the $t\bar{t}$ system and a hadronic W decay gives two OS leptons and one fake lepton which has a 50% probability to have positive or negative sign. A $t\bar{t}Z$ event either with a $t\bar{t}$ dileptonic decay and a Z hadronic decay, or with a $t\bar{t}$ all-hadronic and a leptonic Z decay, also produces two OS leptons and an additional fake object. Events from $t\bar{t}$ with dileptonic decay can also enter the 3ℓ final state with an additional mis-reconstructed object. Given that all these SM processes produce events with two OS leptons and one additional *any sign* object, if we take as lepton 0 the one with OS with respect to the other two, that lepton will always be a prompt lepton. Leptons 1 and 2 are required to be tight and have $p_{\mathrm{T}} > 20$ GeV. As said, lepton 0 will rarely be a non-prompt lepton, thus no additional requirements on it are imposed. To reject events from $t\bar{t}Z$, all same-flavour OS pairs are required to satisfy $|m(\ell^+\ell^-) - 91.2| > 10$ GeV. To remove events from low mass resonances, an additional invariant mass requirement on all same-flavour OS pairs is set to $|m(\ell^+\ell^-)| > 12$ GeV. Finally, to remove additional backgrounds with Z decays to $Z \to \ell\ell\gamma^* \to \ell\ell\ell'(\ell')$ where the fourth very low momentum lepton is not reconstructed, the three-lepton invariant mass has to satisfy $|m(3\ell) - 91.2| > 10$ GeV. There must be three jets in the event of which at least two b-tagged, or at least four jets of which at least one b-tagged. No additional requirement is made on τ leptons and all jets also reconstructed as hadronic taus are treated as other analysis jet.

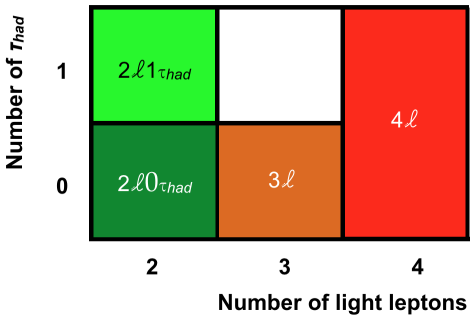

Figure 6.3: Schematic representation of the $t\bar{t}H$ signal regions divided by light lepton and τ lepton multiplicities.

4ℓ channel

This is a very clean channel, therefore the lepton isolation is loosened to `Gradient`. The lepton total charge is required to be zero. To reject events from $t\bar{t}Z$ and ZZ backgrounds, events must satisfy $|m(\ell^+\ell^-) - 91.2| > 10$ GeV and, for the same reasons as in the 3ℓ channel, all same flavour OS pairs must satisfy $m(\ell^+\ell^-) > 12$ GeV. The four-lepton invariant mass is required to be 100 GeV $< m(4\ell) <$ 350 GeV to reduce contamination from $Z \to 4\ell$ at low mass and $t\bar{t}Z$ at high mass. To reduce possible contaminations from other Higgs boson production processes and to avoid overlap with other Higgs analyses, a Higgs boson veto $|m(4\ell) - 125| > 5$ GeV is applied. There must be at least two jets in the event of which at least one b-tagged. Hadronic decays of τ leptons are treated as any other jet.

A schematic view of the signal regions as a function of the light lepton and τ lepton multiplicities is provided in Fig. 6.3.

From now on, we will focus on the features of the $2\ell 0\tau_{had}$ channel.

6.4 Background estimation in the $2\ell 0\tau_{had}$ channel

The main irreducible backgrounds originate from $t\bar{t}V$ (where $V = W, Z$) and diboson production and are estimated through simulations and validated in dedicated control regions. Selections performed on reconstructed objects are meant to provide a sample as free as possible from reducible backgrounds, such as electron with mis-reconstructed charge or fake leptons. In the $2\ell 0\tau_{had}$ channel, reducible backgrounds are estimated using specific data-driven techniques, discussed in Chapter 4.

6.4.1 Prompt SM backgrounds estimation

The main source of prompt leptons in the $2\ell 0\tau_{had}$ channel arises from $t\bar{t}W$ and diboson production which, as shown in Fig. 6.4 can lead to a final state very similar to the signal one.

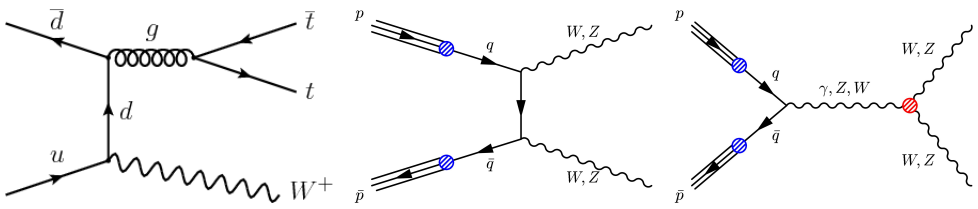

(a) (b) (c)

Figure 6.4: Feynman diagrams for $t\bar{t}W$ (a) and diboson (b), (c) LO production at the LHC.

To mimic the $t\bar{t}H$ signal topology, $t\bar{t}W$ channel must have a leptonic decay of the $W^{\pm}$ boson and a semi-leptonic decay of the $t\bar{t}$ pair. Since the jet multiplicity of the $t\bar{t}W$ process is lower than the one from the $t\bar{t}H$ decay, the $N_{jets} \geq 5$ requirement helps to reduce the $t\bar{t}W$ contamination. In a similar way, $t\bar{t}Z$ production with a lost lepton from the Z decay and a semi-leptonic $t\bar{t}$ decay features a similar state as the signal region. Regarding diboson production with associated heavy flavour jets, WZ+jets events can contribute to the $2\ell 0\tau_{had}$ signal region with a leptonic decay of both the W and the Z bosons, where a lepton from Z is lost due to the selection cuts or detector acceptance; $ZZ(\rightarrow \ell\ell\ell\ell)$+jets events with two lost leptons in the final state can also contribute to the $2\ell 0\tau_{had}$ signal region.
A dedicated validation region is defined to assess the modeling of the $t\bar{t}W$ background. To provide a sample as pure as possible in $t\bar{t}W$, events are required to have two SS leptons and at least four jets. The region also requires the presence of at least two b-tagged jets. To suppress charge mis-identification backgrounds, events with two electrons must satisfy $m_{ee} < 75$ GeV or $m_{ee} > 105$ GeV and $E_{\mathrm{T}}^{\mathrm{miss}} > 50$ GeV. Since high-energetic jets from $t\bar{t}W$ are expected, the scalar sum of jets transverse momenta H_{T} is required to be greater than 220 GeV in the ee and $e\mu$ channels. The definition of the $t\bar{t}W$ validation region is the result of an optimization study aimed to find the best combination of kinematic cuts to better constrain $t\bar{t}W$ events in that region. The $t\bar{t}W$ contribution in the validation region is 22% of the total background, as clear from Fig. 6.5.

Residual contamination from fake leptons and charge mis-identification cannot be completely suppressed. Negligible contribution from $t\bar{t}(Z/\gamma^*)$ is

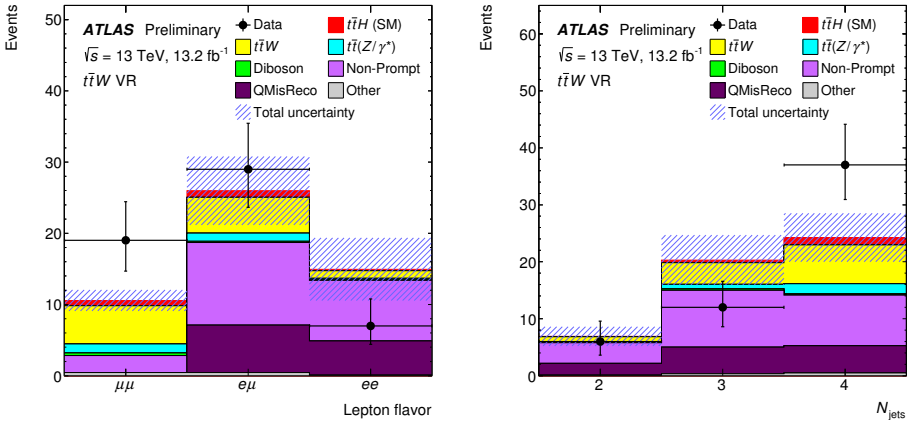

(a) (b)

Figure 6.5: Flavour categories (a) and number of jets (b) in the $t\bar{t}W$ validation region. Rare processes include tZ, $t\bar{t}WW$, tribosons, $t\bar{t}t\bar{t}$ and tH production. The red region corresponds to the $t\bar{t}H$ SM signal.

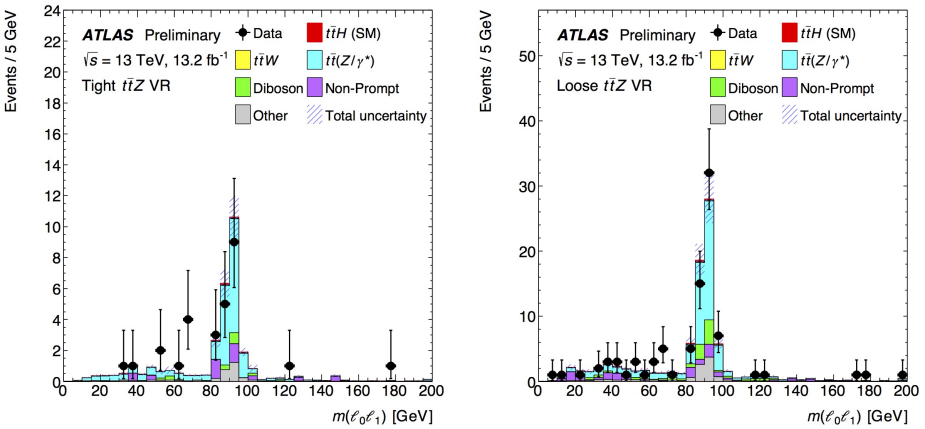

(a) (b)

Figure 6.6: Invariant mass distribution of the two OS leptons (lepton 0 and lepton 1) for the tight (a) and loose (b) $t\bar{t}Z$ validation regions. Rare processes include tZ, $t\bar{t}WW$, tribosons, $t\bar{t}t\bar{t}$ and tH production. The red region corresponds to the $t\bar{t}H$ SM signal.

also visible in the validation region. Considering also the very low statistics, which amounts to ∼50 events, data are consistent with SM prediction, though a slight excess (around 1.5 σ) of events is observed in the $\mu\mu$ channel. The normalization for the $t\bar{t}Z$ background is assessed in a three-lepton valida-

tion region, given the very poor statistics in regions containing two leptons. Besides three leptons, the $t\bar{t}Z$ validation region requires at least one OS same-flavour pair with invariant mass $|m_{\ell\ell} - m_Z| < 10$ GeV. Jet multiplicity can fit multiple combinations: at least four jets two of which b-tagged (*tight* $t\bar{t}Z$), at least four jets one of which b-tagged or at least three jets two of which b-tagged (last two configurations are indicated as *loose* $t\bar{t}Z$ and intended to gain statistics). The $t\bar{t}Z$ purity is around 68% for the tight VR and around 58% in the loose validation region, where a higher component from diboson processes is present, as shown in Fig. 6.6. Also in this case, contribution from fake leptons, diboson, and additional rare backgrounds cannot be completely suppressed. Data agree with MC within the quoted uncertainties.

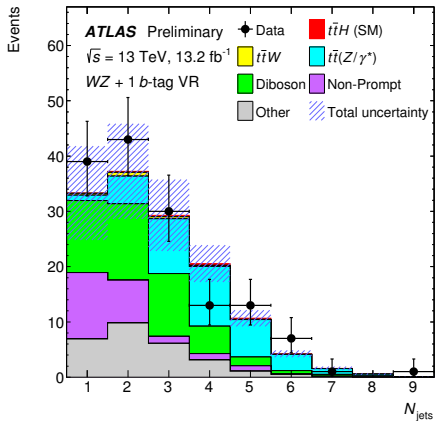

Figure 6.7: Jet multiplicity in the $WZ + 1$ b-tag validation region. Rare processes include tZ, $t\bar{t}WW$, tribosons, $t\bar{t}t\bar{t}$ and tH production. The red region corresponds to the $t\bar{t}H$ SM signal.

To probe the normalization of diboson (mainly WZ) processes with c or b-quarks, a diboson validation region is defined by the presence of 3ℓ with a Z candidate and at least one jet.

A summary of all VR selection cuts is provided in Table 6.14. The fraction of events from diboson in the VR amounts to 33%, as shown in Fig. 6.7, and the jet multiplicity spectrum shows a fair agreement between data and expectations.

Table 6.15 provides a summary of the expected and observed events in each validation region as well as the fraction of events for the target processes.

Tight $t\bar{t}Z$	3ℓ lepton selection At least one $\ell^+\ell^-$ pair with $\lvert m(\ell^+\ell^-) - 91.2\text{ GeV}\rvert < 10$ GeV $N_{\text{jets}} \geq 4$ and $N_{\text{bjets}} \geq 2$
Loose $t\bar{t}Z$	3ℓ lepton selection At least one $\ell^+\ell^-$ pair with $\lvert m(\ell^+\ell^-) - 91.2\text{ GeV}\rvert < 10$ GeV $N_{\text{jets}} \geq 4$ and $N_{\text{bjets}} \geq 1$, or $N_{\text{jets}} = 3$ and $N_{\text{bjets}} \geq 2$
WZ + 1 b-tag	3ℓ lepton selection At least one $\ell^+\ell^-$ pair with $\lvert m(\ell^+\ell^-) - 91.2\text{ GeV}\rvert < 10$ GeV $N_{\text{jets}} \geq 1$ and $N_{\text{bjets}} = 1$
$t\bar{t}W$	$2\ell 0\tau_{had}$ lepton selection $2 \leq N_{\text{jets}} \leq 4$ and $N_{\text{bjets}} \geq 2$ $H_{\text{T,jets}} > 220$ GeV for ee and $e\mu$ events $E_{\text{T}}^{\text{miss}} > 50$ GeV and ($m(ee) < 75$ or $m(ee) > 105$ GeV) for ee events

Table 6.14: Event selection for the validation regions. In all regions at least one selected light lepton is required to be trigger-matched.

VR	Process fraction (%) over total events	Expected events	Data
Tight $t\bar{t}Z$	68%	32 ± 4	28
Loose $t\bar{t}Z$	58%	91 ± 12	89
WZ + 1 b-tag	33%	137 ± 27	147
$t\bar{t}W$	22%	51 ± 10	55

Table 6.15: Expected and observed event yields in the validation regions. The fraction of events in the validation region expected to arise from the targeted process (in order $t\bar{t}Z$, WZ and $t\bar{t}W$) is provided. The quoted uncertainties include all systematic uncertainties.

6.4.2 Background from electron charge mis-identification

The data-driven technique used to measure charge-flip probabilities is described in Section 5.3 and is not repeated here. This analysis uses a 2D parametrization of the charge mis-identification rates as a function of p_{T} and η and, to obtain the final estimate, applies them to OS data events. Figure 6.8 shows the invariant mass spectra for the OS and SS pairs in data. The slight shift of the peak in the SS spectra is visible as well as the regions used to evaluate background with the side-band method.

The two-dimensional fit uses the following bins: [10, 60, 90, 130, 1000]

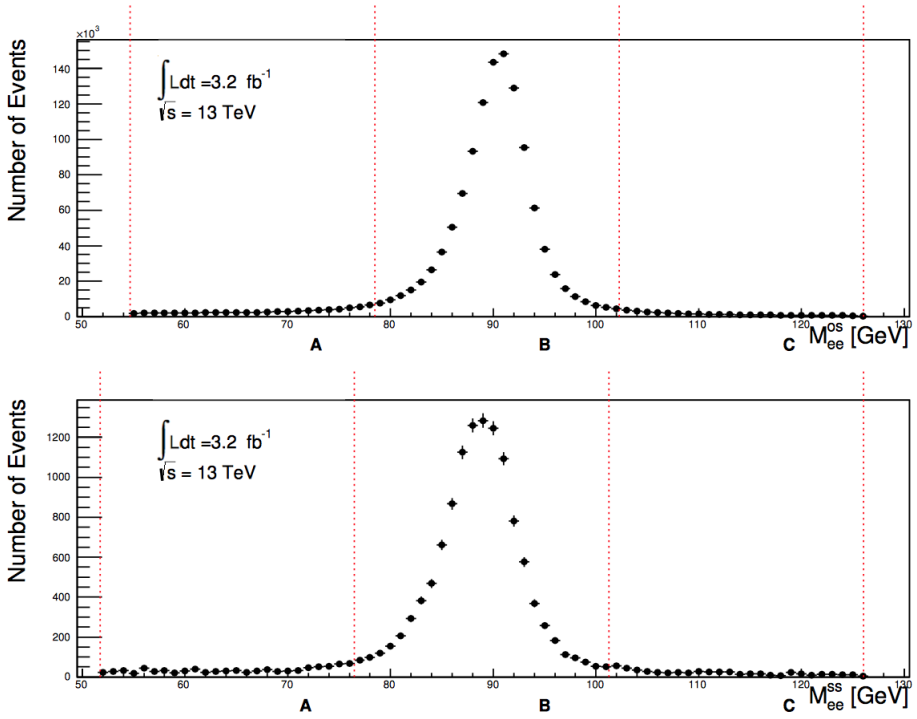

Figure 6.8: Invariant mass spectra for the OS (upper plot) and SS (bottom plot) electron pairs in data. For the SS region the A, B, C regions are the following: $A \in$ [51.7,76.5], $B \in$ [76.5, 101.3] and $C \in$ [101.3, 126.0]. For the OS region: $A \in$ [54.7,78.5], $B \in$ [78.5, 102.3] and $C \in$ [102.3, 126.0].

GeV in p_{T} and [0., 0.6, 1.1, 1.37, 1.52, 1.7, 2.3, 2.47][2] in η. A "closure test"[3] is performed to test the validity of the likelihood fit using simulation, as shown in Fig. 6.9. The test shows a good agreement between simulation-extracted probabilities and the likelihood fit results. Differences from unity between the two measurements are included as source of systematic uncertainty.

Due to the limited statistics in data, the charge-flip probability corresponding to the last p_{T} bin [130, 1000] GeV is extrapolated from the [90, 130] GeV bin using a p_{T} dependent factor extracted from simulated $t\bar{t}$ events, kinematically closer to the high-p_{T} electrons present in the signal region. The

[2] Only electrons in the $2\ell 0\tau_{had}$ channel are required to satisfy $|\eta|$ <1.37. To allow the data-driven charge-flip rates to be applied to the other channels as well, the measurement is performed over the full η range, up to $|\eta|$ <2.4.

[3] With closure test are indicated here, and in the following, simulation based tests aimed to check the validity of a given procedure.

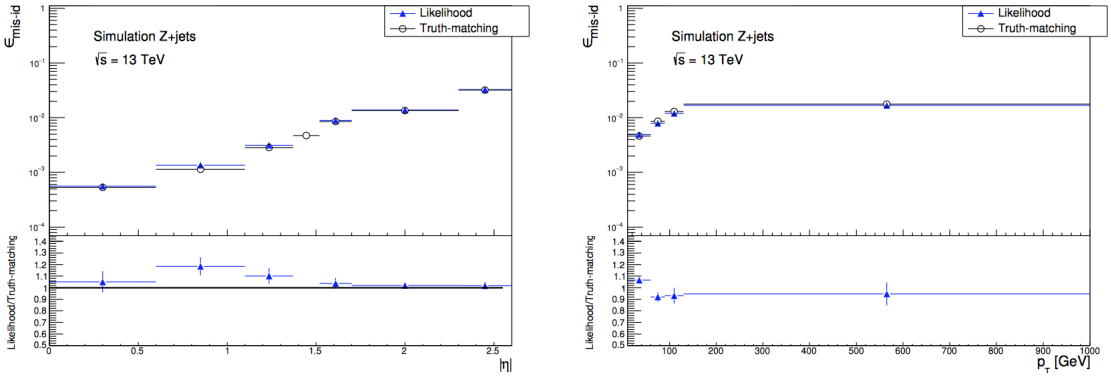

(a) (b)

Figure 6.9: Charge-flip probability closure test: $|\eta|$ (left) and p_{T} (right) dependencies for truth-matched charge-flipped electrons (black) and as resulting from the likelihood fit (blue). Both distributions are extracted using Z+jets MC simulation.

probability in the high-p_{T} region is thus defined as:

$$\epsilon(|\eta|, p_{\mathrm{T}} > 130)_Z = \epsilon(|\eta|, p_{\mathrm{T}} \in [90, 130])_Z^{\mathrm{data}} \times \frac{\epsilon(|\eta|, p_{\mathrm{T}})_{t\bar{t}}^{\mathrm{MC}}}{\epsilon(|\eta|, p_{\mathrm{T}} \in [90, 130])_{t\bar{t}}^{\mathrm{MC}}} \quad (6.2)$$

where $\epsilon(|\eta|, p_{\mathrm{T}})_{t\bar{t}^{\mathrm{MC}}}$ is the charge-flip rate measured in $t\bar{t}$ events using truth-matching.

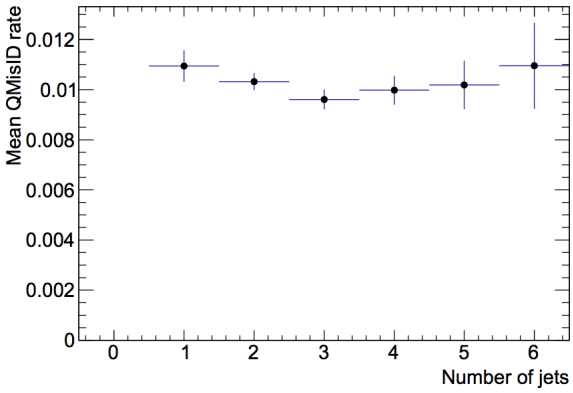

Figure 6.10: Stability of the fraction of $t\bar{t}$ simulated events with one mis-identified electron charge as a function of event jet multiplicity.

An additional check is performed using $t\bar{t}$ simulated events to assess the stability of the charge misidentification probabilities as a function of the number of jets in the events. As clear from Fig. 6.10, rates are all compatible

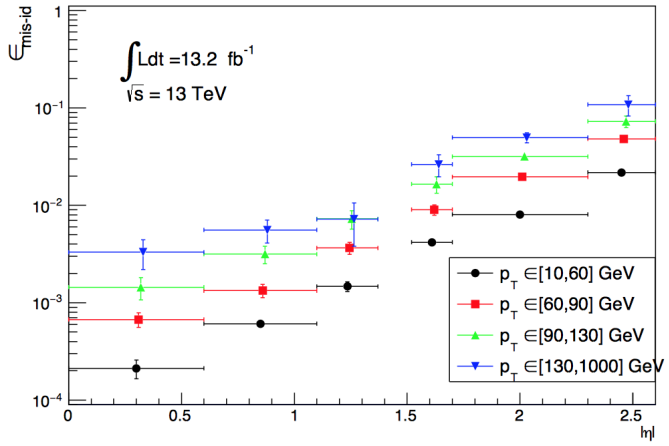

Figure 6.11: Electron charge misidentification probabilities measured in data (black dots, red squares and green triangles) with the likelihood method fit and extrapolated from MC $t\bar{t}$ (blue triangles) for the highest p_{T} bin. Statistical and systematic uncertainties are included in the error bands.

within statistical uncertainties up to six-jets events.

Finally, the two-dimensional charge-flip rates are presented in Fig. 6.11. Rates are applied to OS events in the signal region leading to the following prediction for the ee and $e\mu$ channels:

$$\begin{aligned} N_{CF}^{ee} &= 6.9 \pm 1.3 \ \text{(stat + sys)} \\ N_{CF}^{e\mu} &= 7.1 \pm 1.7 \ \text{(stat + sys)} \end{aligned}$$

for the data corresponding to an integrated luminosity of 13.2 fb^{-1}.

Systematic uncertainties

The main sources of systematic uncertainties affecting the charge-flip measurement are the following:

- the statistical uncertainties from the likelihood method, which can be appreciated from Fig. 6.11;
- the statistical uncertainty on the p_{T} extrapolation procedure, affecting only electrons with $p_{\mathrm{T}} > 130$ GeV;
- the closure test uncertainty which is computed as the difference between the MC likelihood fit probabilities and the rates obtained from truth-matched electrons;

- the variation of the rates due to the Z-peak window choice.

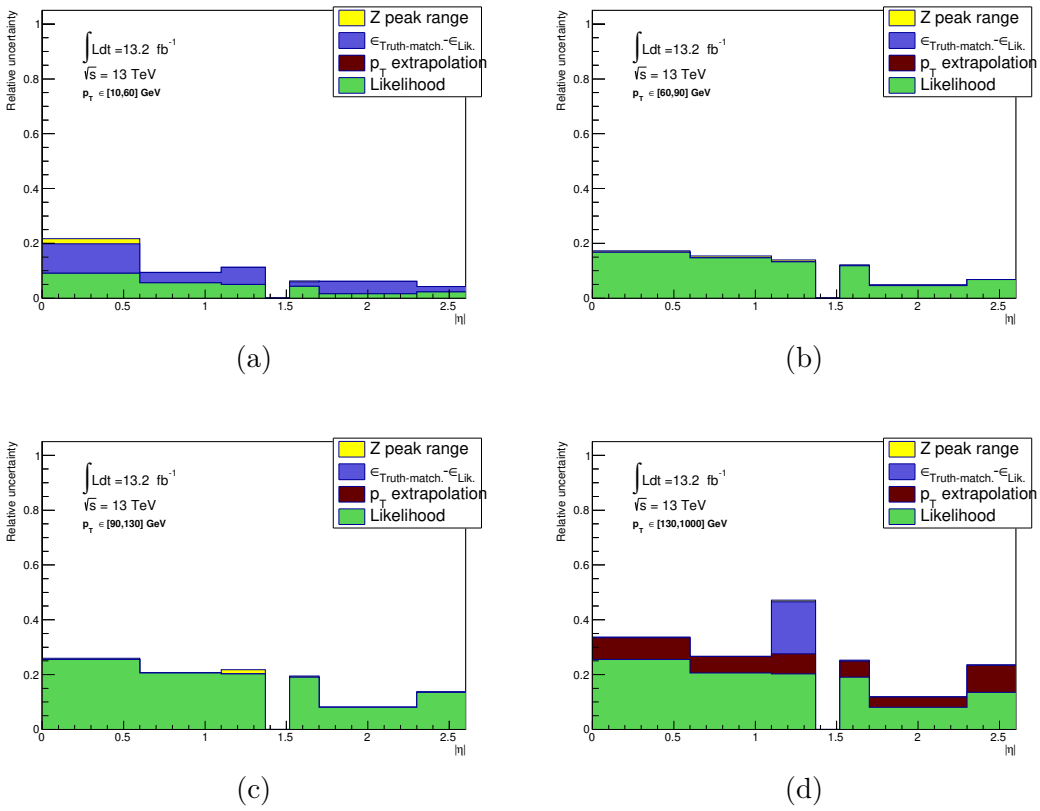

Figure 6.12: Stacked plot of the systematic contribution to the charge-flip measurement as a function of $|\eta|$. Distributions are divided into four p_{T} ranges: $p_{\mathrm{T}} \in$ [10,60] (a), $p_{\mathrm{T}} \in$ [60,90] (b), $p_{\mathrm{T}} \in$ [90,130] (c) and $p_{\mathrm{T}} \in$ [130,1000] (d).

As it is clear from Fig. 6.12, the main systematic uncertainty is due to the likelihood fit uncertainty in each p_{T} range. The closure test uncertainty is dominant in the low p_{T} (6.12a) range.

6.4.3 Background from fake leptons

The data-driven methods used for fake background estimation are presented in Section 5.4. The baseline method adopted in the $t\bar{t}H$ search is the fake factor (FF) (5.4.2) although, given that fake background is the most important background in the $2\ell 0\tau_{had}$ channel, cross-checks providing consistent results are needed. For this reason an alternative estimation is provided using the Matrix Method (see 5.4.1).

The FF method is chosen as baseline given the cut and count nature of the analysis, which does not rely on background shapes. In this section, the estimation of fakes with the FF method will be provided as well as the alternative one using the MM and the comparison between the two indicates the reliability of the fake estimate in the $2\ell 0\tau_{had}$ channel.

6.4.4 Fake estimation using the Fake Factor

The measurement is based on the assumption that the FF is stable with respect to jet multiplicity so that, even if it was measured in a low jet multiplicity region, it can be applied to the signal region. The FF is measured in a region containing exactly two light leptons (and no hadronic taus) with same electric charge. As already stated, the FF depends on lepton kinematics and can vary significantly depending on the region used for its estimation. Therefore, to obtain a sample with similar kinematics to the one of the signal region, leptons are required to have $p_{\mathrm{T}} > 25$ GeV and events shall contain from 2 to 4 jets, at least one of which b-tagged. The kinematic requirements explicitly target a $t\bar{t}$ topology which is indeed the process originating the majority of the fake background in the signal region. For the electron channel, a Z veto is applied to reduce the impact of charge-flip leptons. Only ee and $\mu\mu$ events are used for the measurement of electron and muon FF, leaving the mixed channel $e\mu$ to be used to validate the method in the low jet multiplicity regions. It might be useful to recall here that the FF is defined as:

$$F_{e,\mu} = \frac{N_{TT}}{N_{TL}} \tag{6.3}$$

where N_{TT} is the number of events containing two tight leptons while N_{TL} is the number of events containing one strictly loose lepton. The tight lepton is required to fire the single lepton trigger.
The residual prompt contamination from $t\bar{t}V$, $W^{\pm}Z$ and $W^{\pm}W^{\pm}$ is subtracted from MC simulation. Moreover, to avoid double counting between fake and charge-flip background estimations (see 5.5) data-driven charge misidentified electrons in the TT category and MC truth-matched charge-flipped electrons in the TL, LT and LL regions are subtracted from data.
The main systematic uncertainties affecting the FF measurement are addressed as follows:

- the statistical uncertainty due to the size of the high jet multiplicity side-band regions with one tight and one strictly loose lepton. Three independent systematic are assigned, one per channel.

- the statistical uncertainty on the measured FF, due to the limited size of the fake enriched sample. These uncertainties, affecting F_e and F_μ are kept separate from the previous one to account for the correlations between $e^\pm\mu^\pm$ (based on F_e and F_μ), $e^\pm e^\pm$ (based on F_e) and $\mu^\pm\mu^\pm$ (based on F_μ) fake estimates.

- the validity of the extrapolation procedure from the low multiplicity to the high multiplicity region is tested on MC $t\bar{t}$ events. The closure test provides a comparison between the fake estimation from simulated events containing a non-prompt lepton using truth matching and the FF performed on MC. To increase the precision of the closure test, the subleading lepton p_{T} threshold was lowered to 10 GeV and a more inclusive $|\eta| < 2.5$ for the electron is required.

Flavour	Region	Non-closure	Systematic
e	5 jets	(-24.8±14.1)%	24.8%
e ($\|\eta\| < 2.5$)	5 jets	(-16.3± 10.4)%	16.3%
e p_{T} (25,25) GeV	5 jets	(16.7± 23.0)%	23.0%
μ	5 jets	(-8.72± 9.76)%	9.76%
μ p_{T} (25,25) GeV	5 jets	(18.9± 31.2)%	31.2%

Table 6.16: Result of the closure test performed on $t\bar{t}$ simulated events. The *non-closure* column shows the difference between the predicted number of events in the signal region and the one from truth-matched MC leptons in %. The quoted uncertainty is due to the MC statistical uncertainty. The highest non-closure is taken as systematic uncertainty.

Table 6.16 shows the result of the closure test performed on MC simulation using slightly different regions from the one used for the nominal measurement. The uncertainty is ∼25% for the electron channel and ∼30% for the muon channel.

- an additional systematic uncertainty arises from the prompt processes subtraction in the fake enriched control region. The largest contribution is due to $t\bar{t}V$ events which amount to roughly 20% in the $\mu^\pm\mu^\pm$ low multiplicity regions. The $t\bar{t}V$ normalization uncertainty leads to an uncertainty on F_μ of about 9% and about 5% on F_e.

- the systematic uncertainty on charge-flip events (which are subtracted from the events used in the fake estimate) is propagated to F_e and therefore to the final fake estimation in the $e^\pm e^\pm$ and $e^\pm\mu^\pm$ channels. Since a positive variation in the charge-flip estimation corresponds to a

negative variation in the predicted fakes, the systematic uncertainties associated to charge-misidentification are anti-correlated.

- fake composition contributes as an additional source of uncertainty. The low jet multiplicity region is designed to include mainly $t\bar{t}$ events. Other processes could however contribute to fake leptons in that region, such as W+jets, and might be underestimated if not properly taken into account. Fake composition is assessed by varying the kinematic cuts such as $E_{\mathrm{T}}^{\mathrm{miss}}$, jet multiplicity and p_{T} threshold for b-tagged jets.

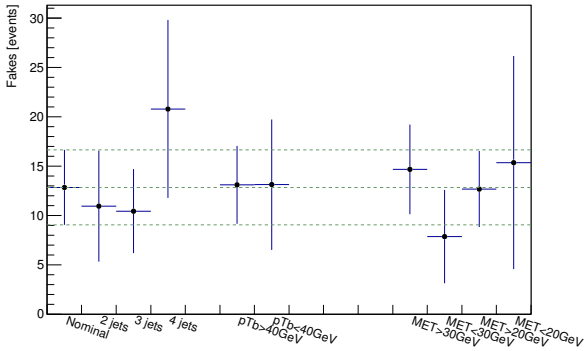

Figure 6.13: Stability of the total (sum of the $e^{\pm}e^{\pm}$ and $\mu^{\pm}\mu^{\pm}$ channels) fake prediction assessed by varying the fake enriched region composition. The uncertainties derive from the statistical error on the CR size and the statistical error on the fake factor.

Fake Factor	Electron	Muon
data	0.36 ± 0.09	0.64 ± 0.12
$t\bar{t}_{MC}$	0.37 ± 0.05	0.53 ± 0.06

Table 6.17: Electron and muon FFs obtained from data and compared to the expected ones from MC simulation. The quoted uncertainties are statistical only.

All the variations in Fig. 6.13 are consistent within the total uncertainty and the largest systematic (which amounts to 19%) arises from the variation observed in the 4 jet bin. This uncertainty is taken as the final systematic uncertainty, assuming the contamination by other processes to be flavour independent. The FFs, obtained as a single value inclusive in p_{T}, both from data and a from $t\bar{t}$ MC are provided in Table 6.17.

Finally, the fake estimation split into channel flavour is provided in Table 6.18.

	Fakes	CR size	F_μ stat	F_μ syst	F_e stat	F_e syst	Qmisid	fake origin
$e^\pm e^\pm$	12.1	2.40	/	/	2.92	2.29	2.29	
$e^\pm \mu^\pm$	12.4	2.60	0.57	0.30	2.26	2.32	1.77	1.87
$\mu^\pm \mu^\pm$	8.71	2.40	1.62	0.85	/	/	/	1.66

Table 6.18: Fake yield predictions divided by channel and associated uncertainties for data corresponding to a luminosity of $\mathcal{L} = 13.2$ fb^{-1}. The $\mu^\pm\mu^\pm$ channel is not affected by the systematic variation associated to charge-flip events. All the other uncertainties are treated as uncorrelated from the uncertainties in the $e^\pm e^\pm$ and $e^\pm\mu^\pm$ channels except for the fake origin. For the mixed channel, the only independent uncertainty is the one associated to the CR size, while all the other terms are treated as correlated to the $e^\pm e^\pm$ and $\mu^\pm\mu^\pm$ channels.

6.4.5 Fake estimation using the Matrix Method

The Matrix Method for fake estimation is presented in Section 5.4.1. The MM returns a *per-event* weight as a combination from the measured *real* and *fake* efficiencies.

Real efficiency measurement

Two sets of regions can be used for the measurements of the real efficiency (i.e. the probability for a *real* lepton to be reconstructed as tight) r. Most importantly, r needs to be assessed in a region as pure as possible in prompt leptons and, preferably, with kinematic features similar to the signal region. Two possible samples suits these needs:

- a region containing leptons originating from the Z boson, defined by the presence of two OS leptons with same flavour and invariant mass $|m_{l^+l^-} - m_Z| < 7.5$ GeV, inclusive in jet multiplicity. Z boson decays have the advantage of providing high statistics however the kinematic features of two leptons originating from a Z decay might differ from the ones of leptons coming from a very dense environment such as the $t\bar{t}H$ production.

- a region containing leptons from $t\bar{t}$ decays and therefore characterized by two OS leptons and an event jet multiplicity in the range [2,3,4], at least one b-tagged jet. The results in this region are compared to the ones obtained from the inclusive $t\bar{t}$ semileptonic and dileptonic MC samples. Compared to Z events, the $t\bar{t}$ topology features a lepton kinematic much closer to the one of the signal region leptons.

In both cases, a *tag-and-probe* technique is used to select interesting events. The *tag* is identified as the lepton matching the single lepton trigger that fired the event, satisfying the tight analysis requirements and, if both leptons are tight and matched to the trigger, having the highest-p_{T}. The remaining lepton is flagged as *probe* and used to measure the efficiency, as it can pass or fail the tight selection. Events which do not contain at least one tight and trigger-matched lepton are discarded. No explicit trigger request is applied to the probe lepton which, in principle, could be also matched to the single lepton trigger. In this way, an unbiased measurement with respect to the trigger selection is ensured. Furthermore, in the real control region we expect to find two prompt, isolated leptons being equally likely to fire an isolated single lepton trigger. In the fake control region, on the contrary, the fake lepton is expected to fail the tighter isolation requirements, having higher probability to be categorized as a probe.
The choice of the real control region depends on different considerations: the purity of prompt leptons in the Z+jets and $t\bar{t}$ samples, the kinematic similarity to the signal region and the charge-flip contamination.
The aim of the first test performed is to assess the purity of the two samples with MC simulation. The purity is assessed on the probe lepton, differentiating between electrons and muons, and defined as:

$$\text{purity} = \frac{\ell^{probe}_{prompt}}{\ell^{probe}_{any}} \tag{6.4}$$

where ℓ^{probe}_{prompt} means that a truth matching requirement is applied to the probe lepton from W/Z decays while the ℓ^{probe}_{any} can also include fake leptons.

Tables 6.19, 6.20, 6.21 and 6.22 show the real efficiency and purity for different MC samples. It is clear that the Z+jets sample (Tab. 6.19) provides a very high purity sample both in the electron and in the muon case, where the probability to select a non-prompt lepton is ∼4% in the worst case scenario. The slightly lower electron efficiency reflects the higher difference between loose and tight defined electrons in the identification and isolation working points, with respect to muons, but will perform better in the fake efficiency measurement. The opposite trend is observed in the muon case, where a high r (∼99%) will be paid at the price of some instability in the f measurement, as we will see later.
Concerning the $t\bar{t}$ sample, the comparison between Tables 6.20, 6.21 and 6.22 shows a similar expected efficiency and purity (around ∼95% for electrons and ∼99% for muons) between flavour configurations. We decided to use different flavour events which allow the reduction of the combinatorial contamination from charge-misidentified electrons, as explained in Section 5.5.

Real efficiency with Z+jets			
Probes ($\times 10^6$)	ℓ^{probe}_{prompt}	ℓ^{probe}_{any}	purity
Electrons			
Loose	5.162 ± 0.004	5.221 ± 0.004	(98.8 ± 0.1)%
Tight	4.279 ± 0.004	4.310 ± 0.004	(99.3 ± 0.1)%
Expected r	(82.89 ± 0.10)%	(82.55 ± 0.09)%	
Muons			
Loose	7.195 ± 0.004	7.198 ± 0.004	(99.9 ± 0.08)%
Tight	6.958 ± 0.004	6.959 ± 0.004	(99.9 ± 0.08)%
Expected r	(96.71 ± 0.08)%	(96.67 ± 0.08)%	

Table 6.19: Expected number of prompt loose and tight probes for electrons and muons compared to the inclusive number of probe leptons in the Z+jets MC sample. The inclusive efficiency and the purity in each case are also shown. Uncertainties are statistical.

Real efficiency with $t\bar{t}$			
Probes ($\times 10^4$)	ℓ^{probe}_{prompt}	ℓ^{probe}_{any}	purity
ee			
Loose	2.575 ± 0.01	2.718 ± 0.01	(94.7 ± 0.5)%
Tight	2.015 ± 0.01	2.040 ± 0.01	(98.7 ± 0.6)%
Expected r	(78.3 ± 0.5)%	(75.0 ± 0.5)%	
$\mu\mu$			
Loose	3.179 ± 0.01	3.312 ± 0.01	(95.9 ± 0.4)%
Tight	2.938 ± 0.01	2.949 ± 0.01	(99.6 ± 0.5)%
Expected r	(92.4 ± 0.4)%	(89.0 ± 0.4)%	

Table 6.20: Expected number of prompt loose and tight probes for electrons and muons compared to the inclusive number of probe leptons in the $t\bar{t}$ MC sample using only same-flavour events ($ee, \mu\mu$). The inclusive efficiency and the purity in each case are also shown. Uncertainties are statistical.

The final decision is to use the $t\bar{t}$ control region. With respect to the Z sample, $t\bar{t}$ provides a slightly lower purity but the kinematic features of $t\bar{t}$ leptons are closer to the ones of the real lepton entering the analysis signal region.

Table 6.23 summarizes the cuts performed to select the control region used for r measurement while Table 6.24 shows the composition of SM background in the region. The r is parametrized as a function of the lepton p_{T}, since no sizable dependence on other kinematic variables is observed.

Real efficiency with $t\bar{t}$			
Probes ($\times 10^4$)	ℓ^{probe}_{prompt}	ℓ^{probe}_{any}	purity
	μe		
Loose	2.77 ± 0.01	2.92 ± 0.01	(95.0 ± 0.5)%
Tight	2.21 ± 0.01	2.24 ± 0.01	(98.8 ± 0.6)%
Expected r	(79.8 ± 0.5)%	(76.8± 0.4)%	
	$e\mu$		
Loose	2.68 ± 0.01	2.80 ± 0.01	(95.6 ± 0.5)%
Tight	2.47 ± 0.01	2.48 ± 0.01	(99.6 ± 0.6)%
Expected r	(92.2 ± 0.5)%	(88.4 ± 0.5)%	

Table 6.21: Expected number of prompt loose and tight probes for electrons and muons compared to the inclusive number of probe leptons in the $t\bar{t}$ MC sample using only different-flavour events ($e\mu, \mu e$). The inclusive efficiency and the purity in each case are also shown. Uncertainties are statistical.

Real efficiency with $t\bar{t}$			
Probes ($\times 10^4$)	ℓ^{probe}_{prompt}	ℓ^{probe}_{any}	purity
	$ee + \mu e$		
Loose	5.35 ± 0.02	5.64 ± 0.02	(94.9 ± 0.5)%
Tight	4.23 ± 0.02	4.28 ± 0.02	(98.8 ± 0.7)%
Expected r	(79.1 ± 0.5)%	(75.9 ± 0.4)%	
	$\mu\mu + e\mu$		
Loose	5.86 ± 0.02	6.11 ± 0.02	(95.8 ± 0.5)%
Tight	5.41 ± 0.02	5.43 ± 0.02	(99.6 ± 0.5)%
Expected r	(92.3 ± 0.5)%	(88.8 ± 0.4)%	

Table 6.22: Expected number of prompt loose and tight probes for electrons and muons compared to the inclusive number of probe leptons in the $t\bar{t}$ MC sample combining all flavour events ($ee, \mu\mu, e\mu$). The inclusive efficiency and the purity in each case are also shown. Uncertainties are statistical.

Figure 6.14 shows the p_{T} distributions for the loose and tight probe leptons. Data distributions are compared to the expected backgrounds as obtained from MC simulation containing a non-prompt probe lepton. Indeed, to avoid any overlap between real and fake efficiency measurements the contribution from non-prompt leptons has to be subtracted from the real control region. As expected, the major contribution to non-prompt leptons arises from $t\bar{t}$ and single t production, steeply falling around ∼80 GeV.

Real CR
2,3,4 jets
≥ 1 b-tagged jet
2 OS leptons
≥ 1 trigger-matched lepton
$\min(p_T^\ell) \geq 10$ GeV
OF leptons

Table 6.23: Definition of the control regions used for measuring the real efficiency.

	Events for r_e	Events for r_μ
$t\bar{t}$	30862 ± 78	40190 ± 93
Single t, tW	1689 ± 16	2334 ± 20
Z+jets	224 ± 39	190 ± 49
W+jets	108 ± 48	62 ± 20
VV	58.8 ± 4.8	69.2 ± 8.6
$t\bar{t}W$	26.95 ± 0.23	35.50 ± 0.28
$t\bar{t}Z$	25.95 ± 0.55	33.76 ± 0.66
QMisID	—	—
Tot. pred.	32994 ± 101	42914 ± 109
Data	35787	44725

Table 6.24: Sample composition in the real control region corresponding to an integrated luminosity of 13.2 fb^{-1}. Errors are statistical only.

Fake efficiency measurement

In contrast to the real control region, the fake efficiency control region is specifically designed to be enriched in fake leptons originating from $t\bar{t}$ decays. The origin of the fake lepton is checked with simulation and proves to be consistent between the region used for the fake efficiency measurement and in the signal region.

Table 6.25 shows the cuts defining the fake control region used to measure fake efficiency. Since the SS region for electrons is affected by charge-flip contamination, which needs to be properly taken into account, a cut is applied on the electron-electron channel to reduce contribution of Z boson decays where an electron underwent charge-flip. The invariant mass of the ee pair is required to be at least 7.5 GeV away from the Z mass. Furthermore, to reduce the contamination from low mass resonances, a minimum invariant mass cut

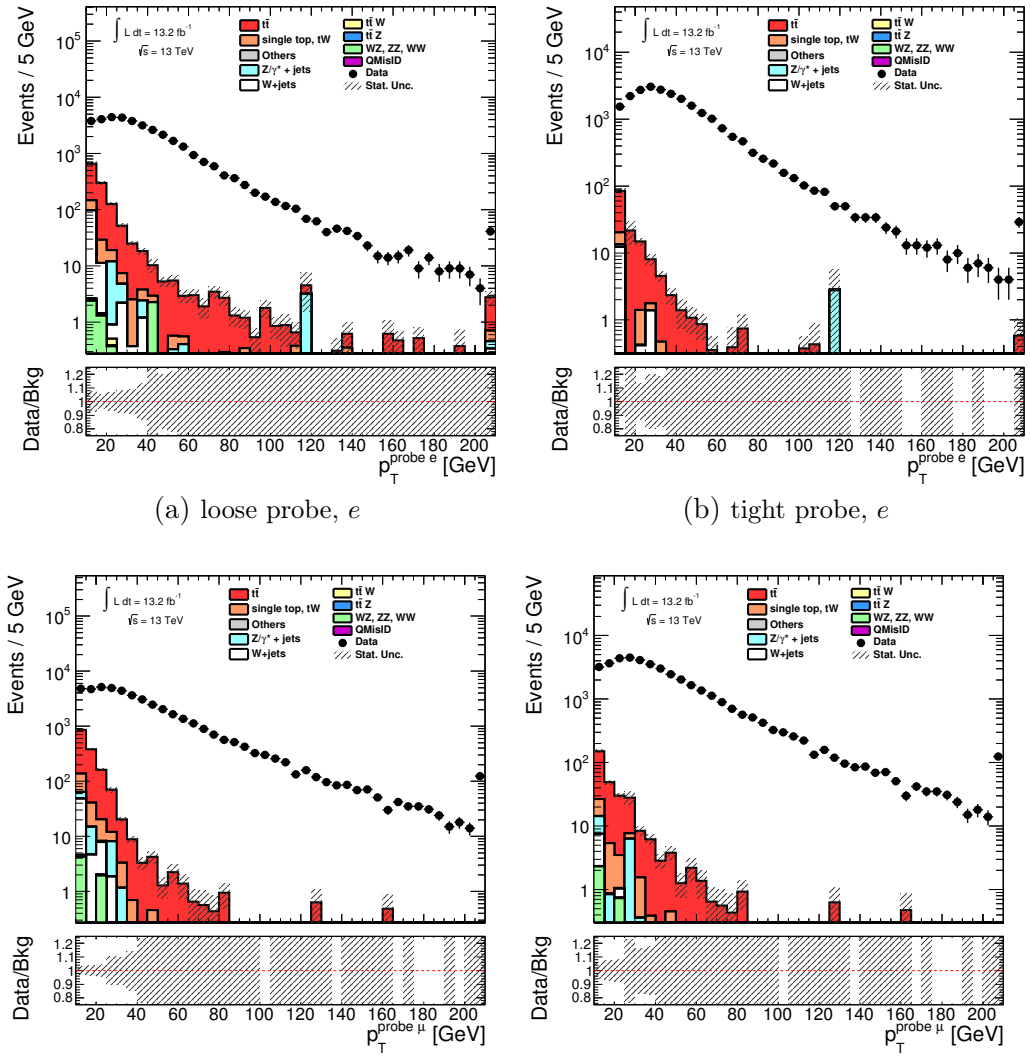

(a) loose probe, e (b) tight probe, e

(c) loose probe, μ (d) tight probe, μ

Figure 6.14: Probe lepton p_T distribution in the real control region, for electrons and muons loose (a), (c) and tight (b), (d) events. Events where the probe is truth matched to a non-prompt lepton are shown. Those events are subtracted before measuring the real efficiency.

on same-flavour leptons of 20 GeV is also applied. The overlap with the charge mis-identification background is treated in the following way: events from MC simulation are subtracted from data if the probe lepton is prompt or charge-flip using truth matching, before the fake efficiency measurement. The latter are subtracted to avoid overlap with the data-driven charge-flip

Fake CR
2,3,4 jets
≥ 1 b-tagged jet
2 SS leptons
≥ 1 trigger-matched lepton
$\min(p_T^\ell) \geq 10$ GeV
$\mu\mu$ for ϵ_μ, inclusive flavour for ϵ_e
$\lvert m(\ell\ell) - m_Z \rvert \geq 7.5$ GeV for (ee)
$m(\ell\ell) \geq 20$ GeV (for same flavour leptons)

Table 6.25: Definition of the control region used for measuring the fake efficiency.

estimation and subsequent double counting. The probability to have two fake leptons in one event is assessed with simulation and is found to be negligible.

Table 6.26 shows the inclusive background composition in the fake control region. The fake lepton contribution to total event yields is included in the total simulation while the charge-flip background is estimated from data. It is clear that the major contribution arises from $t\bar{t}$ (∼70%) events, with a significant (∼12%) contribution from charge-flip probes. Figure 6.15 shows the p_{T} distribution in the fake control region in data and the contribution from prompt and charge-flip (in the electron case) probe leptons which needs to be subtracted. We see that the high-p_{T} region for muons shows a problematic trend from 80 GeV on, where all the loose probes also pass the tight selection. Indeed the two distributions share the same events in data and MC, which results in a very high fake efficiency in the last p_{T} bin. This feature is a consequence of the fact that the `Loose` and `FixedCutTightTrackOnly` muon isolation working points perform very similarly for high-p_{T} muons and the isolation difference between loose and tight leptons is not effective anymore. This feature is not observed in the electron case.

The p_{T} distributions, especially in the muon case, impact on the binning choice for efficiency parametrization. Both for r and f the efficiencies measured on data are compared to the MC $t\bar{t}$ simulation. Contrarily to the real control region where the probe lepton in $t\bar{t}$ is required to be prompt, in the fake control region the lepton is required to be a non-prompt lepton, originating either from a heavy-flavour or light-flavour hadron secondary decay (vetoing on electrons from charge mis-identification). The comparison between efficiencies measured in data and in MC is provided in Fig. 6.16.

From the comparison between real and fake efficiencies in data and MC

	Events for f_e	Events for f_μ
$t\bar{t}$	1382 ± 16	1039 ± 15
Single t, tW	131.2 ± 4.8	111.3 ± 4.4
Z+jets	-49 ± 81	32.0 ± 9.6
W+jets	148 ± 32	104 ± 41
$t\bar{t}W$	23.50 ± 0.22	20.08 ± 0.21
$t\bar{t}Z$	7.35 ± 0.18	6.06 ± 0.15
VV	25.8 ± 6.3	18.9 ± 3.3
QMisID	241.2 ± 1.4	—
Tot. pred.	1910 ± 88	1331± 45
Data	2523	1608

Table 6.26: Sample composition in the fake control region corresponding to an integrated luminosity of 13.2 fb^{-1}. Errors are statistical only. All fake backgrounds are included in simulation, and charge-flip background is estimated from data. The negative contribution from Z+jets events is due to large SHERPA negative MC weights and covered by very large statistical uncertainty.

the following conclusions are drawn. First, electron r (Fig. 6.16a) in data and MC shows a ∼10% tension; this is a consequence of the fact that we cannot fully trust MC simulation in the electron case when excluding probe leptons from charge-misidentified events. Indeed, the truth matching requirement explicitly demands the probe lepton to be originated from a W decay, excluding those probes for which a trident event happened. However, we already know that MC description is not fully reliable and a ∼10% discrepancy between data and simulation is fully consistent with the magnitude of the charge-flip rates as measured in Section 6.4.2. Indeed, the data/MC agreement shows a significant improvement in the muon case (Fig. 6.16b).
Regarding f, both in the electron and in the muon cases the agreement between data and MC is within the quoted uncertainties. Due to the problematic range in the muon p_{T} region, and to guarantee the stability of the MM which requires substantial (at least $> 10\%$) difference between r and f in each p_{T} range, muon f uses only one bin for the range $f \in$ [25,200] GeV. A perfect agreement between data and MC r, f is anyway not expected and is indeed the reason motivating the need for a data-driven technique for background estimation. However, MC efficiencies are important to test the auto-consistency of the method, as will be shown in the following section.

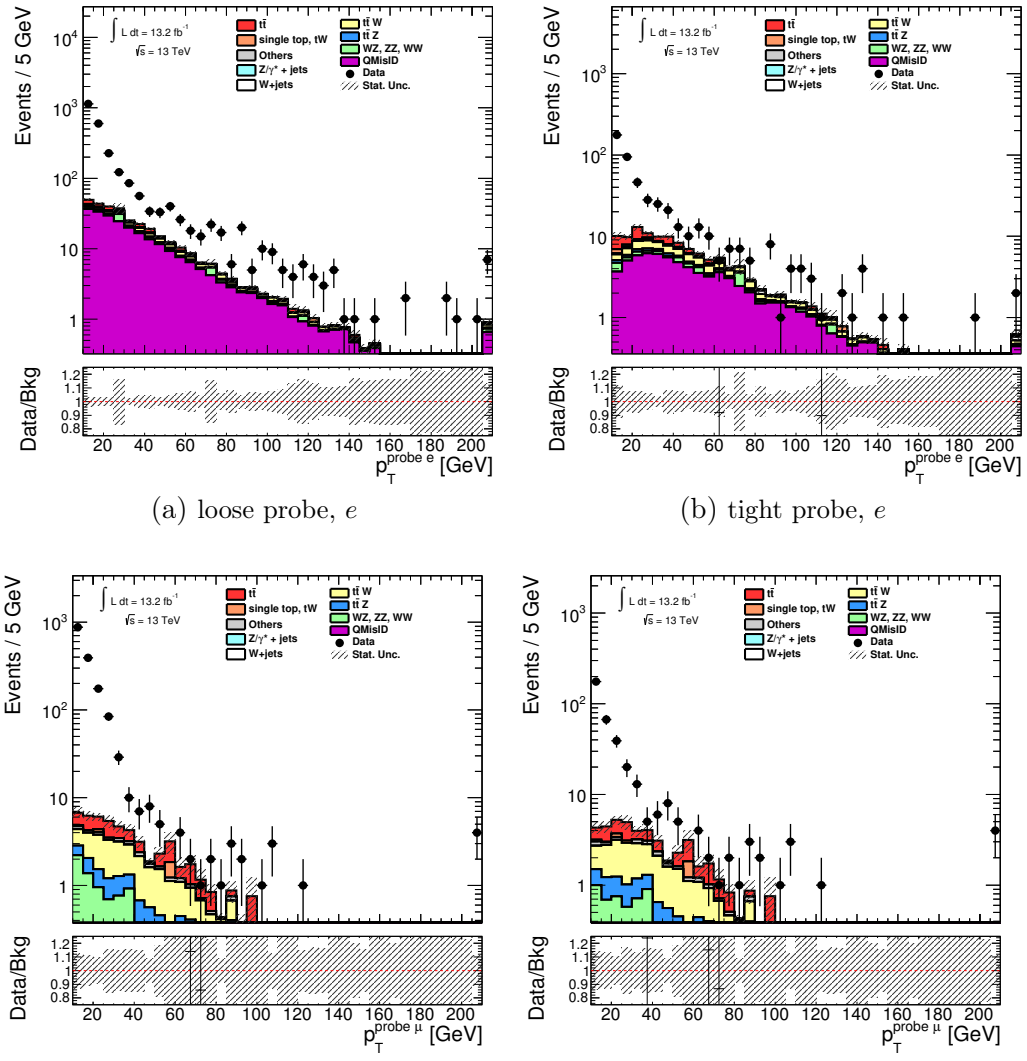

(a) loose probe, e (b) tight probe, e

(c) loose probe, μ (d) tight probe, μ

Figure 6.15: Probe lepton p_T distribution in the fake control region, for electrons and muons loose (a), (c) and tight (b), (d) events. Events where the probe is truth matched to a prompt lepton, as well as events with data-driven charge-flip electrons, are shown. Those events are subtracted before measuring the efficiency.

Matrix Method closure test

Before applying the method to data, its effectiveness is assessed relying on a pure simulation-based test. The closure test is performed in two distinct regions, eventually combined together. The first region is the one used for the r, f measurement, i.e. the *low multiplicity region* in which $N_{jets} \in [2,3,4]$.

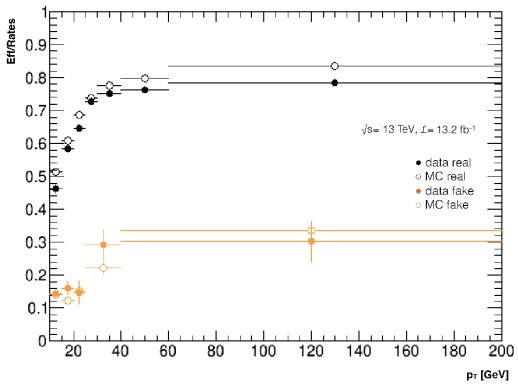

(a)

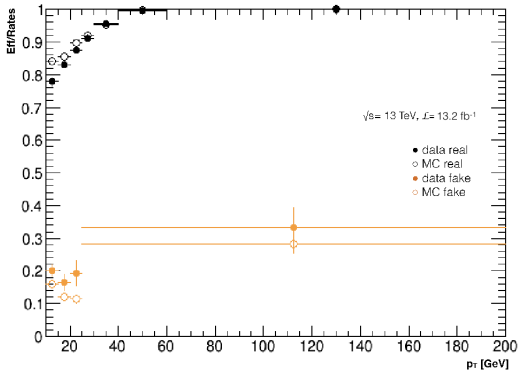

(b)

Figure 6.16: Real (black) and fake (orange) efficiencies for electrons (a) and muons (b). Data correspond to the full dots while MC is shown as empty dots. Error bars represents the statistical uncertainty due to the denominator sample.

The complementary region, and most interesting one, is the *high multiplicity region*, i.e. the signal region, where we require $N_{jets} \geq 5$. In this test only the $t\bar{t}$ MC background is used, being the most significant one in SR.
The test is performed in the following way: first, a subset of $t\bar{t}$ events containing two SS tight leptons and at least one truth-matched fake lepton are selected (named *Fakes from* $t\bar{t}$ in Table 6.27). These events, inclusively or divided according to jet multiplicity, are compared to the predicted number of events by the MM, obtained applying the values of r and f found in MC to $t\bar{t}$ SS events, without any explicit requirement on lepton origin (*Fakes from MM* in Table 6.27). In both samples, events containing at least one charge-flip electron are vetoed.

	ee	$e\mu$	$\mu\mu$
Closure test in low jet multiplicity region			
Fakes from $t\bar{t}$	28.6 ± 1.3	50.5 ± 1.8	13.6 ± 0.9
Fakes from MM	21.5 ± 1.1	40.9 ± 1.2	11.0 ± 0.5
Non-closure (MM- $t\bar{t}$)/$t\bar{t}$	-24.8 ± 7.4[%]	-19 ± 5.1 [%]	-15 ± 8.9[%]
Closure test in high jet multiplicity region (SR)			
Fakes from $t\bar{t}$	4.6 ± 0.5	7.1 ± 0.7	2.1 ± 0.4
Fakes from MM	3.9 ± 0.4	6.5 ± 0.5	2.2 ± 0.2
Non-closure (MM- $t\bar{t}$)/$t\bar{t}$	-15.2 ± 18.0[%]	-8.5 ± 13.1 [%]	+4.8 ± 20.3 [%]

Table 6.27: Comparison between event yields in the low number of jets multiplicity region (upper part of the table) and in the signal region (lower part of the table) from pure simulation and from the Matrix Method. Uncertainties associated to the measurement are statistical only. The non-closure in each channel is also shown. Events are normalized to an integrated luminosity of 13.2 fb^{-1}.

The result are here produced without applying any re-weighting factor (such as the scale factors) to MC events, being a simulation-to-simulation test. Any non-closure observed in signal region accounts for the differences deriving from using rates measured in the low jet multiplicity region extrapolated to the SR.

Figure 6.17 shows the result of the closure test divided by channel flavour and jet multiplicity. Some tension is observed in the bin corresponding to events containing two jets, while a very good agreement between the MM and the $t\bar{t}$ predictions is obtained for events contain 2 or 3 jets and in the signal region. The agreement is worse in regions containing electrons, and is probably due to the truth-matching veto on charge-flip events, performed on the $t\bar{t}$ sample, which can differently affect the various jet multiplicity regions. The inclusive comparison, divided into CR and SR, between MM and $t\bar{t}$ predictions is also provided in Table 6.27. We see that the highest non-closure is observed in the ee CR (-24%) while it remains below 20% in all other regions. In the SR, however, the non-closure is covered by large statistical uncertainties.

Results on data

Now that the method is validated on simulation, it is applied in the same way to data. As done for the closure test, the MM is applied to data both in the control region with low number of jet and in the signal region.

Jet multiplicity distributions are shown in Fig. 6.18 for both the control

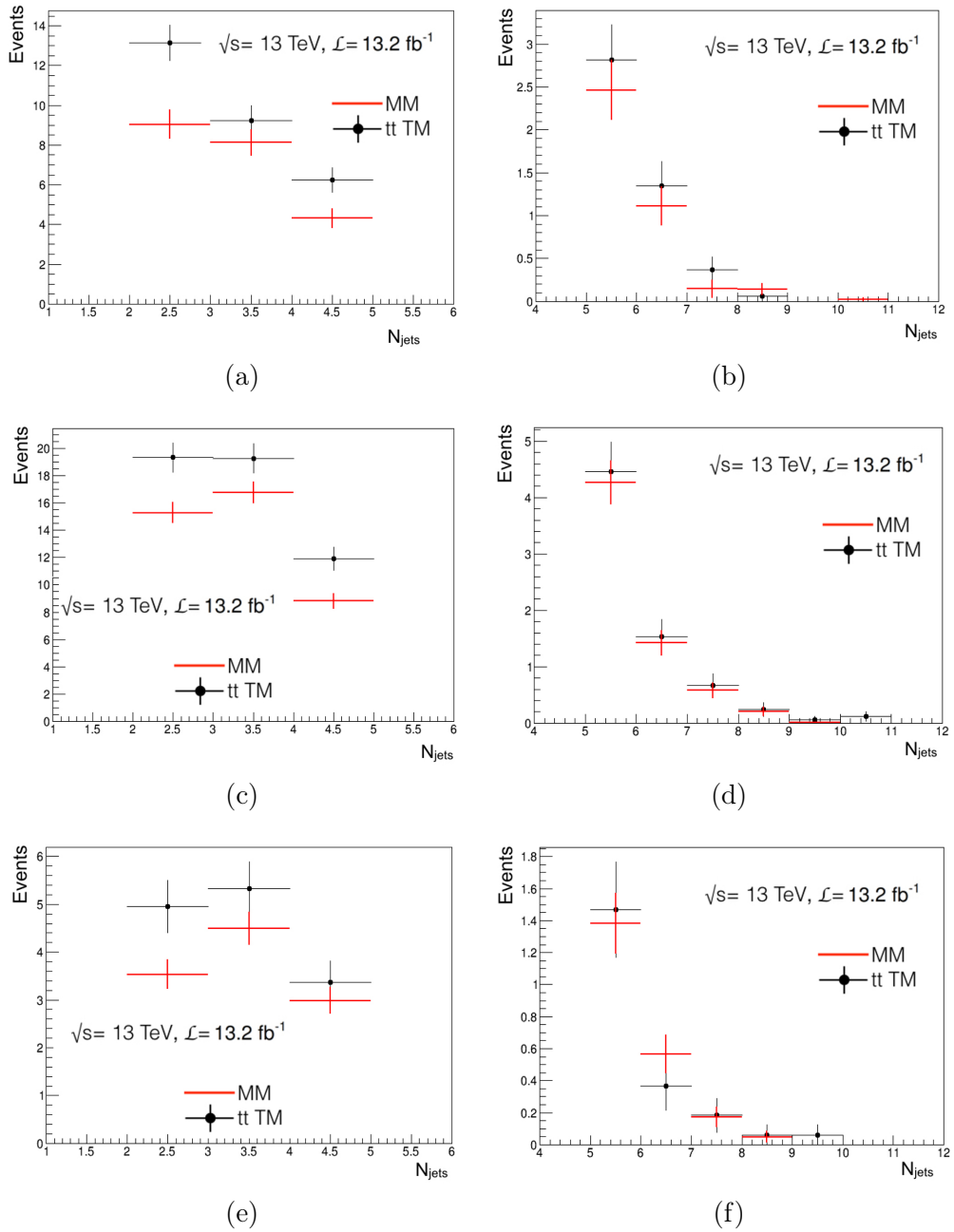

Figure 6.17: Closure test result in the low number of jet multiplicity region ($2 \leq N_{jets} \leq 4$) for and in the SR ($N_{jets} \geq 5$) in the ee (a),(b), $e\mu$ (c),(d) and $\mu\mu$ (e),(f) channels as a function of jet multiplicity. Uncertainties are statistical only.

and the signal regions.

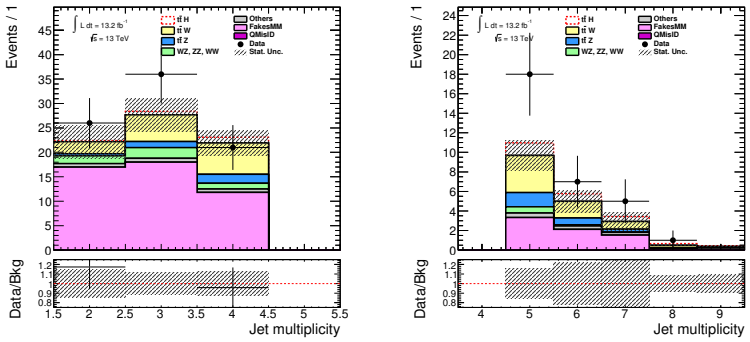

(a) $\mu\mu$, low N_{jets} CR (b) $\mu\mu$, SR

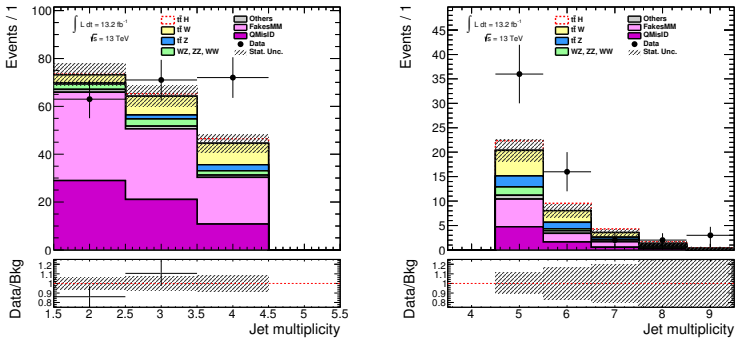

(c) $e\mu$, low N_{jets} CR (d) $e\mu$, SR

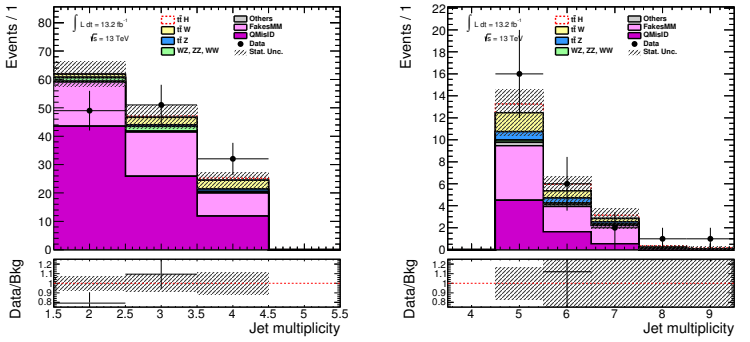

(e) ee, low NJ CR (f) ee, SR

Figure 6.18: Number of events in the $2\ell 0\tau_{had}$ channel in the low jet multiplicity control region (left plots) and in the signal region (right plots). Data and main background are shown: fakes from MM (pink), $t\bar{t}Z$, $t\bar{t}W$, WW, ZZ, WZ background processes. Error bars account for statistical uncertainty only. In the bottom part of each plot the data/bkg ratio is computed.

	Opposite-sign control region	Same-sign control region
Probe e origin - tight	∼95% heavy-flavour	∼90% heavy-flavour
	∼5% γ conversions	∼10% γ conversions
Probe e origin - strictly loose	∼90% heavy-flavour	∼90% heavy-flavour
	∼10% misidentified jets	∼10% γ conversions

Table 6.28: Origin of probe fake leptons in the OS and in the SS control regions. The total percentage refers to the number of events obtained from $t\bar{t}$, single t, Z/W+jets backgrounds.

The overlap with charge-flip events is taken into account using OS events weighted for the data-driven charge mis-identification probability. Those events, inserted inside the MM equation, are also weighted by the real and fake efficiencies. The underlying assumption is that the fake composition in the OS region is similar to the one in SS control region. This assumption was checked using MC simulation to assess the fake lepton composition between the two regions and is shown in Table 6.28. Therefore the fake origin composition is very similar between the OS and the SS regions where the majority of fake leptons originates from heavy-flavour jet secondary decays.

For the cases in which the probe electron is strictly loose, a ∼10% of the fake lepton composition arises from misidentified jets. To assess the impact from OS/SS fake composition on the MM estimation, the charge-flip subtraction is also performed using MC simulation. The total contribution from charge-flip events in this case is evaluated using all MC processes containing an electron with mis-reconstructed charge and subtracted from data using the data-driven method. [htb!]

The results are shown in Table 6.29 and 6.30. Results obtained from the two independent measurements look consistent within the quoted statistical uncertainties. The two MM estimations also look consistent with the results from the FF, available only for the mixed flavour channel. Indeed, the ee and $\mu\mu$ low number of jet multiplicity regions are used to measure the electron and muon FF and cannot be re-used for their validation.

The MM provided an extremely important cross-check for the FF, allowing to conclude that a reliable fake estimation measurement in the $2\ell 0\tau_{had}$ signal region is obtained.

Low jet multiplicity region (CR)			
	$\mu\mu$	$e\mu$	ee
Matrix Method (1, DD QMisID)	46.74 ± 5.33 (12.17)	85.90 ± 26.48 (7.37)	39.25 ± 6.48 (12.74)
Matrix Method (2, MC QMisID)	49.09 ± 5.61	109.55 ± 8.84	37.69 ± 5.50
Fake Factor	—	81.73 ± 7.19	—

Table 6.29: MM fakes estimate in the low jet multiplicity region, and comparison with the FF method (where available). On the Matrix Method prediction, only the statistical error from the side-bands population and the error resulting from the statistical uncertainty on the rates (in brackets) are shown. Matrix Method (1) refers to the number of fakes using data-driven QMisID subtraction. Matrix Method (2) refers to the number of fakes using fully simulation-based background subtraction, where additional large uncertainties should be added for the MC QMisID subtraction. On the Fake Factor prediction, the error is the combination of statistical and systematic uncertainties. Data correspond to an integrated luminosity of 13.2 fb^{-1}.

Signal region (SR)			
	$\mu\mu$	$e\mu$	ee
Matrix Method (1, DD QMisID)	6.97 ± 2.06 (1.90)	8.38 ± 2.64 (1.98)	8.48 ± 2.65 (2.90)
Matrix Method (2, MC QMisID)	7.33 ± 2.17 ± 3.0	13.71 ± 3.26 ± 5.7	8.96 ± 2.49 ± 2.8
Fake Factor	8.71 ± 2.89	12.39 ± 3.49	12.07 ± 3.77

Table 6.30: MM fakes estimate in the signal region, and comparison with the FF method. Matrix Method (1) refers to the number of fakes using data-driven QMisID subtraction where only the statistical error from the sidebands population and the error resulting from the statistical uncertainty on the rates (in brackets) are shown. Matrix Method (2) refers to the number of fakes using fully simulation-based background subtraction, where additional large systematic uncertainties are added (around 60 % associated to the fake rate estimation and 10% associated to the real efficiency) mainly originated from the MC QMisID subtraction and the different fake composition in the signal and control regions. On the Fake Factor prediction, the error is statistical only. Data correspond to an integrated luminosity of 13.2 fb^{-1}.

6.5 Description of the systematic uncertainties

Systematic uncertainties originate from the finite/limited knowledge of physical processes modeling, background estimation and detector simulation. The general treatment of systematic uncertainty is done by varying them by one standard deviation ($\pm\sigma$) with respect to the nominal distribution. Uncertainties may affect the normalization of the samples, the shape of the distributions or both. In the following, a description of the main systematic uncertainties will be given, while a detailed description of all the systematic uncertainties and how they are applied can be found in Appendix A.

The low cross-section for $t\bar{t}H$, $t\bar{t}W$ and $t\bar{t}Z$ production make it difficult to perform high precision measurements based on data. For this reason, analysis where these processes enter as signal, or backgrounds, are particularly sensitive to MC modeling and sensitive to the corresponding systematic uncertainties.
Cross-section for $t\bar{t}H$ production is calculated at LO and NLO in QCD for proton-proton collisions at $\sqrt{s} = 13$ TeV [151]. The calculation uses the five-flavour scheme and the MSTWNLO2008 [152] parton distribution function. The quoted PDF uncertainty corresponds to the 68% CL error set. The central choice for the renormalization and factorization scales is the following: $\mu_0 = \mu_R = \mu_F = H_T/2$. The systematic uncertainties on μ_R and μ_F is assessed by varying each scale independently up and down by a factor of two. The CERN Yellow Report [74] provides an alternative NLO QCD calculation with a slightly higher cross-section value, but in agreement within the quoted uncertainties. Since the contribution from NLO EW correction to $t\bar{t}H$ production is small ($\sim$1%) it is not taken into account in the cross-section value used in ATLAS. The A14 tune optimizes 10 parameters corresponding to multiparton interactions, initial and final state radiation. These variations were reduced to a subset of tune variations, of which one pair is sensitive to underlying event effects, another pair to jet structure effects and three pairs to extra jet production.

Cross-section calculation for $t\bar{t}V$ production is performed in a similar way at LO and NLO using MG5_aMC. Also in this case, electroweak corrections are available and can have up to 5% effect on the total cross-section, depending on the photon density assumed, but are not used here.

Table 6.31 shows the summary of $\sqrt{s} = 13$ TeV cross-section prediction for $t\bar{t}H$ and $t\bar{t}V$ production: the shown NLO cross-sections are the ones used for simulation normalization in the analysis.
The dominant diboson background arises from WZ events including contributions from $WZ + b\bar{b}$, $WZ + c\bar{c}$ and WZ + light quark production. The

	$t\bar{t}H$ cross section [pb]	
	LO	NLO
MG5_aMC	$0.3579 \pm 0.0003^{+30.0\%+1.7\%}_{-21.5\%-2.0\%}$	$0.4608 \pm 0.0016^{+5.7\%+2.0\%}_{-9.0\%-2.3\%}$
CERN Yellow Report	-	$0.5085^{+5.7\%+8.8\%}_{-9.3\%-8.8\%}$(PDF incl. α_S)

Process	Cross section [pb]			
	LO		NLO	
$pp \to t\bar{t}W^{\pm}$	$3.777 \pm 0.003 \cdot 10^{-1}$	$^{+23.9\%}_{-18.0\%}$ $^{+2.1\%}_{-1.6\%}$	$5.662 \pm 0.021 \cdot 10^{-1}$	$^{+11.2\%}_{-10.6\%}$ $^{+1.7\%}_{-1.3\%}$
$pp \to t\bar{t}Z$	$5.273 \pm 0.004 \cdot 10^{-1}$	$^{+30.5\%}_{-21.8\%}$ $^{+1.8\%}_{-2.1\%}$	$7.598 \pm 0.026 \cdot 10^{-1}$	$^{+9.7\%}_{-11.1\%}$ $^{+1.9\%}_{-2.2\%}$

Table 6.31: The LO and NLO total production cross-section at $\sqrt{s} = 13$ TeV for $t\bar{t}H$ (upper table) and $t\bar{t}V$ (bottom table). The quoted uncertainties are due to the QCD scale (left) and PDF (right) variations. Electroweak NLO corrections are not included in the cross-section calculation and are expected to have a negligible impact.

WZ + light quark mistag rate (i.e. the tagging efficiency for jets arising from light quarks or gluons) can be validated using the jet multiplicity in WZ events without b-tagged jets, for which data were found to match MC predictions within errors up to 5 jets. The $\bar{s}g \to WZ + c$ is analogous to $\bar{s}g \to W + c$ which was measured by the ATLAS Collaboration [153] to agree with predictions at the <20% level and limited by PDF accuracy. Besides specific considerations related to the VV+ jets production, the light jet mistag rate and charm tagging have an associated systematic uncertainties which is applied in the analysis. Given that no measurement is available for the $WZ + b\bar{b}$ production, and that Run 1 analysis performed a template fit and extracted a $WZ + b\bar{b}$ scale factor compatible with one but with a very large uncertainty, a 50% overall normalization uncertainty is applied to WZ events.

Among the experimental systematics, the uncertainty arising from the JVT association method has the largest impact. It is approximately 2.5% for jets with $p_{\mathrm{T}} < 60$ GeV, which populate high jet multiplicity final states as the ones in this search. Pile-up interaction modeling and jet energy scale also contribute significantly. Regarding pile-up modeling, uncertainties are determined by varying the assumed inelastic cross-section by $^{+16\%}_{-6\%}$. Lepton reconstruction and trigger efficiency have a negligible impact compared to the just stated systematic uncertainties.

The luminosity uncertainty estimated on the combined 2015 + 2016 datasets yields a value of 2.3%. It is derived from van der Meer scans performed in

August 2015 and May 2016. Since luminosity enters both the background estimations and the conversion between observed yields and effective $t\bar{t}H$ cross-section, its final impact on μ is almost 20%. The effect, and the importance, of luminosity uncertainty in physics measurements motivates the need for a very precise luminosity detector such as LUCID (see Appendix B).

The impact of the most important systematic uncertainties on the measurement of μ, evaluated after the global fit combining all analysis signal regions, is given in Table 6.32.

Uncertainty Source	$\Delta\mu$	
Non-prompt leptons and charge misreconstruction	+0.56	-0.64
Jet-vertex association, pile-up modeling	+0.48	-0.36
$t\bar{t}W$ modeling	+0.29	- 0.31
$t\bar{t}H$ modeling	+0.31	-0.15
Jet energy scale and resolution	+0.22	-0.18
$t\bar{t}Z$ modeling	+0.19	-0.15
Luminosity	+0.19	-0.15
Diboson modeling	+0.15	-0.14
Jet flavor tagging	+0.15	-0.12
Light lepton (e, μ) and τ_{had}ID, isolation, trigger	+0.12	-0.10
Other background modeling	+0.11	-0.11
Total systematic uncertainty	+1.1	-0.9

Table 6.32: Summary of the post-fit effect of systematic uncertainties on μ. The fit is done by simultaneously considering all $t\bar{t}H$ signal regions ($2\ell 0\tau_{had}$, $2\ell 1\tau_{had}$, 3ℓ and 4ℓ). Due to correlations between different uncertainties, the total can differ from the sum in quadrature of individual sources.

As we will see in the following Section (Sec. 6.6), where systematic uncertainties directly enter the fit, correlations among uncertainties are taken into account in the following way:

- luminosity uncertainty: affecting signal and background normalization, is correlated across each signal region and across samples;
- fake estimation uncertainty: treated independently in the $2\ell 1\tau_{had}$ channel. Given that the FF is used both in the $2\ell 0\tau_{had}$ and 3ℓ signal regions, the uncertainty on F_e and F_μ is treated as correlated across, respectively, electron and muon signal regions. The uncertainty on the fake

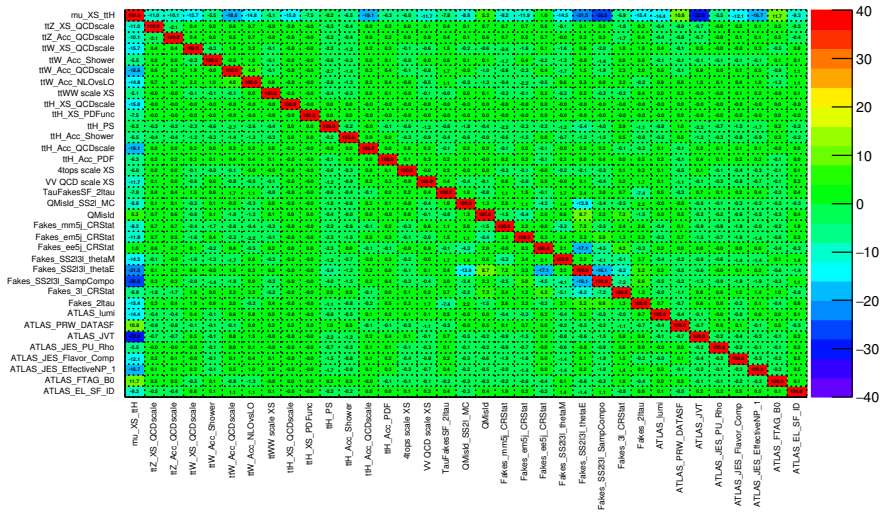

Figure 6.19: Systematic uncertainties correlation matrix.

enriched sample composition is also correlated among each 2ℓ and 3ℓ signal region.

- charge mis-identification: it is treated as correlated across all $2\ell 0\tau_{had}$ and 3ℓ categories when subtracted from the fake estimation and anti-correlated with the systematic on the charge mis-identification. Moreover, the uncertainty propagated from the charge mis-identification procedure is correlated across all $2\ell 0\tau_{had}$ categories.

- theory uncertainty on $t\bar{t}H$ and $t\bar{t}V$: treated as fully correlated across all channels.

- object uncertainties: treated as fully correlated across all channels.

Figure 6.19 shows the correlation matrix for the systematic uncertainties with correlations greater than 5%.

6.6 Measurement of the $t\bar{t}H$ Signal Strength

Statistical analysis is performed using `TtHFitter` [154], interfaced with `HistFactory` [155] which is a tool to build parametrized pdfs sufficiently flexible to describe many analyses based on template histograms. The statistical procedure for signal strength extraction is presented in Section 5.6. All the six signal regions are treated, and implemented, as distinct Poisson terms in the likelihood function. They are provided to the fit framework as

a single bin histogram containing the expected background, signal and observed data yields. The fit is performed using a likelihood function under the S+B hypothesis in the six signal regions (ee, $e\mu$, $\mu\mu$, 3ℓ, $2\ell 1\tau_{had}$ and 4ℓ). The $2\ell 0\tau_{had}$ signal region, which provides the highest sensitivity due to the higher number of expected signal events is split into the three flavours combinations. Theory and experimental systematic uncertainties, defined in Section 6.5, are implemented as nuisance parameters with given uncertainties, which the fit is allowed to further constrain. The minimization of the likelihood $\mathcal{L}(\mu, \theta)$ function with respect to all its parameters returns the *best-fit* value of the measured signal strength.

	$2\ell 0\tau_{had}$ ee	$2\ell 0\tau_{had}$ $e\mu$	$2\ell 0\tau_{had}$ $\mu\mu$	$2\ell 1\tau_{had}$	3ℓ	4ℓ
$t\bar{t}W$	2.9 ± 0.7	9.1 ± 2.5	6.6 ± 1.6	0.8 ± 0.4	6.1 ± 1.3	—
$t\bar{t}(Z/\gamma^*)$	1.55 ± 0.29	4.3 ± 0.9	2.6 ± 0.6	1.6 ± 0.4	11.5 ± 2.0	1.12 ± 0.20
Diboson	0.38 ± 0.25	2.5 ± 1.4	0.8 ± 0.5	0.20 ± 0.15	1.8 ± 1.0	0.04 ± 0.04
Non-prompt leptons	12 ± 6	12 ± 5	8.7 ± 3.4	1.3 ± 1.2	20 ± 6	0.18 ± 0.10
Charge misreconstruction	6.9 ± 1.3	7.1 ± 1.7	—	0.24 ± 0.03	—	—
Other	0.81 ± 0.22	2.2 ± 0.6	1.4 ± 0.4	0.63 ± 0.15	3.3 ± 0.8	0.12 ± 0.05
Total background	25 ± 6	38 ± 6	20 ± 4	4.8 ± 1.4	43 ± 7	1.46 ± 0.25
$t\bar{t}H$ (SM)	2.0 ± 0.5	4.8 ± 1.0	2.9 ± 0.6	1.43 ± 0.31	6.2 ± 1.1	0.59 ± 0.10
Data	26	59	31	14	46	0

Table 6.33: Expected and observed yields in the six signal region categories corresponding to an integrated luminosity of $\mathcal{L}$=13.2 fb^{-1}. Uncertainties in the background expectations due to systematic effects and limited MC statistics are shown. *Other* backgrounds include tZ, tWZ, $tHqb$, tHW, $t\bar{t}t\bar{t}$ and triboson production. Background yields are estimated using the procedures presented in Section 6.4.

Table 6.33 shows the pre-fit yields in the six signal regions for backgrounds, expected signal, data, and their corresponding systematic uncertainties. Figures 6.20 and 6.21 show, respectively for the $2\ell 0\tau_{had}$, $2\ell 1\tau_{had}$ and 3ℓ channels, data/MC comparisons for the number of electrons in the event and the jets plus b-jets multiplicity (provided as $N = N_{b-tags} + N_{jets}$) in the signal regions. Both the $e\mu$ and $\mu\mu$ channels in the $2\ell 0\tau_{had}$ signal region show a data excess over the total SM prediction around $\sim 2\ \sigma$. A $\sim$2.4 σ data excess is also present in the $2\ell 0\tau_{had}$ signal region, mostly originated from events containing four jets one of which b-tagged, as visible from Figure 6.20b. Any of these three excesses, anyway, shows a significant deviation from the total SM prediction.

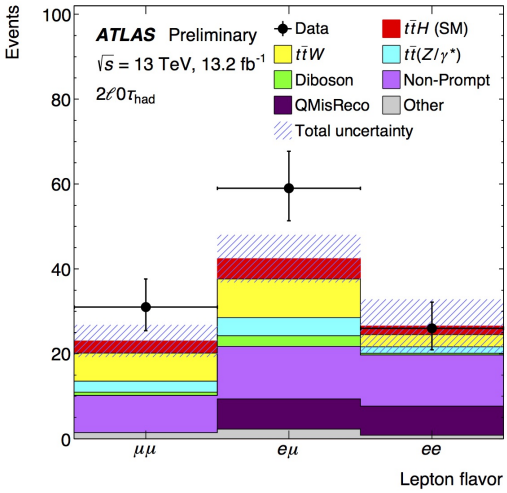

(a)

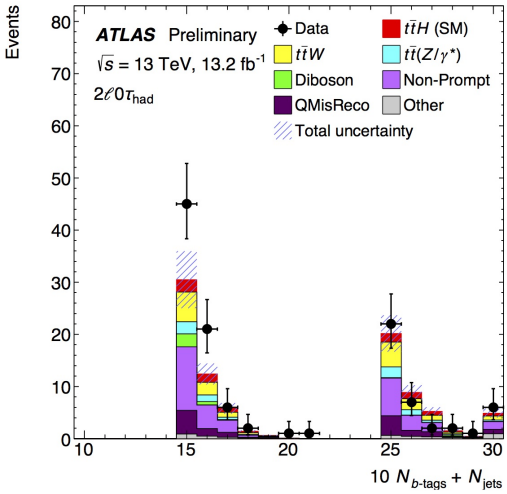

(b)

Figure 6.20: Events in the $2\ell 0\tau_{had}$ signal region: (a) lepton flavor composition; (b) 10× the number of b-tagged jets plus the total number of jets. The signal is set to the SM expectation ($\mu_{t\bar{t}H} = 1$) and the background expectation is pre-fit. The hatched region shows the total uncertainty on the background plus SM signal prediction in each bin. Charge mis-reconstruction background is indicated as "QMisReco."

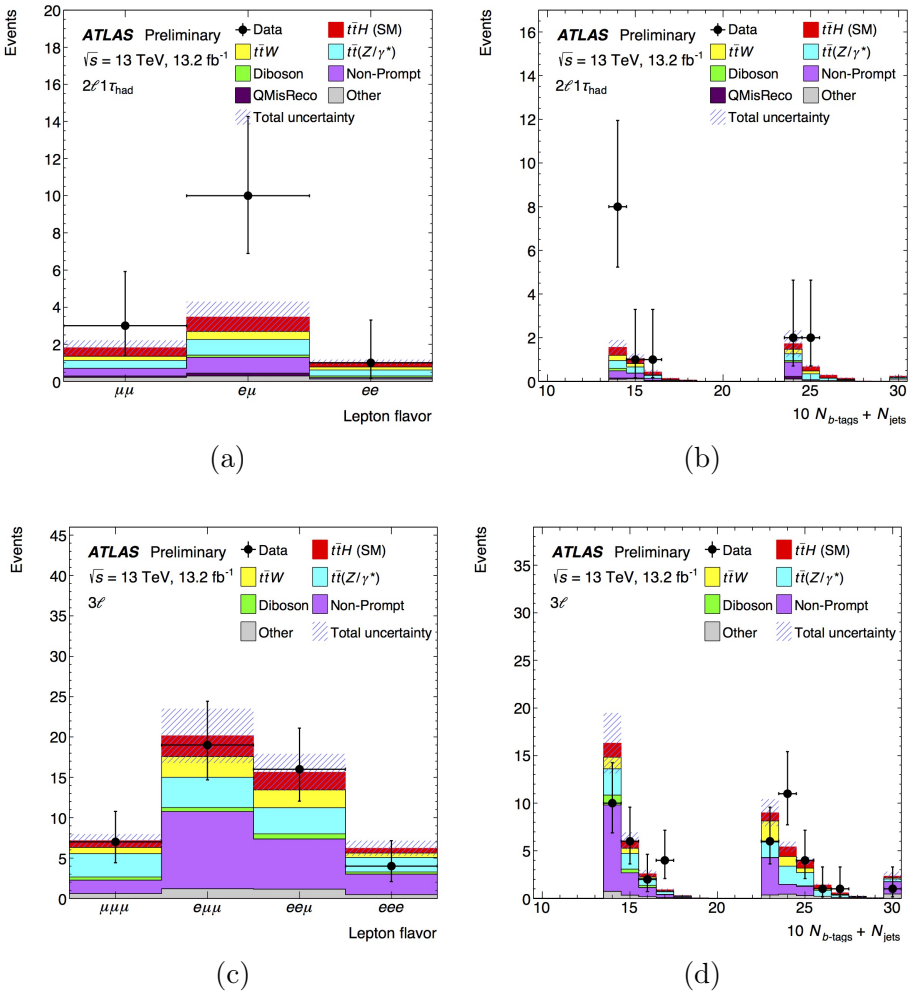

Figure 6.21: Lepton flavour composition in the $2\ell 1\tau_{had}$ signal region (a) and in the 3ℓ signal region (c). $10\times$ the number of b-tagged jets plus the total number of jets in the $2\ell 1\tau_{had}$ signal region (b) and in the 3ℓ signal region (d).The signal is set to the SM expectation ($\mu_{t\bar{t}H} = 1$) and the background expectation is pre-fit. The hatched region shows the total uncertainty on the background plus SM signal prediction in each bin. Charge mis-reconstruction backgrounds are indicated as "QMisReco."

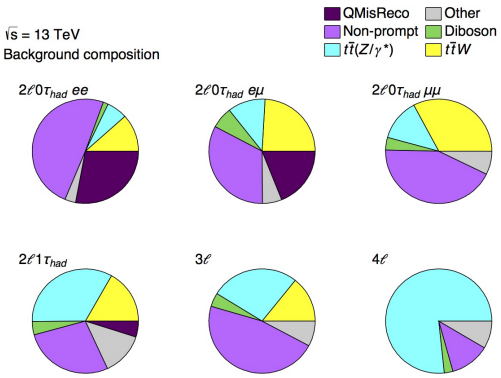

Figure 6.22: Backgrounds composition breakdown in the various signal regions. First row: $2\ell 0\tau_{had}$ signal region splitted into flavor. Second row: $2\ell 1\tau_{had}$, 3ℓ and 4ℓ signal regions.

Figure 6.22 shows the contribution from various backgrounds in the different signal regions. The major background in the $2\ell 0\tau_{had}$ channel originates from events with non-prompt leptons, contributing as ∼50 % in the ee channel and ∼45% in the $e\mu$ and $\mu\mu$ channels. In the ee channel the second largest background originates from charge mis-identification and $t\bar{t}W$ events. A similar composition is observed also in the $e\mu$ channel. Being unaffected by charge mis-identification, the $\mu\mu$ channel second most significant background arises from $t\bar{t}W$ events. Events containing non-prompt leptons also play a significant role in the 3ℓ(∼50%) and in the $2\ell 1\tau_{had}$ (∼30%) channels while are almost negligible in the 4ℓ (∼10%) channel. Indeed, the contribution from $t\bar{t}Z$ events in the $2\ell 1\tau_{had}$, 3ℓ and 4ℓ signal regions significantly increases. Table 6.34 shows the post-fit yields in the six signal regions, and a comparison between pre- and post-fit signal region total yields is provided in Fig. 6.23. Background expectations were updated to reflect the values of systematic uncertainty nuisance parameters after the fit to data. The uncertainty on the total background estimation is smaller than for the pre-fit values due to anti-correlations between the nuisance parameters obtained during the fit.

The impact of systematic uncertainties on the best-fit value μ can be assessed by looking at Figure 6.24. The information that can be extracted from this plot is the following: the $x-$axis shows the number of standard deviations the nuisance parameter had to fluctuate to adjust data/MC agreement in the fit. The dot indicates how the parameter had to be *pulled* up or down during the fit. Most of the systematic uncertainties are within 1σ from the nominal (indicated by the dashed vertical lines) value, a part from the JVT uncertainty which, as already mentioned, is pretty large and impact most the best-fit value for μ. Most of the nuisance parameters are unchanged or

	$2\ell 0\tau_{had}$ ee	$2\ell 0\tau_{had}$ $e\mu$	$2\ell 0\tau_{had}$ $\mu\mu$	$2\ell 1\tau_{had}$	3ℓ	4ℓ
$t\bar{t}W$	3.2 ± 0.9	10.4 ± 2.9	7.4 ± 1.8	1.0 ± 0.5	6.5 ± 1.5	—
$t\bar{t}(Z/\gamma^*)$	1.53 ± 0.29	4.3 ± 0.9	2.6 ± 0.6	1.7 ± 0.4	11.3 ± 1.9	1.08 ± 0.20
Diboson	0.40 ± 0.26	2.6 ± 1.5	0.8 ± 0.5	0.21 ± 0.15	1.9 ± 1.0	0.04 ± 0.04
Non-prompt leptons	9 ± 4	11 ± 4	8.9 ± 3.3	1.9 ± 1.6	15 ± 4	0.17 ± 0.10
Charge misreconstruction	7.2 ± 1.4	7.6 ± 1.8	—	0.25 ± 0.03	—	—
Other	0.83 ± 0.16	2.3 ± 0.6	1.5 ± 0.4	0.66 ± 0.16	3.4 ± 0.8	0.12 ± 0.05
Total background	22.2 ± 3.4	39 ± 5	21 ± 4	5.7 ± 1.7	39 ± 5	1.42 ± 0.24
$t\bar{t}H$ (2.5 × SM)	5.3 ± 1.8	13 ± 4	7.6 ± 2.5	4.0 ± 1.2	16 ± 5	1.5 ± 0.5
Data	26	59	31	14	46	0

Table 6.34: Post-fit background, signal, and observed yields in the six signal region categories corresponding to an integrated luminosity of $\mathcal{L}$=13.2 fb^{-1}. Uncertainties in the background expectations due to systematic effects and limited MC statistics are shown. *Other* backgrounds include tZ, tWZ, $tHqb$, tHW, $t\bar{t}t\bar{t}$ and triboson production.

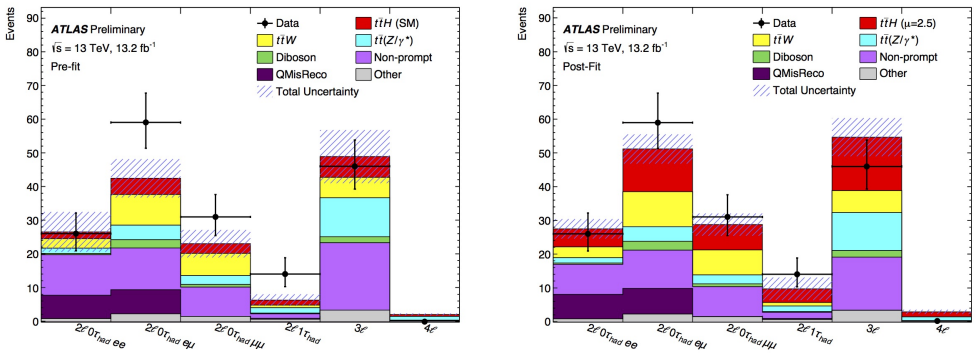

(a) (b)

Figure 6.23: Pre- (a) and post-fit (b) yields in the $t\bar{t}H$ signal regions. Data, total background and expected signal events (red contribution in the plot) are presented. The combined fit with all the six signal regions yields a $\mu = 2.5$.

slightly better constrained after fit. The uncertainty on fakes in the $2\ell 0\tau_{had}$, $2\ell 1\tau_{had}$ and 3ℓ channels (2^{nd},4^{rd} and 6^{th} points in the plot) also significantly (around ± 0.3) impact the best-fit value for μ and are not, or slightly, reduced from the fit. Their corresponding pulls are within $\pm 0.5\sigma$ from the fit nominal value.

Figure 6.25 shows the best-fit value of μ which, for the $2\ell 0\tau_{had}$ channel only is:

$$\mu_{2\ell 0\tau_{had}} = 4.0^{+1.2}_{-1.1}(\text{stat})^{+1.7}_{-1.3}(\text{syst}) \tag{6.5}$$

where the deviation from the expected SM $\mu = 1$ is mainly driven by the

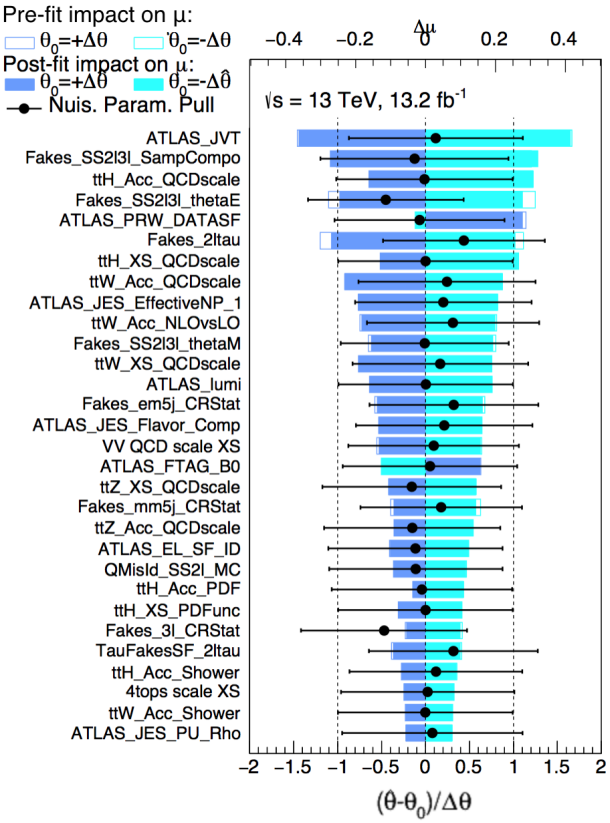

Figure 6.24: Ranking of the nuisance parameters used in the six signal regions fit according to their effect on μ. Top 30 nuisance parameters are presented in the plot. The empty blue rectangles correspond to pre-fit impact, while the filled blue ones to post-fit impact. Light (dark) blue bands correspond to downward (upwards) systematic uncertainty variations in the fit.

slight excesses in the $e\mu$ and $\mu\mu$ channels. The same stands for the μ value measured using the $2\ell 1\tau_{had}$ signal region only. The six signal regions combination leads to:

$$\mu = 2.5 \pm 0.7(\text{stat})^{+1.1}_{-0.9}(\text{syst}). \tag{6.6}$$

The 95% CL upper limit on μ is presented in Figure 6.26. For the 4ℓ channel, zero events are observed and the 68% CL upper limit is shown. Information are also presented in Table 6.35.

In presence of a SM $t\bar{t}H$ signal, the fit is expected to yield a signal strength of $\mu = 1.0\ ^{+0.7}_{-0.6}\ (\text{stat})\ ^{+0.9}_{-0.8}\ (\text{syst})$. The p-value associated with the null $t\bar{t}H$ hypothesis ($\mu = 0$) is 0.015, corresponding to 2.2 σ, while the p-value associated with the SM expectation $\mu = 1$ is 0.09, corresponding to 1.3 σ. Interpreted as a limit on the $t\bar{t}H$ signal strength, experimental data provide

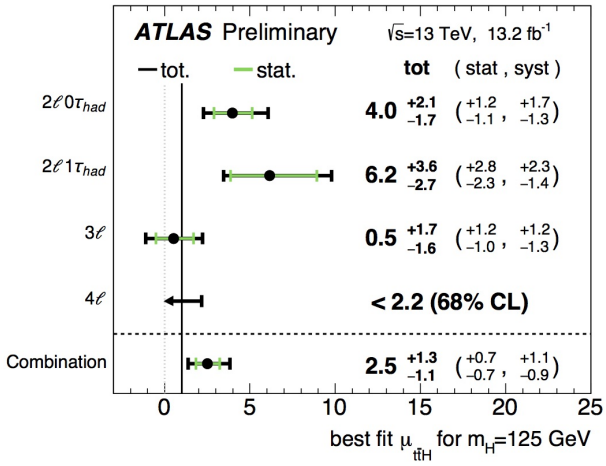

Figure 6.25: Best fit values of the $t\bar{t}H$ signal strength separated into different final states and combined. The SM predicted signal strength is μ=1. In the 4ℓ channel no events are observed in data and the 68% CL upper limit is shown.

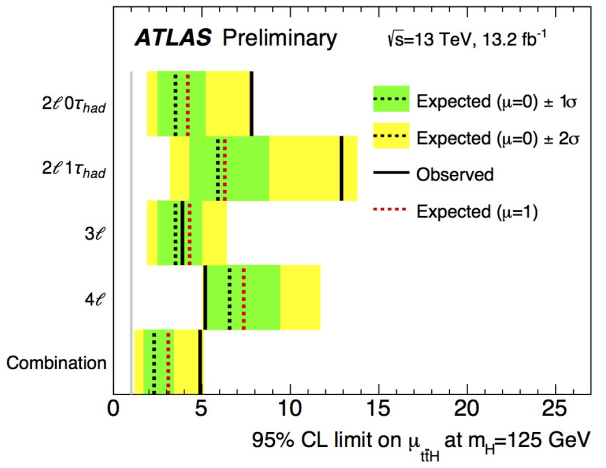

Figure 6.26: Upper limits on the $t\bar{t}H$ signal strength at 95% CL separated into different final states and combined. The median upper limit that would be set in presence of a SM $t\bar{t}H$ signal is shown as dashed line as well as the $\pm1\sigma$ (green) and $\pm2\sigma$ (yellow) bands. The observed upper limit is shown as black solid line.

$\mu < 4.9$ at 95% CL.

Category	Best-fit $\mu_{t\bar{t}H}$	Observed (expected) 95% CL upper limit	Signal-injected 95% CL upper limit
$2\ell 0\tau_{had}$	$4.0\ ^{+1.2}_{-1.1}\ ^{+1.7}_{-1.3}$	$7.8\ (3.5\ ^{+1.7}_{-1.0})$	4.2
$2\ell 1\tau_{had}$	$6.2\ ^{+2.8}_{-2.3}\ ^{+2.3}_{-1.4}$	$12.9\ (5.9\ ^{+2.9}_{-1.6})$	6.3
3ℓ	$0.5\ ^{+1.2}_{-1.0}\ ^{+1.2}_{-1.3}$	$3.9\ (3.5\ ^{+1.5}_{-1.0})$	4.3
4ℓ	< 2.2 (68% CL)	$5.2\ (6.6\ ^{+2.9}_{-1.4})$	7.4
Combined	$2.5\ ^{+0.7}_{-0.7}\ ^{+1.1}_{-0.9}$	$4.9\ (2.3\ ^{+1.1}_{-0.6})$	3.1

Table 6.35: Best-fit values of the signal strength $\mu_{t\bar{t}H}$ and 95% CL measured upper limits. For the best-fit values, the first uncertainty is statistical and the second systematic. For the expected upper limits, under the $\mu_{t\bar{t}H} = 0$ hypothesis, the median is reported, and the uncertainties give the 68% expected range. The signal-injected upper limit is the expected upper limit which would be set in the presence of a SM $t\bar{t}H$ signal with $\mu_{t\bar{t}H} = 1$. For the 4ℓ category, as zero events are observed, a 68% CL upper limit is shown in place of the best-fit value.

6.7 Analysis improvements

As shown from the signal strength measurement presented in Section 6.6, the results are limited both by statistical and systematic uncertainties, with different impacts depending on the considered signal region. The analysis presented in the previous sections was consequently further optimized using the full 2015-2016 data (corresponding to $\int \mathcal{L}dt = 36.1$ fb^{-1} [156]). A huge effort was put into reducing the impact of systematic uncertainties, mainly coming from data-driven techniques for background estimation. For this purpose, the cut and count analysis was revisited and it was decided that multivariate analysis techniques should be adopted [157]. As a general statement, cut and count analyses constrain a certain type of phase space by applying a sequence of rectangular cuts. On the contrary, MVA techniques, exploiting correlations in a multidimensional input parameter space, are able to provide a more robust selection with respect to uncertainties and a better efficiency for the same rejection power. The first attempt to use MVA for the $t\bar{t}H$ multilepton analysis was a Run 1 study [158].
There are several types of MVA methods[4], such as *Boosted Decision Trees* (BDT) or *Neural Networks* (NN).
Multivariate techniques are adopted for this analysis in multiple ways. First, a lepton MVA discriminates between prompt and non-prompt leptons. Sec-

[4] The purpose of this section is to present in a very general way which are the improvements and the results.

ondly, a multivariate based method for charge mis-identification suppression is used[5]. Lastly, event MVA further helps to discriminate signal from background and the multivariate tagger (the BDT output) is entering the final fit for signal strength measurement. Aside from analysis strategy updates, new signal regions are added to the ones present in the previous search: one lepton plus two hadronic τ (1ℓ+$2\tau_{had}$), two OS leptons plus one τ (2ℓOS+$1\tau_{had}$) and three leptons plus one τ ($3\ell + 1\tau_{had}$).
Furthermore, the definition of $t\bar{t}V$ and diboson control regions was improved, which allowed to reduce the theoretical uncertainty associated to these processes. Finally, the Matrix Method became the baseline method for fake background estimation, which resulted in a significant improvement and fundamental evolution of the FF method to predict shape information for the fake background, needed for MVA techniques.
Under the hypothesis of no $t\bar{t}H$ production, we observed an excess of events over the expected SM background with a significance of 4.1 σ.

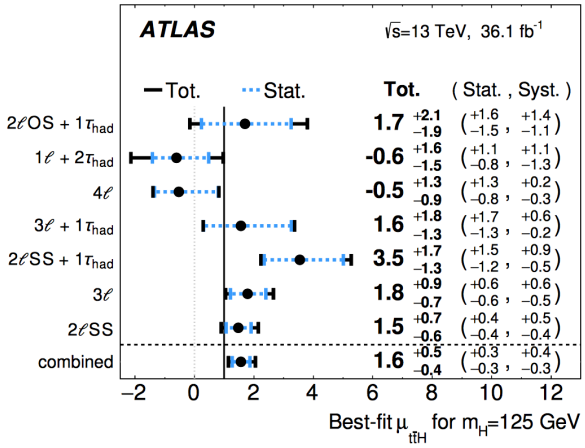

Figure 6.27: Observed best-fit values of the $t\bar{t}H$ signal strength and uncertainties divided into final state category and combined. The individual values for channels μ are obtained fitting all the signal regions with each channel signal strength floating independently.

Figure 6.27 shows the signal strength best-fit. Note that in the fit μ is unconstrained and can yield negative values. The value of μ is obtained both for each decay channel and for their combination. Individual channel results are extracted from the full fit with separate parameters of interest. The signal strengths extracted from the single channels are consistent within

[5] A common MVA tool was provided by the ATLAS `IsolationFakeForum` [159] to handle charge mis-identification background.

34% with each other. The combined measured signal strength is:

$$\mu = 1.6^{+0.5}_{-0.4}(\text{tot.})^{+0.3}_{-0.3}(\text{stat.})^{+0.4}_{-0.3}(\text{syst.}) \tag{6.7}$$

and the measured $t\bar{t}H$ cross section, compared to the predicted theoretical cross section is:

$$\sigma(t\bar{t}H)_{\text{obs}} = 790^{+150}_{-150}(\text{stat.})^{+170}_{-150}(\text{syst.})\text{fb} \tag{6.8}$$
$$\sigma(t\bar{t}H)_{\text{exp}} = 507^{+35}_{-50}\text{fb} \quad . \tag{6.9}$$

In the 4ℓ, $1\ell{+}2\tau_{had}$, $2\ell\text{OS}{+}1\tau_{had}$ and $3\ell{+}1\tau_{had}$ channels the measurement of μ is dominated by statistical uncertainties while statistical and systematic errors are of comparable size in the $2\ell\text{SS}$, 3ℓ and $2\ell\text{SS}{+}1\tau_{had}$ channels.
The results provided by the $t\bar{t}H$ in multi-lepton final states were eventually combined with other $t\bar{t}H$ channels studying the Higgs decays into $b\bar{b}$, $\gamma\gamma$ and $ZZ^* \to 4\ell$ (in a single category including all $t\bar{t}$ decays). The overlap between the various signal regions was found to be negligible.

The values of μ obtained by the different analyses (compatible at 38%) and the combination outcome is shown in Table 6.36, where it is clear that the sensitivity is driven by the multi-lepton channels combination.

Channel	Best-fit $\mu_{t\bar{t}H}$ (observed)	Best-fit $\mu_{t\bar{t}H}$ (expected)	Observed (expected) significance
Multilepton	$1.6^{+0.5}_{-0.4}$	$1^{+0.4}_{-0.4}$	4.1 σ (2.8 σ)
$H \to b\bar{b}$	$0.8^{+0.6}_{-0.6}$	$1^{+0.6}_{-0.6}$	1.4 σ (1.7 σ)
$H \to \gamma\gamma$	$0.6^{+0.7}_{-0.6}$	$1^{+0.8}_{-0.6}$	0.9 σ (1.7 σ)
$H \to 4\ell$	<1.9	$1^{+3.2}_{-1.0}$	— (0.6 σ)
Combined	$1.2^{+0.3}_{-0.3}$	$1.0^{+0.3}_{-0.3}$ 4.2 σ	3.8 σ

Table 6.36: Summary of observed and expected μ measurement and $t\bar{t}H$ production significance from individual analyses and their combination. As no events are observed in the $H \to 4\ell$ analysis, a 68% CL upper limit on $\mu_{t\bar{t}H}$ is reported.

This chapter presented a search for $t\bar{t}H$ production into multi-lepton final states, with particular attention to the two SS lepton final states. A first attempt towards the evidence was made by the analysis performed on 13.2 fb^{-1}, fundamental to lay the bases towards the full 2015 and 2016 result (corresponding to 36.1 fb^{-1}). Some of the techniques developed for the first round of the analysis, such as the Matrix Method fake estimation or the multivariate techniques, were fundamental towards the evidence of $t\bar{t}H$ production at 4.2σ. This result is extremely important because it allowed a

first measurement of the $t\bar{t}H$ production cross-section which was found to be in agreement with SM expectations.
With the newly incoming statistics it will be also possible to perform differential measurements, considering for instance the Higgs boson p_{T} spectrum, allowing for potential NP discovery in distribution tails. Differential measurements are in fact already possible for some Higgs boson channels, as in the so-called *golden channel*: $H \to ZZ^* \to 4\ell$ [160].
No indirect evidence for new physics was found in the search for the $t\bar{t}H$ production so far, and the observed value of the signal strength is compatible with the Standard Model expectations at 95% CL. Nevertheless this channel provides one of the most interesting and challenging Higgs channels towards new physics discoveries.

Chapter 7

Search for $H^{\pm\pm}$, N_R and W_R production

This chapter presents a search for BSM particles appearing in LRSM, discussed in Section 1.4.1. The analysis searches for the production of doubly charged Higgs bosons as well as right-handed W bosons and Majorana neutrinos.
This search is performed using the 2015 and 2016 total dataset collected with the ATLAS detector at $\sqrt{s} = 13$ TeV, corresponding to a total integrated luminosity of $\mathcal{L}$ =36.1 fb^{-1} [161]. This chapter defines the analysis objects and event selection (Section 7.2), outlines the analysis strategy (Section 7.4), the background estimation (Section 7.6) and the results (Section 7.9). Finally, the search for the production of right-handed W bosons and neutrinos is presented (Section 7.10).

7.1 Analysis overview

As presented in Section 2.5, the main production mechanism for $H^{\pm\pm}$ is pair production via Drell-Yan process. The analysis assumes the vacuum expectation value of the Higgs triplet, containing the $H^{\pm\pm}$, to be zero, so that only decays into leptons are possible (as explained in Section 2.5.1). However, only final states containing two, three or four light ($\ell = e, \mu$) leptons are considered in this analysis. The SM background differs both for its topology and for its impact across the analysis regions. For instance, events containing three leptons are mostly affected by diboson, while for events containing two electrons the major backgrounds are Drell-Yan and fakes. Therefore, according to lepton multiplicity, different control and validation regions are

defined to constrain backgrounds.
The mass of the $H^{\pm\pm}$ is not predicted by the theory and different mass hypotheses for the new particle are tested, varying from 200 GeV to 1300 GeV. Masses below 200 GeV are not taken into account in this analysis, as they are excluded by previous searches (as from Section 2.5). Despite the assumption that the $H^{\pm\pm}$ only decays into pairs of leptons, its branching ratio to electrons, muons, or mixed flavour final states is model dependent. For this reason, the search will treat the $H^{\pm\pm}$ branching ratio as a free parameter and perform a scan over all its possible combinations (as detailed in Section 7.9).

	Lepton multiplicity					
	0	1	2	3	4	5
$m_{H^{\pm\pm}} = 200$ GeV						
Loose	0.04%	1.3%	12.2%	35.3%	50.9%	0.2%
Tight	0.2%	2.8%	16.8%	40%	40%	0.2%
$m_{H^{\pm\pm}} = 500$ GeV						
Loose	0.02%	0.5%	6.3%	31.1%	61.7%	0.4%
Tight	0.04%	0.9%	8.1%	33.7%	57.2%	0.5%
$m_{H^{\pm\pm}} = 1000$ GeV						
Loose	0.01%	0.4%	5.2%	29.9%	64.4%	0.5%
Tight	0.03%	0.7%	6.6%	31.8%	60.8%	0.2%

Table 7.1: Fraction of signal events as a function of the exclusive lepton multiplicity in three different signal samples: $m_{H^{\pm\pm}}$ [GeV]$= \{200, 500, 1000\}$. Signal acceptance is calculated dividing the number of events containing from zero up to five leptons by the number of total generated events. Signal acceptance is evaluated both for the analysis *loose* and for *tight* lepton definitions. Events with two, three or four leptons always contain at least one SS lepton pair.

Signal acceptance for different mass hypotheses is provided in Table 7.1, where leptons are selected using the *loose* and *tight* lepton definitions provided in Section 7.3. The baseline selection has an efficiency to four leptons ranging from 40% to 60% and, as expected, the number of events containing four leptons (i.e. two pairs) is higher than the events containing exactly one pair. It is also visible that tightening the selection from loose to tight, 6% of events migrate from the four lepton into the three lepton category. That means that the two and three lepton categories are fundamental to retrieve events where a fourth lepton is lost due to selection acceptance.

7.2 Data and simulated samples

7.2.1 Data

The data used in this analysis are collected during 2015 (periods D-J5) and 2016 (periods A-L), with a center-of-mass energy of $\sqrt{s}$= 13 TeV and a bunch spacing of 25 ns. The total integrated luminosity recorded by the ATLAS detector and satisfying the GRL requirements is $\int \mathcal{L}dt$ =36.1 fb^{-1}. The analysis is performed using three different ATLAS derivations: `EXOT12` for the nominal analysis selection, `EXOT19` for electron fake measurement and `HIGG3D3` for muon fake measurement, described in Section 5.2.

According to lepton flavour and multiplicity, events are collected using different sets of triggers. The trigger choice is the result of a number of considerations:

- $e^{\pm}e^{\pm}$, $e^{\pm}e^{\pm}e^{\mp}$ and $e^{\pm}e^{\pm}e^{\mp}e^{\mp}$ events are selected using a dielectron trigger, `HLT_2e17_lhloose`, applying a threshold on the electron transverse energy E_{T} = 17 GeV. Moreover, the identification requirement on the electron is the `LHLoose` working point, without any further requirement on the electron isolation. The choice of the dielectron trigger is driven by the fact that all the available single electron triggers, despite providing higher acceptance, implement a tighter ID requirement than the baseline loose analysis electron.

- $\mu^{\pm}\mu^{\pm}$, $\mu^{\pm}\mu^{\pm}\mu^{\mp}$ and $\mu^{\pm}\mu^{\pm}\mu^{\mp}\mu^{\mp}$ events are selected with a logical OR combination of two single muon triggers `HLT_mu26_ivarmedium` OR `HLT_mu50`. The first trigger applies a p_{T} threshold of 26 GeV on the muon while the second one a p_{T} threshold of 50 GeV. Furthermore, the first trigger also applies an isolation requirement on the muon according to the `medium` working point, as discussed in Section 6.2.1.

- $e^{\pm}\mu^{\pm}$ events are selected with a mixed flavour dilepton trigger `HLT_e17_lhloose_nod0_mu14` requiring one electron and one muon with, respectively, a E_{T} threshold of 17 GeV and a p_{T} threshold of 14 GeV. A `LHLoose` requirement is applied on the electron identification and no on-line d_0 requirement is applied.

- finally, all the other channels, containing at least three mixed flavour leptons, namely, $\ell^{\pm}\ell^{\pm}\ell'^{\mp}$, $\ell^{\pm}\ell'^{\pm}\ell^{\mp}$, $\ell^{\pm}\ell^{\pm}\ell'^{\mp}\ell'^{\mp}$ and $\ell'^{\pm}\ell^{\pm}\ell'^{\mp}\ell^{\mp}$, are selected using a logical OR combination of all the above stated trigger items: `HLT_2e17_lhloose` OR `HLT_mu26_ivarmedium` OR `HLT_mu50` OR `HLT_e17_lhloose_nod0_mu14`.

7.2.2 Monte Carlo samples

MC samples used in this search are summarized in Table 7.2.

Physics process	Event generator	Parton shower	PDF set	Tuning	σ (pb)
$H^{\pm\pm}$	Pythia 8	Pythia 8	NNPDF2.3 NLO	A14	-
$Z/\gamma^* \to ee/\mu\mu/\tau\tau$	Powheg-Box v2	Pythia 8	CT10	AZNLO	5852
$t\bar{t}$	Powheg-Box v2	Pythia 8	NNPDF3.0 NLO	A14	831
single t	Powheg-Box v2	Pythia 6	CT10	Perugia 2012	143
$t\bar{t}W$, $t\bar{t}Z/\gamma^*$	MG5_aMC@NLO 2.2.2	Pythia 8	NNPDF2.3 NLO	A14	1.326
$t\bar{t}H$	MG5_aMC@NLO 2.3.2	Pythia 8	NNPDF2.3 NLO	A14	0.509
ZZ, WZ	Sherpa 2.2.1	Sherpa	NNPDF3.0 NLO	Sherpa default	22
Other (inc. $W^{\pm}W^{\pm}$)	Sherpa 2.1.1	Sherpa	CT10	Sherpa default	166

Table 7.2: Simulated signal and background event samples used in the search for $H^{\pm\pm}$ production: the corresponding ME generator, PS, PDF set used for the ME and set of tuned parameters are shown for each sample. The predicted cross-sections for $H^{\pm\pm}$ production are reported in Table 7.3.

- **Signal**: the $H^{\pm\pm}$ signal sample is generated at LO using Pythia 8 implementing the left-right symmetric package with the NNPDF2.3LO PDF set. The production of $H^{\pm\pm}$ only occurs via Drell-Yan pair production. The theoretical cross-section is calculated at $\sqrt{s} = 14$ TeV with NLO accuracy [162]. The NLO corrections to $H^{\pm\pm}$ production account for virtual gluon exchange, gluon and quark emission, and increase the LO cross-sections by 20-30%. The cross-section is consequently rescaled from $\sqrt{s} = 14$ TeV to $\sqrt{s} = 13$ TeV with the CTEQ6 PDF set and normalized to the NLO values by using the *k-factors*, defined as $k = \sigma_{NLO}/\sigma_{LO}$, reported in Table 7.3.

  The couplings of the $H^{\pm\pm}$ to light lepton pairs ($h_{\ell\ell'}$) are assumed to be the same for $H_L^{\pm\pm}$ and $H_R^{\pm\pm}$. The decay width of the $H^{\pm\pm}$ to leptons depends on the coupling value $h_{\ell\ell'}$ and they are set to $h_{\ell\ell'}$ =0.02. This choice guarantees a negligible decay width compared to the detector resolution. The couplings to τ leptons, namely $h_{\ell\tau}$ and $h_{\tau\tau}$ are set to zero. A total of 23 signal samples are generated with different mass hypotheses, from 200 GeV up to 1300 GeV, in steps of 50 GeV.

- **Drell-Yan processes:** are modelled using Powheg-Box v2 interfaced to Pythia 8 for PS. The CT10 set of PDF is used to calculate the hard scattering process while non-perturbative effects are modelled with the AZNLO tune in combination with the CTEQ6L1 PDF set. To simulate the emission of photons from electroweak vertices and charged

$m(H^{\pm})$[GeV]	$\sigma(H_L^{\pm\pm})$ [fb]	k-factor ($H_L^{\pm\pm}$)	$\sigma(H_R^{\pm\pm})$ [fb]	k-factor ($H_R^{\pm\pm}$)
300	13	1.25	5.6	1.25
400	3.9	1.24	1.7	1.24
500	1.4	1.24	0.61	1.24
600	0.58	1.23	0.25	1.24
700	0.26	1.23	0.11	1.23
800	0.12	1.22	0.054	1.23
900	0.062	1.22	0.027	1.23
1000	0.032	1.22	0.014	1.24
1100	0.017	1.23	0.0076	1.24
1200	0.0094	1.23	0.0042	1.25
1300	0.0052	1.24	0.0023	1.26

Table 7.3: NLO cross-sections for pair production of $H_L^{\pm\pm}H_L^{\mp\mp}$ and $H_R^{\pm\pm}H_R^{\mp\mp}$ in pp collisions at $\sqrt{s}$ =13 TeV together with the correction factors k used to obtain those values from the LO prediction. The values are here provided for representative mass points in steps of 100 GeV.

leptons, PHOTOS++ version 3.52 [149] is used. The process generation is divided into 19 samples with subsequent invariant mass intervals to guarantee a good statistical coverage over the entire mass range.
Higher order corrections are applied to Drell-Yan events to scale the mass-dependent cross-section computed at NLO in QCD with the CT10 PDF set and to NNLO in QCD with the CT14NNLO PDF set. The corrections are calculated with VRAP [163] for QCD effects and additional NLO electroweak corrections are implemented with MCSANC [164].
An additional $Z \to ee$ sample is generated with SHERPA 2.2.1 and used to measure the probability of electron charge mis-identification, as explained in Section 7.6. This choice is justified by the fact that the electron p_{T} spectrum modelling implemented in SHERPA offered a better description with respect to the one provided by POWHEG-BOX v2, especially for electron pair invariant masses close to the Z boson mass. SHERPA uses Comix [165] and OpenLoops [166] to calculate the matrix elements up to two partons at NLO and up to four partons at LO in QCD.

- $\boldsymbol{t\bar{t}}$: is simulated using POWHEG-BOX v2, with the NNPDF3.0 PDF set, interfaced with PYTHIA for parton showering. The A14 parameter set together with the NNPDF2.3 PDF set is used for tuning the shower. Moreover, top-quark spin correlations are preserved through the use of

MadSpin [167]. The predicted $t\bar{t}$ production cross-section is calculated with Top++2.0 [168] to NNLO in perturbative QCD, including soft-gluon resummation to NNLL order.

- **Single top**: the production of a single top associated with a W boson is modelled with Powheg-Box v2 v2 using CT10 PDF in the matrix element calculations. The single top production via $s-$ or $t-$channel is instead generated with Powheg-Box v2. This generator uses the four-flavour scheme for the NLO QCD ME calculation together with the fixed four-flavour PDF CT10f4. Pythia 6 is used for the PS, hadronization and underlying event simulation with the CTEQ6L1 PDF and the Perugia 2012 tune.

- ***ttV***: these processes are generated at LO with MadGraph v2.3.2 with the NNPDF2.3 set, interfaced with Pythia 8 for showering configured with the A14 tune.

- **Diboson**: the modeling of processes involving diboson decays to leptons, namely $VV \to 4\ell, 3\ell + 1\nu, 2\ell + 2\nu$, is performed using Sherpa 2.2.1, containing at ME all diagrams with four electroweak vertices. They are calculated up to three partons at LO accuracy and up to one $(4\ell, 2\ell + 2\nu)$ or zero partons $(3\ell + 1\nu)$ at NLO QCD using Comix and OpenLoops. The PDF used is NNPDF3.0NNLO.
  Diboson processes involving one hadronic boson decay are predicted by Sherpa 2.1.1. They are calculated for up to three additional partons at LO accuracy and up to one (ZZ) or zero (WW, WZ) additional partons at NLO using Comix and OpenLoops with the CT10 PDF set. Loop-induced diboson production with both gauge bosons decaying fully leptonically are also simulated with Sherpa 2.1.1.
  Given that diboson production is one of the main background for many of the analysis channels, additional diboson samples for WZ and ZZ production are generated with Powheg-Box v2 interfaced with Pythia 8 using the CT10 PDF set for the ME and the CTEQL1 PDF for PS. Non-perturbative effects are modelled with the AZNLO tune. These additional samples allow to estimate the theoretical uncertainties on the diboson cross-section calculation, as discussed in Section 7.8.

7.3 Object definition

To be able to apply data-driven techniques for background estimation, the analysis exploits two types of lepton definition, called *loose* and *tight*.

Tables 7.4 and 7.5 describe the selection criteria for electrons and muons, respectively.

Requirement	Signal electrons (tight)	Background electrons (loose)
Identification	`LHMedium`	`LHLoose`
Isolation	`Loose`	-
p_{T}	$p_{\mathrm{T}} > 30$ GeV	$p_{\mathrm{T}} > 30$ GeV
η	$\lvert\eta\rvert < 2.47$ and veto $1.37 < \lvert\eta\rvert < 2.47$	$\lvert\eta\rvert < 2.47$ and veto $1.37 < \lvert\eta\rvert < 2.47$
$\lvert d_0\rvert/\sigma_{d_0}$	$\lvert d_0\rvert/\sigma_{d_0} < 5$	$\lvert d_0\rvert/\sigma_{d_0} < 5$
$\lvert z_0 \sin\theta\rvert$	$\lvert z_0 \sin\theta\rvert < 0.5$ mm	$\lvert z_0 \sin\theta\rvert < 0.5$ mm

Table 7.4: Object definition requirements for tight (left) and loose (right) electrons. It is worth noting that loose electrons can either fail the `LHMedium` identification or the `Loose` isolation requirements, or both.

Requirement	Signal muons (tight)	Background muons (loose)
Identification	`Medium`	`Medium`
Isolation	`FixedCutTightTrackOnly`	fail `FixedCutTightTrackOnly`
p_{T}	$p_{\mathrm{T}} > 30$ GeV	$p_{\mathrm{T}} > 30$ GeV
η	$\eta < 2.5$	$\eta < 2.5$
$\lvert d_0\rvert/\sigma_{d_0}$	$\lvert d_0\rvert/\sigma_{d_0} < 3$	$\lvert d_0\rvert/\sigma_{d_0} < 10$
$\lvert z_0 \sin\theta\rvert$	$\lvert z_0 \sin\theta\rvert < 0.5$ mm	$\lvert z_0 \sin\theta\rvert < 0.5$ mm

Table 7.5: Object definition requirements for tight (left) and loose (right) muons. Loose muons have a looser selection cut on the significance of the transverse impact parameter $|d_0|/\sigma_{d_0}$ (relaxed from 3 to 10) and have to fail the `FixedCutTightTrackOnly` isolation requirement.

Having higher probability to be fake, loose leptons are explicitly required to fail the isolation or identification tight requirements. In the muon case, they also have a relaxed cut on the transverse impact parameter significance. Consequently, both the electron and muon tight leptons are not a sub-sample of the loose ones.

Jets are reconstructed with an anti-k_t radius of 0.4 and they are accepted if $p_{\mathrm{T}} > 25$ GeV and $|\eta| < 2.5$. *Bad jets*, originated from beam background or from noisy calorimetric cells, are removed. To suppress the contribution from pile-up jets, the JVT cut is applied to jets belonging to the fiducial region $p_{\mathrm{T}} < 60$ GeV and $|\eta| < 2.4$. Jets originating from b-hadron decays are

identified by the MV2c10 algorithm using the 77% efficiency working point (see Section 4.4). To reduce the contamination due to the $t\bar{t}$ and top process, events are discarded if containing at least one b-jet.

After electron, muon and jet reconstruction, possible objects duplication is resolved using the dedicated overlap removal procedure (discussed in Section 4.6). The procedure follows the same steps of the one described in Table 6.13 in the search for $t\bar{t}H$ production. The only exception regards τ leptons which, not entering this analysis selections, do not need to be taken into account. The procedure is summarized in Table 7.6.

Keep	Remove	ΔR cone size or tracks
electron	CT muon	sharing an ID track (no muon spectrometer track)
muon	electron	sharing an ID track
electron	jet	0.2
jet	electron	0.4
muon	jet	(0.2 or "ghost-matched" to muon) and (jet tracks $\leq$2)
jet	muon	0.4

Table 7.6: Summary of the overlap removal steps performed on electrons, muons, and jets.

7.4 Analysis regions

Analysis regions are defined on the basis of the event lepton multiplicity. The main background to this search, besides the one arising from fake leptons, are Drell-Yan and diboson production. Events with mis-reconstructed electron charge contribute only to channels containing electrons in the final state while the diboson background contributes, with different impact, to all the analysis regions.
Control and validation regions are designed to constrain different background processes:

- *fake leptons*: this background contributes to all the analysis regions and is evaluated using data-driven methods, as discussed in Section 7.6. The regions used to validate the fake background estimation are reported in Table 7.7 and are the *same-charge validation region* (SCVR) and the *three lepton validation region* (3LVR).

- *Drell-Yan*: it enters the signal regions when one of the final state electron undergoes charge-flip. A dedicated control region is designed to extract the normalization of this process: the *opposite-charge control region* (OCCR), defined by the presence of exactly two OS electrons. The normalization factor extracted from the OCCR is applied to all the electron regions where a contribution from Drell-Yan events is present (as discussed in more details in Section 7.9). The goodness of the charge mis-identification estimate is assessed in the SCVR (Table 7.7).

- *diboson*: it enters all the analysis regions and its contribution is separately assessed in different control regions, divided by lepton multiplicity and flavour combination, namely the *diboson control regions* (DBCR). In all the DBCRs, the presence of at least one Z boson is required by applying a cut on the OS and same-flavour pair: 81.2 GeV $< m(\ell^+\ell^-) <$ 101.2 GeV. Diboson events are validated in the 3LVR (Table 7.7).

Region / Channel	Control Regions			Validation Regions			Signal Regions		
	OCCR	DBCR	4LCR	SCVR	3LVR	4LVR	1P2L	1P3L	2P4L
Electron channel	$e^\pm e^\mp$	$e^\pm e^\pm e^\mp$		$e^\pm e^\pm$	$e^\pm e^\pm e^\mp$		$e^\pm e^\pm$	$e^\pm e^\pm e^\mp$	
Mixed channel	-	$e^\pm\mu^\pm\ell^\mp$	$\ell^\pm\ell^\pm$ $\ell^\mp\ell^\mp$	$e^\pm\mu^\pm$	$e^\pm\mu^\pm\ell^\mp$ $\ell^\pm\ell^\pm\ell'^\mp$	$\ell^\pm\ell^\pm$ $\ell^\mp\ell^\mp$	$e^\pm\mu^\pm$	$e^\pm\mu^\pm\ell^\mp$ $\ell^\pm\ell^\pm\ell'^\mp$	$\ell^\pm\ell^\pm$ $\ell^\mp\ell^\mp$
Muon channel	-	$\mu^\pm\mu^\pm\mu^\mp$		$\mu^\pm\mu^\pm$	$\mu^\pm\mu^\pm\mu^\mp$		$\mu^\pm\mu^\pm$	$\mu^\pm\mu^\pm\mu^\mp$	
$m(e^\pm e^\pm)$ [GeV]	$[130, 2000]$	$[90, 200)$		$[130, 200)$	$[90, 200)$		$[200, \infty)$	$[200, \infty)$	
$m(\ell^\pm\ell^\pm)$ [GeV]	-	$[90, 200)$	$[60, 150)$	$[130, 200)$	$[90, 200)$	$[150, 200)$	$[200, \infty)$	$[200, \infty)$	$[200, \infty)$
$m(\mu^\pm\mu^\pm)$ [GeV]	-	$[60, 200)$		$[60, 200)$	$[60, 200)$		$[200, \infty)$	$[200, \infty)$	
b-jet veto	✓	✓	✓	✓	✓	✓	✓	✓	✓
Z veto	-	inverted	-	-	✓	-	-	✓	✓
$\Delta R(\ell^\pm, \ell^\pm) < 3.5$	-	-	-	-	-	-	✓	✓	-
$p_{\mathrm{T}}(\ell^\pm\ell^\pm) > 100$ GeV	-	-	-	-	-	-	✓	✓	-
$\sum \lvert p_{\mathrm{T}}(\ell)\rvert > 300$ GeV	-	-	-	-	-	-	✓	✓	-
$\Delta M/\bar{M}$ requirement	-	-	-	-	-	-	-	-	✓

Table 7.7: Summary of all regions used in the analysis. The table is split into three blocks: the upper block indicates the final states for each region, the middle block indicates the mass range of the corresponding final state, and the lower block indicates the event selection criteria for the region. The application of a selection requirement is indicated by a check-mark (✓). In the three lepton regions, $\ell^\pm\ell^\pm\ell'^\mp$ indicates that SS leptons have the same flavour, while the OS lepton has a different flavour.

A summary of all the analysis regions is provided in Table 7.7. A detailed description of the selection criteria used to define signal regions is provided in Section 7.5.

A lower mass bound of 60 GeV is imposed on the SS lepton pair invariant mass in all channels to discard events from low-mass resonances. In the electron channel, to ensure orthogonality between the Z region used for the extraction of the charge-flip rates and the control region, the lower mass bound is increased to 130 GeV. With respect to the electron channel, to increase the statistical size of the mixed flavour channel and of the three lepton regions, the lower mass bound is decreased from 130 GeV to 90 GeV. As the charge mis-identification background does not affect the muon channel, the lower mass bound stays as loose as 60 GeV.
The regions containing four leptons are characterized by very low number of events and their optimization procedure are treated separately in the following. This region is particularly powerful and is explored for the first time in ATLAS.

7.5 Signal regions optimization

The striking feature of the signal topology is the possibility to exploit the properties of the pair production mode. To define signal regions, divided on the basis of lepton multiplicity, we need to find, and cut on, variables with high discrimination power between signal and SM backgrounds.
As presented in Table 7.1, under the hypothesis of 100% $H^{\pm\pm}$ branching ratio to light leptons, the majority of the events contains four leptons and exactly two SS pairs. Events with two or three leptons gain sensitivity as long as the branching ratio to leptons decrease to values below 100% (as will be clearly presented in Section 7.9). Signal regions are separately optimized according to the number of leptons and lepton pairs.

7.5.1 Two and three lepton signal region optimization

The signal we are interested in has a precise topology. Pairs of $H^{\pm\pm}$, heavy bosons with same mass are typically produced back-to-back. From the decay of the $H^{\pm\pm}$ into pairs of leptons with same charge we expect the typical distribution of a two-body decay. The opposite statement is true for SS leptons from SM backgrounds. It is sufficient to think that for ZZ production SS leptons, being uncorrelated, are more randomly located in the ATLAS detector. Moreover, given the high mass of the expected resonance, we expect leptons in the final state to have high transverse momentum.
The variables we exploit for the optimization are consequently the ΔR distance between the two SS leptons, the transverse momentum of the SS pair and the scalar sum of all reconstructed objects in the final state. The main

background in the two and three lepton signal regions depends on lepton flavour. Electron channels are almost equally affected by Drell-Yan, diboson and fake contamination while for the mixed and muon channels the major background is diboson and fakes.
Four lepton final states from diboson production, where one or two leptons are lost due to selection acceptance, provides a pair of OS close-by leptons and, possibly, a third any-sign lepton. Requiring the SS leptons to be close inside the detector helps to reject a substantial fraction of these type of events. Three signal mass hypotheses are tested $m_{H^{\pm\pm}} = \{500, 600, 700\}$ GeV against the SM background, assuming a branching ratio of 100% in each lepton flavour category.

Figures 7.1 and 7.2 show the $\Delta R(\ell^{\pm}, \ell^{\pm})$ distribution divided into flavour channel and lepton multiplicity. As expected, SS leptons originating from signal decay cluster at moderate $\Delta R(\ell^{\pm}, \ell^{\pm})$, both for the 1P2L and the 1P3L signal regions. Based on these distributions, a cut on $\Delta R(\ell^{\pm}, \ell^{\pm})$ <3.5 is chosen.
As already anticipated, another powerful cut which is applied to reduce the SM background is the one involving the SS pair transverse momentum. Figures 7.3 and 7.4 indeed show the $p_{\mathrm{T}}(\ell^{\pm}, \ell^{\pm})$ distributions before and after optimization for the 1P2L and 1P3L signal regions respectively. The SS pair is shifted towards higher transverse momenta, and the shift increases with the signal invariant mass. A minimum requirement on the SS leptons transverse momentum at $p_{\mathrm{T}}(\ell^{\pm}, \ell^{\pm}) > 100$ GeV is chosen.
Figure 7.5 additionally shows the distributions for the scalar sum of all lepton p_{T} in the 1P3L signal region. Also in this case the signal boost can be exploited and a lower p_{T} cut at 300 GeV is set. The combination of the three above stated cuts results in a ∼10 times background rejection in all channels, as shown in Fig. 7.1, 7.2, 7.3, 7.4 and 7.5. These distributions are produced using the combination of all the selection criteria defining the 2L and 3L signal regions: $\Delta R(\ell^{\pm}, \ell^{\pm})$ <3.5, $p_{\mathrm{T}}(\ell^{\pm}, \ell^{\pm}) > 100$ GeV and $\sum p_{\mathrm{T}}^{\ell} >$ 300 GeV.

The variable which is used to set limits on the $H^{\pm\pm}$ production cross-section, in the absence of any excess over the Standard Model signal, is the invariant mass of the SS pair, shown in Fig. 7.6. Under the hypothesis of 100% branching ratio to leptons, as expected, the signal region containing exactly two SS leptons is the less sensitive one, with the lowest $s/\sqrt{b}$ significance. This is a consequence both of the low signal efficiency for events containing exactly two leptons and of the higher background contamination from Standard Model events containing exactly two leptons. The three lepton signal region, on the contrary, features a lower Standard Model background and a ∼30% signal efficiency. Moreover, in 1P3L the majority of the back-

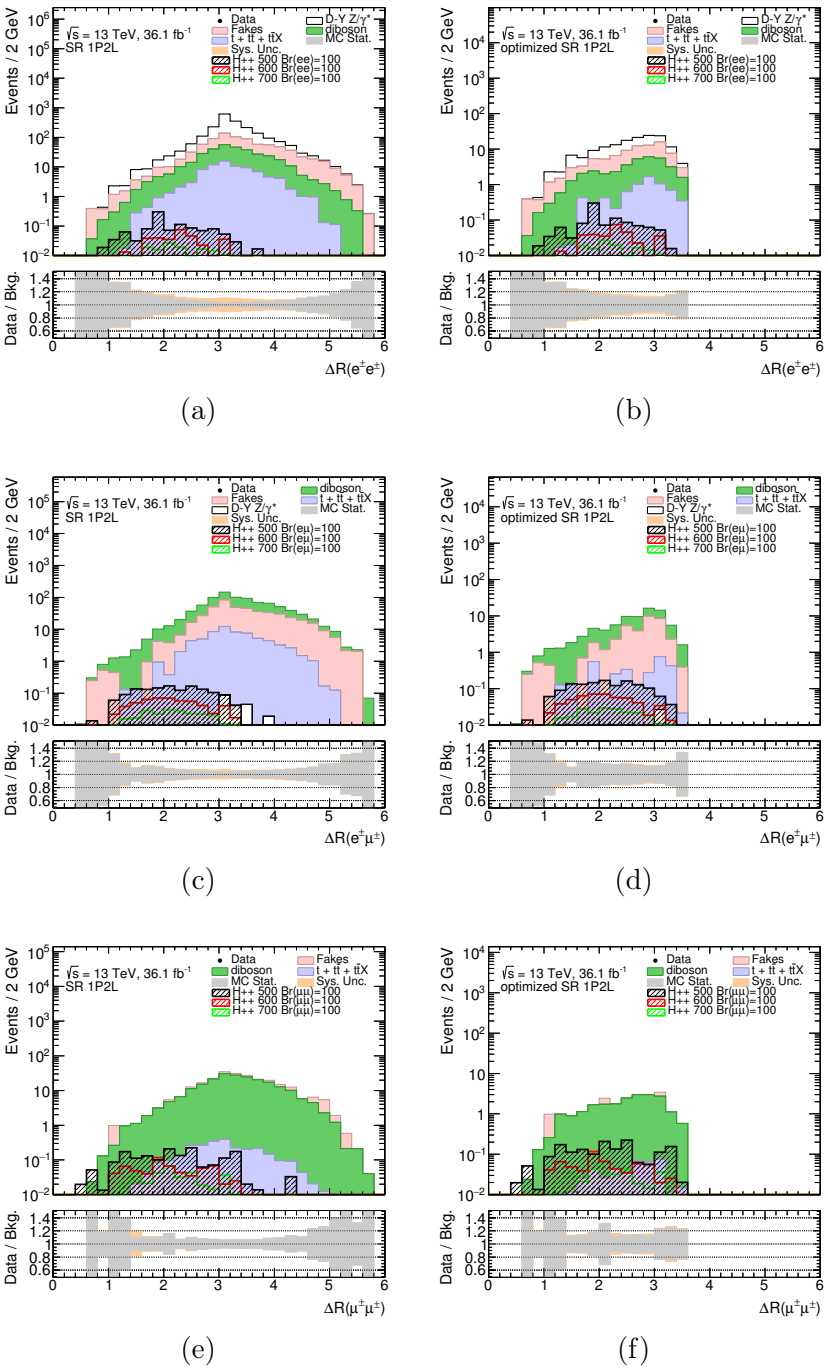

Figure 7.1: 1P2L signal region $\Delta R(\ell^{\pm}, \ell^{\pm})$ distributions for the electron (a), (b), mixed (c), (d) and muon (e), (f) channels respectively before and after optimization.

ground consists of diboson events, for which very few events with SS invariant masses above 400 GeV are observed.

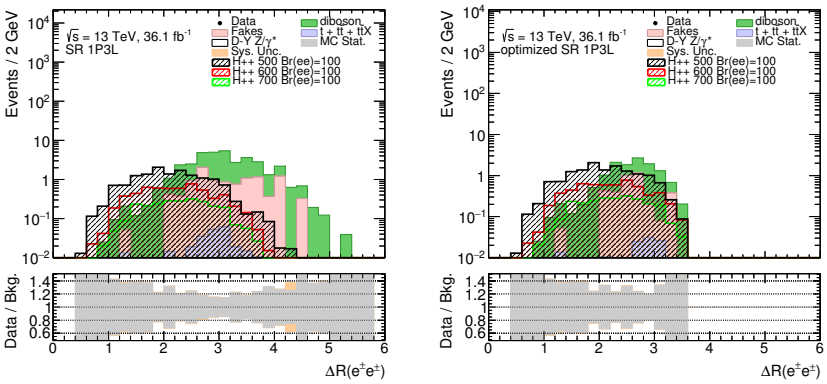

(a) (b)

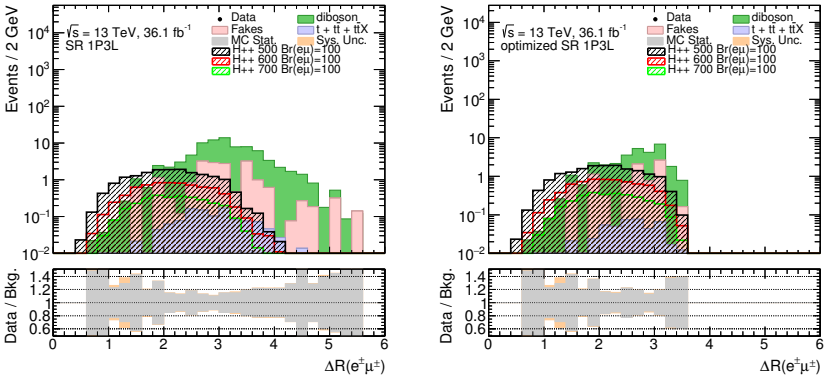

(c) (d)

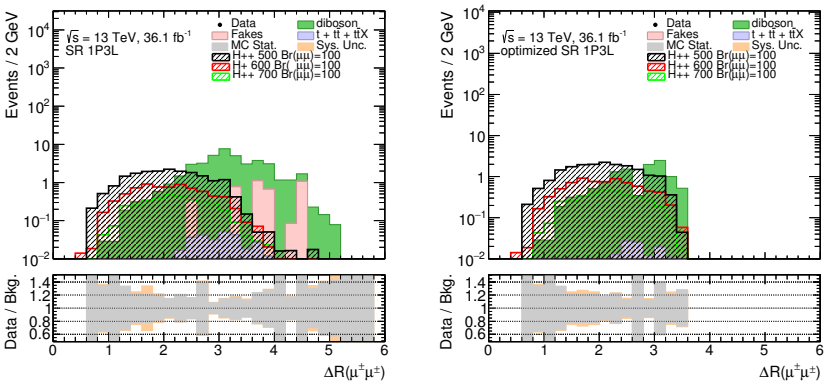

(e) (f)

Figure 7.2: 1P3L signal region $\Delta R(\ell^{\pm}, \ell^{\pm})$ distributions for the electron (a), (b), mixed (c), (d) and muon (e), (f) channels respectively before and after SR optimization.

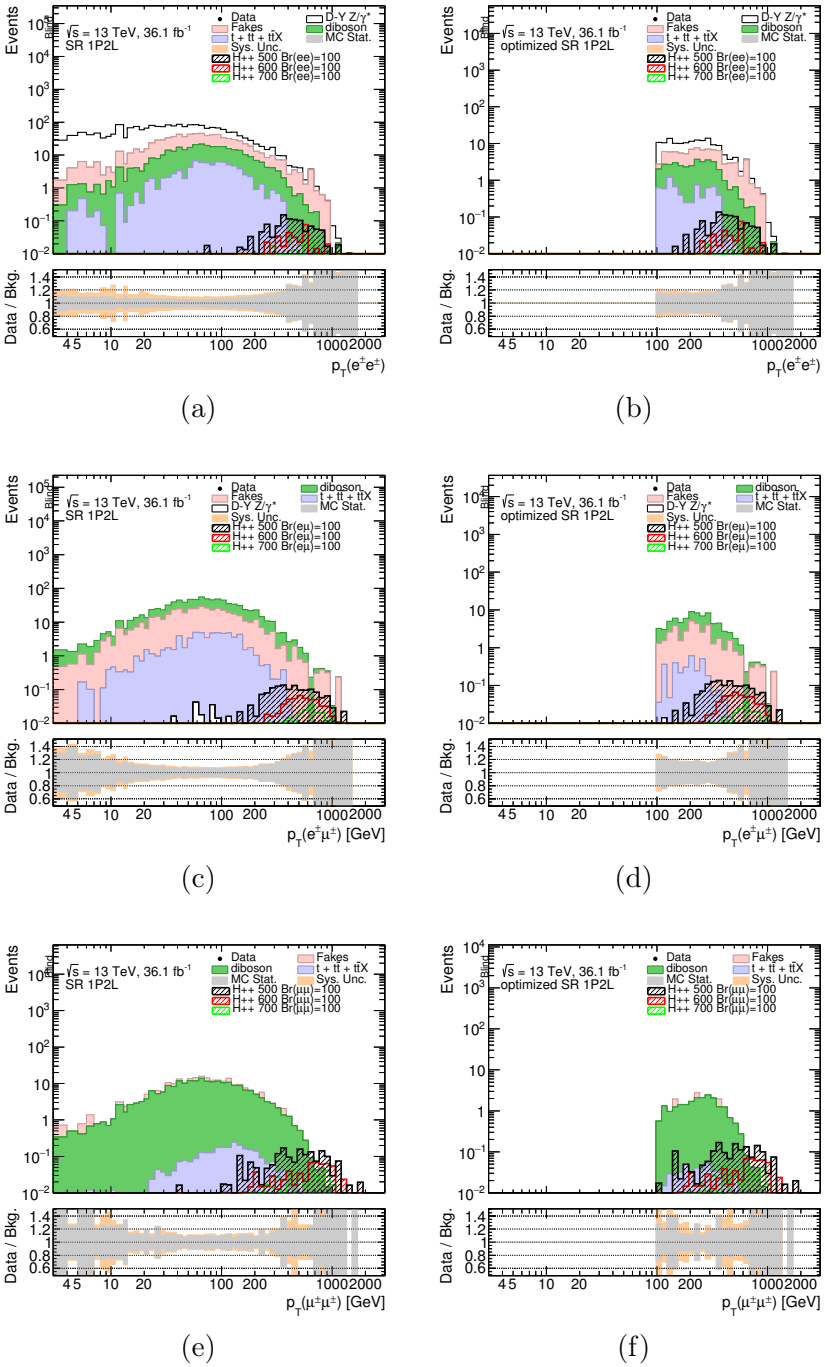

Figure 7.3: 1P2L signal region $p_{\mathrm{T}}(\ell^{\pm},\ell^{\pm})$ distributions for the electron (a), (b), mixed (c), (d) and muon (e), (f) channels respectively before and after SR optimization.

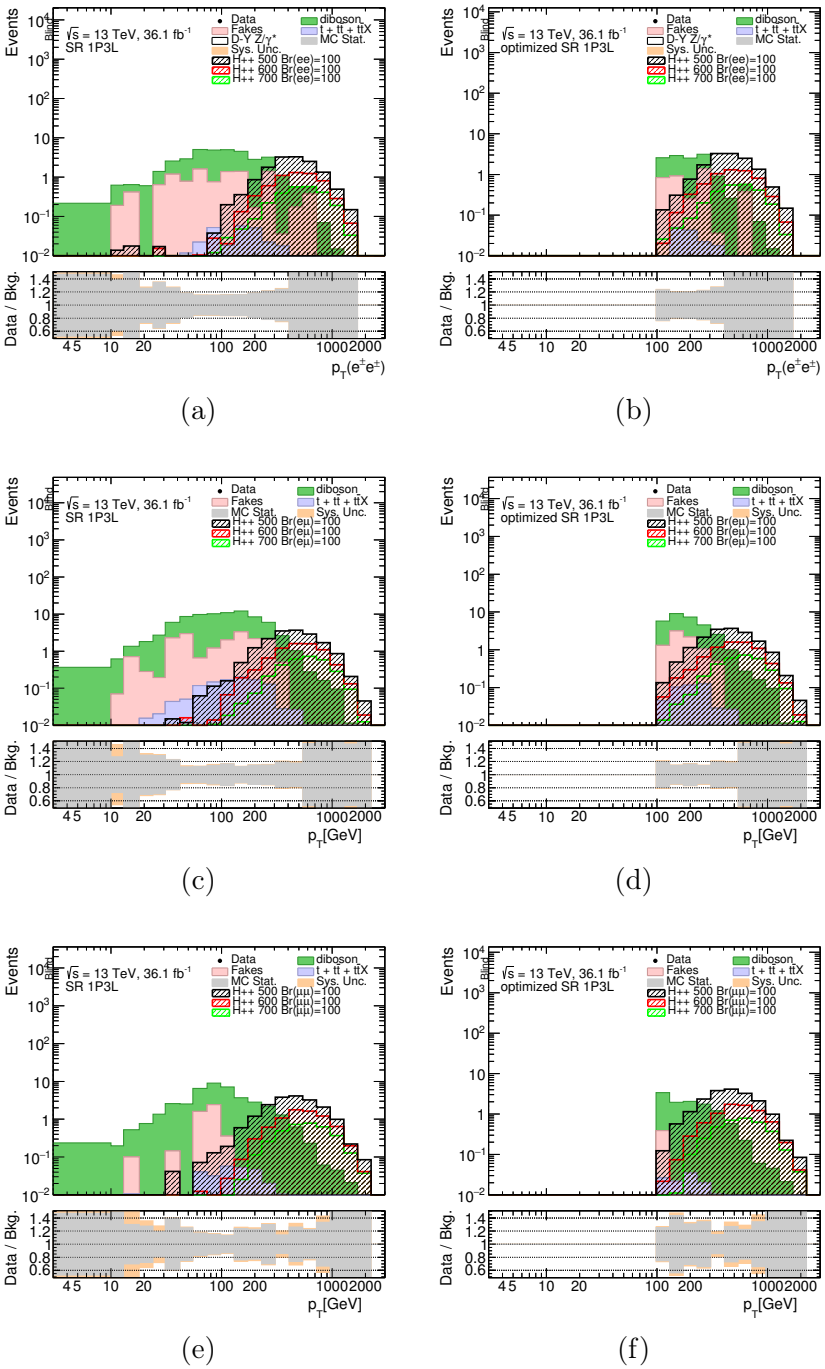

Figure 7.4: 1P3L signal region $p_{\mathrm{T}}(\ell^{\pm},\ell^{\pm})$ distributions for the electron (a), (b), mixed (c), (d) and muon (e), (f) channels respectively before and after SR optimization.

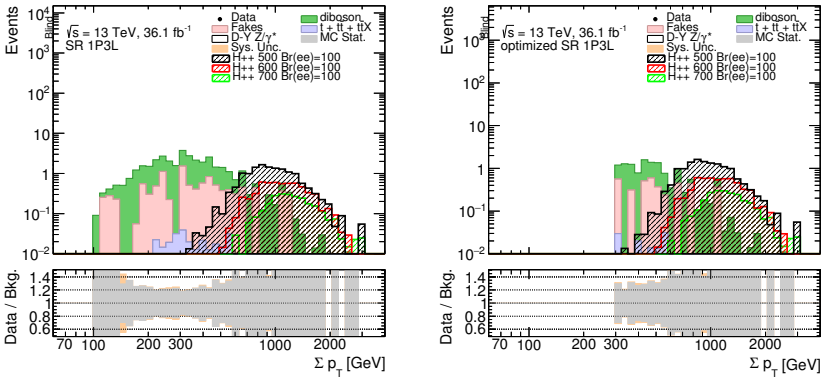

(a)

(b)

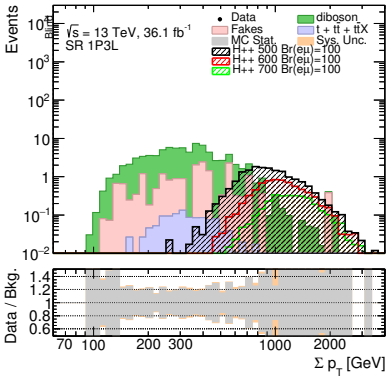

(c)

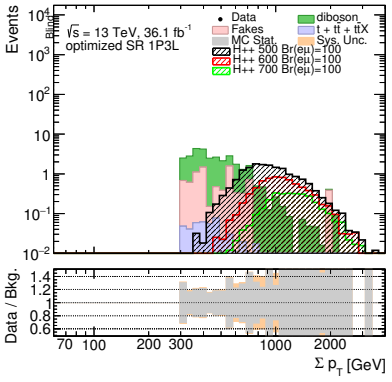

(d)

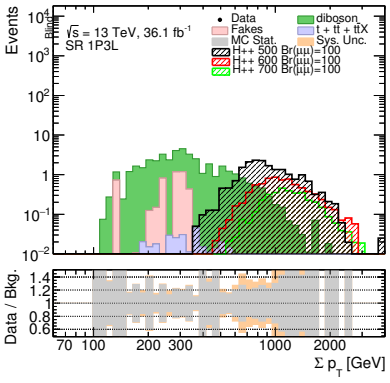

(e)

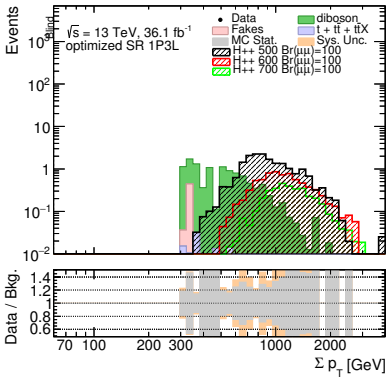

(f)

Figure 7.5: 1P3L signal region p_{T} scalar sum of all leptons distributions for the electron (a), (b), mixed (c), (d) and muon (e), (f) channels respectively before and after SR optimization.

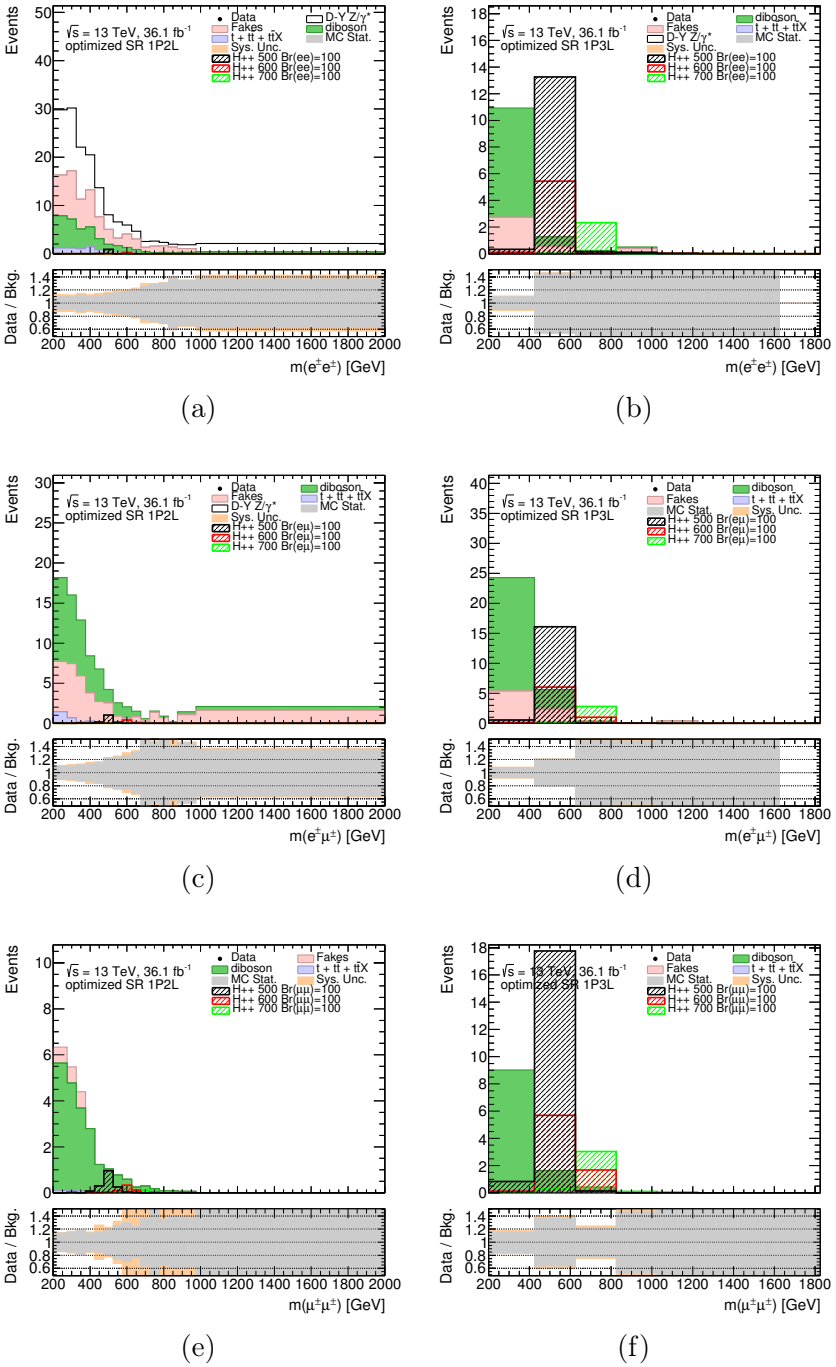

Figure 7.6: Invariant mass distributions for the SS lepton pair in the electron 7.6a, 7.6b, mixed 7.6c, 7.6d and muon 7.6e, 7.6f channels respectively for SR 1P2L and 1P3L.

7.5.2 Four lepton signal region optimization

Let us now focus only on events containing exactly two SS lepton pairs. The main background for this kind of signature is originated from ZZ, WZ (in which the W boson decays hadronically and the two jets in the final state are reconstructed as leptons), $H \to ZZ$, VH and $t\bar{t}H$ production. Some of the main processes are illustrated in the Feynman diagrams in Fig. 7.7.

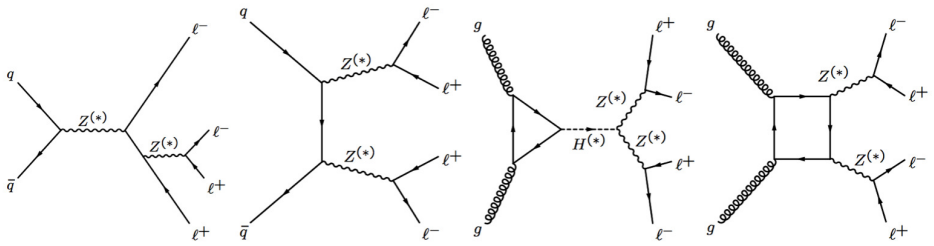

Figure 7.7: Main SM backgrounds to the $H^{\pm\pm}$ signature decaying into four lepton final states: the first and second diagrams show ZZ production while the third and fourth diagrams present two types of $H \to ZZ$ production.

Accordingly to the process cross-section (see Table 7.2), the main contribution arises from ZZ production. A full leptonic decay of both the Z bosons leads to a final state containing four leptons with zero total charge, exactly as the $H^{\pm\pm}$ signal. Once leptons, originating from ZZ events, are randomly paired accordingly to the SS requirement, the kinematic properties of a ZZ decay are no longer conserved.
To define the four leptons signal region, we look into lepton kinematics, such as p_{T} and η distributions and we compute the invariant mass of the SS pairs. We expect the difference between the invariant masses of the SS pairs to be a powerful variable since, for signal, it peaks at zero while for background it follows a flatter distribution.

Figure 7.8 shows the $\Delta R_{\ell^\pm\ell^\pm}$, $\Delta R_{H^{\pm\pm}H^{\pm\pm}}$ and N_{jets} distributions in the 2P4L signal region, divided by lepton flavours, for the four electrons and four muons representative channels. Three signal mass hypotheses are shown, corresponding to $m_{H^{\pm\pm}} = \{200, 500, 1100\}$ GeV, as well as the dominant background from ZZ production. As in the signal regions containing two or three leptons, the ΔR distributions for leptons originating from the $H^{\pm\pm}$ decay confirm that they are closer than $\Delta R_{\ell^\pm\ell^\pm}$ <3.5. However, the ZZ background is randomly distributed over the full ΔR region and makes it impossible to effectively cut on this variable to reject the background. No ZZ background is present in events requiring the presence of two SS and

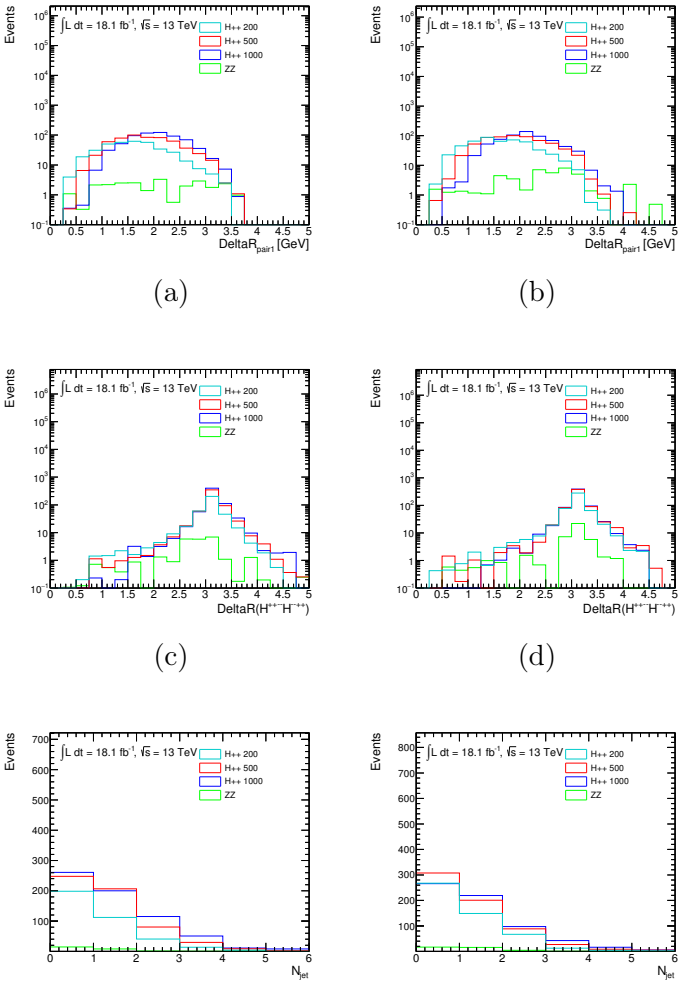

(a) (b)

(c) (d)

(e) (f)

Figure 7.8: Kinematic distributions for the ΔR between two SS leptons in the event, ΔR between the two same-sign particle pairs and number of jets: (a), (c), (e) for the $e^{\pm}e^{\pm}e^{\pm}e^{\pm}$ channel, (b), (d), (f) for the $\mu^{\pm}\mu^{\pm}\mu^{\pm}\mu^{\pm}$ channel.

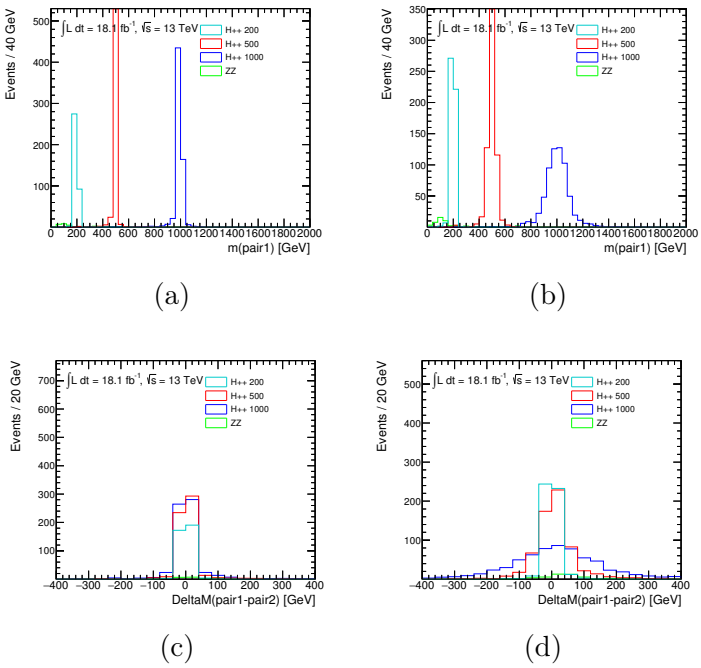

Figure 7.9: Invariant mass distributions of the two SS lepton pairs in the event: (a), (c) for the $e^{\pm}e^{\pm}e^{\pm}e^{\pm}$ channel, (b), (d) for the $\mu^{\pm}\mu^{\pm}\mu^{\pm}\mu^{\pm}$ channel.

same-flavour leptons.
Figure 7.9 shows the difference between the invariant masses of the two pairs in the four electrons and four muons channels. The variable is powerful in distinguishing between signal and background events. The mass resolution is substantially worse in channels containing muons while electron channel invariant mass distributions present a narrower peak.
To perform signal region optimization, we now use as figure of merit the signal efficiency times acceptance and not the significance, as was done in the optimization of $t\bar{t}H$ signal regions. Indeed, despite being the dominant one, the ZZ background is very small in the signal regions containing four leptons. For this reason optimizing signal efficiency is preferred instead of significance optimization.

Signal selection efficiency

The basic selection in this signal region requires four tight leptons with zero total charge and the invariant mass of each SS lepton pair is required to be above 200 GeV.

Due to the different lepton resolutions in different energy regimes, the selection efficiency might vary accordingly both to lepton flavour and to the $H^{\pm\pm}$ invariant mass point and hence the efficiency curves are provided divided both into flavour and as a function of $H^{\pm\pm}$ mass. Assuming the following relations for the $H^{\pm\pm}$ decay widths:

$$2 \times \Gamma(ee) = 2 \times \Gamma(\mu\mu) = \Gamma(e\mu) \tag{7.1}$$

the event fraction split into flavours is reported in Table 7.8.

Expected Event Fractions					
N_{eeee}	$N_{\mu\mu\mu\mu}$	$N_{ee\mu\mu}$	$N_{e\mu e\mu}$	$N_{eee\mu}$	$N_{\mu\mu e\mu}$
1/16	1/16	1/8	1/4	1/4	1/4

Table 7.8: Fraction of events split by channel, assuming a $H^{\pm\pm}$ decay probability of P(ee) = 1/4, P($\mu\mu$)=1/4 and P($e\mu$)=1/2.

There are six possible flavour combinations in the four lepton signal region, covering all possible decay channels for the $H^{\pm\pm}$ boson to light leptons. The signal efficiency times acceptance is defined in the following way:

$$\epsilon \times A = \frac{N(\text{selection, trigger})}{N(\text{initial})} \tag{7.2}$$

First, we want to assess how signal efficiency varies accordingly to the set of considered triggers. The lowest unprescaled single lepton triggers are, respectively for 2015 and 2016:

- 2015: `HLT_e24_lhmedium_L1EM20VH`, `HLT_e60_lhmedium`, `HLT_e120_lhloose`, `HLT_mu50`, `HLT_mu20_L1MU15`;
- 2016: `HLT_e26_lhtight_nod0`, `HLT_e60_lhmedium_nod0`, `HLT_e140_lhloose_nod0`, `HLT_mu50`, `HLT_mu26_ivarmedium`.

The dilepton triggers are:

- 2015: `HLT_2e17_lhloose`, `HLT_2mu10`, `HLT_e17_lhloose_nod0_mu14`;
- 2016: `HLT_2e17_lhloose`, `HLT_2mu14`, `HLT_e17_lhloose_nod0_mu14`.

The efficiency times acceptance is calculated using several configurations. First, the nominal signal efficiency is measured using only the requirement of events containing four tight leptons and two SS pairs with zero total charge, as shown in Fig. 7.10a.

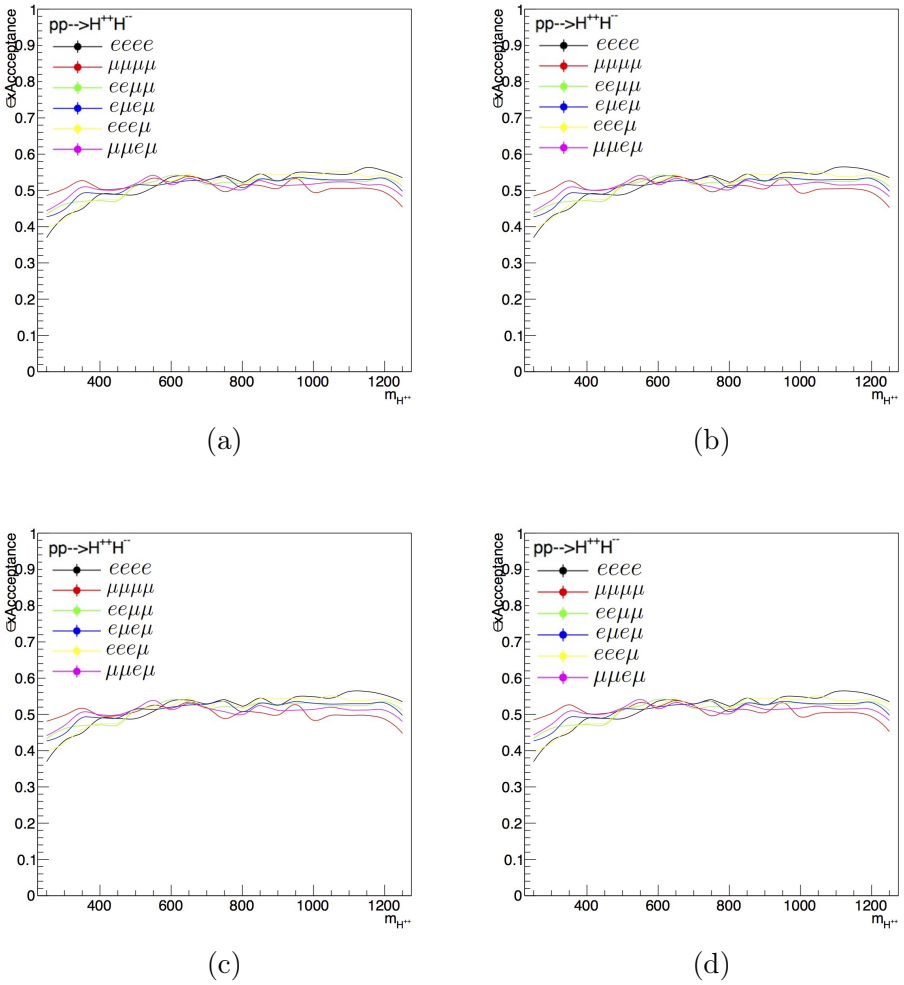

Figure 7.10: Baseline signal efficiency (a), signal efficiency times acceptance using single lepton triggers (b), dilepton triggers (c) or the logical OR combination of single and dilepton triggers (d).

The baseline signal acceptance into pairs of SS leptons is around 50% and quite stable with respect to both the $H^{\pm\pm}$ mass point and the channel flavour. Figures 7.10b and 7.10c show, respectively, the signal acceptance using single or dilepton triggers, in addition to the baseline selection. The trigger choice has an impact of less than ∼1% on the baseline signal acceptance and using single or dilepton triggers leads to roughly the same acceptance. Figure 7.10d allows to conclude that there is no gain using the logical OR combination of the two trigger sets and, in analogy with most of the two and three leptons

control, validation and signal regions, the dilepton trigger chains for 2015 and 2016 are used.
Given that the major background to this signal region arises from ZZ events, they can be effectively reduced using a Z veto cut. Additionally, since we are targeting events containing two SS pairs with almost exactly the same invariant mass, we apply a further cut on the invariant mass difference. These cuts are defined as follows:

- reject events containing at least one OS pair whose invariant mass is less than 10 GeV apart from the Z boson mass peak: $|m_{\ell\ell} - m_Z| < 10$ GeV, where m_Z is the PDG value for the Z boson mass. This cut will be applied to all flavour channels, except for the $e^{\pm}e^{\pm}\mu^{\mp}\mu^{\mp}$ events where an opposite-sign same flavour couple is not present;
- we define the variable $\Delta M/\bar{M}$, where $\bar{M} = (m^{++} + m^{--})/2$ and cut on it. The width of the SS pair invariant mass distribution grows with the $H^{\pm\pm}$ mass and is also dependent on the channel flavour, having electrons and muons different momentum resolutions. This effect becomes even more evident at high masses.

We now evaluate signal efficiency after applying these two cuts.

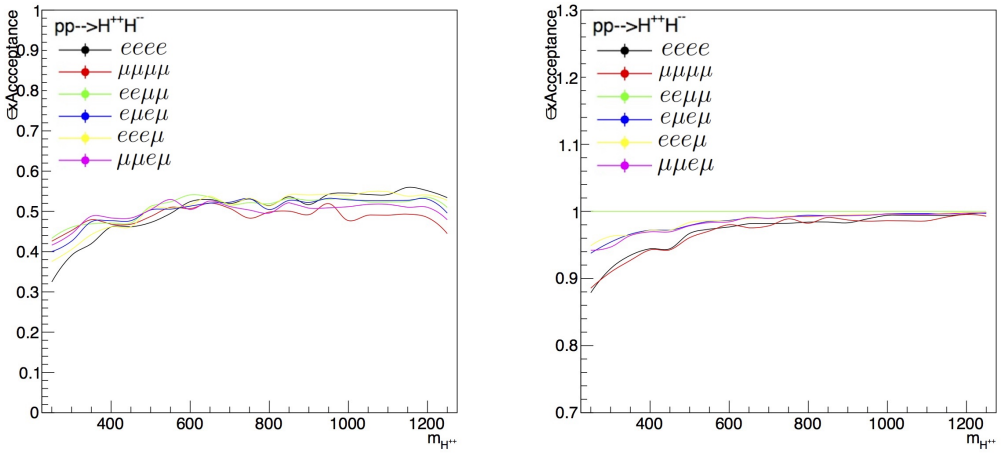

(a) (b)

Figure 7.11: Signal efficiency times acceptance after applying the Z veto cut (a) and normalized to the number of events before applying the cut (baseline selection plus trigger requirement) (b).

Figure 7.11b shows the overall signal acceptance after Z veto, and the same quantity normalized to the initial number of events 7.11b. It is worth

noting that this selection requirement has a negligible impact at high masses (less than 5%) and that the signal losses are around 10% at lower $H^{\pm\pm}$ masses. Given that this cut allows to reject most of the ZZ background we keep the Z veto despite the 10% loose at low masses.

Regarding the $\Delta M/\bar{M}$ cut optimization, different studies are performed. This variable shows a dependence both on the channel and on the $H^{\pm\pm}$ mass hypothesis. The ΔM resolution gets worse as the muon multiplicity in this final state increases due to the decreasing muon resolution at large p_{T}. In principle, a fixed efficiency working point at 90% could be set. However this cut would be too dependent on the $H^{\pm\pm}$ mass hypothesis, thus the possibility to apply a cut based on a different combination of the ΔM and $\bar{M}$ variables is exploited.

The ΔM variable depends on the $H^{\pm\pm}$ mass and it is dominated by the resolution, assumed to follow a Gaussian distribution centered around zero. The spectrum of the ΔM distribution is fitted with a Gaussian shape and its standard deviation σ is evaluated for each $H^{\pm\pm}$ mass point and shown in Fig. 7.12.

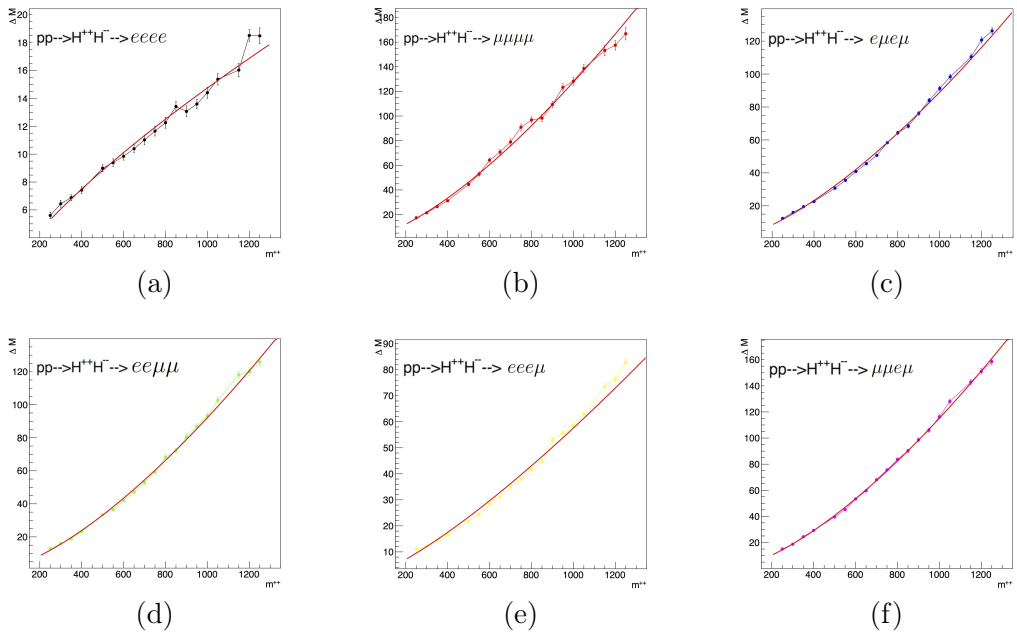

Figure 7.12: Standard deviation resulting from the fit of the ΔM distribution as a function of the $H^{\pm\pm}$ mass. Plots are provided for the $eeee$ (a), $\mu\mu\mu\mu$ (b), $e\mu e\mu$ (c), $ee\mu\mu$ (d), $eee\mu$ (e) and $\mu\mu e\mu$ (f) channels respectively.

Each curve in Fig. 7.12 is parametrized using a function of the type $\Delta M =$

$\alpha \times \bar{M}^{\beta}$, where α and β are two parameters which are extracted from a fit. Therefore, the $\Delta M/(\alpha \times \bar{M}^{\beta})$ is selected as the discriminating variable, since it is less dependent on the $H^{\pm\pm}$ mass, as will be shown later.
The parameters extracted by the fit interpolation are reported in Table 7.9.

	$eeee$	$\mu\mu\mu\mu$	$e\mu e\mu$	$ee\mu\mu$	$eee\mu$	$\mu\mu e\mu$
α	0.09	0.005	0.003	0.004	0.007	0.004
β	0.74	1.46	1.47	1.46	1.30	1.50

Table 7.9: Fit result for α and β parameters divided into channel flavour.

The fitted parameters are similar among channels apart from $eeee$ events, where the ΔM has a different resolution. Once the parameters are found, we compute the signal and acceptance efficiency for each flavour as a function of the $\Delta M/(\alpha \times \bar{M}^{\beta})$ variable, as shown in Fig. 7.13.

If we require the cut to be $\Delta M/(\alpha \times \bar{M}^{\beta})$ <3, all signal efficiencies, at each mass point, lie in the range $85\% < \epsilon < 95\%$. Therefore, the 2P4L region is defined as containing events with:

- exactly two SS pairs;
- event total charge equal to zero;
- events where at least one OS same-flavour pair satisfies $|m_{\ell\ell} - m_Z| <$ 10 GeV;
- $\Delta M/(\alpha \times M^{\beta})$ <3.

The final signal times acceptance efficiency is shown in Fig. 7.14. The new set of cuts provides a ∼50% signal efficiency across the $H^{\pm\pm}$ mass range. Figure 7.14b shows the overall signal even loss compared to the initial nominal selection, which amounts to ∼10%.
The $\Delta M/(\alpha \times \bar{M}^{\beta})$ selection corresponds to ΔM values ranging from 15 GeV to 50 GeV for $m_{H^{\pm\pm}}$ = 200 GeV, 30 GeV to 160 GeV for $m_{H^{\pm\pm}}$= 500 GeV, and 50 GeV to 500 GeV for $m_{H^{\pm\pm}}$= 1000 GeV, where the lower cuts correspond to electron channels and the higher one to muon channels.

Figure 7.15 shows the bidimensional plane of the m^{--} versus m^{++} mass pairs for the ZZ background for the $e^{\pm}e^{\pm}e^{\mp}e^{\mp}$, $\mu^{\pm}\mu^{\pm}\mu^{\mp}\mu^{\mp}$ and $e^{\pm}\mu^{\pm}e^{\mp}\mu^{\mp}$ channels. In the $e^{\pm}e^{\pm}\mu^{\mp}\mu^{\mp}$, $e^{\pm}e^{\pm}e^{\mp}\mu^{\mu}$ and $\mu^{\pm}\mu^{\pm}e^{\mp}\mu^{\mu}$ channels, no diboson background survives the SS pair cut of the event selection.
Diboson events are randomly distributed in the 2D mass plane and mainly concentrated at low invariant masses. It is clear that after the $\Delta M/(\alpha \times \bar{M}^{\beta})$

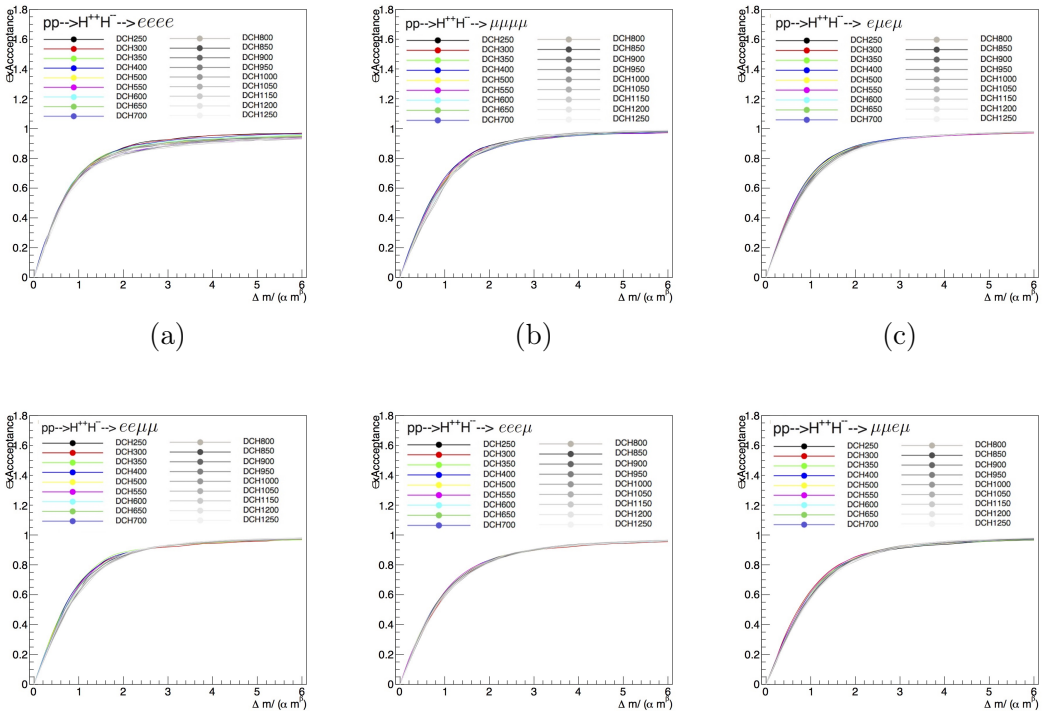

(a) (b) (c)

(d) (e) (f)

Figure 7.13: Signal efficiency times acceptance as a function of the $\Delta M/\alpha \times \bar{M}^{\beta}$ cut for the *eeee* (a), *μμμμ* (b), *eμeμ* (c), *eeμμ* (d), *eeeμ* (e) and *μμeμ* (f) channels respectively. Plots are normalized to *baseline* (signal region definition, trigger requirement and Z veto) selection.

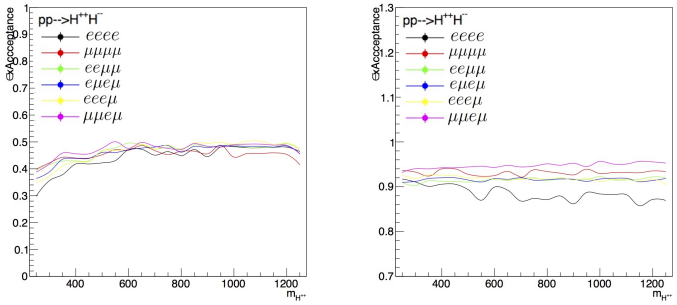

(a) (b)

Figure 7.14: Signal efficiency times acceptance as a function of the $H^{\pm\pm}$ mass (a) and normalized to the number of events after initial and trigger selection (b).

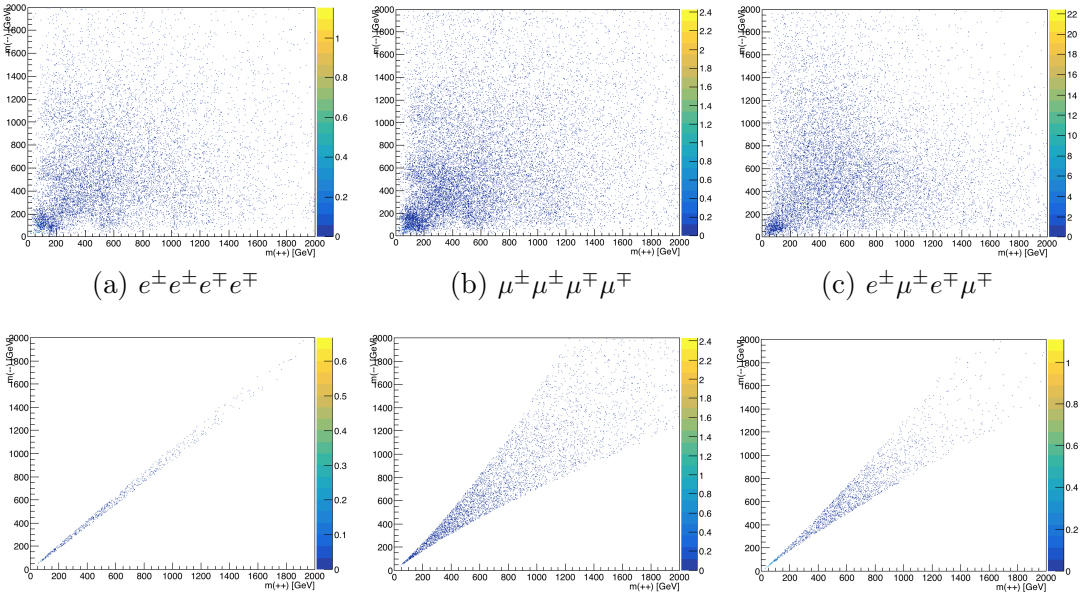

(a) $e^{\pm}e^{\pm}e^{\mp}e^{\mp}$ (b) $\mu^{\pm}\mu^{\pm}\mu^{\mp}\mu^{\mp}$ (c) $e^{\pm}\mu^{\pm}e^{\mp}\mu^{\mp}$

(d) $e^{\pm}e^{\pm}e^{\mp}e^{\mp}$ (e) $\mu^{\pm}\mu^{\pm}\mu^{\mp}\mu^{\mp}$ (f) $e^{\pm}\mu^{\pm}e^{\mp}\mu^{\mp}$

Figure 7.15: Scatter plot of m^{--} versus m^{++} diboson ZZ same-sign masses before the application of the $\Delta M/\alpha \times \bar{M}^{\beta}$ cut (a), (b), (c) and after (d), (e), (f) in the $e^{\pm}e^{\pm}e^{\mp}e^{\mp}$, $\mu^{\pm}\mu^{\pm}\mu^{\mp}\mu^{\mp}$ and $e^{\pm}\mu^{\pm}e^{\mp}\mu^{\mp}$ channels.

the majority of the ZZ background is discarded from the signal region event selection.

7.6 Background estimation

Reducible backgrounds in this search are estimated using data-driven techniques, shown in Chapter 5. This section presents how the charge misidentification probability and fake lepton backgrounds are measured.

7.6.1 Electron charge misidentification background

The measurement of charge-flip probability is based on the procedure explained in Section 5.3. A scale factor is derived in this analysis from the different charge-flip probabilities measured in simulation and experimental data, and used to correct the simulation itself. The *origin* information of the considered electron can be acquired by using truth matching and, for all electrons which are classified as *charge-flips*, a *correction factor* is applied to simulation.
For simulated events containing at least one electron, its origin is checked and the following correction factors

- for prompt electrons: $SF = \frac{1-P(\text{CF;data})}{1-P(\text{CF;MC})}$
- for charge-flip electrons: $SF = \frac{P(\text{CF;data})}{P(\text{CF;MC})}$

are applied. The mass intervals used to define both the peak and the sideband regions are reported in Table 7.10.

Event type	Z peak region	side-bands
opposite-sign (OS)	$\lvert m(ee) - m_{\text{OS}}(Z)\rvert < 14\,\text{GeV}$	$14\,\text{GeV} < \lvert m(ee) - m_{\text{OS}}(Z)\rvert < 18\,\text{GeV}$
same-sign (SS)	$\lvert m(ee) - m_{\text{SS}}(Z)\rvert < 15.8\,\text{GeV}$	$15.8\,\text{GeV} < \lvert m(ee) - m_{\text{SS}}(Z)\rvert < 31.6\,\text{GeV}$

Table 7.10: Definitions of main regions and sideband regions for OS and SS Z peak events. The position of the Z peak, as measured in the two regions, is indicated by $m_{\text{OS}}(Z)$ and $m_{\text{SS}}(Z)$.

The two peak regions are presented in Fig. 7.16 which shows that the SS peak is clearly shifted, by approximately 2 GeV, to lower energy and slightly broader than the OS peak, due to bremsstrahlung energy loss.
The charge mis-identification probability is expressed as a function of both electron η and p_{T}, $P(p_{\text{T}}, \eta)$. However, this parametrization can be factorized by considering that the shape of the η dependence is very similar for all p_{T} bins. The parametrization eventually becomes:

$$P(p_{\text{T}}, \eta) = f(\eta) \times \sigma(p_{\text{T}}) \tag{7.3}$$

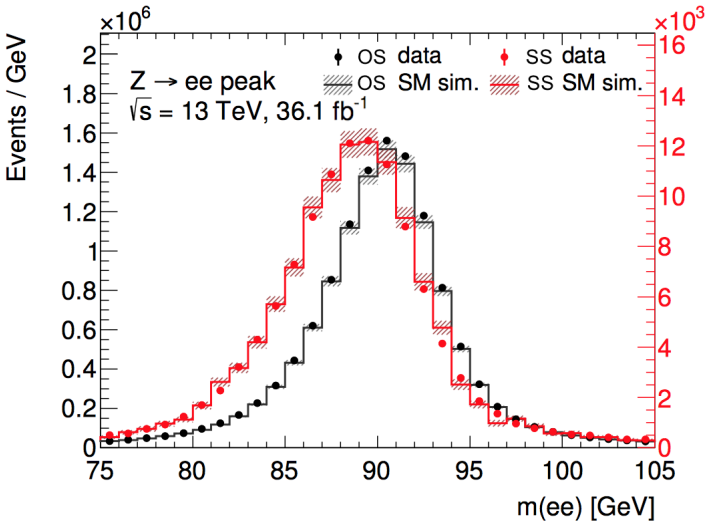

Figure 7.16: Dielectron mass distributions for OS (black) and SS (red) pairs for data (filled circles) and MC simulation (continuous line). The latter includes a correction for charge mis-identification. The hatched band indicates the statistical error and the luminosity uncertainty summed in quadrature applied to MC simulated events.

which is the product of two one-dimensional functions. The number of free parameters entering the 1D×1D likelihood fit is the product of the number of bins used for the p_{T} and η parametrizations: $N_{p_{\mathrm{T}}} \times N_{\eta}$. To reduce the number of parameters, the η function is normalized to one ($\int f(\eta) d\eta = 1$), leading to $N_{p_{\mathrm{T}}} + N_{\eta} - 1$ degrees of freedom. The one dimensional fit has a smaller statistical uncertainty and allows to measure the charge-flip probability up to electrons with $p_{\mathrm{T}} > 200$ GeV. This is indeed the reason why, with respect to the charge mis-identification approach used in Section 6.4.2, we decided to use the corrected simulation instead of re-weighting OS data. In fact, given that we are interested in more energetic electrons, we need a reliable charge-flip estimate up to very high-p_{T}.

The result of the likelihood fit is presented in Fig. 7.17 and, as expected from the considerations stated in Section 5.3, they increase with both p_{T} and η. The mismodelling is clearly visible in the η distribution near the transition region while the p_{T} data over simulation ratio is relatively flat up to high momenta. The p_{T} and η bins were chosen to provide the largest possible granularity in regions with higher mismodeling, taking into account the available statistics.

To check that the 1D×1D parametrization does not introduce any bias, the charge-flip rates obtained from the likelihood fit on MC are compared to the

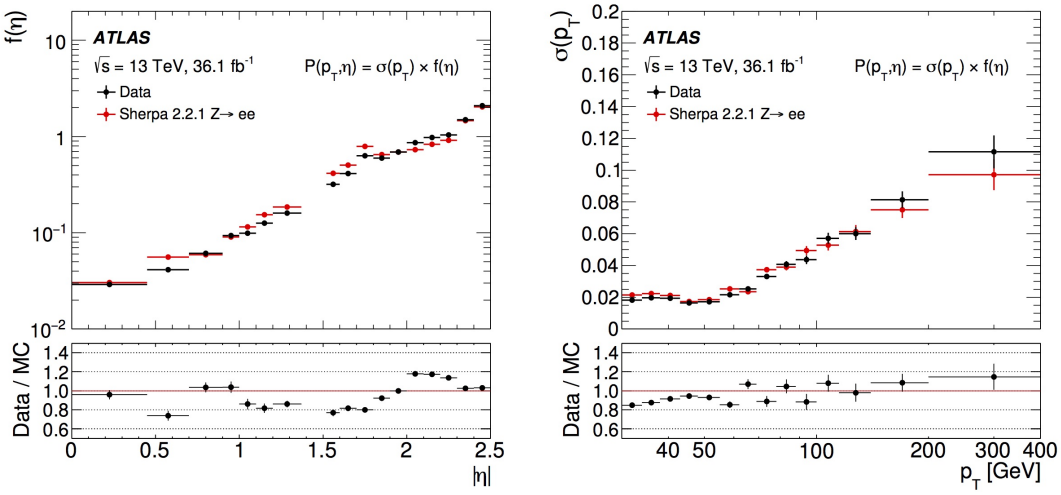

(a) (b)

Figure 7.17: Comparison of the factors composing the charge misidentification probability $P(p_{\mathrm{T}}, \eta) = f(\eta) \times \sigma(p_{\mathrm{T}})$ measured in data and in simulation, using the likelihood fit in the $Z/\gamma^* \to ee$ region. The area of the distribution of $f(\eta)$ was normalized to unity. Error bars correspond to the statistical uncertainty estimated with the likelihood fit. The $|\eta|$ (a) and p_{T} (b) misidenfitication probability functions are shown.

2D true charge-flip rate parametrization, where the latter is measured by dividing the number of charge-flip electrons over prompt ones in MC. A very good agreement is obtained, as shown in Fig. 7.18.

To test the method, SS events with invariant mass in the range $|m_{ee} - m_Z| < 15.8$ GeV are selected from data and compared to simulation before and after the correction factors are applied. As shown in Fig. 7.19, after the application of the charge-flip scale factors, data/MC agreement significantly improves. The $e^{\pm}e^{\pm}$ invariant mass in Fig. 7.19b recovers the ∼20% disagreement in the Z peak mass region and the leading electron p_{T} also shows an improved agreement between data and simulation both at low and at high momenta, as shown in Fig. 7.19d. These distributions allow to conclude that the procedure described in this section effectively corrects the simulation mismodeling for charge-flip events.

Systematic uncertainties on charge-flip background

The data-driven method used for determining the charge mis-identification rates carries a set of systematic uncertainties. First, the likelihood fit assigns

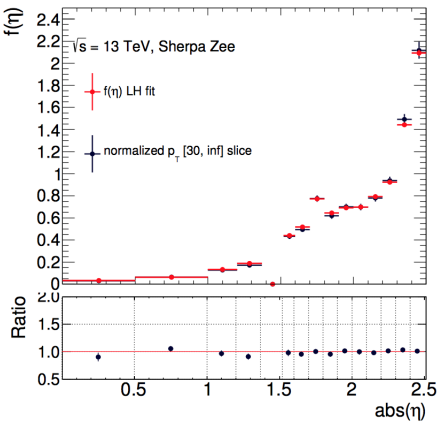

Figure 7.18: Comparison between the true MC 2D charge-flip parametrization (black dots) and the result of the likelihood fit applied to simulation using the 1D×1D parametrization (red dots).

to the rate an uncertainty which gets propagated to the scale factors. The scale factors are varied corresponding to the magnitude of the uncertainty to obtain the final statistical uncertainty on the charge-flip background prediction. A second uncertainty is a consequence of the mass range selected to identify the Z peak and the side-band regions. The mass ranges are varied to assess the systematic uncertainty due to the selection of the Z mass window.

7.6.2 Fake lepton background

Background from fake leptons is estimated with the data-driven fake factor method described in Section 5.4.2. The measurement is performed in two different regions, depending on the lepton flavour.

Electron fake factor is measured by selecting a region in data that predominantly contains fake electrons. Events cannot be selected using the nominal dielectron trigger, since the electrons firing it are likely to be originated from the interaction point. For this reason, a specific set of single electron triggers is required, providing a sufficiently loose identification requirement compatible with the loose electron definition. Single electron triggers satisfying these constraints are prescaled triggers, which cannot be simply combined using a logical OR. The triggers used for the fake factor measurement are reported in Table 7.11, divided for different p_{T} ranges.

Depending on its p_{T}, each electron is required to match a specific trigger. The electron fake enriched control region is identified by the following

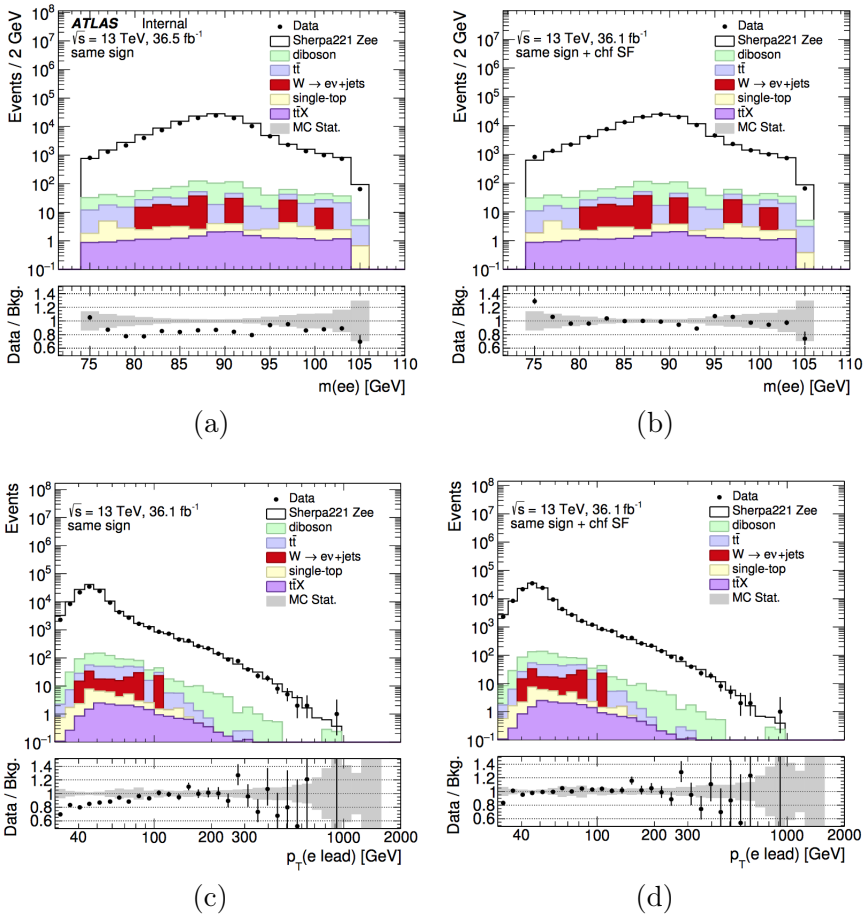

Figure 7.19: Same-sign events selected in the Z boson peak region providing a comparison between data and the expected SM background. Left plots and right plot show data/MC agreement, respectively before and after applying the charge-flip scale factors, for the electron invariant mass m_{ee} (a), (b) and the leading electron p_{T} (c), (d) distributions.

requirements:

- events with two or more tight electrons are discarded. Events with more than one loose electron can still enter the selection. To reduce the contribution from Drell-Yan events, any pair of tight or loose electrons with invariant mass within 20 GeV from the Z mass are also discarded (71.2 GeV $< m_{ee} <$ 111.2 GeV).

- to clean the sample from $W \to e\nu$ events, the missing E_{T} is required to be less than 25 GeV.

Trigger name	p_{T} [GeV]	Trigger prescale
HLT_e26_lhvloose_nod0_L1EM20VH	$30 - 65$	112.4
HLT_e60_lhvloose_nod0	$65 - 125$	25.6
HLT_e120_lhloose_nod0	$125 - 145$	6.69
HLT_e140_lhloose_nod0	$145 - \infty$	1

Table 7.11: Single electron prescaled triggers used for the fake enriched region. The p_{T} ranges in which each trigger is used are specified, as well as the trigger prescale.

- to reduce the contribution from $t\bar{t}$ events, a b-jet veto is also applied, consistently to what is done in all the other analysis regions. This cut also helps to reduce the contribution from other top events.

Most of these events contain exactly one electron and the residual prompt electron contribution is subtracted using simulation. The MC samples used for the subtraction are W+jets, Drell-Yan, $t\bar{t}$, diboson and single top. The region is consequently enriched with events produced from dijet processes.

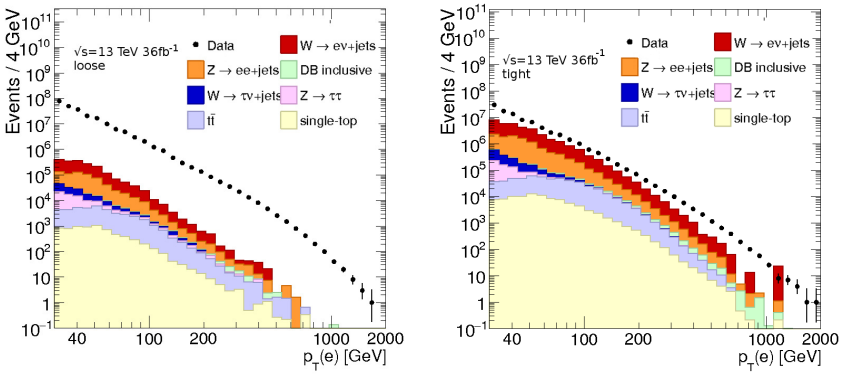

(a) (b)

Figure 7.20: Fake enriched regions in the nominal selection: (a) p_{T} distribution of loose and tight (b) p_{T} electrons in the fake enriched region. All the distributions show data events and the prompt MC component subtracted from data.

Figure 7.20 shows the electron p_{T} distributions for the loose (denominator events) and tight (numerator events) for the fake factor measurement. It is visible that the MC subtraction impacts more the tight than the loose region distribution, amounting up to 50% of all electrons and mainly consisting of W+jets events.

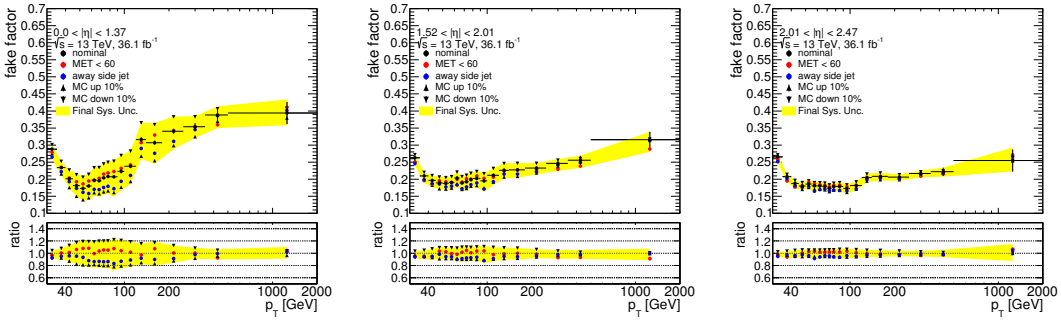

(a) (b) (c)

Figure 7.21: Measured fake factor as a function of the electron p_{T} divided into different η bins: 0< $|\eta|$ <1.37 (a), 1.52< $|\eta|$ <2.01 (b) and 2.01< $|\eta|$ <2.47 (c). Each systematic variation accounted for in the measurement of the fake factor is separately shown in the plot as well as the total systematic band (in yellow).

Figure 7.21 shows the resulting fake factors. The combined systematic uncertainty, which for very high p_{T} electrons is only 20%, is obtained by adding in quadrature the total statistical uncertainty and all the variations shown in these distributions.
Systematic uncertainties are the result of several variations which are aimed to test different aspects of our background modeling. The following variations are adopted with respect to the nominal selection:

- to probe the modeling of the W+jets MC sample, and to test the effect of additional W+jets events in the region used to estimate the electron fake factor, the cut on the $E_{\mathrm{T}}^{\mathrm{miss}}$ is loosened to 60 GeV;
- to account for the cross-section and luminosity uncertainties, all MC samples are scaled by 10% up and down.
- to assess the impact of a different composition of fake leptons, an *away side jet* with a $\Delta\phi$ distance from the electron above 2.4 is required, and with a p_{T} of 30 GeV.

The largest contribution to the uncertainty arises from the $E_{\mathrm{T}}^{\mathrm{miss}}$ requirement and the 10% MC variation in the first η slice. The fake factor measurement is relatively stable up to very high electron p_{T}.

Muon fake factor is measured using a tag and probe also targeting a dijet topology. Events are selected requiring the presence of a jet (the tag) and a

reconstructed muon (the probe). The two objects are required to be back-to-back and their angular distance must satisfy $\Delta\phi > 2.7$. The dijet selection, as in the electron case, provides a sample with high statistics. Given that the lower p_{T} threshold trigger used for the nominal muon event selection, namely `HLT_mu26_ivarmedium`, requires isolation on muons, this trigger cannot be used in the measurement of muon fake factor. As in the electron case, it is replaced by a non-isolated, but prescaled, low p_{T} threshold trigger: `HLT_mu24`, as in Table 7.12.

Trigger name	p_{T} [GeV]	Trigger prescale
`HLT_mu24`	$30 - 50$	~ 45
`HLT_mu50`	$50 - \infty$	1

Table 7.12: Single muon triggers used for the fake enriched region. The p_{T} ranges in which each trigger is used are specified as well as the trigger prescale, where present.

The high p_{T} region can still use the unprescaled `HLT_mu50`, where no isolation requirement is applied on muons. As already discussed for electrons, muons are matched to the trigger according to their p_{T} range. The sample used for the muon fake factor measurement must satisfy the following requirements:

- the event must contain a muon with $p_{\mathrm{T}} > 25$ GeV and a jet with $p_{\mathrm{T}} > 35$ GeV;
- the $E_{\mathrm{T}}^{\mathrm{miss}}$ has to be below 40 GeV, to discard W+jets events;
- no b-jets in the event, to suppress $t\bar{t}$ and other top backgrounds.

The distributions for the fake factor numerator and denominator muons are reported in Fig. 7.22. The major contribution from prompt SM background in the muon fake enriched region arises from W+jets events. These events are subtracted from simulation. The fake factor as a function of the muon p_{T} is shown in Fig. 7.23, together with its systematic uncertainty. Systematic uncertainties are evaluated by altering the dijet events nominal selection in the following way:

- the effect of an additional W+jets contamination is assessed by changing upward and downward the requirement on the $E_{\mathrm{T}}^{\mathrm{miss}}$ by 10 GeV;

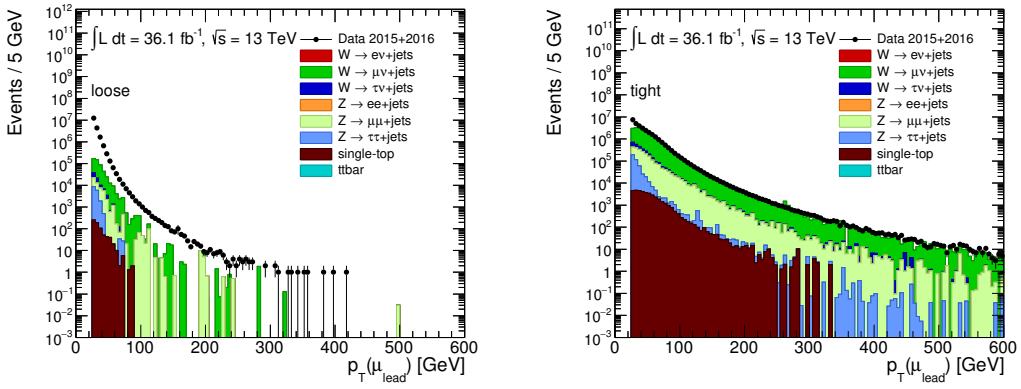

(a) (b)

Figure 7.22: Muon fake enriched region where di-jet events are selected: p_{T} distribution for muons failing the isolation requirement (a) and for isolated muons (b). All the distributions show data events and the prompt MC component subtracted from data, to ensure a fake dominated region.

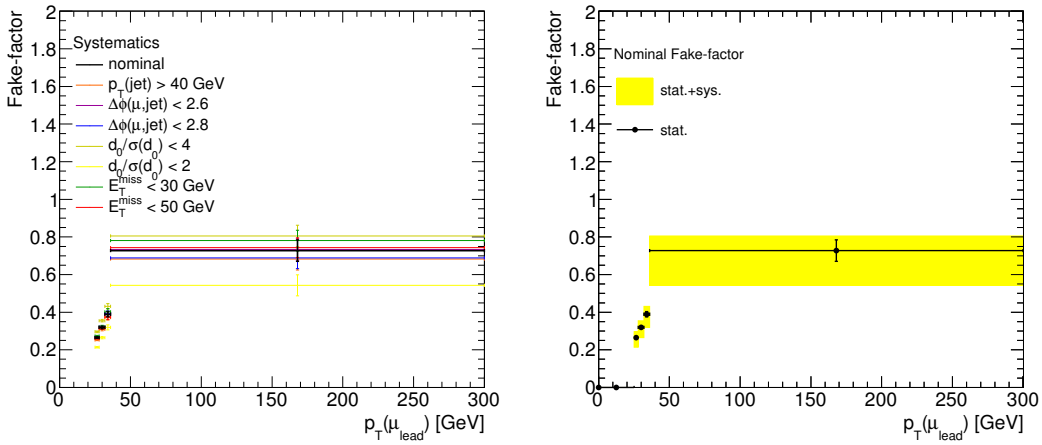

(a) (b)

Figure 7.23: Muon fake factors as a function of the muon p_{T}. The nominal value is illustrated by the black points while each systematic effect is included separately in (a). The total uncertainty is illustrated in (b) together with the nominal measurement.

- the definition of the tight muon is altered by varying up and down the selection on $|d_0|/\sigma_{d_0}$ by one unit. This change is intended to probe the possible different origins of fake leptons. Indeed, fake muons originate

from the in-flight decay of mesons with different flavour composition and lifetimes and their fraction can change from the nominal relative fraction by changing the $|d_0|/\sigma_{d_0}$ cut;

- the topology of the event is changed by rising the jet p_{T} selection up to 40 GeV. In this way the collimation of the fake lepton is altered and we obtain a further handle on how the isolation of the fake muon impacts the fake factor measurement;

- the back-to-back requirement on the jet and the reconstructed muon ($\Delta\phi(\mu, jet)$) is also altered up and down by 0.1, also affecting the fake muon isolation.

The effect of each systematic variation is presented in Fig. 7.23a and the total systematic band in Figure 7.23b. The latter is estimated by comparing the statistical uncertainty on the nominal measurement with the maximum deviation between the nominal fake factor and each systematic measurement. The largest deviation is taken as total uncertainty and varies between $\sim$10% and $\sim$20% across the p_{T} range.

7.7 Distributions in control and validation regions

In this section the distributions for data and expected backgrounds are presented. In the following, prompt lepton backgrounds are estimated with MC simulation while the background from charge mis-identification and fakes are estimated with the data-driven methods presented in Section 7.6. Control and validation regions are reported in Table 7.7. In the following, distributions are shown before (*pre-fit*) performing the statistical analysis for data interpretation under the $H^{\pm\pm}$ production hypothesis.

7.7.1 Control regions

The control regions used in this analysis are aimed to extract the normalization of the Drell-Yan and the diboson background. Each background is separately normalized according to flavour and lepton multiplicity. The regions are separated into the diboson control region (DBCR) and the opposite-charge control region (OCCR).

Diboson control region (DBCR)

The diboson control region (see Table 7.7) is used to constrain the diboson background normalization. Representative event distributions are shown for the electron, muon and mixed flavour channels in Fig. 7.24. All distributions exhibit a good data/simulation agreement.

A four lepton diboson control region (4LCR) is used to constrain the diboson normalization for the 2P4L signal region (Fig. 7.25). All the six flavour combinations of the 4LCR are joined into one unique region to increase the population of the sample.

Opposite-charge control region (OCCR)

The opposite-charge control region (see 7.7) is used to constrain the $Z \to ee$ background, contaminating the signal region for the electron channels. The definition of this control region provides a sample dominated in $Z \to ee$ events. Representative event distributions are shown in Fig. 7.26. Good agreement is observed within the quoted uncertainties.

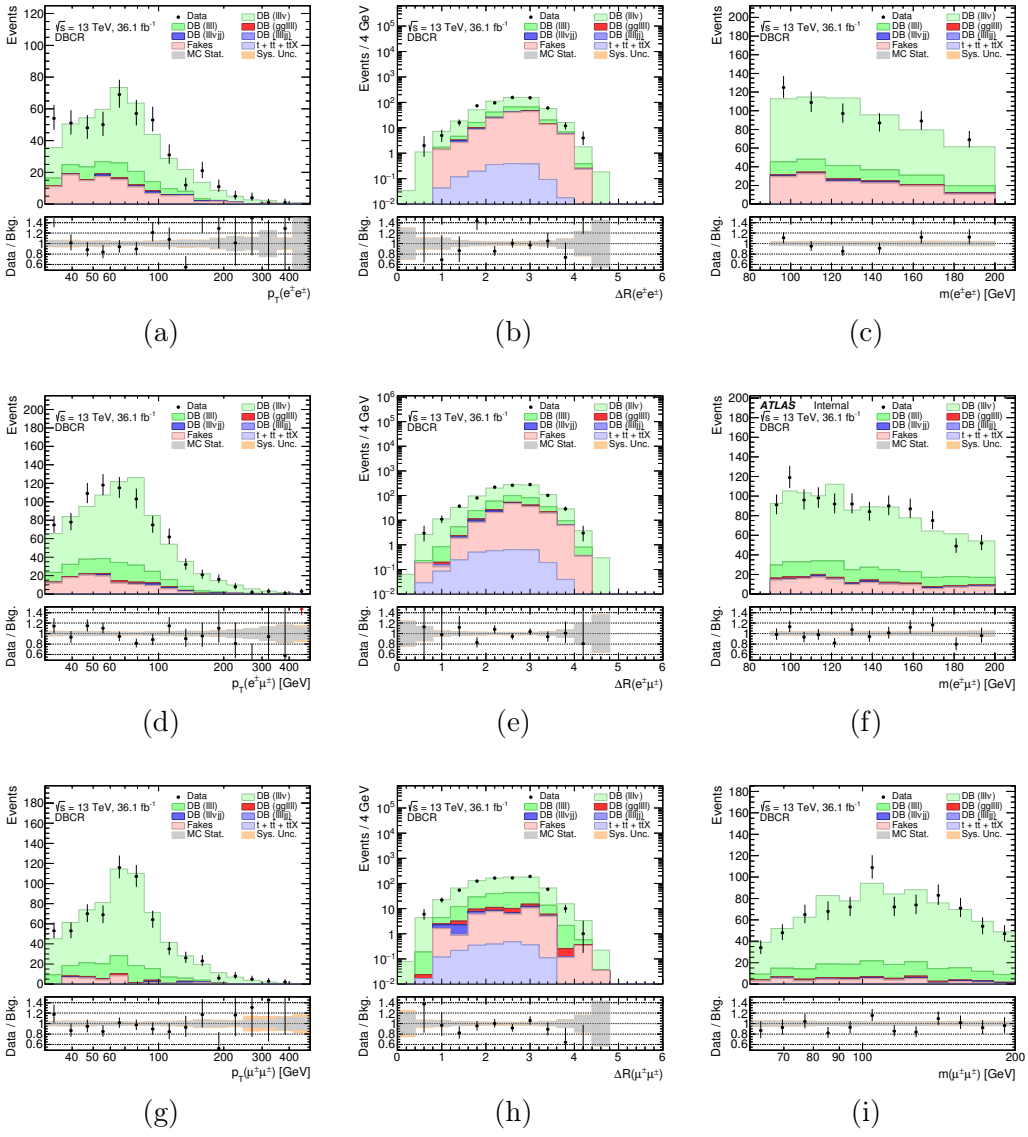

(a) (b) (c)

(d) (e) (f)

(g) (h) (i)

Figure 7.24: Pre-fit event distributions in the diboson control region: $p_{\mathrm{T}}(e^{\pm}, e^{\pm})$ of the SS leptons (left plots), $p_{\mathrm{T}}(e^{\pm}, e^{\pm})$ of the SS leptons (middle plots) and their invariant mass (right plots), presented for the electron (a), (b), (c), mixed (d), (e), (f) and muon (g), (h), (i) channels.

7.7.2 Validation regions

The purpose of the validation regions is to validate background estimations in regions similar but mutually exclusive to the signal regions. They are separated accordingly to lepton multiplicity into the same-charge, three

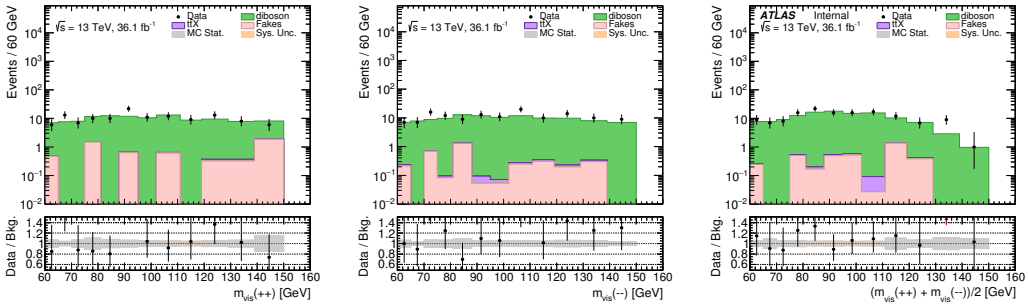

(a) (b) (c)

Figure 7.25: Pre-fit event distributions in the four lepton diboson control region (a) invariant mass of the positive pair, (b) invariant mass of the negative pair, (c) and mean invariant mass of the two pairs.

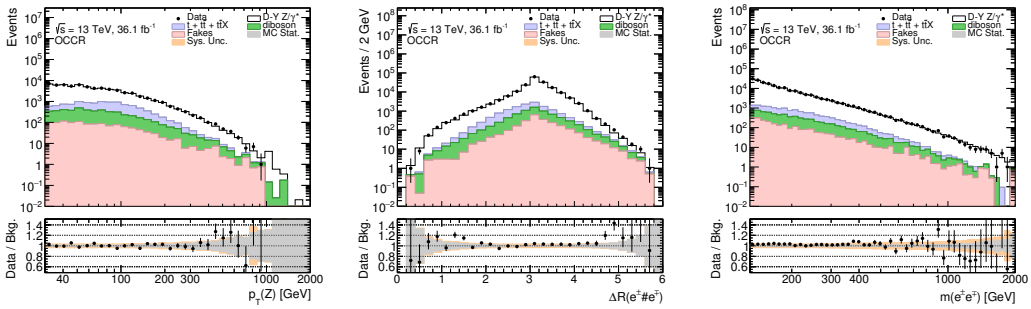

(a) (b) (c)

Figure 7.26: Pre-fit event distributions in the opposite-charge control region for the electron channel. (a) $p_{\mathrm{T}}(e^{\pm}, e^{\pm})$ of the SS electrons, (b) $\Delta R(e^{\pm}, e^{\pm})$ separation of the SS electrons, (c) and $m(e^{\pm}e^{\pm})$ distribution of all electrons in the event.

lepton and four lepton validation regions, referred to as SCVR, 3LVR and 4LVR.

Same-charge validation region (SCVR)

The same-charge validation region is used to mainly test the fake and diboson backgrounds estimations. In the electron channel, this is also useful to test the modeling of the charge-flip background, mostly due to $Z \to ee$ events.

Distributions in these regions are separately shown for electrons, $e\mu$ and muon channels in Fig. 7.27.

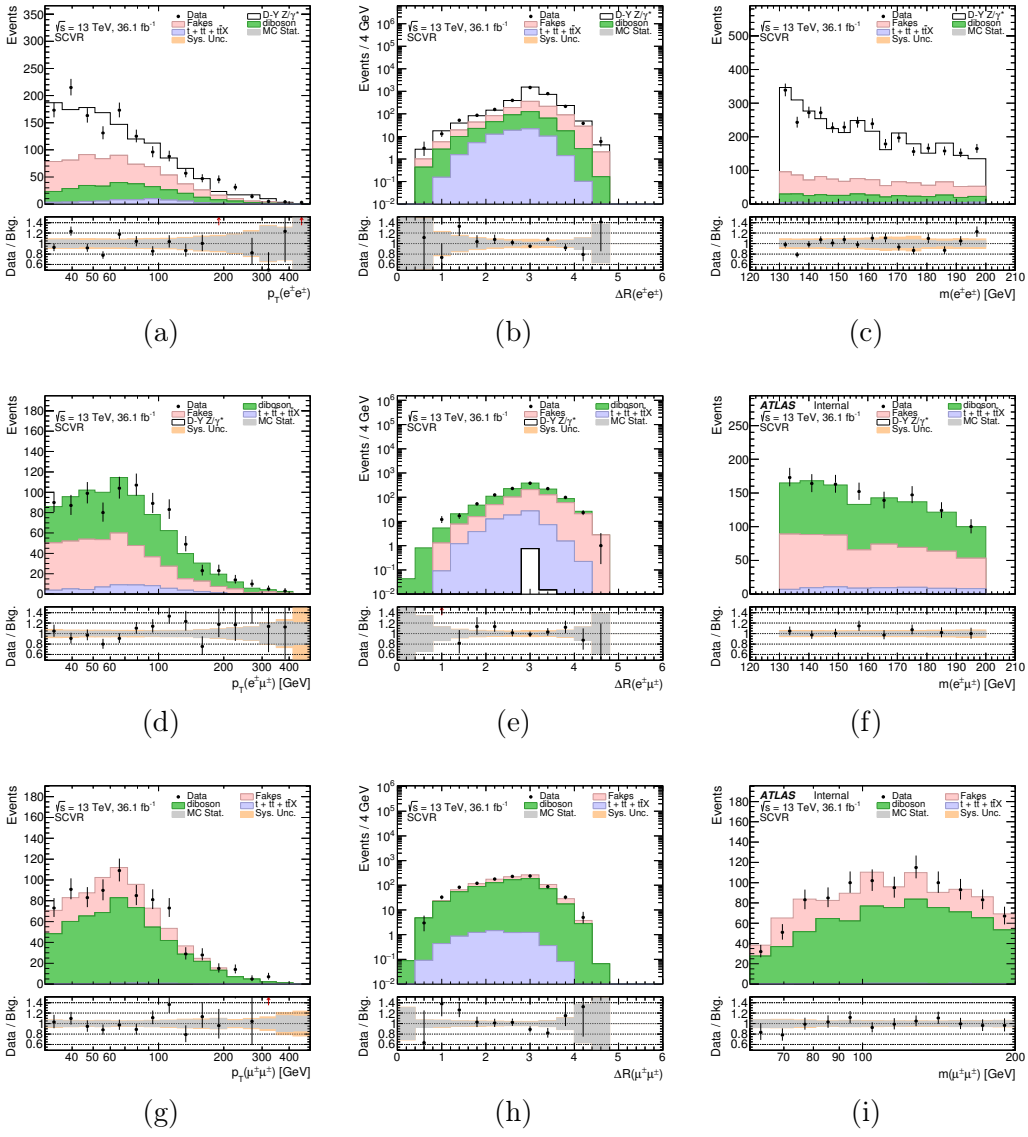

Figure 7.27: Pre-fit event distributions in the same-charge validation region: $p_{\mathrm{T}}(e^{\pm},e^{\pm})$ of the SS leptons (left plots), $p_{\mathrm{T}}(e^{\pm},e^{\pm})$ of the SS leptons (middle plots) and their invariant mass (right plots), presented for the electron (a), (b), (c), $e\mu$ (d), (e), (f) and muon (g), (h), (i) channels.

Three-lepton validation region (3LVR)

The three lepton validation region (3LVR) is defined to test the modeling of the prompt diboson background in all the analysis channels.

Distributions in this region are presented in Fig. 7.28. Despite the low

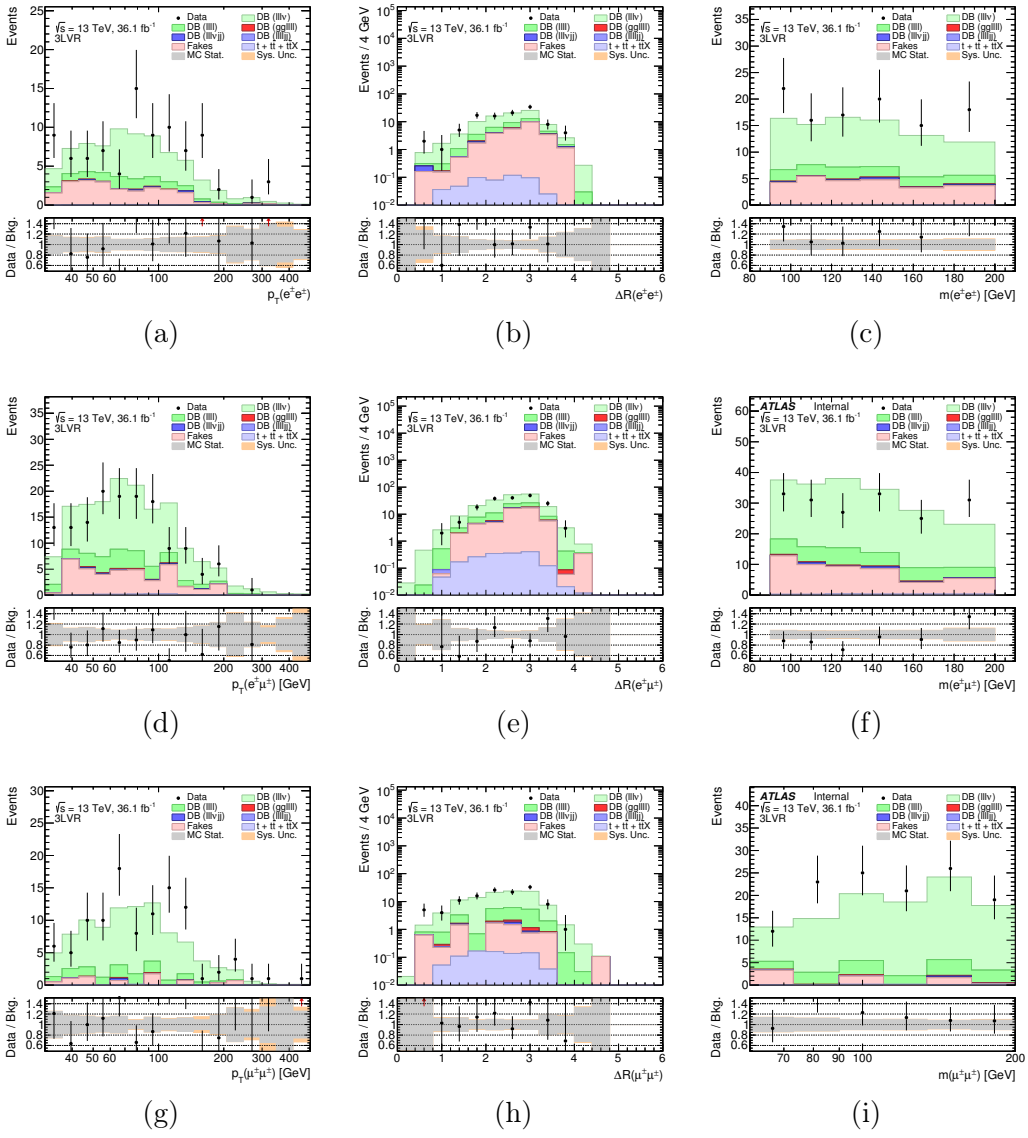

Figure 7.28: Event distributions in the three lepton validation region: $p_{\mathrm{T}}(e^{\pm}, e^{\pm})$ of the SS leptons (left plots), $p_{\mathrm{T}}(e^{\pm}, e^{\pm})$ of the SS leptons (middle plots) and their invariant mass (right plots), presented for the electron (a), (b), (c), mixed (d), (e), (f) and muon (g), (h), (i) channels.

statistical power of these distributions, good agreement is observed between data and the model.

The four leptons validation region (4LVR) (Table 7.7) is used to validate

the MC prediction in a diboson and $t\bar{t}X$ dominated region. All the six channel flavours are merged into one channel. As clear from Fig. 7.29 only three data events are observed in 4LVR.

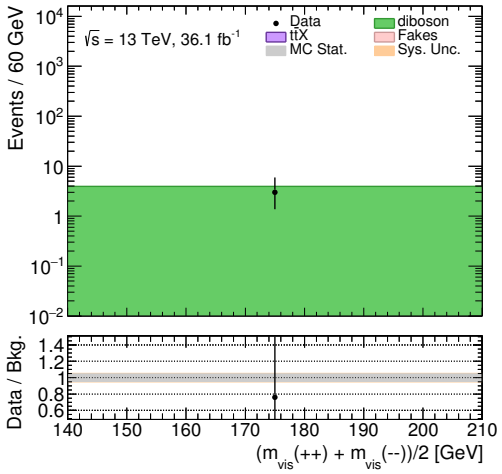

(a)

Figure 7.29: Data/MC in the 4LVR in one mass bin only from 150 to 200 GeV.

7.7.3 Signal regions

Signal regions are presented here as divided into lepton multiplicity namely 1P2L, 1P3L and 2P4L. The estimated background normalizations, provided in the following distributions, are the result of the fit procedure which is presented in Section 7.9. The fit, as will be shown, has a negligible impact (few %) on the pre-fit background yields. The distributions shown are the invariant mass of the SS pair while, for the 2P4L signal region, it is the mean of the two SS pairs invariant masses.

Figures 7.30 and 7.31 show the invariant mass distributions in signal regions. Different signal mass hypotheses are shown together with the expected total SM background for $H^{\pm\pm}$ masses of 450 GeV, 650 GeV and 850 GeV and different branching ratio combinations.
The signal region containing two electrons is equally affected by Drell-Yan, diboson and fake backgrounds, while in regions containing muons the majority of the background is due to diboson events. Only one event is observed in the four lepton signal region, as shown in Fig. 7.30d and in the event display 7.32. The event passes both the analysis Z veto and the $\Delta M/(\alpha \times \bar{M}^{\beta})$ cut, but is consistent with a ZZ event having one on-shell$Z$ mass in the low

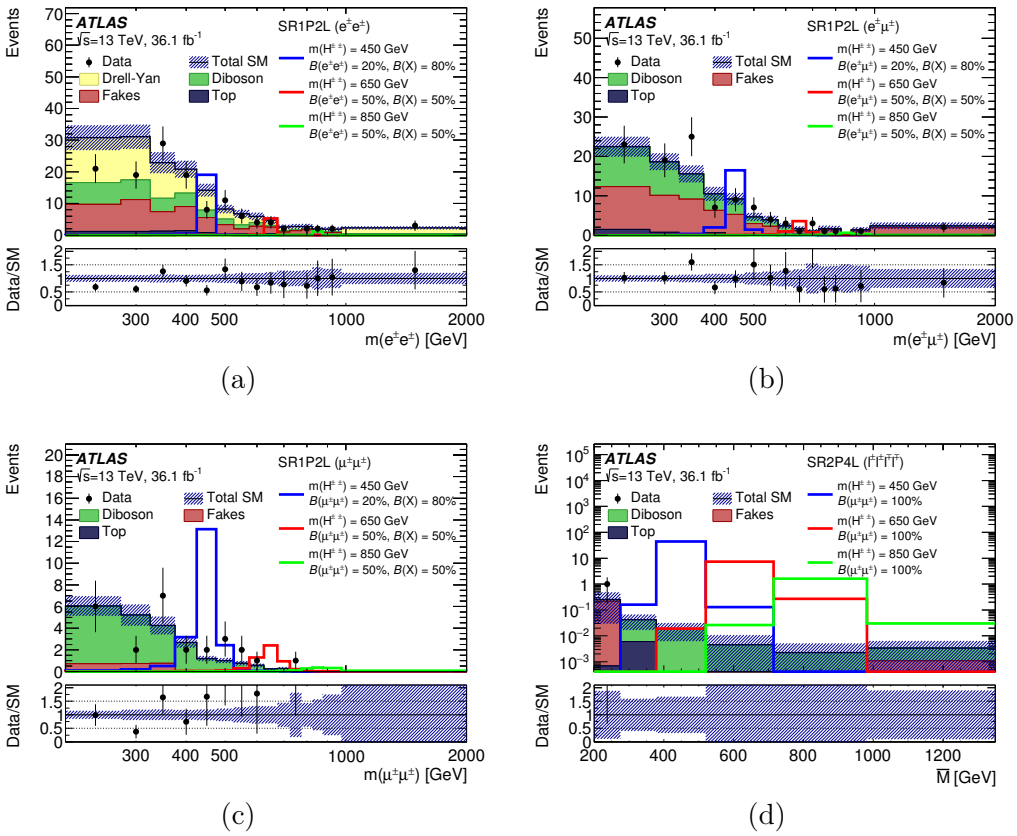

Figure 7.30: Invariant mass distributions in the 1P2L signal region for the $e^{\pm}e^{\pm}$ (a), the $e^{\pm}\mu^{\pm}$ (b) and the $\mu^{\pm}\mu^{\pm}$ (c) channels. Figure (d) shows in the mean invariant mass distribution for events containing four leptons in 2P4L.

peak tail.
The two lepton signal regions are mainly sensitive to $H^{\pm\pm}$ decays where the branching ratio to leptons is below 100%. As an example, in Fig. 7.30 signal samples are shown under the hypotheses of $BR(e^{\pm}e^{\pm})$ =20% + $BR(X)$ = 80 % for $m_{H^{\pm\pm}}$ = 450 GeV and $BR(e^{\pm}e^{\pm})$ =50% + $BR(X)$ = 50 % for $m_{H^{\pm\pm}}$ = 650, 850 GeV. On the contrary, the four lepton signal region is mainly sensitive when the $H^{\pm\pm}$ boson uniquely decays to light leptons $BR(\ell^{\pm}\ell^{\pm})$ = 100 %, as shown in Fig. 7.30d. Three lepton signal regions are also sensitive to the same branching ratio hypothesis, which corresponds to a $BR(\ell^{\pm}\ell^{\pm})$ = 100 % into light leptons, as shown in Fig. 7.31.
No excess over the SM background is found.

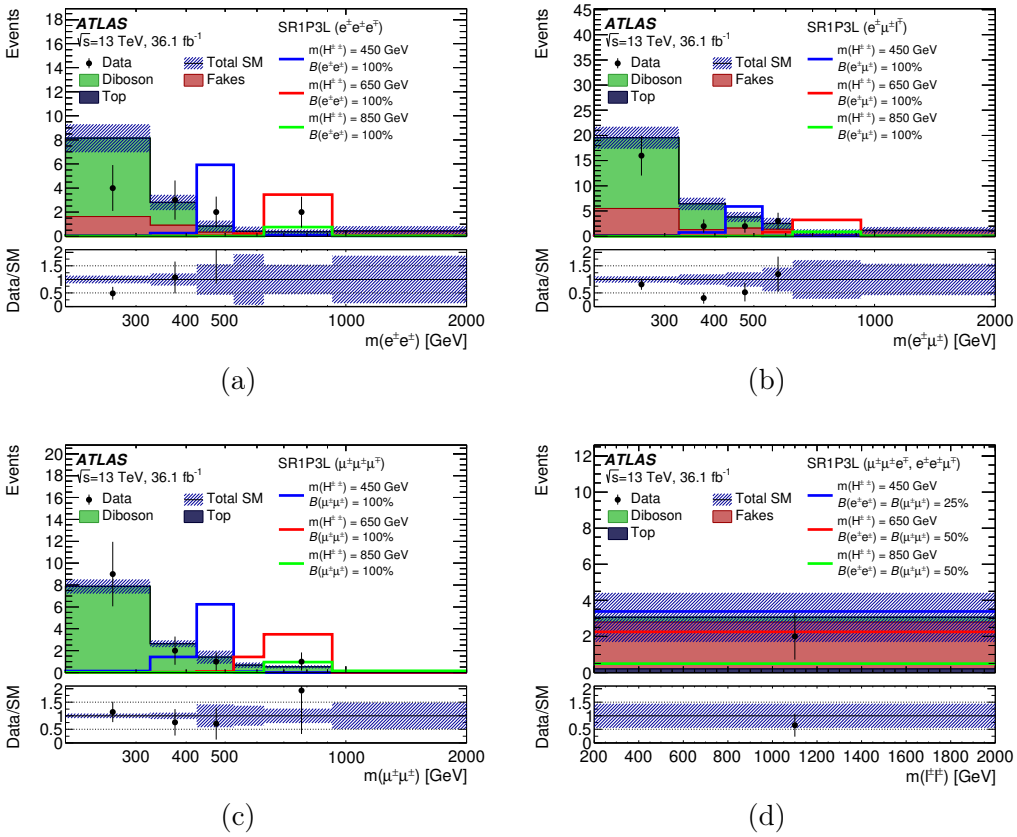

Figure 7.31: Invariant mass distributions for the SS lepton pair in the 1P3L signal region for events containing three electrons (a), four muons (b) and with an electron and muon SS pair (c) events. Figure (d) shows the invariant mass for the cases where a SS same-flavour pair is present ($e^{\pm}e^{\pm}\mu^{\mp}$ or $\mu^{\pm}\mu^{\pm}e^{\mp}$).

7.8 Description of systematic uncertainties

The systematic uncertainties affecting this measurement can be divided into theoretical and experimental uncertainties, affecting signal and background predictions.

Theoretical uncertainties

The cross-sections used to normalize the simulated samples are varied to account for the energy scale and the PDF uncertainties entering the cross-section calculation.
The theoretical uncertainty due to the PDF choice for the Drell-Yan background is assessed by taking into account different components [169]. First

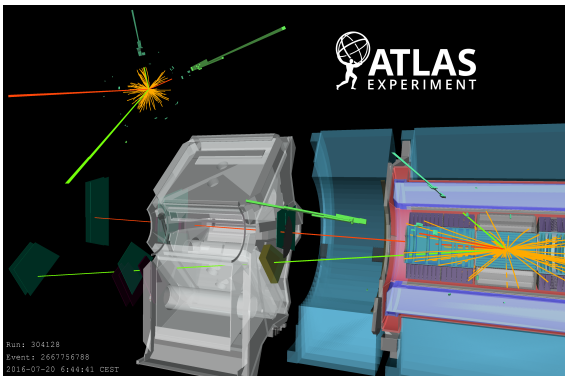

Figure 7.32: Event display for the event observed in the four lepton signal region. This event contains two electrons and two muons with a positive (red) and negative (green) charged lepton in each flavour. The positive and negative electrons have a p_{T} of 190 GeV and 74 GeV and an η of 1.56 and 0.99, respectively. The positive and negative muons have a p_{T} of 57 GeV and 130 GeV and η of 1.88 and 2.35 respectively. The SS invariant masses of the two pairs are 228 GeV and 207 GeV, while the OS masses are 163 GeV for the electron pair and 79 GeV for the muon pair, respectively.

the nominal PDF (which is CT14NNLO) is compared to alternative PDFs [170]: CT10NNLO, MMHT14, NNPDF3.0, ABM12, HERAPDF2.0 and JR14. The uncertainty due to the choice of the QCD renormalization μ_r and factorization μ_f scales is evaluated by taking the maximum and minimum value of this observable calculated with 7 variations [171], obtained by varying the renormalization and factorization scale up and down for each of the following combinations: $\mu_r \in [0.5, 1, 2]$ and $\mu_f \in [0.5, 1, 2]$ where the nominal setting corresponds to $\mu_r = \mu_f = 1$.
The uncertainty for the PDF CT14NNLO is estimated using the 90% CL CT14NNLO PDF error set [170]. Rather than using a single nuisance parameter to describe the 28 eigenvectors of this PDF set, a re-diagonalized set of 7 PDF eigenvectors is used, treated as separate nuisance parameters. The sum in quadrature of these eigenvectors matches the original error envelope well. Additionally, the value of α_s used 0.118 is varied by $\pm$ 0.003. The EW correction uncertainty is assessed by comparing the nominal additive $(1+\delta_{EW} + \delta_{QCD})$ treatment with the multiplicative approximation $((1+\delta_{EW})(1+\delta_{QCD}))$ treatment of the EW correction in the combination of the higher-order EW and QCD effects. The uncertainty in the photon-induced correction is calculated based on the uncertainty of the quark masses and the photon PDF.
The total theoretical uncertainty amounts to 6% for diboson [172] production

and between 8% and 13% for $t\bar{t}X$ [173] production. The diboson generator, SHERPA 2.2.1, used for the analysis, is assigned an additional theoretical uncertainty arising from the comparison with the POWHEG-BOX v2 predictions. This uncertainty varies from 5% to 10% depending on the analysis region.
The theoretical uncertainty on the NLO $pp \to H^{\pm\pm}$ cross-section calculation is around 15% and includes the renormalization and factorization scale dependence and the PDF uncertainty. The theoretical uncertainty due to the used set of tuning parameters in PYTHIA 8 [140] as well as the choice of alternative PDFs is also tested. The tuning parameter mainly changes the modeling of initial-final state radiation and MPI interactions. Moreover two alternative PDF set were used instead of the nominal NNPDF2.3NLO: CTEQ6L1 and CT09MC1 at LO. The final effect, as a result of each systematic variation, is shown in Fig. 7.33.

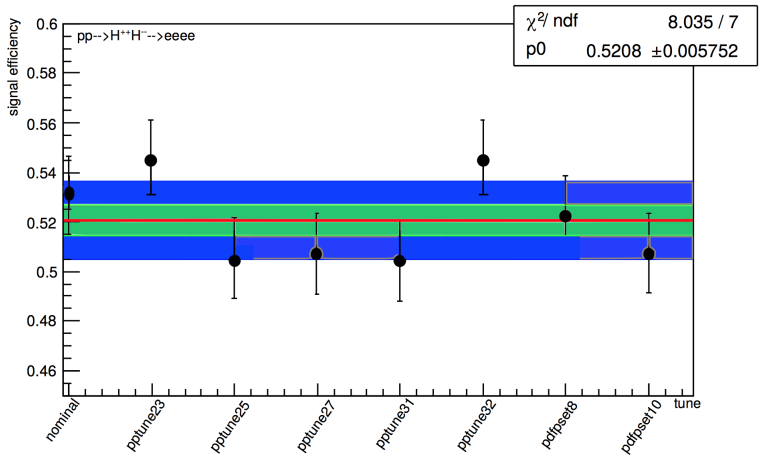

Figure 7.33: Alternative tuning and PDF set configuration in PYTHIA 8, used to produce a test signal sample for $pp \to H^{\pm\pm} \to 4e$. Here *tune23* refers to an up/down alteration of the beam remnants and MPI interaction, *tune25* assess different shapes and substructure altering shower parameters, *tune27* alters the $t\bar{t}$ gap, *tune31* changes the jet 3/2 ratio while the *tune32* the $t\bar{t}$ gap, the dijet decorrelation and the Z boson p_{T}. Regarding PDF configuration, *tune8* corresponds to the CTEQ6L1 and *tune10* to the CT09MC1 PDF set. Green and blue band correspond to the 1σ and 2σ variations from the mean obtained value, which is indicated by the red line.

The first point shows signal efficiency obtained with PYTHIA 8 nominal setting, while each of the following points correspond to each of the considered systematic variations. It is clear that each of the variation lies within

2σ from the nominal value and all points agree with each other the statistical uncertainties within few % and therefore these additional systematic variations on signal are ignored in the final fit.

Experimental uncertainties

Detector related uncertainties account for the different reconstruction, identification, isolation and trigger efficiencies of leptons in data compared to the one in simulation. The scale factor applied to MC events are varied by 1σ up and down. Additional systematic uncertainty are associated to the lepton energy, or momentum, calibration and resolution of electrons and muons.
As discussed in Sections 7.6.1 and 7.6.2 both the charge mis-identification probability and the fake factor measurements carry their own systematic uncertainties. They were discussed in the corresponding sections and are not repeated here.
A significant contribution arises from the statistical uncertainty in the MC samples and data sideband regions. The statistical uncertainty varies from 5% to 40% depending on the signal region.

A summary of all systematic uncertainties is presented in Table 7.13. It shows weather the systematic is applied as a normalization factor, or it affects also shape information, and the affected samples.

Systematic Effect	Systematic Type	Effect	Affected MC Samples
Luminosity	exp.	norm.	all
Expected Yield fit	exp.	norm.	DY, diboson
Lepton Efficiencies	exp.	shape + norm.	all
Lepton Scale & resolution	exp.	shape + norm.	all
MC statistics	exp.	shape + norm.	all
Charge-flip method	exp.	shape + norm.	-
Fake Background method	exp.	shape	-
PDF choice	th.	shape + norm.	DY
PDF variation	th.	shape + norm.	DY
MC modeling	th.	shape + norm.	DY

Table 7.13: Summary of systematic effects considered in the analysis. The first column corresponds to the source of systematic uncertainty, the second and the third column give the type of the source (experimental/theoretical and normalization/shape), and the last column lists MC samples affected by the systematic effect.

7.9 Limits on $H^{\pm\pm}$ mass and cross section

The fit procedure is presented in Chapter 5.6. No evidence for a signal over the SM expectation is found in this search: upper limits on the doubly charged Higgs production cross-section are set. The *flavour-blind* four lepton signal region (2P4L) is the region with the largest sensitivity under the hypothesis: $BR(H^{\pm\pm} \to e^{\pm}e^{\pm}) + BR(H^{\pm\pm} \to e^{\pm}\mu^{\pm}) + BR(H^{\pm\pm} \to \mu^{\pm}\mu^{\pm}) = 100\%$.
The fit is performed under two $H^{\pm\pm}$ branching ratio hypotheses:

$$BR(e^{\pm}e^{\pm}) + BR(e^{\pm}\mu^{\pm}) + BR(\mu^{\pm}\mu^{\pm}) = 100\%, \;\; BR(X) = 0 \qquad (7.4)$$

$$BR(e^{\pm}e^{\pm}) + BR(e^{\pm}\mu^{\pm}) + BR(\mu^{\pm}\mu^{\pm}) \leq 100\%, \;\; BR(X) \neq 0 \qquad (7.5)$$

scanning over the branching ratio combinations $BR(H^{\pm\pm} \to \ell^{\pm}\ell^{\pm})$ ranging from 1% to 5% with 1% intervals, and from 10% to 100% in steps of 10% intervals. The four lepton signal region is by far the most powerful region in the first fit configuration (100% branching ratio to light leptons), providing a 40-50% efficiency and a total expected background of 0.33 events. Indeed, as it will be shown later, the expected limit obtained using only four lepton events, provides the same sensitivity as the combined fit using all the signal regions.

Background process	Fitted in	Normalization factor
Drell-Yan	OCCR	1.03 ± 0.04
Diboson	DBCR ($e^{\pm}e^{\pm}$)	1.02 ± 0.07
Diboson	DBCR ($\mu^{\pm}\mu^{\pm}$)	0.98 ± 0.05
Diboson	DBCR ($e^{\pm}\mu^{\pm}$)	1.02 ± 0.05

Table 7.14: Summary of the fitted yields. First column presents the background process, the second column indicates the control region used to constrain its normalization and the last column gives the fitted value.

A first fit is performed using the background only hypothesis in control regions, where systematic uncertainties are described as nuisance parameters and shared between control and validation regions. Additional free parameters describe the normalization for four different types of backgrounds; Drell-Yan process normalization is extracted from the OCCR; diboson normalization is separately assessed using the three DBCR. Hence three different normalization factors are obtained, respectively for the electron, $e\mu$ and muon channels. Furthermore, an additional parameter is defined to constrain the diboson normalization in the 4LCR. The very good agreement, between

	OCCR $e^{\pm}e^{\mp}$	DBCR $e^{\pm}e^{\pm}e^{\mp}$	DBCR $e^{\pm}\mu^{\pm}\ell^{\mp}$	DBCR $\mu^{\pm}\mu^{\pm}\mu^{\mp}$	4LCR $\ell^{\pm}\ell^{\pm}\ell^{\mp}\ell^{\mp}$
Observed events	184 569	576	1025	797	140
Total Post-fit	184 570 ± 430	574 ± 24	1025 ± 32	797 ± 28	140 ± 12
Drell–Yan	169 980 ± 990	–	–	–	–
Diboson	5060 ± 900	449 ± 28	909 ± 35	775 ± 29	138 ± 12
Fakes	2340 ± 300	123 ± 15	113 ± 14	19.9 ± 6.5	1.31 ± 0.16
Top	7200 ± 250	1.58 ± 0.06	2.90 ± 0.11	2.04 ± 0.08	0.37 ± 0.01
Total Pre-fit	179 394 ± 6100	565 ± 22	1014 ± 34	819 ± 28	122 ± 4
Drell–Yan	164 905 ± 5607	–	–	–	–
Diboson	4891 ± 954	440 ± 15	896 ± 30	796 ± 27	121 ± 4
Fakes	2362 ± 307	124 ± 15	115 ± 14	21 ± 6	1.32 ± 0.16
Top	7197 ± 251	1.58 ± 0.06	2.90 ± 0.10	2.04 ± 0.09	0.37 ± 0.01

Table 7.15: The number of pre- and post-fit predicted background events in control regions, compared to the data. Uncertainties correspond to the total uncertainties in the predicted event yields, and are smaller for the total than the sum of the components in quadrature due to correlations between these components. Background processes with a negligible yield are marked with (–).

data and background predictions, in all the analysis control regions (see Section 7.7.1) obtained already before performing the fit reduces the impact of this latter when constraining the background normalization factors. Indeed, as clear from Table 7.14, the fit changes background normalization from its initial value (set to one) of few %. The normalization factors extracted from the control regions are applied into the validation regions, using Eq. 5.31. Table 7.15 shows the pre- and post-post fit yields in the analysis control regions. A very good agreement between the observed and the total expected events after fit is observed.
A very good post-fit agreement is also observed in validation regions, as from Table 7.16, which strengths the confidence that the fitting procedure is working properly.
After the background only fit, the exclusion fit is performed, combining control and signal regions. The signal regions are fitted under the hypothesis of a signal strength for $H^{\pm\pm}$ production of μ=1 all $H^{\pm\pm}$ masses with a fitted μ parameter below one ($\mu < 1$) can be excluded. On the contrary, the analysis is not enough sensitive to exclude all the $H^{\pm\pm}$ mass points with a post-fit $\mu > 1$. The pre- and post-fit yields in signal regions are presented in Table 7.17. A very good agreement between observed and after fit predicted background is found in all the signal regions.

	SCVR $e^{\pm}e^{\pm}$	SCVR $e^{\pm}\mu^{\pm}$	SCVR $\mu^{\pm}\mu^{\pm}$	4LVR $\ell^{\pm}\ell^{\pm}\ell^{\mp}\ell^{\mp}$
Observed events	3237	1162	1006	3
Total Post-fit	3330 ± 210	1119 ± 51	975 ± 50	4.62 ± 0.40
Drell–Yan	2300 ± 190	–	–	–
Diboson	319 ± 25	547 ± 23	719 ± 30	4.59 ± 0.4
Fakes	640 ± 65	502 ± 54	249 ± 47	–
Top	71.5 ± 6.8	70.5 ± 2.6	6.93 ± 0.27	0.033 ± 0.001
Total Pre-fit	3246 ± 228	1117 ± 60	999 ± 51	4.03 ± 0.14
Drell–Yan	2219 ± 200	–	–	–
Diboson	311 ± 19	539 ± 21	737 ± 28	4.00 ± 0.14
Fakes	645 ± 66	507 ± 55	256 ± 42	–
Top	71.3 ± 6.9	70.8 ± 2.74	6.95 ± 0.27	0.033 ± 0.001

	3LVR $e^{\pm}e^{\pm}e^{\mp}$	3LVR $e^{\pm}\mu^{\pm}\ell^{\mp}$	3LVR $\mu^{\pm}\mu^{\pm}\mu^{\mp}$	3LVR $\mu^{\pm}\mu^{\pm}e^{\mp}, e^{\pm}e^{\pm}\mu^{\mp}$
Observed events	108	180	126	16
Total Post-fit	88.1 ± 5.8	192.9 ± 9.9	107.0 ± 5.1	27.0 ± 3.9
Diboson	64.4 ± 5.8	147.3 ± 9.0	100.9 ± 5.0	4.72 ± 0.79
Fakes	23.3 ± 3.0	43.9 ± 4.9	5.3 ± 1.2	21.3 ± 3.4
Top	0.50 ± 0.03	1.73 ± 0.09	0.82 ± 0.05	1.01 ± 0.15
Total Pre-fit	87.3 ± 6.1	193 ±11	109.6 ± 5.3	27.3 ± 3.9
Diboson	63.3 ± 4.9	147.9 ± 8.8	4.69 ± 0.79	103.4 ± 4.9
Fakes	23.5 ± 3.09	44.3 ± 5.02	5.43 ± 1.14	21.7 ± 3.33
Top	0.50 ± 0.03	1.73 ± 0.09	0.82 ± 0.05	1.01 ± 0.16

Table 7.16: The number of pre- and post-fit predicted background events in two-lepton, three-lepton and four-lepton validation regions (top), compared to the data. The number of predicted background events in two-lepton and four-lepton validation regions (top) and three-lepton validation regions (bottom) after the fit, compared to the data. Uncertainties correspond to the total uncertainties in the predicted event yields, and are smaller for the total than the sum of the components in quadrature due to correlations between these components. Background processes with a negligible yield are marked with the en dash (–).

The effect of systematic uncertainties, which are constrained using data in control region during the fit, can be assessed by looking at the pull plot

	1P2L $e^{\pm}e^{\pm}$	1P2L $e^{\pm}\mu^{\pm}$	1P2L $\mu^{\pm}\mu^{\pm}$	2P4L $\ell^{\pm}\ell^{\pm}\ell^{\mp}\ell^{\mp}$
Observed events	132	106	26	1
Total Post-fit	160 ± 14	97.1 ± 7.7	22.6 ± 2.0	0.33 ± 0.23
Drell–Yan	70 ± 10	–	–	–
Diboson	30.5 ± 3.0	40.4 ± 4.5	20.3 ± 1.8	0.11 ± 0.06
Fakes	52.2 ± 5.0	53.1 ± 5.8	1.94 ± 0.47	0.22 ± 0.19
Top	7.20 ± 0.97	3.62 ± 0.53	0.42 ± 0.03	0.007 ± 0.002
Total Pre-fit	156 ± 15	98.1 ± 8.3	23.4 ± 2.19	0.33 ± 0.23
Drell–Yan	67 ± 10	–	–	–
Diboson	29.5 ± 2.6	40.9 ± 4.7	20.9 ± 2.0	0.10 ± 0.06
Fakes	52.6 ± 5.0	53.5 ± 5.9	2.01 ± 0.43	0.22 ± 0.19
Top	7.12 ± 0.98	3.58 ± 0.54	0.42 ± 0.04	0.007 ± 0.002

	1P3L $e^{\pm}e^{\pm}e^{\mp}$	1P3L $e^{\pm}\mu^{\pm}\ell^{\mp}$	1P3L $\mu^{\pm}\mu^{\pm}\mu^{\mp}$	1P3L $\mu^{\pm}\mu^{\pm}e^{\mp}, e^{\pm}e^{\pm}\mu^{\mp}$
Observed events	11	23	13	2
Total Post-fit	13.0 ± 1.6	34.2 ± 3.6	13.2 ± 1.3	3.1 ± 1.4
Diboson	9.5 ± 1.3	23.1 ± 2.9	13.1 ± 1.3	0.27 ± 0.14
Fakes	3.3 ± 0.67	10.7 ± 1.7	–	2.6 ± 1.2
Top	0.14 ± 0.02	0.45 ± 0.04	0.12 ± 0.01	0.19 ± 0.08
Total Pre-fit	12.8 ± 1.63	34.7 ± 3.82	13.6 ± 1.49	3.15 ± 1.38
Diboson	9.32 ± 1.24	23.4 ± 2.9	13.5 ± 1.5	0.30 ± 0.16
Fakes	3.33 ± 0.68	10.9 ± 1.7	–	2.7 ± 1.2
Top	0.14 ± 0.02	0.45 ± 0.04	0.12 ± 0.01	0.19 ± 0.08

Table 7.17: The number of pre- and post-fit predicted events in the two-lepton, three-lepton and four-lepton signal regions, compared to the data. Uncertainties correspond to the total uncertainties in the predicted event yields, and are smaller for the total than the sum of the components in quadrature due to correlations between these components. Background processes with a negligible yield are marked with (–).

in Fig. 7.34. Remembering that most of the systematic uncertainties are treated as a $\pm 1\sigma$ variation from the nominal value, in the case they do not impact much on the fit results, the after fit values for systematics should still

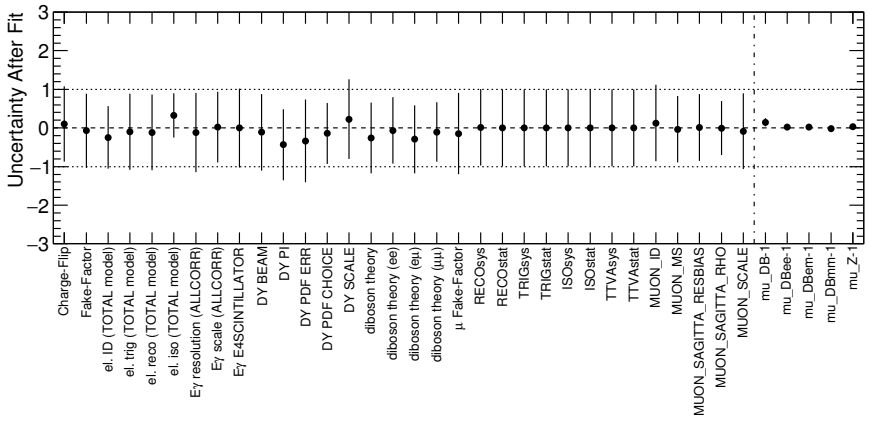

(a)

Figure 7.34: Systematic pulls for the combined fit. Values between -1 and 1 indicate the nominal 1 standard deviation band of the uncertainty.

lay inside the $\pm 1\sigma$ band. This is true for all the systematic uncertainties in Fig. 7.34. This means that the post-fit values of the systematic uncertainty remain similar to their pre-fit values. Huge pulls of systematic uncertainties, which does not occur here, usually indicate a non proper understanding of the corresponding systematic uncertainty.

The effect of each systematic uncertainty in each region is separately presented in Tables 7.18, 7.19 and 7.20. All systematic uncertainties with an impact less than 0.2% on the total post-fit background prediction are not shown in these tables. Most of the experimental uncertainties are negligible with respect to the statistical uncertainty and in some cases fitted away by the transfer factor procedure in Eq. 5.31. The two lepton signal regions are mainly affected by the systematic uncertainty due to data-driven background estimations ($\sim$5%) and from the statistical uncertainty ($\sim$5%). The three lepton channels are also mainly affected by the diboson theory uncertainty and by the statistical error. The total systematic uncertainties in this channels vary from $\sim$40% to $\sim$10% and the diboson uncertainty has a similar impact across all the three leptons signal regions ($\sim$few%). In the four lepton signal region, the highest systematic uncertainty arises from the diboson theoretical uncertainty which amounts to $\sim$80% and from the size of the samples; all other uncertainty have an impact below $\sim$5%. A summary of all post-fit systematic uncertainties over all the analysis regions is presented in Fig. 7.35.

Uncertainty of channel	1P2L ($e^{\pm}e^{\pm}$)
Total background expectation	159.68
Total background systematic	±13.97 [8.75%]
Charge-Flip	±11.13 [7.0%]
Total stat. error	±6.40 [4.0%]
Fake-Factor ele	±4.48 [2.8%]
Lumi	±3.66 [2.3%]
mu_Z	±2.50 [1.6%]
Electron scale	±1.69 [1.1%]
Electron Iso	±1.56 [0.98%]
Electron ID	±1.28 [0.80%]
DY PI	±0.46 [0.29%]
Electron resolution	±0.38 [0.24%]
	1P2L ($e^{\pm}\mu^{\pm}$)
Total background expectation	97.13
Total background systematic	±7.67 [7.90%]
Fake-Factor ele	±5.20 [5.4%]
Total stat. error	±4.54 [4.7%]
Lumi	±1.50 [1.5%]
Charge-Flip	±0.84 [0.86%]
Electron scale	±0.57 [0.59%]
Mu trig (SYS)	±0.39 [0.40%]
Fake-Factor muon	±0.34 [0.36%]
Electron Iso	±0.30 [0.31%]
Muon SagittaResBias	±0.22 [0.22%]
Mu Trig (STAT)	±0.20 [0.20%]
Mu Reco (SYS)	±0.20 [0.20%]
	1P2L ($\mu^{\pm}\mu^{\pm}$)
Total background expectation	22.65
Total background systematic	±1.98 [8.72%]
Total stat. error	±1.53 [6.8%]
Lumi	±0.71 [3.1%]
Fake-Factor muon	±0.43 [1.9%]
Muon reco (SYS)	±0.19 [0.85%]
Muon SagittaResBias	±0.07 [0.31%]
Muon Trig (SYS)	±0.05 [0.24%]
Muon Iso (STAT)	±0.04 [0.20%]

Table 7.18: Breakdown of the dominant uncertainties on background estimates. The given total statistical error is a quadratic sum of individual statistical errors of each bin in the region. Uncertainties are ordered from the largest to smallest in total (last column).

Uncertainty of channel	1P3L ($e^{\pm}e^{\pm}\mu^{\mp}$ or $\mu^{\pm}\mu^{\pm}e^{\mp}$)	1P3L ($e^{\pm}\mu^{\pm}\ell^{\mp}$)
Total background expectation	3.05	34.21
Total background systematic	±1.36 [44.39%]	±3.64 [10.64%]
Total stat. error	±1.28 [41.9%]	±2.65 [7.7%]
Diboson theory ($e\mu$)	±0.09 [2.9%]	±2.08 [6.1%]
mu_DBem	±0.01 [0.46%]	±1.19 [3.5%]
Fake-Factor muon	±0.43 [14.2%]	±1.11 [3.3%]
Lumi	±0.02 [0.52%]	±0.80 [2.3%]
Fake-Factor ele	±0.06 [2.1%]	±0.73 [2.1%]
Electron scale	±0.00 [0.12%]	±0.21 [0.62%]
Muon Reco (SYS)	±0.00 [0.15%]	±0.21 [0.61%]
Electron Iso	±0.00 [0.12%]	±0.18 [0.53%]
Uncertainty of channel	1P3L ($e^{\pm}e^{\pm}e^{\mp}$)	1P3L ($\mu^{\pm}\mu^{\pm}\mu^{\mp}$)
Total background expectation	12.97	13.18
Total background systematic	±1.59 [12.23%]	±1.26 [9.58%]
Diboson theory ($\mu\mu$)	±0.00 [0.00%]	±0.91 [6.9%]
Total stat. error	±1.31 [10.1%]	±0.68 [5.1%]
mu_DBmm	±0.00 [0.00%]	±0.66 [5.0%]
Lumi	±0.33 [2.5%]	±0.45 [3.4%]
Muon Reco (SYS)	±0.00 [0.00%]	±0.24 [1.8%]
Muon SagittaResBias	±0.00 [0.00%]	±0.09 [0.65%]
Muon scale	±0.00 [0.00%]	±0.08 [0.62%]
Electron ID	±0.10 [0.73%]	±0.00 [0.00%]
mu_DBee	±0.69 [5.3%]	±0.00 [0.00%]
Electron Resolution	±0.07 [0.58%]	±0.00 [0.00%]
Electron Iso	±0.15 [1.2%]	±0.00 [0.00%]
Electron Scale	±0.07 [0.55%]	±0.00 [0.00%]
diboson theory (ee)	±0.67 [5.2%]	±0.00 [0.00%]
Fake-Factor ele	±0.46 [3.5%]	±0.00 [0.00%]

Table 7.19: Breakdown of the dominant uncertainties on background estimates. The given total statistical error is a quadratic sum of individual statistical errors of each bin in the region. Note that the individual uncertainties can be correlated, and do not necessarily add up quadratically to the total background uncertainty. Uncertainties are ordered from the largest to smallest in total (last column).

Uncertainty of channel	2P4L
Total background expectation	0.33
Total background systematic	±0.23 [70.65%]
total stat. error	±0.23 [69.4%]
Diboson theory	±0.04 [12.8%]
mu_DB	±0.01 [3.0%]
Lumi	±0.00 [1.2%]
Muon reco (SYS)	±0.00 [0.62%]
Electron Iso	±0.00 [0.27%]

Table 7.20: Breakdown of the dominant uncertainties on background estimates. The given total statistical error is a quadratic sum of individual statistical errors of each bin in the region. Uncertainties are ordered from the largest to smallest in total (last column).

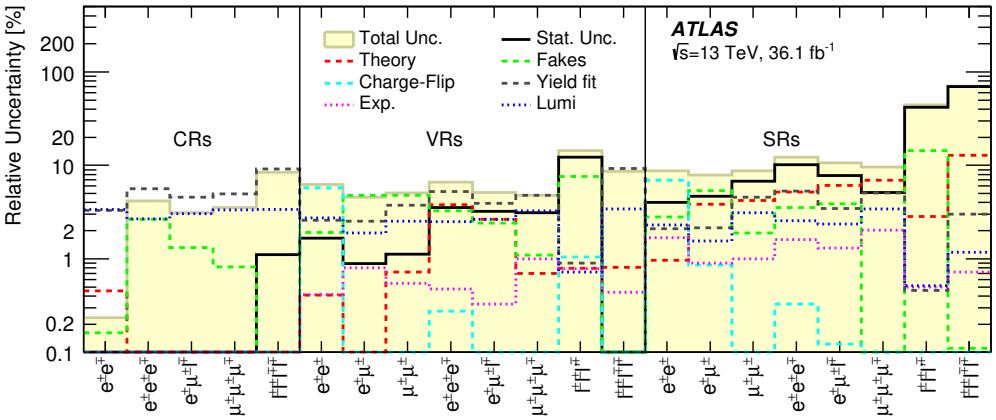

Figure 7.35: Relative uncertainties in the total background yield estimation after the fit. *Stat. Unc.* corresponds to reducible and irreducible background statistical uncertainties. *Yield fit* corresponds to the uncertainty arising from fitting the yield of diboson and Drell–Yan backgrounds. *Lumi* corresponds to the uncertainty in the luminosity. *Theory* indicates the theoretical uncertainty in the physics model used for simulation (e.g. cross-sections). *Exp.* indicates the uncertainty in the simulation of electron and muon efficiencies (e.g. trigger, identification). *Fakes* is the uncertainty associated with the model of the fake background. Individual uncertainties can be correlated, and do not necessarily add in quadrature to the total background uncertainty, which is indicated by *Total Unc.*

Expected sensitivity in four lepton signal region

The signal region containing four leptons is separately fitted considering only $H^{\pm\pm}$ decays to light leptons $BR(H^{\pm\pm} \to \ell^{\pm}\ell^{\pm})$ =100%. Only four leptons control, validation and signal regions are used in this fit.

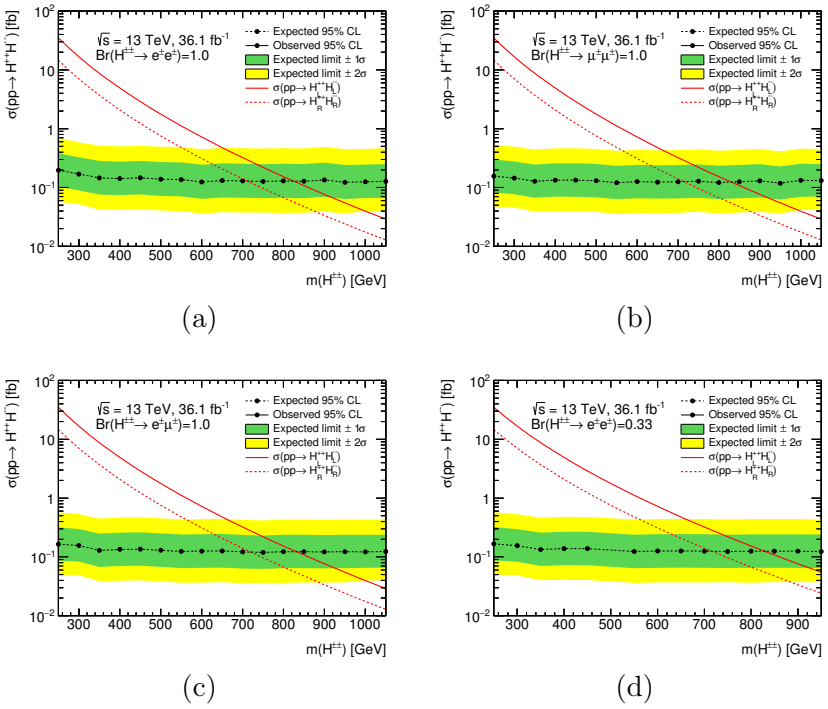

Figure 7.36: Signal region 2P4L only limit for the $pp \to H^{\pm\pm}H^{\pm\pm}$ production cross-section as a function of the $H^{\pm\pm}$ mass in the $BR(e^{\pm}e^{\pm}) = 100\%$ (a), $BR(\mu^{\pm}\mu^{\pm}) = 100\%$ (b), $BR(e^{\pm}\mu^{\pm}) = 100\%$ (c) and $BR(\ell^{\pm}\ell^{\pm}) = 33\%$ (d) assumptions.

Figure 7.36 shows the exclusion fit result for the following branching ratio hypotheses: $BR(e^{\pm}e^{\pm}) = 100\%$, $BR(\mu^{\pm}\mu^{\pm}) = 100\%$, $BR(e^{\pm}\mu^{\pm}) = 100\%$ and $BR(\ell^{\pm}\ell^{\pm}) = 33\%$. The y axis shows the cross-section for $\sigma(pp \to H^{\pm\pm}H^{\mp\mp})$ for the pair production while on the x axis different $H^{\pm\pm}$ mass points are shown. The theoretical cross-sections for both the right- and left-handed $H^{\pm\pm}$ states are presented in red lines. Each black dot corresponds to the expected cross-section limit obtained fitting each $H^{\pm\pm}$ mass hypothesis. The point in which the theoretical cross-section prediction crosses the expected limit sets the expected lower mass limit on the $H^{\pm\pm}$ mass and the corresponding cross-section limit. The expected sensitivity is similar among channel flavour. The expected lower mass limit for the left-handed $H^{\pm\pm}$ is 830 GeV while for the right-handed $H^{\pm\pm}$ is 710 GeV.

Results for the combined signal region

All signal regions are eventually combined together to extract the final result. Few representative 95% CL cross-section upper limits as a function of the $H^{\pm\pm}$ mass are presented in Fig. 7.37, for different branching ratio combinations into light leptons only.

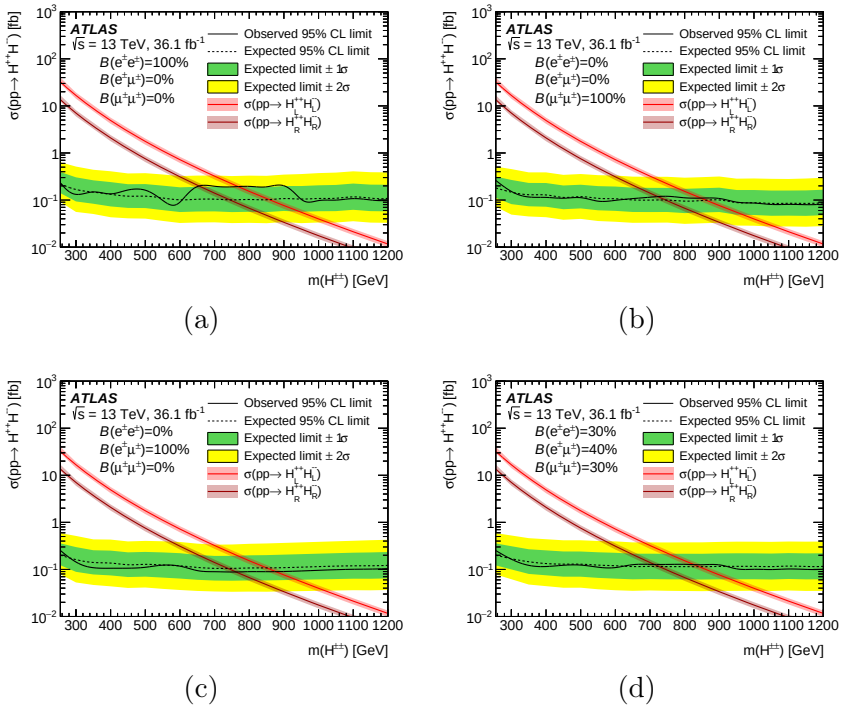

Figure 7.37: 95% C.L. upper cross-section limit of $pp \to H^{\pm\pm}H^{\mp\mp}$ for $BR(H^{\pm\pm} \to e^{\pm}e^{\pm}) + BR(H^{\pm\pm} \to e^{\pm}\mu^{\pm}) + BR(H^{\pm\pm} \to \mu^{\pm}\mu^{\pm}) = 100\%$ and several branching ratio working points presented in form $BR(ee)/Br(e\mu)/Br(\mu\mu)$: (a) 1.0/0.0/0.0, (b) 0.0/0.0/1.0, (c) 0.0/1.0/0.0 and (d) 0.3/0.4/0.3.

Limits for the scenario $BR(H^{\pm\pm} \to e^{\pm}e^{\pm})$ =100%, shown in Fig. 7.37a, exhibit a wide one standard deviation discrepancy between 600 GeV and 900 GeV masses due to the two observed events in the corresponding range in the three electron signal region. This feature is not present for muons or mixed flavour final states and the corresponding signal regions lead the exclusion fit.

Under the assumption of 100% decays into light leptons, fit results are visualized in a bidimensional plane having on the y axis the $H^{\pm\pm}$ branching ratio into muon pairs and on the x axis the one to electron pairs. For each $BR(H^{\pm\pm} \to e^{\pm}e^{\pm})$ and $BR(H^{\pm\pm} \to \mu^{\pm}\mu^{\pm})$ combination the corresponding

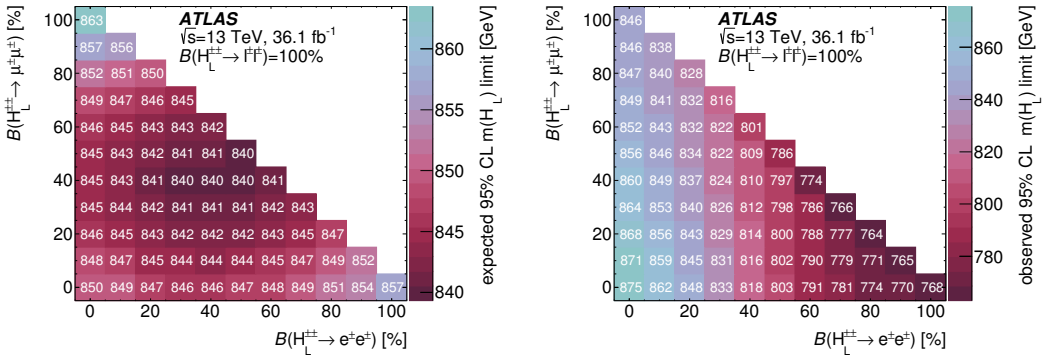

(a) (b)

Figure 7.38: Expected (a) and observed (b) lower limit on the $H_L^{\pm\pm}$ mass for all branching ratio combinations that sum to 100%.

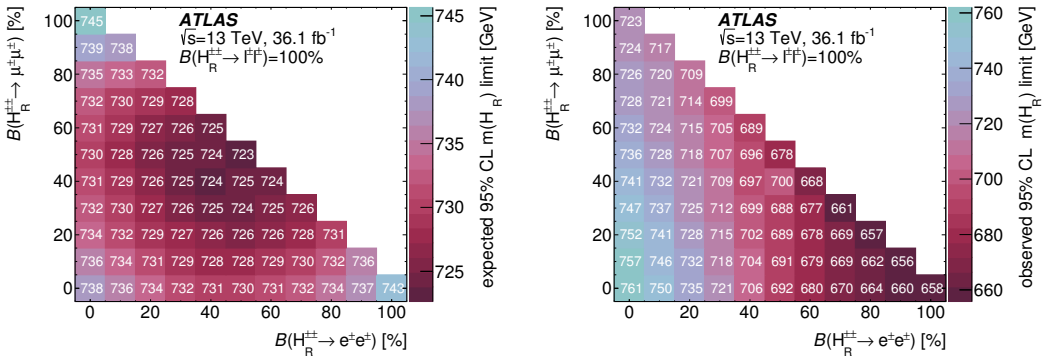

(a) (b)

Figure 7.39: Expected (a) and observed (b) lower limit on the $H_R^{\pm\pm}$ mass for all branching ratio combinations that sum to 100%.

$BR(H^{\pm\pm} \to e^{\pm}\mu^{\pm})$ is automatically fixed by the total sum, which has to be 100%. The expected and observed lower limits for $H_L^{\pm\pm}$ and $H_R^{\pm\pm}$ are shown respectively in Fig. 7.38 and 7.39. Lower mass limits for $H_L^{\pm}$ vary from 750 to 850 GeV accordingly to the branching ratio hypotheses; limits for $H_R^{\pm\pm}$ are less stringent due to the predicted lower production cross-section for the right-handed $H^{\pm\pm}$ compared to the left-handed one.

Data are then interpreted under the branching ratio hypothesis $BR(H^{\pm\pm} \to \ell^{\pm}\ell^{\pm}) + BR(H^{\pm\pm} \to X)$ =100%. The results of the exclusion fit are presented in Fig. 7.40 and 7.41 respectively for the left- and right-handed $H^{\pm\pm}$ final

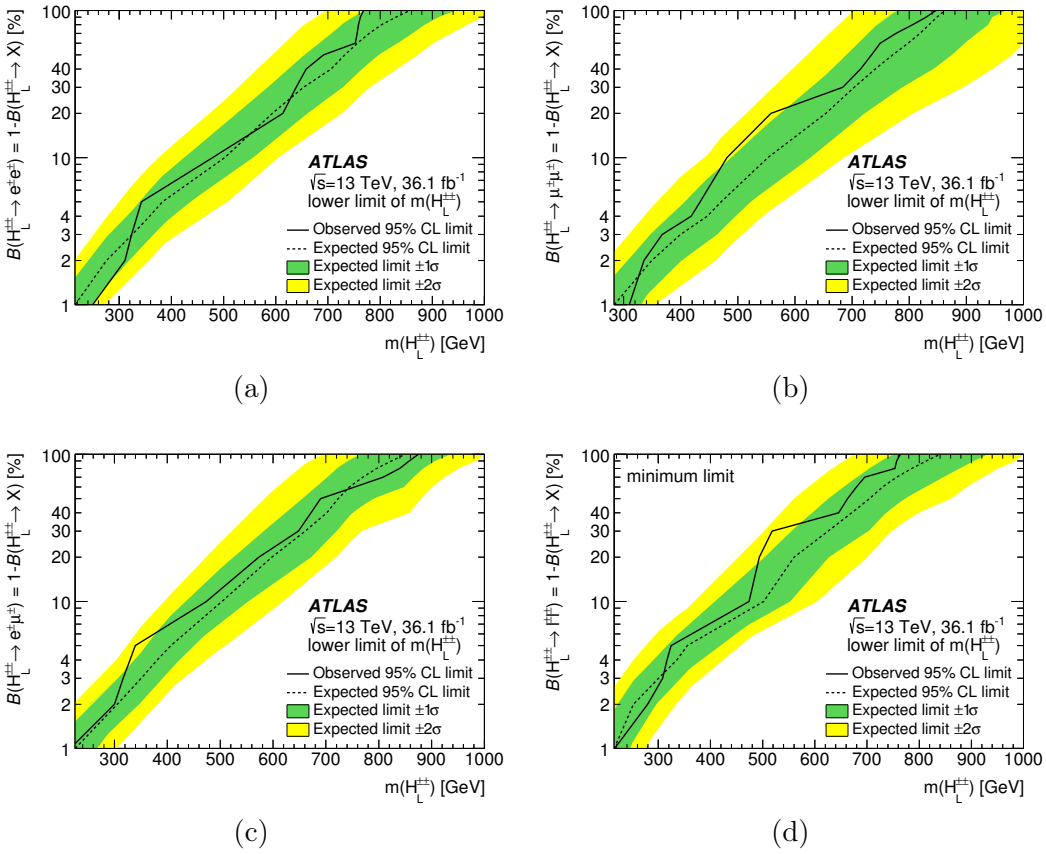

Figure 7.40: Lower limit on the $H_L^{\pm\pm}$ mass as a function of branching ratio $BR(H_L^{\pm\pm} \to \ell^\pm\ell^\pm)$. Several cases are presented where: (a) $H_L^{\pm\pm}$ decays only into electrons and "X",(b) $H_L^{\pm\pm}$ decays only into muons and "X", and(c) $H_L^{\pm\pm}$ decays only into electron-muon pairs and "X", where "X" does not enter any of the signal regions. Plot (d) shows the minimum observed and expected limit as a function of $BR(H_L^{\pm\pm} \to \ell^\pm\ell^\pm)$.

states. On the y axis is reported the total branching ratio into light leptons, while the x axis shows the $H^{\pm\pm}$ mass. Each point corresponds to the lower observed limit extracted by distributions of the type reported in Fig. 7.37. Technically, as said, the fit is performed by rescaling each branching ratio combination to give a sum below 100%. These distributions are particularly powerful because they proof that even for total branching ratio to leptons around 10%, doubly charged Higgs boson masses below 450 GeV for $H_L^{\pm\pm}$ and 320 GeV for $H_R^{\pm\pm}$ can still be excluded. Figures 7.40d and 7.41d present the minimum observed limit among each flavour combination.
It is worth mentioning that the expected 95% CL upper cross-section limits

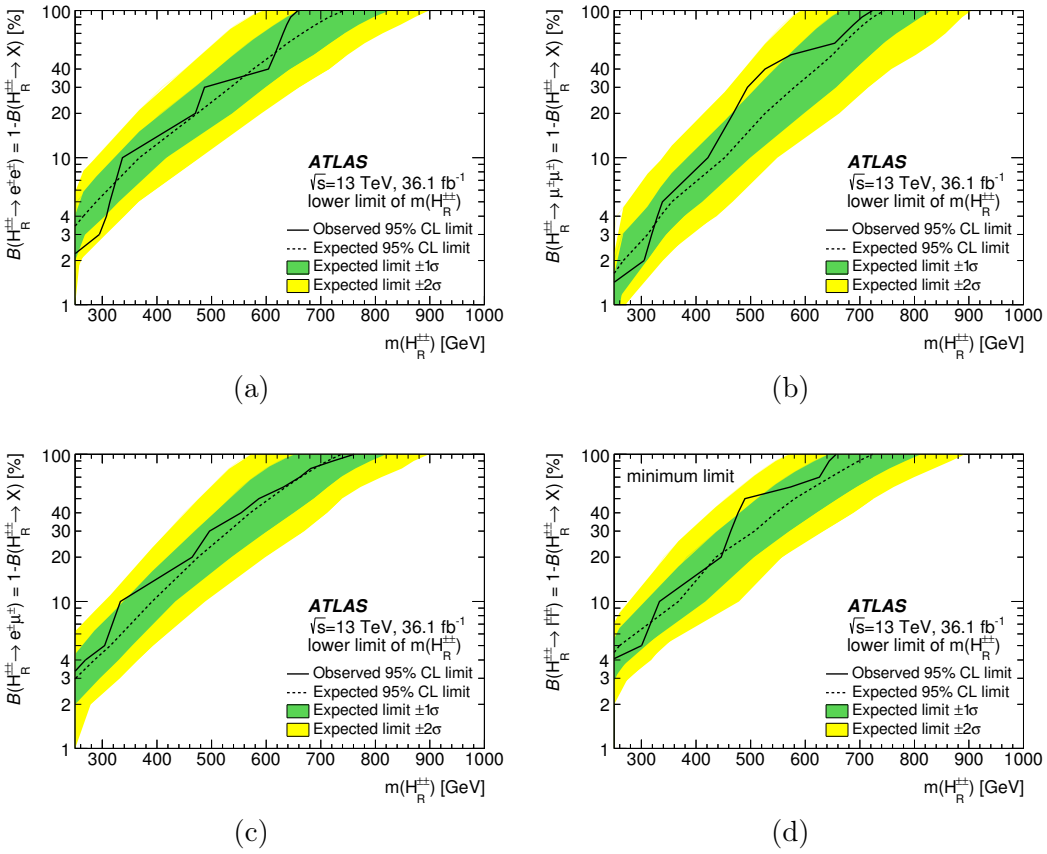

Figure 7.41: Lower limit on the $H_R^{\pm\pm}$ mass as a function of branching ratio $BR(H_R^{\pm\pm} \to \ell^\pm\ell^\pm)$. Several cases are presented where: (a) $H_R^{\pm\pm}$ decays only into electrons and "X", (b) $H_R^{\pm\pm}$ decays only into muons and "X", and (c) $H_R^{\pm\pm}$ decays only into electron-muon pairs and "X", where "X" does not enter any of the signal regions. Plot (d) shows the minimum observed and expected limit as a function of $BR(H_R^{\pm\pm} \to \ell^\pm\ell^\pm)$.

are reaching 0.1 fb which corresponds to 3/4 signal events, i.e. the theoretical hard limit of 95% C.L exclusion.

7.10 Search for W_R and N_R production

The hypothesis of Majorana neutrino is very appealing, since the final state is a subset of the one used in the search for $H^{\pm\pm}$ production. The W_R decays in two jets, thus we require two SS leptons and the presence of two additional hard jets. Depending on the nature of the neutrino, being a

Dirac or a Majorana particle, the final state can either contain two OS or SS leptons. This search is divided into two orthogonal channels: the OS plus two jets and the SS plus two jets. The two analyses use similar objects and event selections however, due to the nature of the opposite- and same-sign lepton final states, the SM backgrounds are substantially different. They are estimated through MC simulation for the OS case and through data-driven techniques in the SS case. Here we focus on the search into SS leptons pairs.

7.10.1 Object definition and analysis regions

The analysis is performed using the same dataset used for the $H^{\pm\pm}$ search, presented in Section 7.2.1. In line with the $H^{\pm\pm}$ search, the major backgrounds to this search arises from Drell-Yan, diboson and fake leptons. All the simulated SM samples for background processes are presented in Section 7.2.2. However, the generator used to describe $Z/\gamma^* \to ee$ events was changed from POWHEG-BOX v2 to SHERPA 2.2.1 given the very poor statistics obtained for $Z/\gamma^* \to ee$ plus two jets events provided by the former. Events are simulated using the NNPDF3.0NLO PDF set at ME with the SHERPA default tuning parameters.

Signal simulation

Signal events are generated with MADGRAPH5 (MG5) offering a good description of the decay chain of off-shell particles as in the cases where we have a virtual W_R^*. The left-right symmetric model is produced with the Mathematica package FEYNRULES [174], implemented in MG5 and integrated into the ATLAS production chain using MADGRAPHCONTROL. The simulation includes a Majorana right-handed neutrino N_R, giving an admixture of 50% same- and opposite-sign lepton pairs. In case of a Dirac N_R, only opposite-sign leptons would be produced, and the measured cross-section should be twice the simulated one. Signal samples do not include lepton flavour-mixing decay vertices. Several signal samples are generated under both the mass hierarchies hypothesis $m_{W_R} > m_{N_R}$ and $m_{N_R} > m_{W_R}$.

An example of the truth mass distributions for the W_R and N_R signal process is presented in Fig. 7.42, while Table 7.21 summarizes the combinations of W_R and N_R mass points simulated for the analysis.

The analysis additionally requires the presence of two jets with high transverse momentum. The p_{T} and η selection for jets are the result of an optimization study to evaluate the sensitivity (parametrized as $s/\sqrt{b}$) varying the p_{T} and η cut values on jets. The maximum sensitivity is reached requiring

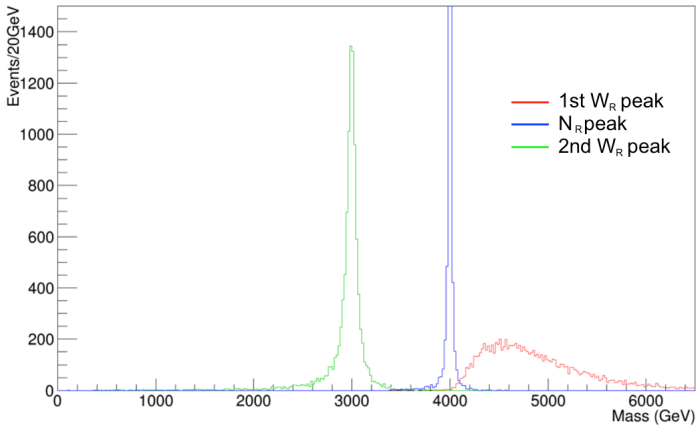

Figure 7.42: Mass distributions for on-shell W_R (green), N_R (blue) and off-shell W_R^* (red) particles for pole mass values of $m_{W_R} = 3$ TeV and $m_{N_R} = 4$ TeV generated with MG5. Under this specific hierarchy choice the first W_R in the decay chain is off-shell, while the second one is on-shell. Since there is only an on-shell decay for the N_R particle in this example, the m_{N_R} distribution is noticeably wider than in the $m_{N_R} < m_{W_R}$ case.

m_{W_R} [GeV]	m_{N_R} [GeV]
600	50, 150, 300, 450, 500, 600, 700, 900, 1200
1000	700, 800, 1000, 1100
1200	50, 300, 600, 900, 1100, 1200, 1500, 1800, 2400
1500	1000, 1100, 1200
1800	50, 450, 900, 1350, 1500, 1600, 1700, 2700, 3600
2400	50, 600, 1200, 1800, 1900, 2100, 2300, 3600, 4800
3000	30, 50, 150, 300, 750, 1500, 1600, 1800, 2250, 2900, 4500, 6000
3500	50, 875, 1750, 2625, 3400, 5250, 7000
3600	50, 900, 1800, 2700, 3500, 5400, 7200
4000	400
4200	50, 1050, 2100, 3150, 4100, 6300, 8400
4500	50, 1125, 2250, 3375, 4400
5000	50, 500, 1250, 2500, 3750, 4900

Table 7.21: Grid of simulated W_R and N_R mass points used in the analysis.

$|\eta|$ <2.0 and $p_{\mathrm{T}} > 100$ GeV, over a baseline test jet selection corresponding to the kinematic cuts $|\eta|$ <2.8 and $p_{\mathrm{T}} > 50$ GeV. The expected sensitivity in signal region is shown in Fig. 7.43.

These cut combinations, despite being optimal for signal region definition,

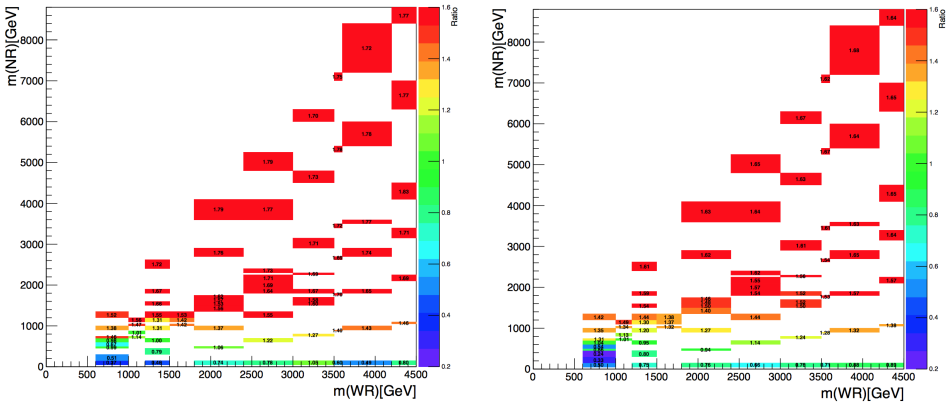

(a) (b)

Figure 7.43: Ratio between analysis sensitivities obtained for the jet cut $|\eta| < 2.0$ and $p_{\mathrm{T}} > 100$ GeV over the one obtained for $|\eta| < 2.8$ and $p_{\mathrm{T}} > 50$ GeV in the N_R/W_R bidimensional mass plane for the ee (a) and $\mu\mu$ (b) channels.

reduce the available statistics in control and validation regions. In those regions, consequently, the p_{T} cut on jets is lowered to 50 GeV. The analysis has limited sensitivity in the regime $m_{W_R} \gg m_{N_R}$ where the two jets originating from the W_R decay are *boosted*, meaning that a specific approach to reconstruct a two merged jet topology is required.

Analysis regions

As in the search for $H^{\pm\pm}$ production, this analysis divides the phase space into control, validation and signal regions. All the analysis regions require the presence of two same-flavour leptons (ee or $\mu\mu$) and at least two high-p_{T} jets. Similarly, a b-jet veto is also applied to all jets with $p_{\mathrm{T}} > 20$ GeV and $|\eta| <2.5$ to reject the SM background involving top quarks.
Control, validation and signal regions are orthogonally defined based on the invariant mass cut applied on SS leptons as follows:

- *control regions*: the muon channel requires 60 GeV$< m(\mu^{\pm}\mu^{\pm}) <$300 GeV; the electron channel uses a higher cut on the invariant mass because the region $m(e^{\pm}e^{\pm}) <$110 GeV is used for the measurement of the charge-flip probabilities and cannot be used as a control region. The electron control region is consequently defined by 110 GeV$< m(e^{\pm}e^{\pm}) <$300 GeV. Nevertheless, the region 60 GeV$< m(e^{\pm}e^{\pm}) <$110 GeV is used as an additional validation region to verify the estimation

of the charge mis-identification background in events with two high-p_{T} jets.

- *validation regions*: the validation region is defined by the presence of a SS lepton pair with invariant mass 300 GeV$< m(\ell^{\pm}\ell^{\pm}) <$400 GeV, for both lepton flavours.

  As stated, both in control and validation regions the jet p_{T} cut is lowered to 50 GeV while in the signal region the cut is set to 100 GeV.

- *signal regions*: the signal region definition is symmetrically defined for electrons and muons as containing two SS leptons with invariant mass above $m(\ell^{\pm}\ell^{\pm}) >$400 GeV. Moreover, to reduce the contamination from the main backgrounds such as Z+jets, WZ+jets and ZZ+jets, the invariant mass of the two leading jets is required to be $m(jj) >$110 GeV and the scalar sum of lepton and the two leading jets p_{T} must satisfy $H_{\mathrm{T}} >$ 400 GeV. These latter cuts on the jet invariant mass and event energy are not used in control and validation regions to increase the available statistics.

All analysis regions are summarized in Table 7.22.

Selection \ Region	Z peak VR	Control region	Validation region	Signal region
$m(e^{\pm}e^{\pm})$ [GeV]	$[60, 110]$	$[110, 300]$	$[300, 400]$	$[400, \infty)$
$m(\mu^{\pm}\mu^{\pm})$ [GeV]	-	$[60, 300]$	$[300, 400]$	$[400, \infty)$
H_{T} [GeV]	-	-	-	$[400, \infty)$
$m(jj)$ [GeV]	-	-	-	$[110, \infty)$
jet p_{T} [GeV]	50 [GeV]	50 [GeV]	50 [GeV]	100 [GeV]
N(jet)	≥ 2	≥ 2	≥ 2	≥ 2
N(b-jet)	0	0	0	0

Table 7.22: Summary of all regions defined in the analysis. Jets considered for the b-jet veto are not subject to the *jet* p_{T} cut defined in the table, but are rather a collection of all jets with $p_{\mathrm{T}} > 20$ [GeV] and $|\eta| < 2.5$.

Figure 7.44 shows the signal efficiency as a function of different W_R and N_R mass combinations.

The efficiencies into electrons and muons are around 30%. The muon channel presents a slightly lower signal efficiency due to tighter isolation working point, with respect to the one used for electrons.

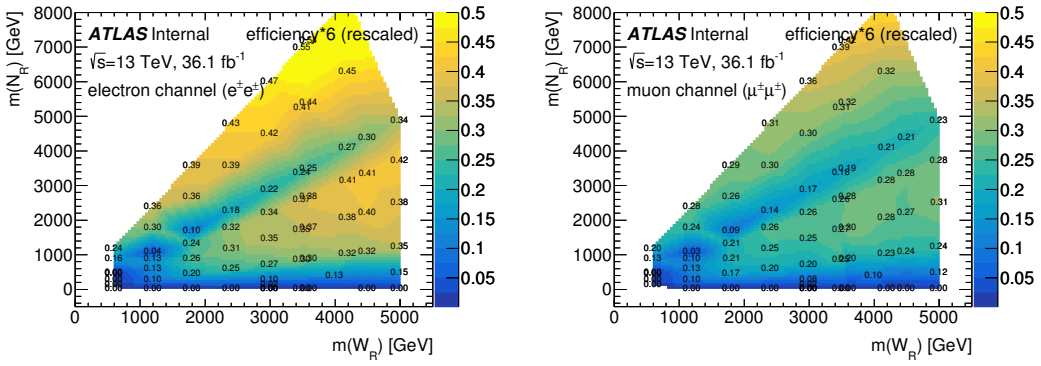

(a) (b)

Figure 7.44: Efficiencies for signal region selection as a function of the different W_R and N_R masses for ee (a) and $\mu\mu$ (b) channel.

7.10.2 Background estimation

The background estimation in this search exactly follows the one presented in Section 7.6. Prompt lepton background is estimated using simulated events while data-driven methods are used for the measurement of the charge mis-identification and fakes.
The charge mis-identification probabilities measured in Section 7.6.1 are here validated in the Z peak region with the additional requirement of two jets in the events. This test is particularly important to assess the validity of the charge-flip background estimation in an environment containing a higher jet multiplicity than the one used in the $H^{\pm\pm}$ search.

Figure 7.45 shows a good agreement between the prediction and data, proving that the data-driven charge-flip background estimation works as expected.

The fake factors for both electrons and muons are measured with the additional requirement of two jets in the events. The background originating from fake leptons can be indeed extremely dependent on jet multiplicity. With respect to the selection outlined in Section 7.6.2, the only change in the region used for the electron fake factor measurement is the additional requirement of two jets with $p_{\mathrm{T}} > 50$ GeV, to reproduce a similar topology to the one present in control, validation and signal regions.

New electron fake factors are shown in Fig. 7.46: the nominal measurement performed with two jets is shown as black dots; the systematic assessment is performed exactly as illustrated in Section 7.6.2. The *inclusive* measurement refers to an inclusive selection in jet multiplicity, i.e. without

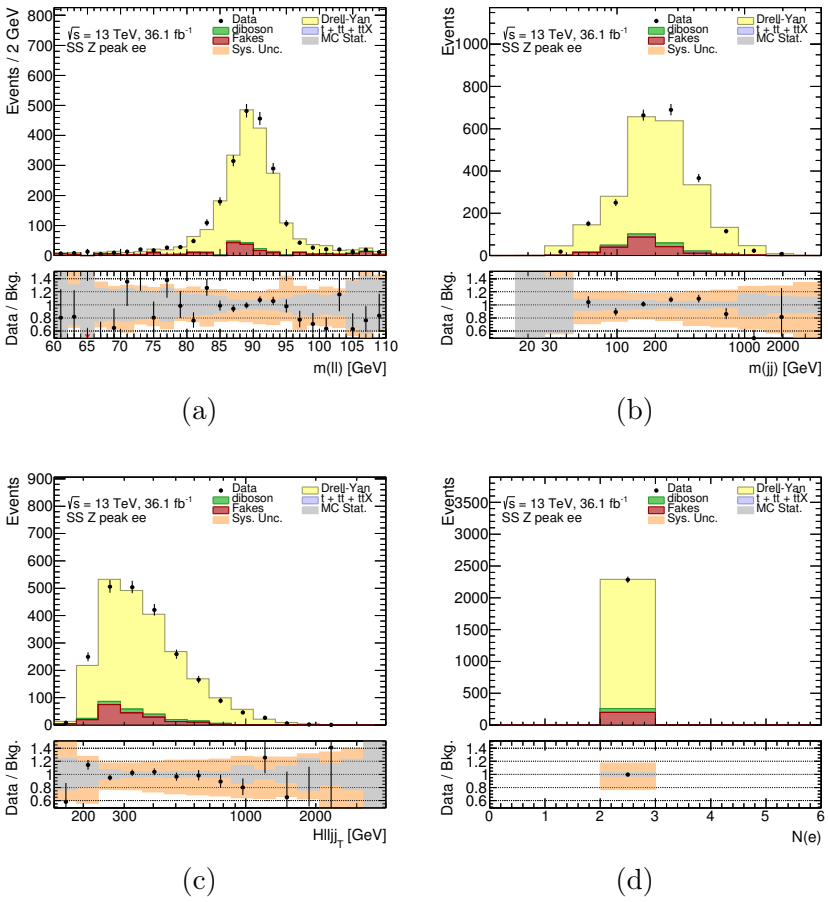

Figure 7.45: Distributions for data and SM background predictions in the electron Z peak validation region (ZVR): (a) invariant mass of the two leptons, (b) invariant mass of the two leading jets, (c) scalar sum of the p_{T} of leptons and two leading jets, and (d) total number of events in the region.

the explicit requirement of two jets events. The nominal fake factor differs from the inclusive measurement by up to 20% in some p_{T} bins and for this reason, despite the higher statistical uncertainty due to the two jet selection, this requirement is kept into the nominal measurement.
The same measurement is performed for the muon fake factor, which uses exactly the same event selection as in Section 7.6.2 with an additional requirement of exactly two jets with p_{T} above 50 GeV. Given that the nominal muon fake factor enriched region requires at least one jet with a $p_{\mathrm{T}} > 35$ GeV being back-to-back with the muon, it is worth noting that one of the 50 GeV jet might correspond to the back-to-back jet.

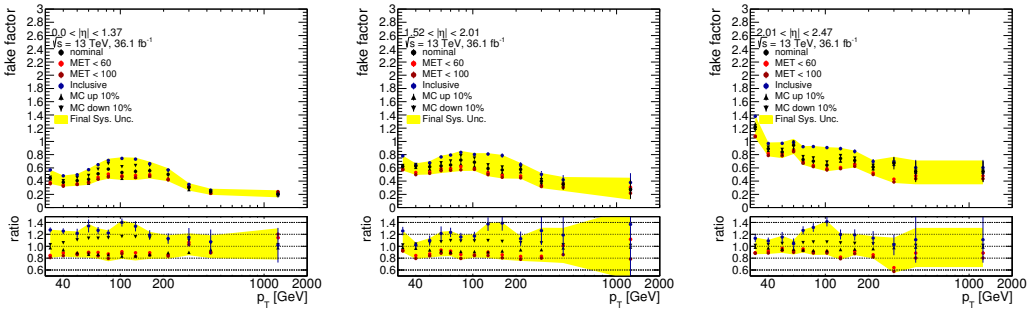

(a) (b) (c)

Figure 7.46: Electron fake factors as a function of electron p_{T} divided into η bins: $0 < |\eta| < 1.37$ (a), $1.52 < |\eta| < 2.01$ (b) and $2.01 < |\eta| < 2.46$ (c).

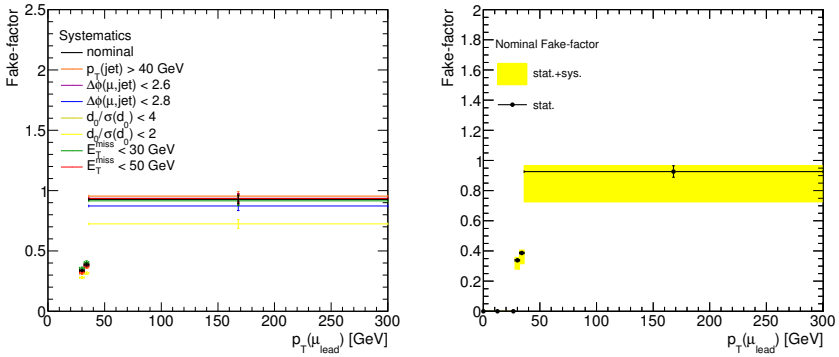

(a) (b)

Figure 7.47: Muon fake-factors as a function of electron p_{T}. Each systematic variation is show separately together with the nominal measurement (a) or summed together into the final systematic total error (b).

The result is shown in Fig. 7.47. If we compare it to Fig. 7.23 we can see that no significant variation from the inclusive jet measurement is observed leading to the conclusion that requiring an additional jet in the event does not change muon fake composition in the fake enriched control region. The overall effect of requiring events with two jets is a slight increase in the total systematic uncertainty, due to the lower statistics of the sample used in the measurement. For this reason, it was decided to use the fake factor measurement adopted for the $H^{\pm\pm}$ search, reported in Fig. 7.23.

7.10.3 Distributions in analysis regions

The control regions defined in the analysis constrain the normalization for background while validation regions are used to validate background estimations, i.e. the charge mis-identification and fakes. All analysis regions are defined in Table 7.22.

Control regions

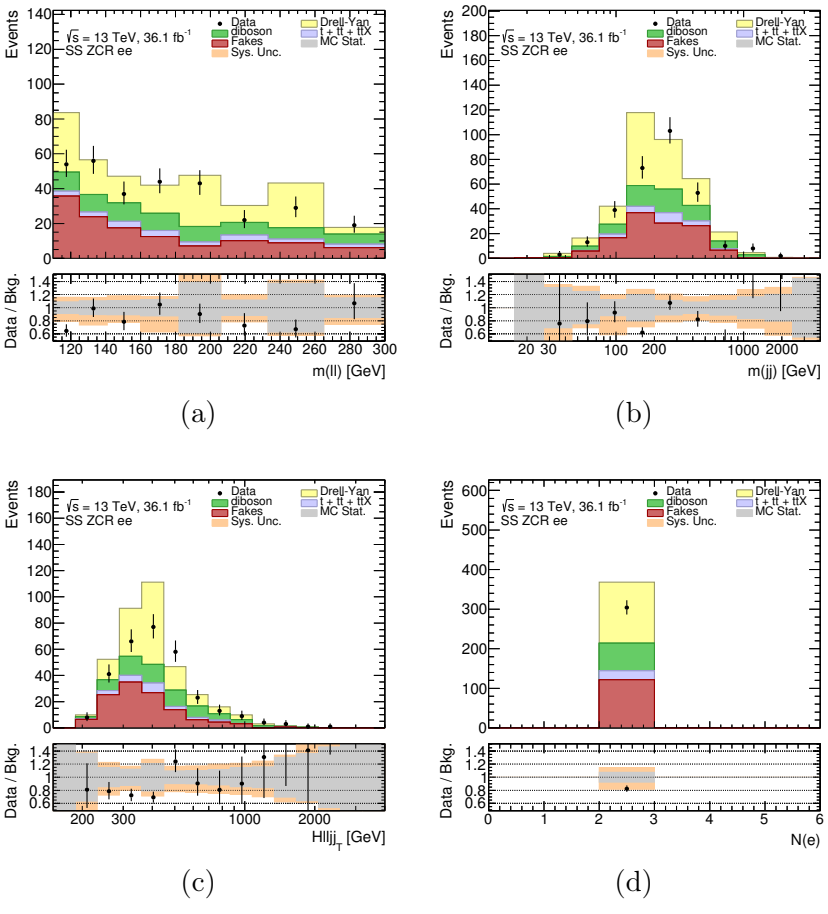

Figure 7.48: Pre-fit distributions for data and SM background predictions in the electron channel control region: (a) invariant mass of the two leptons, (b) invariant mass of the two leading jets, (c) scalar sum of the p_{T} of leptons and two leading jets, and (d) total number of events in the region.

The electron control region is used to constrain the normalization of $Z \to ee$ events, dominating the electron channels due to charge mis-identification,

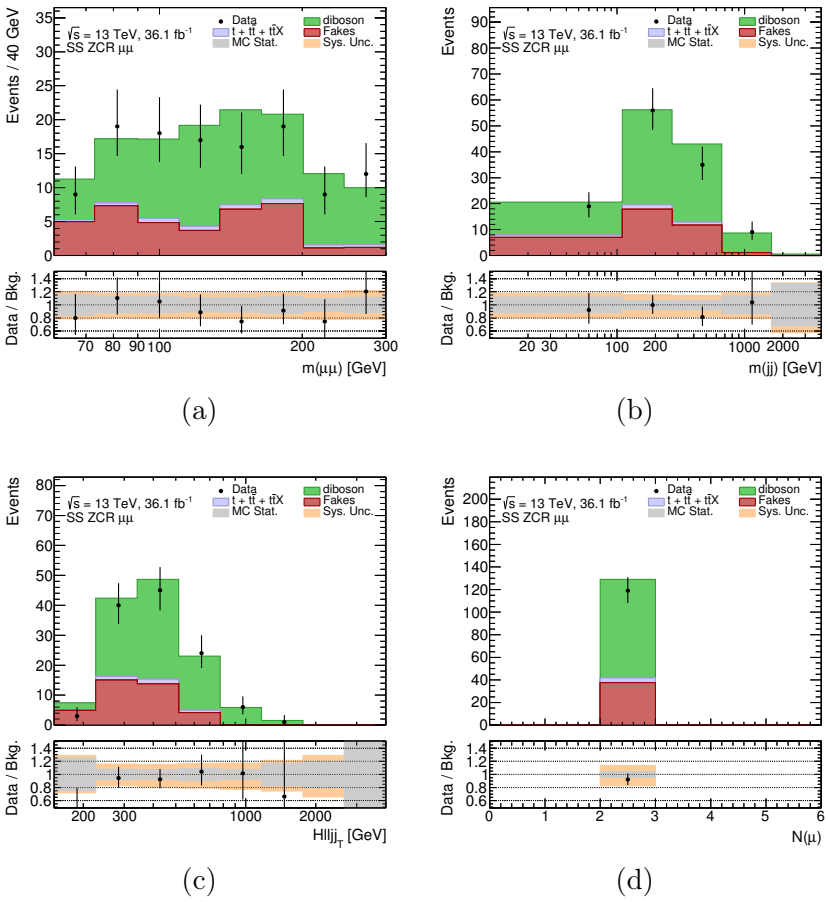

Figure 7.49: Pre-fit distributions for data and SM background predictions in the muon channel control region: (a) invariant mass of the two leptons, (b) invariant mass of the two leading jets, (c) scalar sum of the p_{T} of leptons and two leading jets, and (d) total number of events in the region.

negligible in the muon channel. The diboson background equally enters the electron and the muon channels and both regions are used to extract the background normalization. Representative distributions for the electron and muon control region are shown, respectively, in Fig. 7.48 and 7.49. A good agreement between data and the expected events from simulation is observed.

Validation regions

Validation regions, defined in Section 7.22, are used to validate both the charge-flip background estimation in the electron channel and the diboson prompt lepton contribution from simulation.

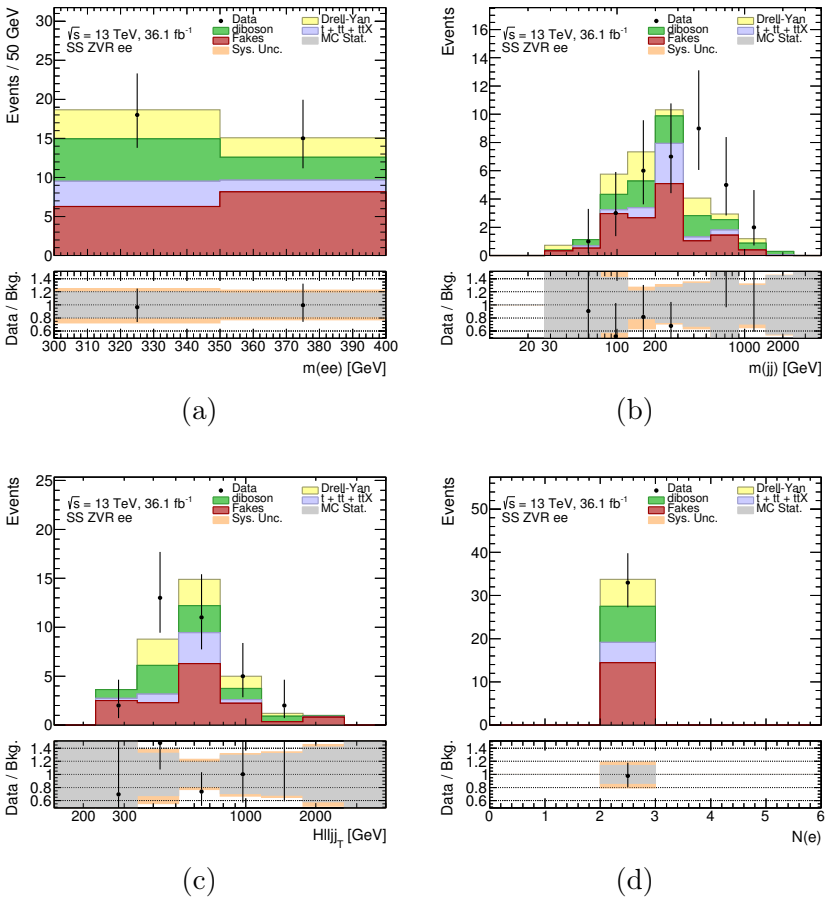

Figure 7.50: Pre-fit distributions for data and SM background predictions in the electron channel validation region: (a) invariant mass of the two leptons, (b) invariant mass of the two leading jets, (c) scalar sum of the p_{T} of leptons and two leading jets, and (d) total number of events in the region.

Distributions for electrons are provided in Fig. 7.50 and for muons in Fig. 7.51. Background in the electron channel are roughly equally divided among Drell-Yan, diboson and fakes, while the muon region is dominated by diboson events and fakes. Despite the low statistics, the agreement between data and simulation allow to conclude that background modeling works properly and can be better assessed looking at the inclusive number of events provided in Fig. 7.50d and 7.51d.

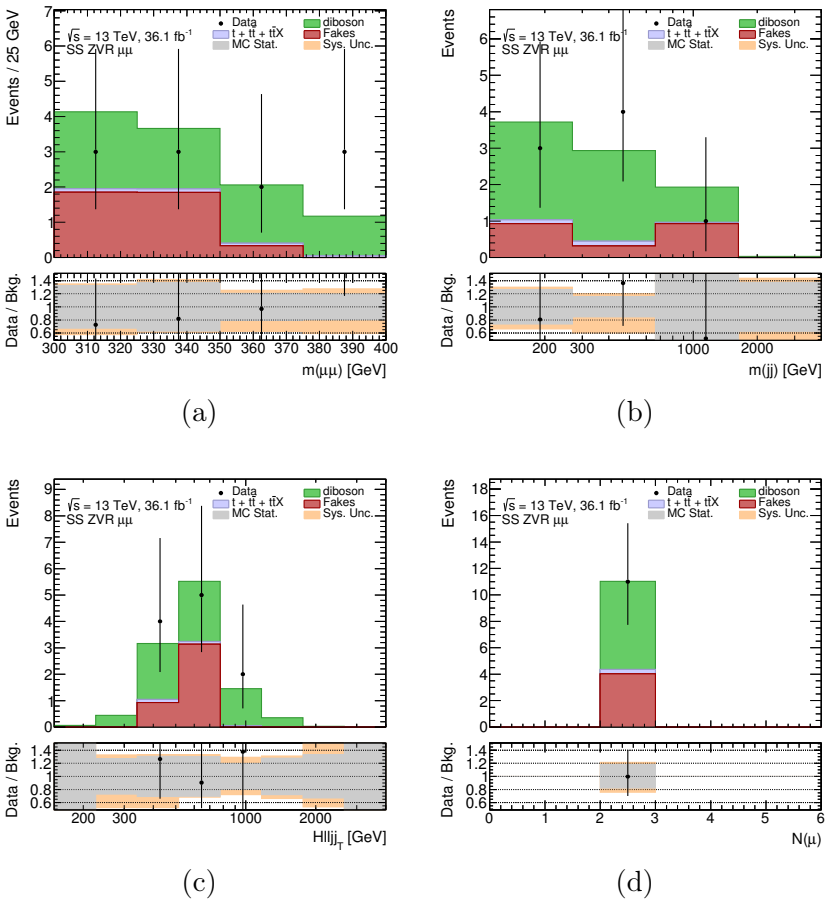

Figure 7.51: Pre-fit distributions for data and SM background predictions in the muon channel validation region: (a) invariant mass of the two leptons, (b) invariant mass of the two leading jets, (c) scalar sum of the p_{T} of leptons and two leading jets, and (d) total number of events in the region.

Signal regions

As defined in Section 7.10.1, signal regions are defined by the presence of two high-p_{T} jets, two same-flavour and SS leptons with invariant mass above 400 GeV in a high-energetic event ($H_{\mathrm{T}} > 400$ GeV). Figures 7.52 and 7.53 show the signal region distributions for the electron and the muon channels. Data are compared to the total background prediction, before performing the fit, and two signal sample distributions are superimposed, reflecting both the mass hierarchy hypotheses $m_{W_R} > m_{N_R}$ and $m_{N_R} > m_{W_R}$. No excess is observed neither in the electron nor in the muon channel.

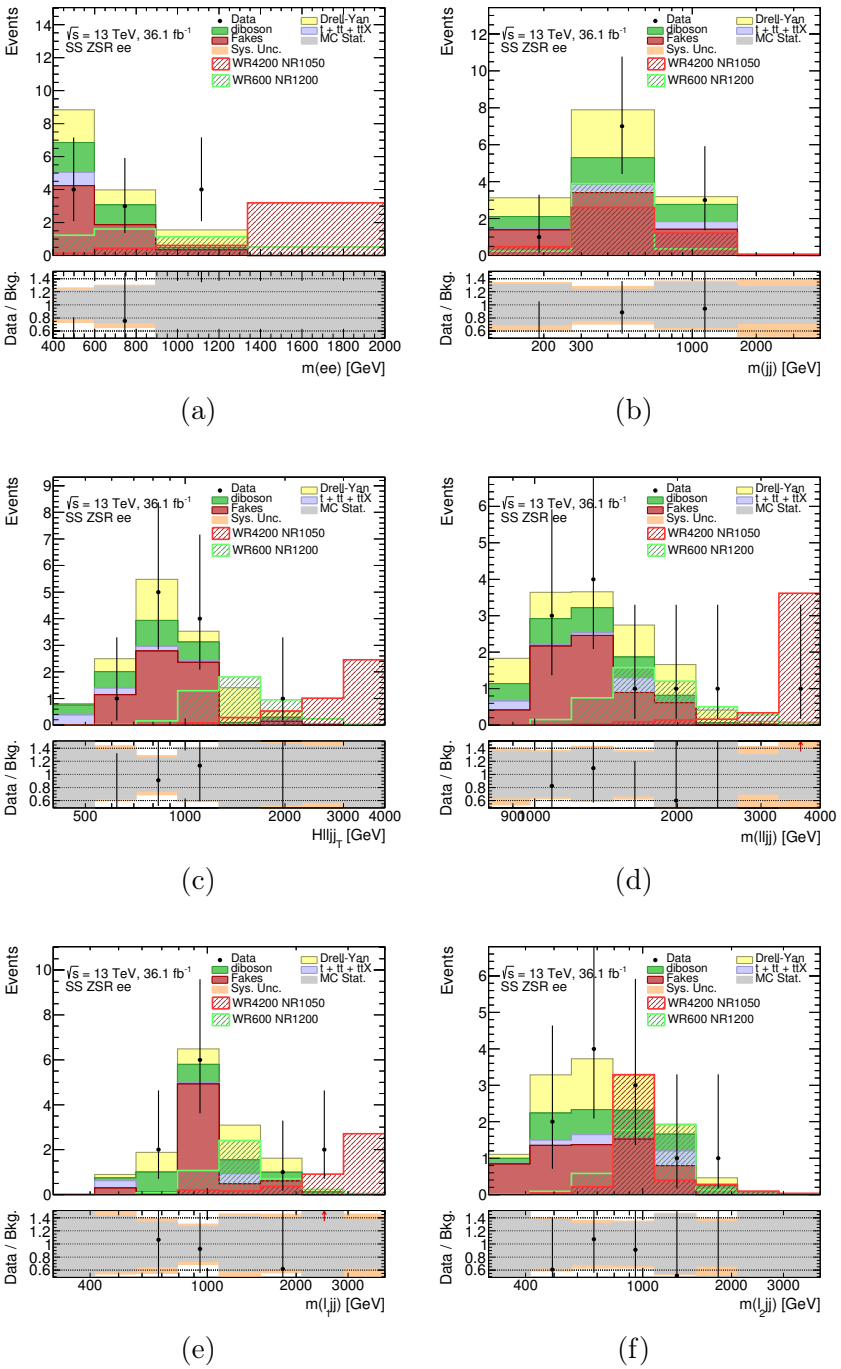

Figure 7.52: Pre-fit distributions for data and SM background predictions in the electron channel signal region: (a) invariant mass of the two leptons, (b) invariant mass of the two leading jets, (c) scalar sum of the p_{T} of leptons and two leading jets, (d) invariant mass of the four selected objects, (e) invariant mass of the two jets and the leading lepton, and (f) invariant mass of the two jets and the subleading lepton.

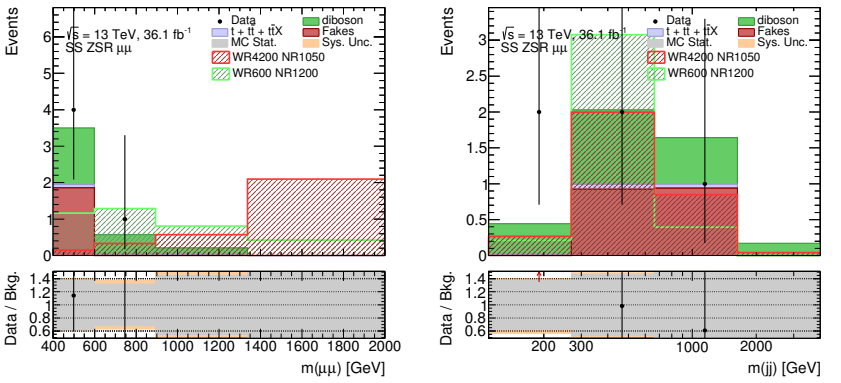

(a)

(b)

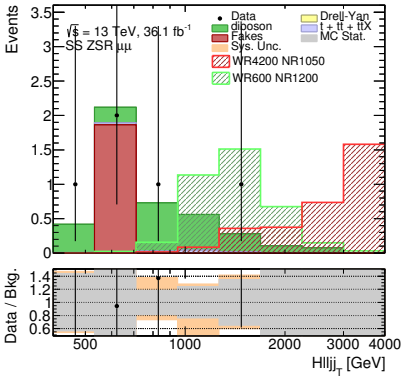

(c)

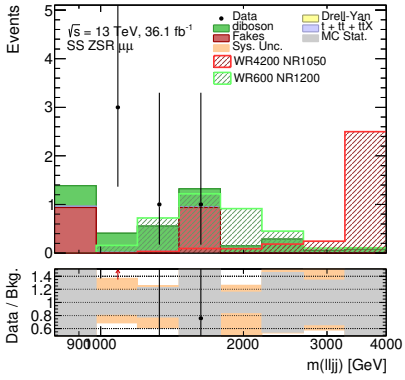

(d)

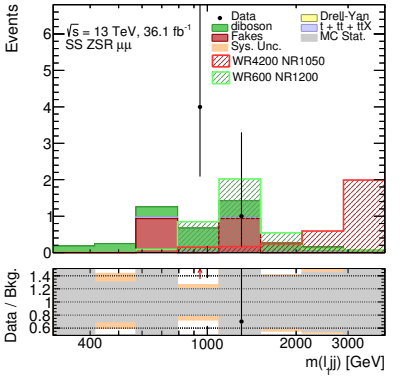

(e)

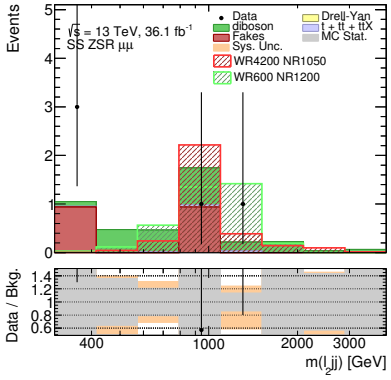

(f)

Figure 7.53: Pre-fit distributions for data and SM background predictions in the muon channel signal region: (a) invariant mass of the two leptons, (b) invariant mass of the two leading jets, (c) scalar sum of the p_{T} of leptons and two leading jets, (d) invariant mass of the four selected objects, (e) invariant mass of the two jets and the leading lepton, and (f) invariant mass of the two jets and the subleading lepton.

7.10.4 Limit on W_R and N_R mass

Since no excess is observed in signal regions, the fitting procedure is aimed to extract a 95% C.L upper limit on the production cross-section for both the W_R and N_R particles, which are interconnected by their respective mass hypotheses and produced together in the Keung-Senjanović process.
The distribution which is fitted in the control and validation regions is the invariant mass of the two leading jets. However, for the signal region, a different variable is chosen.

The m_{jj} distribution is a powerful variable because it directly allows to reconstruct the on-shell mass for the W_R boson. As clear from Fig. 7.52b and 7.53b, respectively for the electron and muon channels, m_{jj} has low sensitivity both at low and high W_R mass points. Indeed, the two representative signal distributions drawn with the green (W_R = 600 GeV and N_R = 1200 GeV) and red (W_R = 4200 GeV and N_R = 1050 GeV) areas, are superimposed to the background, reducing the power of the signal region shape fit.

Regarding the invariant mass of lepton-jet system m_{lljj}, shown for the electron and muon in Fig 7.52c and 7.53c, it poorly discriminates low W_R mass points, performing better only towards W_R higher masses.

On the contrary, the H_{T} variable (provided for electrons in Fig. 7.52c and muons in Fig. 7.53c) is sensitive to both the signal hierarchies, meaning also under the hypothesis $m_{N_R} > m_{W_R}$, which we are particularly interested in this search and explored for the first time.

The fit is performed by following the same strategy discussed in Section 7.9. The additional free parameters in the fit are the Drell-Yan and diboson yields. Drell-Yan is extracted from the electron channel control region and applied to the electron validation and signal regions. Diboson yields is extracted from the simultaneous fit of the muon and electron control regions, and the resulting single normalization factor is applied to both electron and muon validation and signal regions. For the electron control region, Drell-Yan and fakes are the dominant background.

The fitted yields of the Drell–Yan and diboson background are summarized in Table 7.23. The Drell-Yan normalization is scaled-down of ∼20% by the fit while the diboson normalization by ∼10%.

The result of the fitting procedure is summarized in Tables 7.24, 7.25 and 7.26 respectively for control, validation and signal regions. Tables show the pre- and post-fit background predictions and it is clear that a very good agreement between data and prediction is observed in all the analysis regions. The magnitude of systematic uncertainties is summarized in Table 7.27.

Background process	Fitted in	Normalization factor
Drell–Yan	CR ($e^{\pm}e^{\pm}$)	0.80±0.23
Diboson	CR ($e^{\pm}e^{\pm}$) and CR ($\mu^{\pm}\mu^{\pm}$)	0.90±0.15

Table 7.23: Summary of the fitted yields. First column presents the background process, the second column indicated in which regions the yield was fitted, and the last column gives the fitted value.

	CR ($e^{\pm}e^{\pm}$)	CR ($\mu^{\pm}\mu^{\pm}$)
Observed events	304	119
Total Post-fit	305 ± 18	120 ± 11
Drell–Yan	116 ± 29	0 ± 0
Fakes	105 ± 20	37.4 ± 5.7
Diboson	61 ± 11	78 ± 12
Top	22.5 ± 4.1	4.21 ± 0.69
Total Pre-fit	369 ± 36	129.1 ± 8.3
Drell–Yan events	154 ± 14	0 ± 0
Fakes events	122 ± 24	37.7 ± 5.7
Diboson events	69.8 ± 4.8	87.3 ± 4.5
Top events	22.6 ± 4.3	4.19 ± 0.69

Table 7.24: The number of expected (bottom part) and predicted (upper part) background events in control regions after the fit, compared to the data. Uncertainties correspond to the total uncertainties in the predicted event yields, and are smaller for the total than for the individual contributions because the latter are anti-correlated.

The assessment of systematic uncertainties, as determined by the fit, is given by the pull in Figure 7.54, in units of standard deviations. The plot shows the fit stability with respect to systematic uncertainties, where all the nuisance parameters lie in the $\pm 1\sigma$ band from the nominal value, and are not over-constrained by the fit to improve the data/MC agreement.

In signal regions, the dominant uncertainty is the statistical uncertainty, followed by the uncertainty on the fitted yields and the uncertainty on the data-driven fake background estimation techniques.

Limits are extracted for each signal mass hypothesis for the ee and $\mu\mu$ channels separately, since the theoretical model does not constrain the N_{Re} and $N_{R\mu}$ masses to be the same. The results are shown as a two dimensional

	VR ($e^{\pm}e^{\pm}$)	VR ($\mu^{\pm}\mu^{\pm}$)
Observed events	33	11
Total Post-fit	31.3 ± 5.0	10.4 ± 2.2
Drell–Yan	5.8 ± 2.0	0 ± 0
Fakes	13 ± 3.1	4.0 ± 1.2
Diboson	7.6 ± 1.7	6.0 ± 1.5
Top	4.9 ± 1.3	0.33 ± 0.08
Total Pre-fit	34.5 ± 5.6	11.1 ± 2.1
Drell–Yan events	7.0 ± 1.4	0 ± 0
Fakes events	14.4 ± 3.3	4.1 ± 1.2
Diboson events	8.4 ± 1.3	6.7 ± 1.2
Top events	4.7 ± 1.3	0.33 ± 0.08

Table 7.25: The number of expected (bottom part) and predicted (upper part) background events in validation regions after the fit, compared to the data. Uncertainties correspond to the total uncertainties in the predicted event yields, and are smaller for the total than for the individual contributions because the latter are anti-correlated.

	SR ($e^{\pm}e^{\pm}$)	SR ($\mu^{\pm}\mu^{\pm}$)
Observed events	11	5
Total Post-fit	12.9 ± 2.4	4.1 ± 1.4
Drell–Yan	3.4 ± 1.2	0 ± 0
Fakes	5.8 ± 1.6	1.9 ± 1.2
Diboson	2.8 ± 0.69	2.06 ± 0.47
Top	0.91 ± 0.29	0.14 ± 0.03
Total Pre-fit	14.5 ± 2.7	4.3 ± 1.4
Drell–Yan events	4.08 ± 0.9	0 ± 0
Fakes events	6.4 ± 1.7	1.9 ± 1.2
Diboson events	3.1 ± 0.57	2.29 ± 0.35
Top events	0.9 ± 0.28	0.14 ± 0.03

Table 7.26: The number of expected (bottom part) and predicted (upper part) background events in signal regions after the fit, compared to the data. Uncertainties correspond to the total uncertainties in the predicted event yields, and are smaller for the total than for the individual contributions because the latter are anti-correlated.

Uncertainty of channel	CR ($e^{\pm}e^{\pm}$)	VR ($e^{\pm}e^{\pm}$)	SR ($e^{\pm}e^{\pm}$)
Total background expectation	304.77	30.73	12.80
Total background systematic	±17.57 [5.76%]	±5.10 [16.60%]	±2.35 [18.39%]
Total stat. error	±16.94 [5.6%]	±4.23 [13.8%]	±2.13 [16.6%]
Fake-Factor ele	±18.86 [6.2%]	±2.63 [8.5%]	±1.01 [7.9%]
mu_Z	±33.95 [11.1%]	±1.54 [5.0%]	±1.00 [7.8%]
mu_DB	±10.43 [3.4%]	±1.29 [4.2%]	±0.48 [3.7%]
Charge-Flip	±2.42 [0.79%]	±0.83 [2.7%]	±0.30 [2.4%]
Electron iso	±0.41 [0.14%]	±0.24 [0.80%]	±0.21 [1.6%]
JET_Flavor_Composition	±0.55 [0.18%]	±0.07 [0.21%]	±0.18 [1.4%]
Lumi	±4.18 [1.4%]	±0.37 [1.2%]	±0.15 [1.2%]
Electron energy scale	±0.17 [0.06%]	±0.51 [1.7%]	±0.12 [0.93%]
b-tagging	±3.21 [1.1%]	±0.65 [2.1%]	±0.12 [0.90%]
Electron ID	±0.81 [0.26%]	±0.20 [0.65%]	±0.08 [0.64%]
JET_Pileup_RhoTopology	±0.43 [0.14%]	±0.53 [1.7%]	±0.05 [0.38%]
JET_EtaIntercal_Modelling	±0.53 [0.17%]	±0.31 [1.0%]	±0.05 [0.36%]
JET_EffectiveNP_1	±0.12 [0.04%]	±0.54 [1.8%]	±0.05 [0.35%]
JET_Flavor_Response	±0.57 [0.19%]	±0.30 [0.98%]	±0.02 [0.19%]
	CR ($\mu^{\pm}\mu^{\pm}$)	VR ($\mu^{\pm}\mu^{\pm}$)	SR ($\mu^{\pm}\mu^{\pm}$)
Total background expectation	120.15	10.37	4.05
Total background systematic	±10.89 [9.07%]	±2.16 [20.82%]	±1.35 [33.29%]
Total stat. error	±5.00 [4.2%]	±1.86 [17.9%]	±1.30 [32.0%]
mu_DB	±13.42 [11.2%]	±1.03 [9.9%]	±0.35 [8.7%]
Fake-Factor muon	±5.48 [4.6%]	±0.59 [5.7%]	±0.27 [6.7%]
μ_R	±0.09 [0.08%]	±0.20 [1.9%]	±0.10 [2.6%]
Lumi	±1.73 [1.4%]	±0.13 [1.3%]	±0.05 [1.1%]
Muon reco	±0.62 [0.52%]	±0.09 [0.83%]	±0.04 [1.0%]
JET_Flavor_Composition	±0.12 [0.10%]	±0.02 [0.15%]	±0.03 [0.65%]
α_s	±0.03 [0.03%]	±0.01 [0.13%]	±0.02 [0.60%]
b-tagging	±0.65 [0.54%]	±0.05 [0.50%]	±0.02 [0.58%]
JET_JER_NP5	±0.15 [0.12%]	±0.02 [0.20%]	±0.02 [0.58%]
JET_Flavor_Response	±0.16 [0.13%]	±0.04 [0.37%]	±0.02 [0.45%]
Muon SagittaResBias	±0.09 [0.08%]	±0.20 [1.9%]	±0.01 [0.18%]
Muon scale	±0.08 [0.06%]	±0.20 [1.9%]	±0.01 [0.13%]

Table 7.27: Breakdown of the dominant uncertainties on background estimates for the $e^{\pm}e^{\pm}$ (upper table) and $\mu^{\pm}\mu^{\pm}$ (bottom table) channels. Note that the individual uncertainties can be correlated, and do not necessarily add up quadratically to the total background uncertainty. The total statistical error is a quadratic sum of individual statistical errors of each bin in the region.

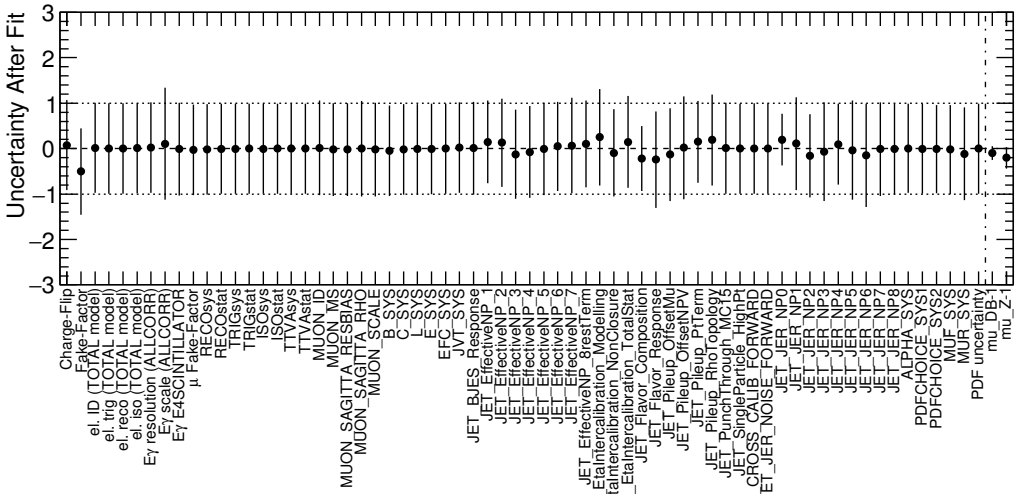

Figure 7.54: Post-fit nuisance parameters expressed in units of standard deviation. The second part of the plot (separated by the dashed line) shows the shift of the yields of the Drell–Yan and diboson backgrounds, expressed in percentage.

exclusion plot, featuring the N_R mass on the y axis and the W_R mass on the x axis. All the signal strength satisfying the condition $\mu < 1$ can be excluded at 95% C.L, while all other signal mass point cannot be excluded being beyond the analysis sensitivity. The expected and observed 95% CL exclusion plot with one and two standard deviation bands for ee and $\mu\mu$ channels are shown respectively in Figures 7.55 and 7.56. These distribution show a similar exclusion power for both the ee and $\mu\mu$ channel. The shrinking $\pm 1{,}2\sigma$ systematic bands, both in the ee and $\mu\mu$ channels, in the region 3 TeV $< m_{W_R} <$ 3.5 TeV and 30 GeV $< m_{N_R} <$ 875 GeV, is the result of the fit interpolation between two subsequent mass points, namely $m_{W_R}, m_{N_R} = \{3000, 300\}$ GeV and $m_{W_R}, m_{N_R} = \{3500, 875\}$ GeV.

Under the Majorana hypothesis, heavy neutrino masses from 50 GeV to 3 TeV can be excluded for heavy right-handed gauge boson masses above 500 GeV. Furthermore, one dimensional exclusion plots are presented to broaden the understanding of the experiment sensitivity. They are made for two extreme mass hypothesis combinations: $m(W_R) = [2/3, 4] \times m(N_R)$. Figure 7.57 provides the expected and observed cross-section as a function of the W_R boson mass.

This search for right-handed W_R and N_R excludes both particles, their masses being in different mass ranges. The lower limit on the N_R mass varies from 50 GeV to 3 TeV for predicted W_R masses above 500 GeV. Similarly, W_R masses can be excluded up to 4.2 TeV independently on the N_R

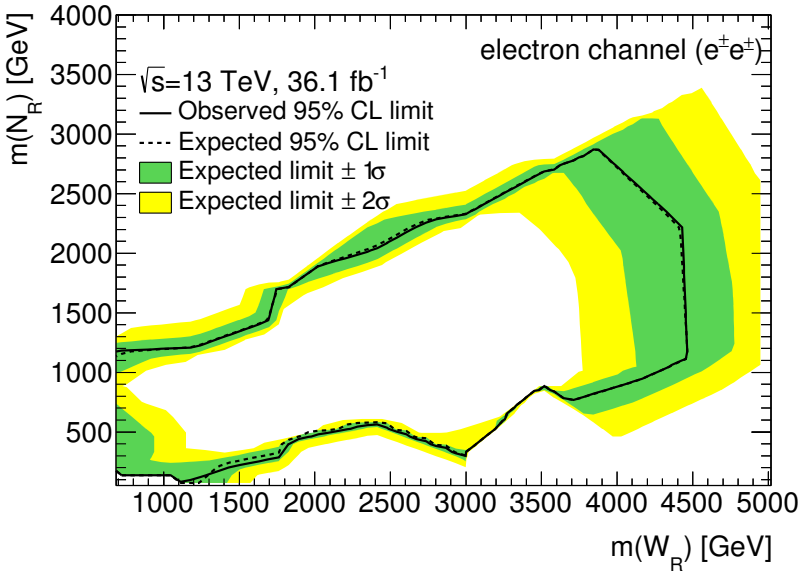

Figure 7.55: Expected and observed 95% CL exclusion plot for the same-charge ee channel with the corresponding one and two standard deviation bands.

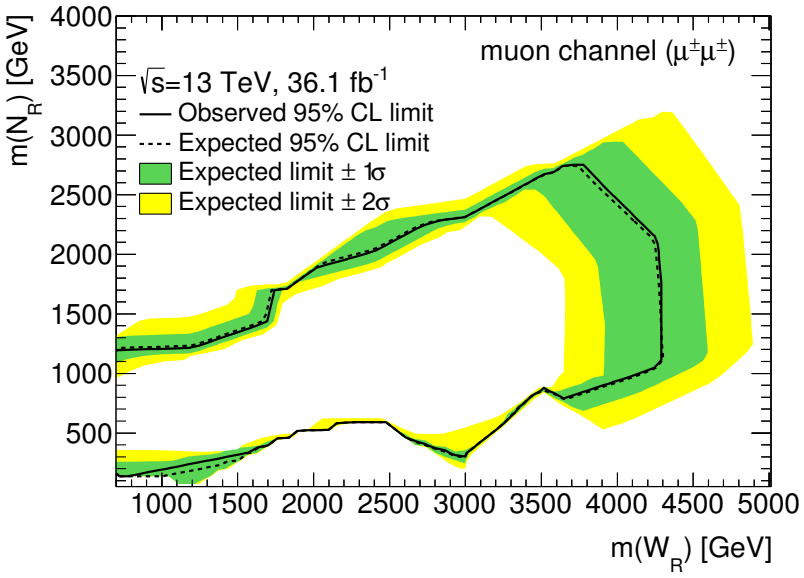

Figure 7.56: Expected and observed 95% CL exclusion plot for the same-charge $\mu\mu$ channel with the corresponding one and two standard deviation bands.

mass, if the latter is within 1 TeV to 3 TeV.

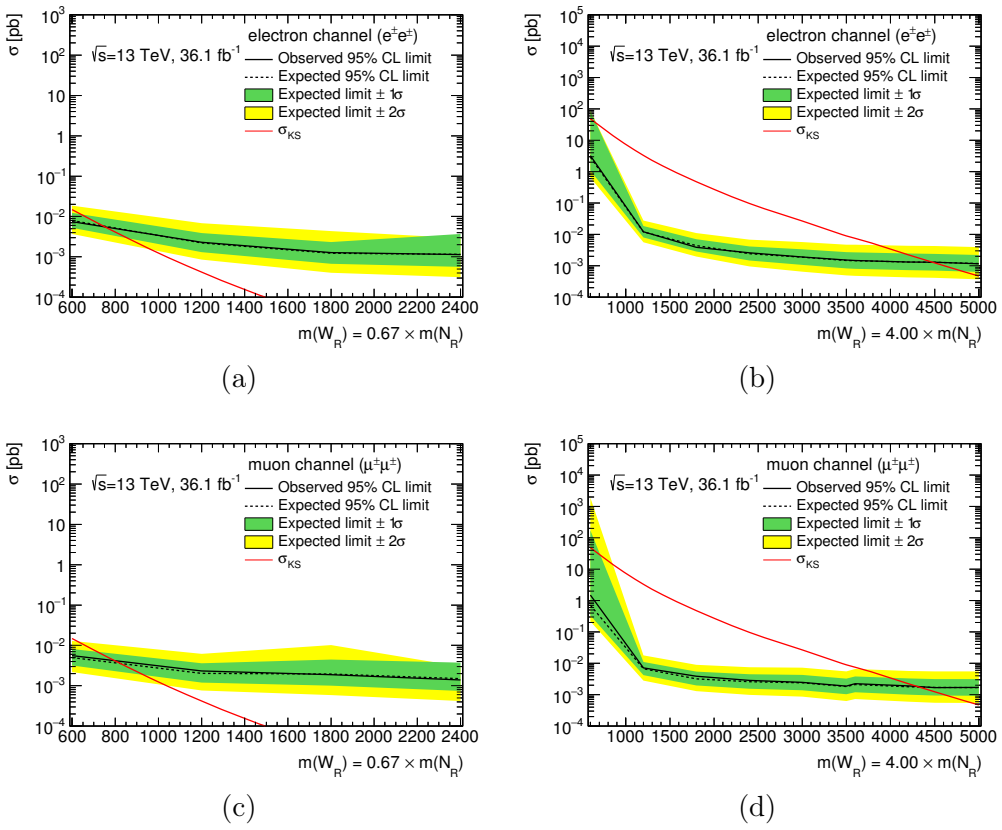

Figure 7.57: Expected and observed upper limit on the Keung-Senjanović process production cross-section at 95% CL as a function of $m(W_R) = k \times m(N_R)$, where: (a) $k = 2/3$, (b) $k = 4$ for the ee channel and (c) $k = 2/3$, (d) $k = 4$ for the $\mu\mu$ channel.

7.11 Future analyses prospects

This chapter exploited the same-sign lepton signature to look for new physics under the phenomenology of left-right symmetric models. Several new particles signatures were investigated, involving new scalar Higgs bosons, vector gauge bosons and leptons. The search provided high sensitivity to the considered new physics model, being extremely powerful in rejecting the SM background. No hints for direct new physics production were found in these searches, allowing the exclusion of a wider phase space compared to the analyses performed by ATLAS at $\sqrt{s} = 7$ or 8 TeV.

The limits on the $H^{\pm\pm}$ mass obtained by this search improve the results from the ATLAS experiment at 8 TeV, increasing the limit reach by ∼300 GeV for both the left- and right-handed $H^{\pm\pm}$ particles. The analysis

performed here only looks into light lepton final states and, consequently, the forthcoming development for the analysis is the inclusion of τ leptons. The analysis is affected by low systematic uncertainties, mainly associated to the data-driven methods used for the background estimation. Such as in the search for $t\bar{t}H$ production, the final states from $H^{\pm\pm}$ decay containing two or three leptons can particularly benefit from improved methods for prompt lepton identification based on multivariate techniques. Indeed, the new multivariate BDT-tagger for charge mis-identification reduction proved to be $\mathcal{O}(10)$ times more efficient than the *traditional* likelihood-fit in rejecting charge-flip electrons. Similarly, the new MVA method developed for the identification of prompt leptons against fakes at the isolation level, proved to be $\sim$40% more efficient in rejecting fakes than the standard isolation working points provided for electrons and muons, such as `FixedCutTight`. The definition of the training and testing MVA samples, used to construct the methods taggers, is obviously analysis dependent. Indeed, different analysis using different isolation and identification lepton working points require their one MVA-tagger defined on the basis of the chosen lepton reconstruction working points.

Besides the possible improvements, the search for $H^{\pm\pm}$ into SS lepton final states will be combined with the orthogonal channel looking at $H^{\pm\pm}$ decays into $W^{\pm}W^{\pm}$.

Similar considerations can be applied to the channel searching for the W_R and N_R production. The ongoing work is to combine the search presented here with the OS channel to provide limits both on the Majorana and Dirac nature of the right-handed neutrinos. The analysis outlined here improves the limits obtained from ATLAS at $\sqrt{s} = 8$ TeV on the N_R mass by 1 TeV and explore the mass hierarchy region $m_{N_R} > m_{W_R}$ for the first time.

Since many BSM theories involve same-sign lepton final states, the natural evolution for these searches is the possibility to perform a single inclusive search for new physics phenomena in a *model independent* way.

Conclusions

The aim of this work was the search for new physics phenomena at the LHC, using the data collected by the ATLAS detector in proton-proton collisions at $\sqrt{s} = 13$ TeV in 2015 and 2016. New physics was searched adopting two approaches: using precise predictions of the Standard Model to look for deviations of its parameters from their expected values and direct searches for the production of new mass resonances, exploiting in both cases the peculiar features of final states containing leptons with same electric charge.

The Standard Model $t\bar{t}H$ production predicts a top-Higgs Yukawa coupling with value $y \sim 1$. This Higgs boson production mechanism is extremely challenging, due to the complexity of the environment deriving from all possible $t\bar{t}H$ decays. Several signal regions are defined and combined together to obtain the final value for the $t\bar{t}H$ signal strength. However, many of these channels are still affected by huge statistical and systematic uncertainties. We performed the analysis on the dataset amounting to 13.2 fb^{-1} and the result on the signal strength is $\mu = 2.5 \pm 0.7(\text{stat.})^{+1.1}_{-0.9}(\text{syst.})$. The results, interpreted as a limit on the $t\bar{t}H$ signal strengths, provided $\mu < 4.9$ at 95% confidence level. Despite being statistically limited, the analysis is dominated by systematic uncertainties mainly arising from data-driven fake lepton estimation and from jet reconstruction procedures. The sensitivity of the cut-and-count analysis is significantly improved using multivariate techniques, both for prompt lepton identification and for event categorization. The first round of the Run 2 analysis was of fundamental importance to understand the limitations of cut-and-count techniques and to study new analysis strategies which eventually resulted in the evidence for $t\bar{t}H$ production with a significance of 4.1 σ and a measured $\mu = 1.6^{+0.3}_{-0.3}(\text{stat.})^{+0.4}_{-0.3}(\text{syst.})$, with the full 2015 and 2016 dataset. Further improvements to the analysis will arise by adding the integrated luminosity of 43.8 fb^{-1} collected in 2017 and from studies aimed to the reduction of systematic uncertainties.

Direct searches for new physics were performed in this work, looking for the production of doubly charged Higgs bosons, right-handed W bosons and heavy neutrinos. No excesses over the Standard Model background predic-

tions were observed in this search into light leptons (electron and muons) and no evidence for $H^{\pm\pm}$, W_R or N_R production was found, under the hypothesis of left-right symmetric models. Limits on $H^{\pm\pm}$ mass, depending on the left- or right-handed $H^{\pm\pm}$ helicity states, vary between 770 GeV and 870 GeV and from 660 GeV to 760 GeV at 95% confidence level, respectively. These limits significantly improve the results obtained by Run 1 analysis at $\sqrt{s} = 8$ TeV, for which the limits on left-handed $H^{\pm\pm}$ varied from 465 GeV to 550 GeV, while for right-handed $H^{\pm\pm}$ from 370 GeV to 435 GeV, at 95% confidence level. The main difference with respect to the previous published analysis is the separate optimization of the signal region containing four leptons, which drives the analysis sensitivity under the assumption of a $H^{\pm\pm}$ branching ratio to light leptons of 100%. The analysis is affected by low systematic uncertainties, mainly arising, as for the $t\bar{t}H$ analysis, from data-driven fake estimations, and the total uncertainty amounts to $\sim$10% in channels containing two leptons. Moreover, even for branching ratios as low as BR($H^{\pm\pm} \to \ell^{\pm}\ell^{\pm}$) $\simeq$10%, limits for the left-handed particle are still above 450 GeV and above 320 GeV for the right-handed particle.

Limits are also set on W_R and N_R masses: N_R masses from 50 GeV to 3 TeV can be excluded when W_R masses are above 500 GeV at 95% confidence level. Similarly, W_R masses are excluded up to 4.2 TeV independently on the N_R masses, if varying between 1 TeV and 3 TeV at 95% confidence level. These results improve the Run 1 results, setting limits on N_R varying from 50 GeV to 2 TeV for W_R masses above 400 GeV. Moreover, in this search, the region $m_{N_R} > m_{W_R}$ is explored for the first time at the LHC.

Driven by the incoming statistics that will be provided by the LHC until the end of Run 2, we can further improve the analyses strategies, including τ leptons in the final states and moving towards model independent searches, sensitive to more general beyond Standard Model scenarios. We can benefit from new techniques, based for instance on multivariate approaches, to reject background from fake and charge mis-identified leptons, reducing the systematic uncertainties and improving analyses sensitivity to new physics phenomena.

Eventually, the multifaceted power of same-sign lepton channels outlined through this thesis, the possibility to improve the background estimation strategies, the low systematic uncertainties and the sensitivity to more than one BSM model open the gate to model independent same-sign searches and makes this final state one of the most interesting for new physics searches at the LHC.

Appendix A

Systematic uncertainties in the search for $t\bar{t}H$ production

Experimental systematic uncertainties are evaluated by the ATLAS performance groups and common to all analysis and applied either as a an overall event re-weighting (which in the following tables is indicated as *Event Weight*) or as *scale factors* rescaling of the transverse momentum (which in tables cab be found as p_{T} *Correction*). All the systematics are evaluated assuming a positive and negative variation of one σ from the nominal value and illustrated in Tables A.2, A.3 and A.1.

Experimental Systematics on b-jets			
Type	Origin	systematics Name	Analysis
	b-tags		
Scale Factors	MV2c20 b-tagger efficiency on b originated jets in bins of η	MV2c20_77_EventWeight_B0-5	✓
	MV2c20 b-tagger efficiency on c originated jets in bins of η	MV2c20_77_EventWeight_C0-3	✓
	MV2c20 b-tagger efficiency on light flavoured originated jets in bins of η and p_T	MV2c20_77_EventWeight_Light0-11	✓
	MV2c20 b-tagger extrapolation efficiency	MV2c20_77_EventWeight_extrapolation	✓
		MV2c20_77_EventWeight_extrapolation_from_charm	✓

Table A.1: Experimental systematics for b-tagged jets in the analysis, using the MV2c20 tagging algorithm used at the 77% Working Point. All of the b-tagging related systematics are applied as event weights.

Experimental Systematics on Leptons				
Type	Description	Systematics Name	Application	Analysis
Trigger				
Scale Factors	Trigger Efficiency	lepSFTrigTight_MU(EL)_SF_Trigger_STAT(SYST)	Event Weight	✓
Muons				
Efficiencies	Reconstruction and Identification	lepSFObjTight_MU_SF_ID_STAT(SYST)	Event Weight	✓
	Isolation	lepSFObjTight_MU_SF_Isol_STAT(SYST)	Event Weight	✓
	Track To Vertex Association	lepSFObjTight_MU_SF_TTVA_STAT(SYST)	Event Weight	✓
p_T Scale	p_T Scale	MUONS_SCALE	p_T Correction	✓
Resolution	Inner Detector Energy Resolution	MUONS_ID	p_T Correction	✓
	Muon Spectrometer Energy Resolution	MUONS_MS	p_T Correction	✓
Electrons				
Efficiencies	Reconstruction	lepSFObjTight_EL_SF_ID	Event Weight	✓
	Identification	lepSFObjTight_EL_SF_Reco	Event Weight	
	Isolation	lepSFObjTight_EL_SF_Isol	Event Weight	✓
Scale Factor	Energy Scale	EG_SCALE_ALL	Energy Correction	✓
Resolution	Energy Resolution	EG_RESOLUTION_ALL	Energy Correction	✓
Hadronic Taus				
Efficiencies	Reconstruction	tauSFLoose_TAU_SF_RECO_TOTAL	Event Weight	✓
	Identification BDT	tauSFTight_TAU_SF_JETID_TOTAL	Event Weight	✓
	Electron Veto BDT	tauSFTight_TAU_SF_ELEOLR_TOTAL	Event Weight	✓
Scale Factor	p_T Scale	TAUS_TRUEHADTAU_SME_TES_TOTAL	p_T Correction	✓

Table A.2: Experimental systematics for muons, electrons and hadronic tau objects. From left: type, description, name of systematics in the code and mode of application. The mode of application indicates the systematic evaluation: overall event re-weighting (Event Weight) or re-scaling (*e.g.* p_T Correction)

Experimental Systematics on Jets and MET				
Type	Origin	Systematics Name	Application	Analysis
Jets				
Jet Vertex Tagger		JVT	Event Weight	✓
Energy Scale	Calibration Method	JET_19NP_	p_T Correction	✓
	(*e.g.*In-Situ)	JET_EffectiveNP_1,2,3,4,5,6restTerm	p_T Correction	
		JET_GroupedNP_1	p_T Correction	✓
	η inter-calibration	JET_EtaIntercalibration_Modelling	p_T Correction	✓
		JET_EtaIntercalibration_TotalStat	p_T Correction	✓
	High p_T jets	JET_SingleParticle_HighPt	p_T Correction	✓
	Pile-Up	JET_Pileup_OffsetNPV	p_T Correction	✓
		JET_Pileup_OffsetMu	p_T Correction	✓
		JET_Pileup_PtTerm	p_T Correction	✓
		JET_Pileup_RhoTopology	p_T Correction	✓
	Non Closure	JET_PunchThrough_MC15	p_T Correction	✓
	Flavour	JET_Flavor_Response	p_T Correction	✓
		JET_BJES_Response	p_T Correction	✓
		JET_Flavor_Composition	p_T Correction	✓
Resolution		JET_JER_SINGLE_NP	Event Weight	✓
MET				
Soft Tracks Terms	Resolution	MET_SoftTrk_ResoPerp	p_T Correction	✓
	Resolution	MET_SoftTrk_ResoPara	p_T Correction	✓
	Scale	MET_SoftTrk_ScaleUp	p_T Correction	✓

Table A.3: The MET systematics are reported here only for information but no cut is applied in the analysis. Jet systematics take into account effects of jets calibration method (*e.g. in situ*), η inter-calibration, high p_T jets, pile-up, non closure, flavour response. They are all diagonalised into effective parameters. The choice of adopting the set of 19 effective parameters was in order to align with other $t\bar{t}H$ analysis and ease combination later on.

Appendix B

LUCID upgrade for Run 2

Luminosity is a key quantity for any physics measurement since it relates the cross-section calculation to the observed number of events (see Section 3.1.2). The uncertainty on luminosity measurement represents the largest systematic uncertainty in many physics analyses and for this reason it is aimed to be kept at the order of few %.

Searches for, and eventual discoveries of, new physics phenomena beyond the SM also rely on accurate information about the delivered and collected luminosity. In many physics analysis, backgrounds are indeed extracted from simulation and luminosity is used to evaluate their normalization. It follows that a non-robust measurement of luminosity impacts the sensitivity to new phenomena signatures. For these reasons, ATLAS performs a redundant luminosity measurement with LUCID (LUminosity Cherenkov Integrating Detector) as main detector and the calorimeters and the ID providing additional measurements for systematics evaluation.

This appendix presents the design of the LUCID detector for Run 2, its new electronics and calibration system. The final 2016 performance on luminosity measurement is also provided. In ATLAS, lucid is part of the Forward Detectors, for which I was Run Coordinator for a total period of four months, most of which during active data-taking.

B.1 Luminosity measurement

The definition of the instantaneous luminosity in terms of the collider parameters is given in Section 3.1.2. This parametrization can also be translated in terms of the average number of inelastic interactions per bunch crossing

(μ^{inel} also called pile-up):

$$\mathcal{L} = \frac{\mu^{inel} f_r n_b}{\sigma^{inel}}. \tag{B.1}$$

Luminosity detectors measure μ^{vis}, which is connected to the real μ^{inel} value by the detector acceptance and efficiency: $\mu^{vis} = \mu^{inel}\epsilon$. Luminosity is consequently rewritten as:

$$\mathcal{L} = \frac{\mu^{inel} f_r n_b}{\sigma^{inel}} = \frac{\mu^{vis} f_r n_b}{\epsilon\sigma^{inel}} = \frac{\mu^{vis} f_r n_b}{\sigma^{vis}} \tag{B.2}$$

where σ^{vis} is the calibration constant measured through dedicated LHC runs, called vdM scans. A vdM scan is a beam-separation scan, where the absolute luminosity can be inferred from direct measurements of the $\Sigma_x\Sigma_y$ parameters, through the relation:

$$\mathcal{L} = \frac{n_b f_r n_1 n_2}{2\pi\Sigma_x\Sigma_y}. \tag{B.3}$$

Luminosity algorithms

ATLAS main luminosity algorithms are based on *Event Counting*, where an event is accepted if a bunch crossing satisfies the criteria required to observe one or more interactions. Those algorithms are mainly divided into EventOR (inclusive counting) and EventAND (coincidence counting). *Hit counting* algorithms and *Particle Rate counting* are also implemented and used to cross-check the linearity of the event counting technique.

Most of the luminosity detectors consist of two symmetric arms with respect to the interaction point, in the forward (A-side) and backward (C-side) directions. In the case of the EventOR algorithm, a bunch crossing is counted if at least one *hit* is observed either from the A or from the C side. As will be explained in more details in Section B.4.1, a hit is defined as the presence of a signal above a given threshold. Assuming that the number of interactions in a bunch crossing follows a Poisson distribution, the probability to observe an OR event can be computed as:

$$P_{\text{EventOR}}(\mu_{vis}^{\text{OR}}) = \frac{\text{N}_{\text{OR}}}{\text{N}_{\text{BC}}} = 1 - e^{-\mu_{vis}^{\text{OR}}} \tag{B.4}$$

where N_{OR} is the number of bunch crossings, during a given time interval, in which at least one *pp* interaction satisfies the event-selection criteria for the OR algorithm, and N_{BC} is the total number of bunch crossings, during the same interval. Solving this equation for μ_{vis}, it returns:

$$\mu_{vis}^{\text{OR}} = -\ln\left(1 - \frac{\text{N}_{\text{OR}}}{\text{N}_{\text{BC}}}\right). \tag{B.5}$$

The EventAND algorithm requires the presence of a hit on both detector sides, condition that can be satisfied either from a single *pp* interaction or from different *pp* interactions occurring in the same bunch crossing. Assuming equal acceptances for the A and C sides, the probability for an AND event is given by the formula:

$$P_{\mathrm{EventAND}}(\mu_{\mathrm{vis}}^{\mathrm{AND}}) = \frac{\mathrm{N_{AND}}}{\mathrm{N_{BC}}} = 1 - 2e^{-(1+\sigma_{vis}^{\mathrm{OR}}/\sigma_{vis}^{\mathrm{AND}})\mu_{vis}^{\mathrm{AND}}/2} + e^{-(\sigma_{vis}^{\mathrm{OR}}/\sigma_{vis}^{\mathrm{AND}})\mu_{vis}^{\mathrm{AND}}} \tag{B.6}$$

which can be solved for μ_{vis}^{AND} by means of numerical inversion.

In the limit $\mu_{vis} \gg 1$, event counting algorithms loose their sensitivity since events with zero observed interactions are less and less likely (effect called *algorithm saturation*). When $\mathrm{N/N_{BC}} = 1$, event counting algorithms cannot be used anymore and need to be replaced with hit counting algorithms. These latter count hits instead of events and, under the assumption that the number of hits in one *pp* interaction follows a Binominal distribution and that the number of interactions per bunch crossing follows a Poisson distribution, the probability to have a hit per bunch crossing is calculated as:

$$P_{\mathrm{HitOR}}(\mu_{vis}^{\mathrm{HitOR}}) = \frac{\mathrm{N_{HitOR}}}{\mathrm{N_{BC}N_{CH}}} = 1 - e^{\mu_{vis}^{\mathrm{HitOR}}} \tag{B.7}$$

where $\mathrm{N_{HitOR}}$ and $\mathrm{N_{BC}}$ are the total number of hits and bunch crossing, respectively, and $\mathrm{N_{CH}}$ is the number of detector channels. The following expression:

$$\mu_{vis}^{\mathrm{OR}} = -\ln\left(1 - \frac{\mathrm{N_{HitOR}}}{\mathrm{N_{BC}N_{CH}}}\right) \tag{B.8}$$

can be used to calculate μ_{vis}.

Online luminosity

LUCID provides luminosity measurement independently on the ATLAS detector running conditions. The *Online Luminosity Calculator* (OLC) determines and publish instantaneous luminosity measurement, such to give feedback to LHC operations, analyzing raw information such as hits and event counts, every 2 seconds. The OLC information is provided as averaged over the number of colliding bunches. The detector main time units are the Bunch Crossing IDentifiers (BCID), which label each bunch of protons from 0 to 3564, and the Lumi-Block (LB), a time interval of $\sim$ 60 s where luminosity is assumed to be constant. Most of ATLAS detectors provide LB-averaged luminosity, while LUCID is the only detector able to provide BCID luminosity for each LB and the OLC calculates the bunch integrated

luminosity using the sum over all colliding BCIDs:

$$\mathcal{L} = \sum_{i \in BCID} \frac{\mu_i^{vis} f_r}{\sigma_{vis}}. \tag{B.9}$$

B.2 LUCID-2 detector

LUCID-1 [175] was installed in 2008 and was used as the main ATLAS luminosity detector for Run 1 (2009-2010) and in combination with other detectors from 2011 to 2013.

B.3 Motivation for the upgrade

After the Run 1 shutdown, LUCID was redesigned in order to cope with the data taking conditions foreseen for Run 2. The tackling of the following problems led to specific new design choices:

- The expected larger pile-up would increase the *migration* background. Migration consists in spurious hits generated by the sum of signals which would be individually under threshold, leading to an overall signal above threshold. In addition, some event counting algorithms were already close to saturation, or already saturated, in Run 1.
- The beam pipe material was changed from stainless steel to aluminium. Monte Carlo simulations showed that this would increase the number of particles hitting LUCID by a factor of 4, with additional impact on luminosity algorithms saturation.
- The bunch spacing reduction from 50 ns to 25 ns.

To cope with the first two effects the acceptance of the detector was reduced by using photomultipliers with window of smaller diameter: from 15 mm to 10 mm [176]. The third data taking condition required a redesign of the electronics. A new set of VME boards (LUCROD) digitize the signals close to the detector to avoid signals distortion and optimize discriminator performances.

B.4 The Design of the LUCID-2 detector

LUCID is composed of two modules (one of which is shown in Fig. B.1) placed around the beam-pipe on both forward ends of ATLAS, 17 m from

the interaction point (IP).
Each module is made of four sets of PMTs and a group of quartz fiber bundle, read-out by standard PMTs placed behind shielding, a few meters away from the other PMTs (see Fig. B.1). The calibration system allows frequent online calibration to compensate for PMTs gain losses or ageing. A system of temperature probes and a cooling apparatus ensure that all the components are kept at the ideal working temperature.

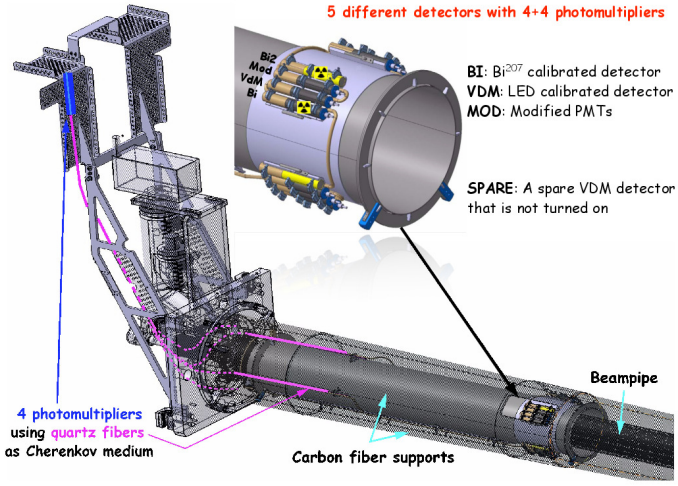

Figure B.1: View of one of the two LUCID detector modules in 2016.

B.4.1 Photomultipliers features

LUCID-2 PMTs are Hamamatsu (R760) with ⌀=10 mm diameter. Out of the 20 available PMTs, 16 only are active during ATLAS normal running conditions and they are arranged into four groups with different features, each group acting as an independent detector:

- four PMTs equipped with a small amount of radioactive ^{207}Bi, deposited on the center of the quartz window for calibration purposes (see Section B.5.1),
- four PMTs calibrated with LED signals (see Section B.5.1),
- four PMTs with a reduced-window of ⌀=7 mm (partially opacified by a thin aluminium layer, in order to further reduce the acceptance),
- four PMTs fed by quartz fiber and located in a lower radiation area about 1 m away from the main detector location.

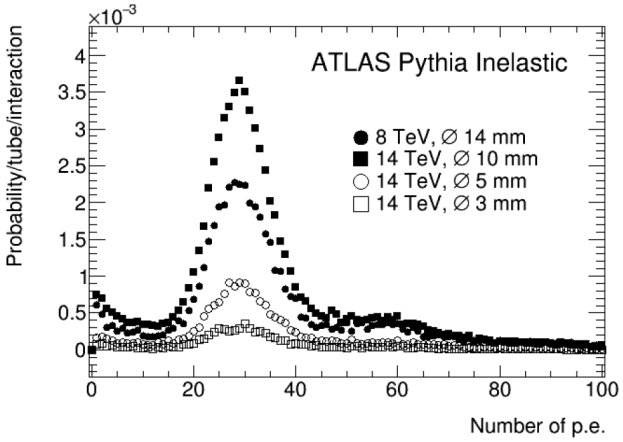

Figure B.2: Photoelectron distribution obtained from a LUCID PMT in a single pp inelastic collision simulated with PYTHIA. The Run 1 ($\sqrt{s}$ =8 TeV) photoelectron spectrum is shown together with different Run 2 ($\sqrt{s}$ =14 TeV) PMT window configurations (10 mm, 5 mm and 3 mm).

The other four PMTs are turned-off and kept as spares and can be switched on at any time if, for any reason, replacing of one of the other groups is needed. Each sensor can, in principle, provide an independent luminosity measurement. Moreover, based on the signal from PMTs, different algorithms using sets of PMTs can also be defined (see Section B.3).
The main feature of the LUCID-2 detector is that it uses the thin quartz window of the PMTs as Cherenkov medium. Considering the quartz window thickness of 1.2 mm, the Cherenkov kinetic energy threshold is ∼175 keV. Charged particles crossing the window produce light, converted into an electrical current in the PMT cathode and amplified by the dynode chain, eventually producing a measurable signal. An analogous principle stands for quartz fibers, also acting as Cherenkov radiator for charged particles. The number of Cherenkov photons generated by charged particles is transformed into the number of photoelectrons (p.e.). A hit is defined when the number of photoelectrons recorded in the event is larger than a given threshold. The threshold choice is arbitrary and follows a compromise between the inclusion of the full signal peak (as in Fig. B.2) and noise suppression. A threshold of 15 p.e. was chosen resulting from previous considerations.

The threshold determines the detector event efficiency ϵ and thus the probability (P) to detect an event (see Section B.1). Signal pulses can also be integrated to provide PMT's charge, used to implement Particle Rate algorithms.

B.5 Electronics

Run 1 LUCID electronics was redesigned for Run 2 to cope with the 25 ns bunch spacing.

The new electronics is composed of two types of VME custom boards, called LUcid ReadOut Driver (LUCROD), as depicted in Fig. B.3. The new boards digitize the signals only 15 m away from the PMTs, minimizing PMT signals distortion and broadening. The signals from PMTs are guided through low loss transmission coaxial cables to the board, preserving the original signal shape and avoiding pole-zero compensation circuity. Being closer to the detector position, the new electronics digitize signals within 25 ns, corresponding to the LHC bunch spacing. One additional electronic board per side (LUMAT), as in Run 1, receives digital information from the A and C LUCID sides and implements coincidence algorithms.
Both the LUCROD and the LUMAT board cumulate hits and event over LB periods and with BCID granularity, on internal FIFOs that are read via VME interface by the TDAQ software at the end of each integration period. A pair of FIFOs is needed for each integrated data: one is incremented while the other is read.

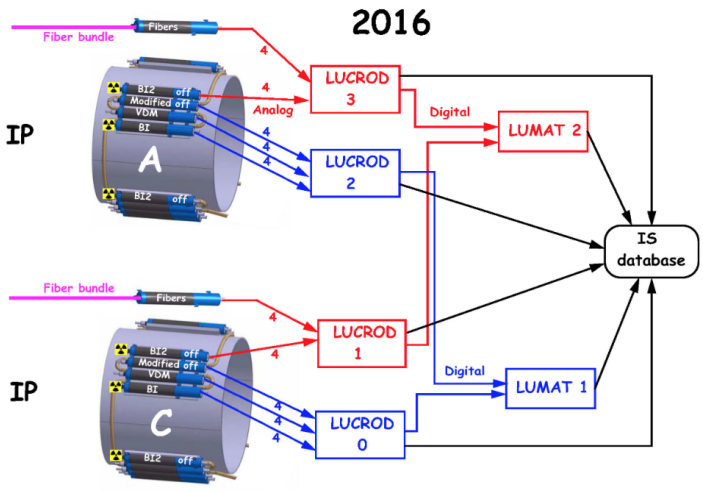

Figure B.3: Scheme of LUCID electronics for 2016 data taking.

LUCROD board

The LUCROD board is a 9U VME custom board featuring 16 lemo analog input channels, 16 lemo analog outputs (amplified input copies), four lemo digital channels, a TTCrq to receive external synchronization signals, and

optical transceivers to deliver digital information. Each input is preamplified by a programmable factor (up to 16), and digitized by a 320 MHz Flash Analog-to-Digital Converter (FADC) with 12-bit resolution for a 1.5 V dynamic range.
In LUCID, the current produced by each PMT is fed to one analog input. Two boards are used for each detector side. Each LUCROD board is also fit with 10 Cyclone IV FPGAs.
Eight FPGAs are directly connected to the inputs, each receiving the digitized data of two channels. In these FPGAs the digitized inputs are summed over each BCID period (25 ns, or 8 samples) providing charge information, and are compared to a programmable threshold to define "hits". While hits and charge are accumulated in 3564-slot FIFOs, 64 samples of the digitized waveforms are made available for VME readout upon the presence of a trigger, selectable between fixed fraction of each LHC orbit, or hit presence. This slow VME readout is used during data-taking to provide a monitoring data stream, representing a hardware sampling of each PMT waveform.
The other FPGAs receive charges and hits, respectively, from two selectable combination of inputs, and provide charge sums, hit sums, and event (at least one hit in the same bunch crossing) sums. In addition, the FPGA receiving hits route them to the output transceiver feeding the optical fiber connected to a LUMAT board.

LUMAT board

The LUMAT boards are 9U VME boards developed by the Bologna INFN research team, and composed by:

- A 9U motherboard, featuring connectors for the VME bus and the FPGA (Cyclone II) used to manage the bus communication protocol;
- A main mezzanine based on a Stratix II (Altera) FPGA, with 1508 pins, placed in the middle of the board, entitled with the task of managing incoming data from EPMCs (Edro Programmable Mezzanine Cards) and handling the subsequent elaboration stages. This board is the most important part of the elaboration process of the information received from the LUCROD boards;
- Two EPMC mezzanine boards host a couple of Spartan VI (Xilinx) FPGAs, which manage bidirectional optical channels. These boards are used to receive data sent from the LUCROD boards using the 8b/10b protocol implemented in the FPGAs. The input connectors of the

board are characterized by four optical fiber links; input bit-rate is 25 Gbit/s, while the total input/output rate is 12.4 Gbit/s;

- S-Link LSC (Link Source Card) mezzanine is used both to transmit elaborated data towards subsequent PC acquisition stages and to record data on disk using a clock optical link (40 MHz) able to send 160 MByte/s;

- A small TTCrq mezzanine receives global signals at 40MHz clock, used also to correct the board's clock phase and synchronize it with the LHC clock.

The board main task is combining data from the two detector sides to produce on-line and off-line luminosity measurements. The resulting patterns are sent to the main FPGA mounted on the board, a Stratix II, for luminosity algorithm implementation. Every algorithm is defined at the per BCID level and is processed in parallel at every clock tick, storing it in the FPGA RAM blocks thanks to operation pipe-lining: read the old value for the bin, add the algorithm value to it, store the updated value. This way each bin is integrated over the LB, at the end of which they are frozen and read through the VME interface; at the same time a loss-less swapping function to a new algorithm array allows to immediately start the data-taking for the new incoming LB. Each algorithm also has a version integrated over both all BCID's and the LB and another version integrated over BCID's but only on a shorter time interval. This latter measurements are read by the ATLAS software to provide online luminosity monitoring and dispatched to the LHC for beam monitoring purposes.

LUCID luminosity algorithms features

The new LUCID-2 is designed to measure the luminosity using two different approaches which are in many aspects complementary with respect to systematic uncertainties, sensitivity to instrumental issues and background contamination. The methods are:

- Event/Hit Counting: these algorithms respectively count the number of event with at least one detected hit or the number of hits in the event. The LUCROD board provides these algorithms for each PMT channel and combines the information from each detector side. The LUMAT board also provides algorithms in single-side mode and in coincidence between the two sides;

- Particle Rate: no threshold is applied on the signal amplitude. The total charge is recorded and it is proportional to the number of particles crossing the detector. These algorithms are provided only by the LUCROD board, for each read-out channel in single-side mode.

Examples of these algorithms hit patterns are presented in Fig. B.4, as provided by the LUMAT board for a run collected in 2016. All algorithms available for on-line and off-line luminosity measurement, besides the single channel ones, are summarized in Table B.1.

Algorithm	Logic Function	Hits	Board
EventOR	OR	≥ 1	LUMAT
EventAND	AND	≥ 1/side	LUMAT
EventORA	OR	≥ 1 on side A	LUCROD/LUMAT
EventORC	OR	≥ 1 on side C	LUCROD/LUMAT
HitSum	OR	sum hits on any side	LUMAT
HitAND	AND	sum hits on any side	LUMAT
Single Channel	-	-	LUCROD

Table B.1: Luminosity algorithm provided by the LUCID boards.

Algorithms based on a combination of information provided by different photomultipliers (Event or Hit counting) are less sensitive to gain fluctuations, which a single tube can undergo during the data taking. However, as visible from Fig. B.4, almost each luminosity algorithm saturated in this run (with a $\langle\mu\rangle = 33$) except for the two bottom plots, which refer to the HitOR B.4e and HitAND B.4f algorithms. This effect depends on the poissonian assumption unde the definition of the algorithm itself (see Section B.1). If the EventOR saturates around a μ of 20 (up to 50 for single sides EventORA and EventORC algorithms), the HitOR algorithm can be used for μ up to 150. That is why during the data taking, it is possible, and needed, to switch the reference algorithm provided both to ATLAS and LHC. The algorithms based on logic AND are usually more affected by systematic uncertanties because the Poisson probability can be simplified only assuming that layout, geometries and efficiencies of the two sides of the detector are similar enough. On the contrary, the particle flow algorithms provide a quantity which is directly proportional to luminosity. These methods are thus free from saturation effects and strictly dependent on the linearity of the read-out chain as well as on the stability of the PMT gain. A robust and reliable calibration system is thus mandatory.

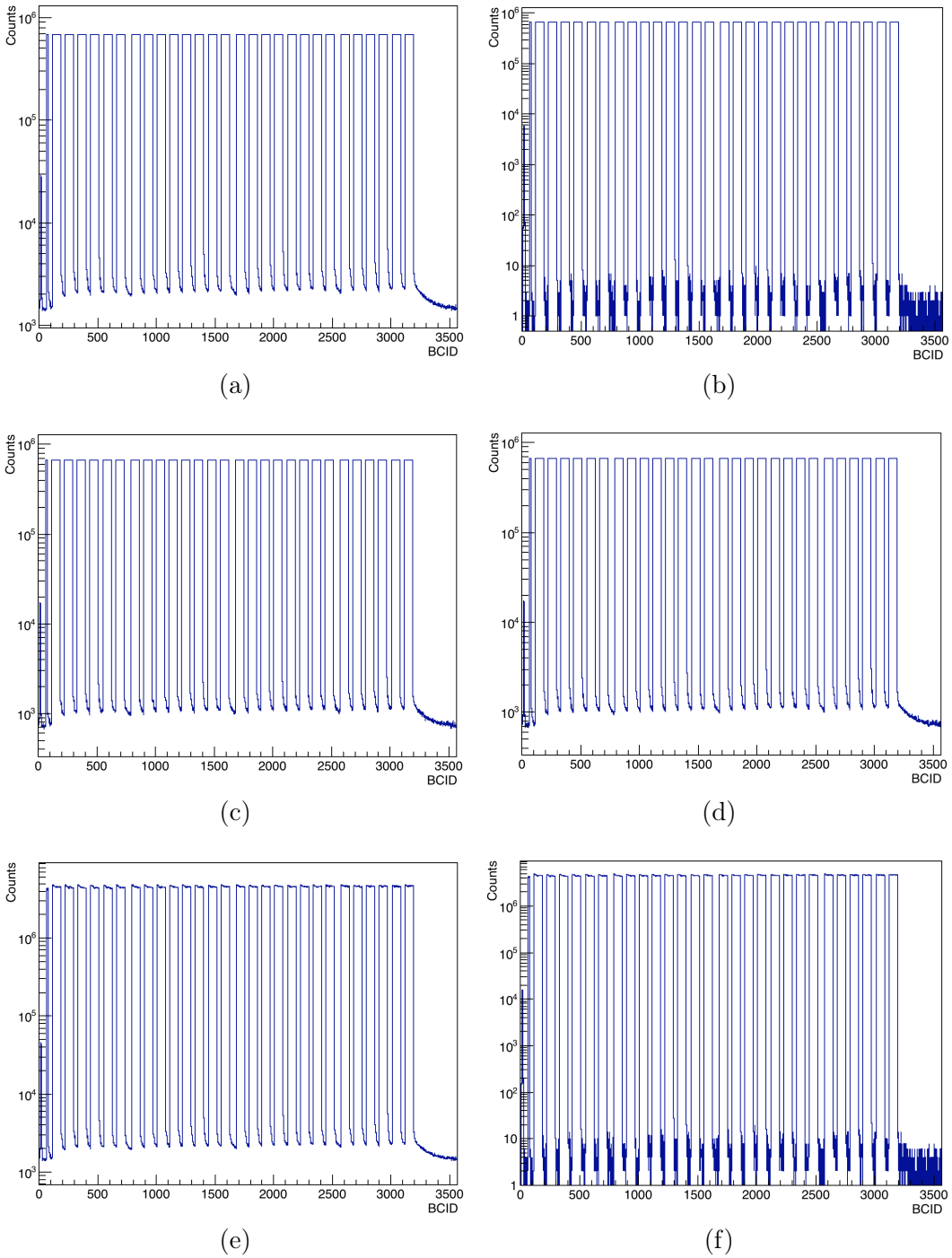

Figure B.4: Luminosity algorithms as provided by the LUMAT board in one LB. Starting from the uppermost left plot, the order of the algorithms is the following: EventOR B.4a, EventAND B.4b, EventORA B.4c, EventORC B.4d, HitSum B.4e and HitAND B.4f. Plots refer to run 302053, collected in 2016, with a $\langle\mu\rangle = 33$.

B.5.1 The calibration system

Stability in the luminosity measurement requires prompt and accurate corrections for gain loss and ageing, both affecting the PMTs during the data taking. Dedicated calibration sessions are performed at the end of each LHC fill since, especially during long runs, the PMT gain is found to be lower than before (up to 5-6%). A change of 5% in gain reflects, in fact, in a 1% change in the luminosity measurement for the hit counting algorithms and in a 5% change in the charge algorithms.
The LUCID-2 calibration system is mainly based on ^{207}Bi sources. ^{207}Bi emission allows accurate calibration of the PMTs since the energy of the monochromatic emitted electrons from internal conversion (1 MeV) reproduces the signal of high-energy charged-particles crossing the same quartz window. Figure B.5 shows the typical amplitude spectrum of ^{207}Bi electrons, recorded by the LUCROD board. It is visible that the distribution presents a peak, whose value depends on the PMT gain and on the board preamplifier settings for each PMT channel (see Section B.5). The position of the peak needs to remain stable since it is used to calibrate the PMTs and to monitor the gain stability with a precision at the % level. Despite the electron monochromatic emission, a width in the ^{207}Bi electron spectrum is present due to the path travelled by electrons inside the quartz window. The peak width is then a consequence of both resolution and geometric effects.

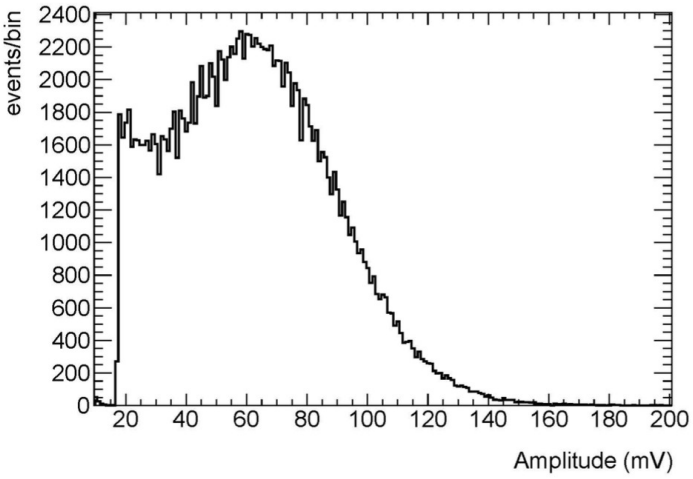

Figure B.5: Recorded amplitude spectrum of ^{207}Bi internal conversion electrons by a LUCID PMT.

Figure B.6 shows the percentage variation of the mean charge value, as a function of time, with respect to a reference run at the beginning of the

2016 data taking, using ^{207}Bi calibration. Gain changes are kept within 5% which, as said, reflects in a luminosity variation of about 1% for hit and event counting algorithms.

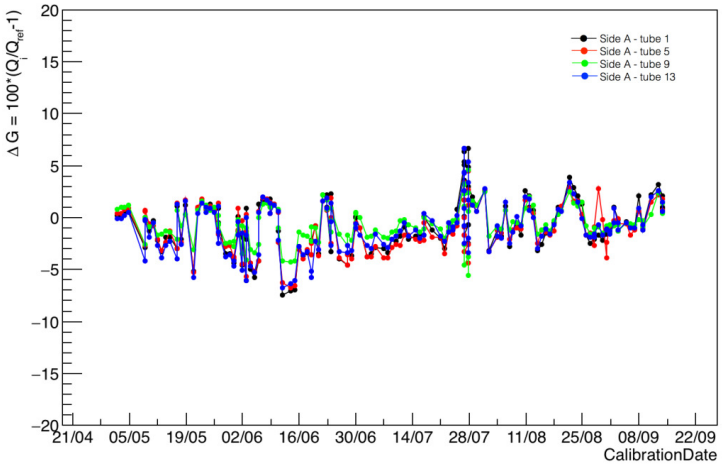

Figure B.6: ^{207}Bi calibration trending plot in 2016. Each point corresponds to a calibration run.

The PMTs which are not provided with a ^{207}Bi source are calibrated using LED signals, pulsed at the LHC orbit frequency of about 11kHz, that can produce large signals in the PMTs.
The stability of the LED signal is not guaranteed better than 5%, thus LEDs (one LED per side) are monitored by a pin diode, ensuring the correction for possible LED instabilities, and placed directly in front of the LED source. The produced light is transported to all PMTs via 4.5 m long, 240 μm diameter quartz fibers. The latter were tested for radiation damage by irradiation with neutrons and gamma at doses equivalent to those expected after 2 years of LHC exposure. In Fig. B.7 the stability of the LED light is shown as monitored by the pin diode, as a function of time in 2016. After an initial drop of about 4%, a rather good stability is maintained for the rest of the data taking period during 2016. LED fibers are connected to the front of the PMTs via fiber connectors. However, during the data-taking it was realized that connectors were a source of background, due to the activation of the material induced by the large particle fluxes. Such problem is absent in the ^{207}Bi-calibrated PMTs where connectors are not present.

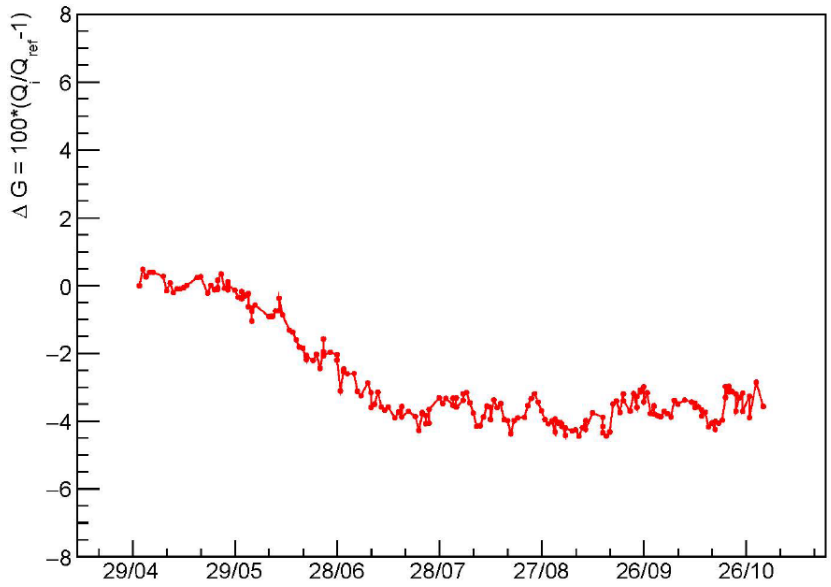

Figure B.7: LED calibration signal as monitored by the pin diode as a function of time in 2016.

Figure B.8 shows the high voltage changes applied to the ^{207}Bi detector (in black for side A and in red for side C) as a function of the integrated luminosity collected during Run 2. It is interesting to note how, after an initial period of *training* in 2015, the PMT gain eventually stabilized during 2016. Little, if no, HV corrections were required during this period.
To ensure a fast and efficient reaction to gain losses, an automatic procedure for PMTs HV adjustment was setup, aimed to recover the gain to its nominal value.
The success of the ^{207}Bi calibrations led to the installation of 4 new ^{207}Bi PMTs per side during the 2016 winter shutdown.

Furthermore, it was noticed that the HV changes needed to compensate the gain loss for ^{207}Bi PMTs were (on average) also fine for the LED-calibrated ones. LED calibration itself was affected by uncertainties about the ageing of the calibration fibers, as said, that cannot be disentangled from the very gain loss of the PMTs under test. Based on these observations, during the 2016 data taking, the HV of LED-calibrated PMTs was adjusted by applying the same change as applied to the ^{207}Bi-calibrated ones.

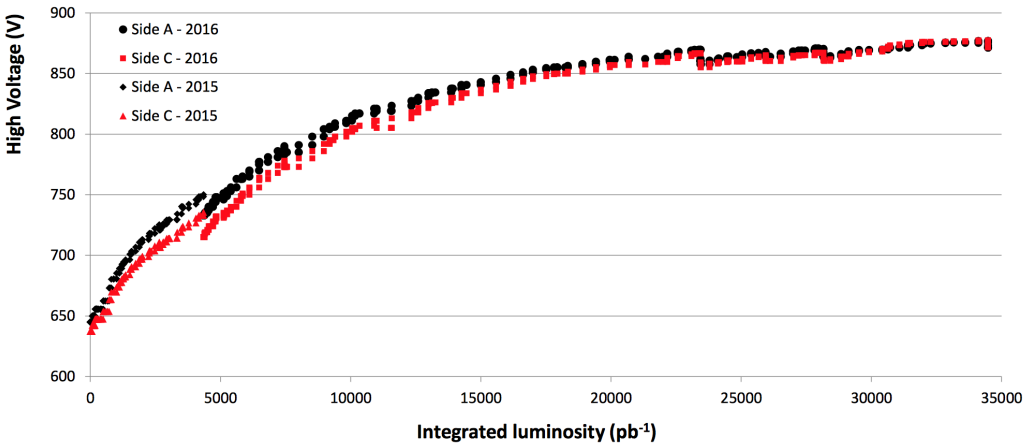

Figure B.8: High voltage change for the ^{207}Bi tubes as a function of the collected integrated luminosity during 2015 and 2016.

B.5.2 Data Acquisition software

The Trigger and Data Acquisition (TDAQ) is the system responsible for managing the interface with the hardware. It is mainly composed of:

- databases and configuration files;
- a graphical user interface (GUI) for control and monitoring;
- a main state machine managing protocols and plug-ins;
- a series of protocols and plug-ins managing the configuration procedures (VME protocol), hardware output read-out, monitoring and storage.

B.6 Luminosity measurement

During the 2015-2016 data-taking operation, the instantaneous luminosity peak value increased from $5{\cdot}10^{33}$ cm^{-2}s^{-1} in 2015 to $13.8{\cdot}10^{33}$ cm^{-2}s^{-1} (see Fig. B.9). At the same time, the maximum number of inelastic interactions per bunch crossing increased from 28 in 2015 to $\sim$50 in 2016 (see Fig. B.10) [177]. For this period LUCID was the ATLAS reference luminometer.

In order to constrain systematic uncertainties, ATLAS cross-checks the luminosity obtained by LUCID using different detectors, namely the electromagnetic, hadronic tile and forward calorimeters, as well as the ID. The

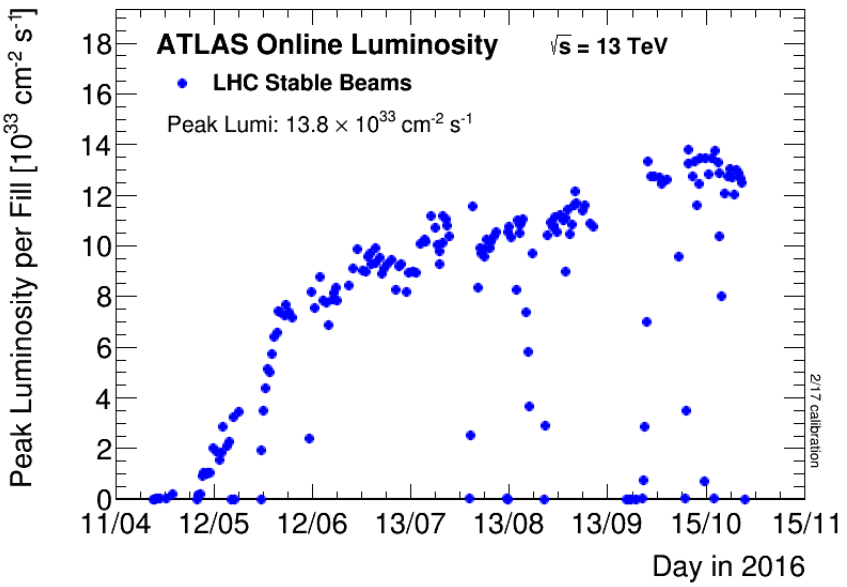

Figure B.9: Peak instantaneous luminosity delivered to ATLAS during stable beams in pp collisions at $\sqrt{s} = 13$ TeV in 2016.

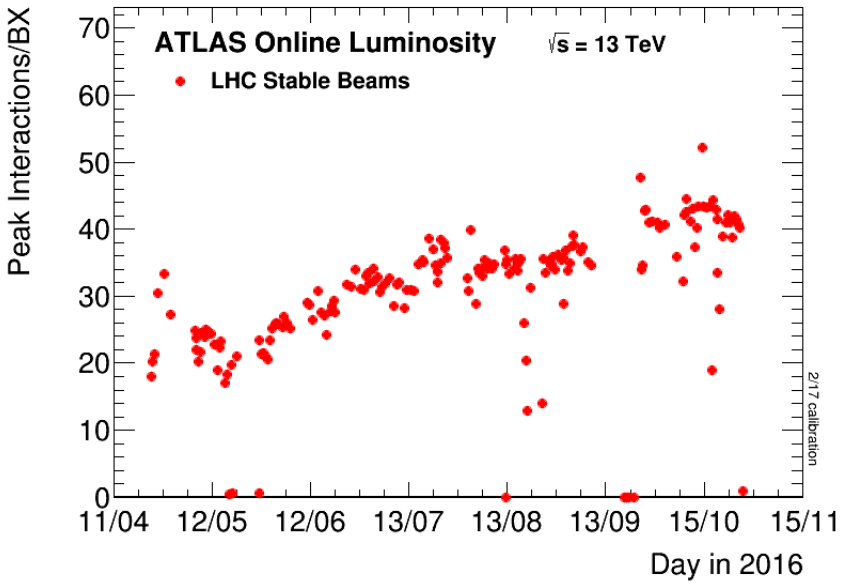

Figure B.10: Maximum number of inelastic collisions per bunch crossing μ during stable beams in pp collisions at $\sqrt{s} = 13$ TeV in 2016. The inelastic cross-section is taken to be 80 mb.

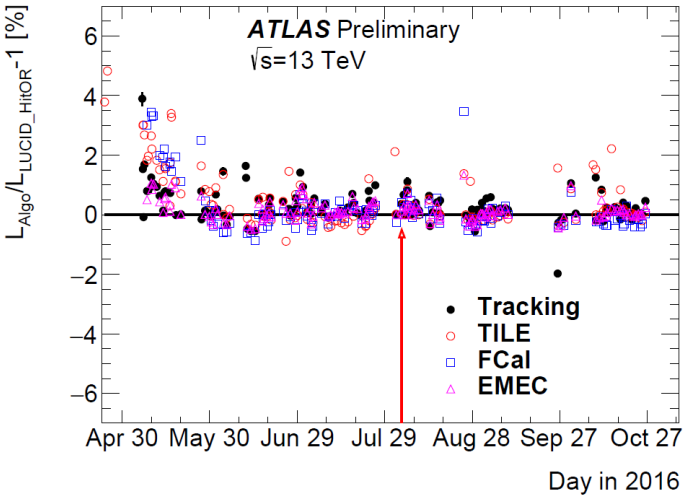

Figure B.11: Fractional difference in run-integrated luminosity between LUCID_HitOR algorithm, the TILE (red circle), EMEC (pink triangle), FCal (blue square) and track-counting (black dot) algorithms as a function of days in 2016.

calorimeters monitor the currents drawn in the different parts of the detectors due to inelastic collisions. They cannot measure luminosity for individual bunch crossings and require a large instantaneous luminosity to be accurate.

The mentioned detectors were cross-calibrated to LUCID in a group of physics runs close to the vdM scan (4^{th} August 2016). The fractional difference between LUCID and the other detectors is shown both in Fig. B.11 and B.12, respectively as a function of days in 2016 and of the fraction of the total integrated luminosity collected in 2016 [177]. These plots show a ∼0.7% run-to-run stability between LUCID and other luminosity measurements. The only exception is the first period, which however only amounts to the 3% of the total luminosity collected in 2016. The long term stability is one of the main components of the overall systematic uncertainty in the luminosity measurement. In 2016 other systematic uncertainties arise from the vdM calibration (∼2%) and the calibration transfer from low-μ (vdM) to high-μ (physics) runs (∼1%). The calibration transfer correction accounts for the fact that the absolute calibration constant (σ^{vis}) is measured with a bunch (and pile-up) configuration different from the one in standard physics runs. A final uncertainty of 2.1% and 2.2% was achieved for 2015 and 2016 respectively.

Thanks to its excellent performance, the new and fast front-end electronics and the renewed calibration procedures, LUCID was providing the official measurement of ATLAS luminosity for physics analysis and the instantaneous

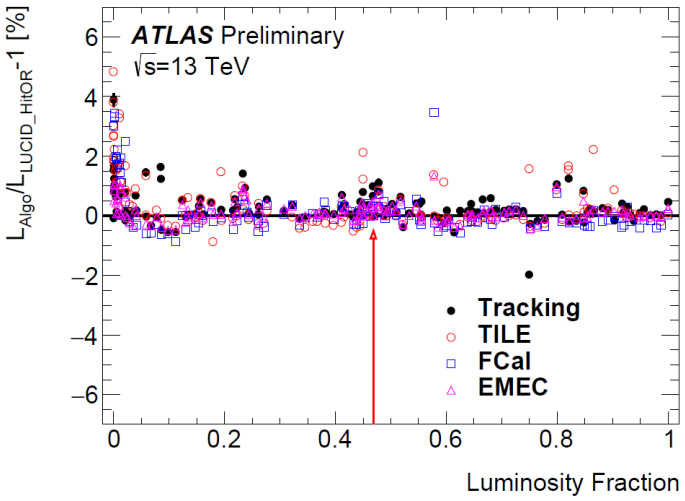

Figure B.12: Fractional difference in run-integrated luminosity between LUCID_HitOR algorithm, the TILE (red circle), EMEC (pink triangle), FCal (blue square) and track-counting (black dot) algorithms as a function of the cumulative delivered luminosity (normalized to 2016 total luminosity).

luminosity to the LHC for beam stability monitoring, through the whole 2015 and 2016 data taking periods.

Bibliography

[1] C. Quigg. *Gauge Theories of the Strong, Weak, and Electromagnetic Interactions*. USA: Princeton University Press, 2013. ISBN: 978-0-691-13548-9.

[2] S. L. Glashow. "Partial Symmetries of Weak Interactions". In: *Nucl. Phys.* 22 (1961), pp. 579–588. DOI: 10.1016/0029-5582(61)90469-2.

[3] S. Weinberg. "A Model of Leptons". In: *Phys. Rev. Lett.* 19 (1967), pp. 1264–1266. DOI: 10.1103/PhysRevLett.19.1264.

[4] A. Salam. "Weak and Electromagnetic Interactions". In: *Conf. Proc.* C680519 (1968), pp. 367–377.

[5] F. Halzen and A. D. Martin. *Quarks and Leptons: an introductory course in modern particle physics*. Wiley, 1984. ISBN: 978-0-471-88741-6.

[6] C. Patrignani et al. "Review of Particle Physics". In: *Chin. Phys.* C40.10 (2016), p. 100001. DOI: 10.1088/1674-1137/40/10/100001.

[7] UA1 Collaboration. "Experimental Observation of Isolated Large Transverse Energy Electrons with Associated Missing Energy at $\sqrt{s} = 540$ GeV". In: *Phys. Lett.* 122B (1983). [,611(1983)], pp. 103–116. DOI: 10.1016/0370-2693(83)91177-2.

[8] UA1 Collaboration. "Experimental Observation of Lepton Pairs of Invariant Mass Around 95 GeV/c^2 at the CERN SPS Collider". In: *Phys. Lett.* 126B (1983), pp. 398–410. DOI: 10.1016/0370-2693(83)90188-0.

[9] UA2 Collaboration. "Evidence for $Z^0 \to e^+e^-$ at the CERN $\bar{p}p$ Collider". In: *Phys. Lett.* 129B (1983), pp. 130–140. DOI: 10.1016/0370-2693(83)90744-X.

[10] UA2 Collaboration. "Observation of Single Isolated Electrons of High Transverse Momentum in Events with Missing Transverse Energy at the CERN $\bar{p}p$ Collider". In: *Phys. Lett.* 122B (1983), pp. 476–485. DOI: 10.1016/0370-2693(83)91605-2.

[11] ATLAS Collaboration. "Observation of a new particle in the search for the Standard Model Higgs boson with the ATLAS detector at the LHC". In: *Phys. Lett.* B716 (2012), pp. 1–29. DOI: 10.1016/j.physletb.2012.08.020.

[12] CMS Collaboration. "Observation of a new boson at a mass of 125 GeV with the CMS experiment at the LHC". In: *Phys. Lett.* B716 (2012), pp. 30–61. DOI: 10.1016/j.physletb.2012.08.021.

[13] P. W. Higgs. "Broken Symmetries and the Masses of Gauge Bosons". In: *Phys. Rev. Lett.* 13 (1964), pp. 508–509. DOI: 10.1103/PhysRevLett.13.508.

[14] F. Englert and R. Brout. "Broken Symmetry and the Mass of Gauge Vector Mesons". In: *Phys. Rev. Lett.* 13 (1964), pp. 321–323. DOI: 10.1103/PhysRevLett.13.321.

[15] ATLAS Collaboration. "Measurement of the W-boson mass in pp collisions at $\sqrt{s} = 7$ TeV with the ATLAS detector". In: *Eur. Phys. J.* C78.2 (2018), p. 110. DOI: 10.1140/epjc/s10052-017-5475-4.

[16] J. H. Christenson et al. "Evidence for the 2π Decay of the K_2^0 Meson". In: *Phys. Rev. Lett.* 13 (4 July 1964), pp. 138–140. DOI: 10.1103/PhysRevLett.13.138.

[17] R. D. Peccei. "QCD, strong CP and axions". In: *J. Korean Phys. Soc.* 29 (1996), S199–S208. arXiv: hep-ph/9606475 [hep-ph].

[18] T. R. Slatyer and C.-L. Wu. "General Constraints on Dark Matter Decay from the Cosmic Microwave Background". In: *Phys. Rev.* D95.2 (2017), p. 023010. DOI: 10.1103/PhysRevD.95.023010.

[19] R. Massey, T. Kitching, and J. Richard. "The dark matter of gravitational lensing". In: *Rept. Prog. Phys.* 73 (2010), p. 086901. DOI: 10.1088/0034-4885/73/8/086901.

[20] Y. F. Li and Z.-Z. Xing. "Neutrinos as Hot or Warm Dark Matter". In: *Acta Phys. Polon.* B42 (2011), pp. 2193–2202. DOI: 10.5506/APhysPolB.42.2193.

[21] IceCube Collaboration. "Search for sterile neutrino mixing using three years of IceCube DeepCore data". In: *Phys. Rev.* D95.11 (2017), p. 112002. DOI: 10.1103/PhysRevD.95.112002.

[22] T. J. Carroll. "New Constraints on Sterile Neutrinos with MINOS/MINOS+ and Daya Bay". In: *Proceedings, 52nd Rencontres de Moriond on Electroweak Interactions and Unified Theories: La Thuile, Italy, March 18-25, 2017*. 2017. eprint: 1705.05064.

[23] JUNO Collaboration. "Neutrino physics with JUNO". In: *Journal of Physics G: Nuclear and Particle Physics* 43.3 (2016), p. 030401. URL: http://stacks.iop.org/0954-3899/43/i=3/a=030401.

[24] MicroBooNE LAr1-ND ICARUS-WA104. "A Proposal for a Three Detector Short-Baseline Neutrino Oscillation Program in the Fermilab Booster Neutrino Beam". In: (2015). arXiv: 1503.01520.

[25] T. Bandyopadhyay and A. Raychaudhuri. "Left–right model with TeV fermionic dark matter and unification". In: *Physics Letters B* 771.Supplement C (2017), pp. 206–212. ISSN: 0370-2693. DOI: https://doi.org/10.1016/j.physletb.2017.05.042.

[26] G. 't Hooft. "Naturalness, chiral symmetry, and spontaneous chiral symmetry breaking". In: *NATO Sci. Ser. B* 59 (1980), pp. 135–157. DOI: 10.1007/978-1-4684-7571-5_9.

[27] Super-Kamiokande Collaboration. "Evidence for oscillation of atmospheric neutrinos". In: *Phys. Rev. Lett.* 81 (1998), pp. 1562–1567. DOI: 10.1103/PhysRevLett.81.1562.

[28] SNO Collaboration. "Neutrino observations from the Sudbury Neutrino Observatory". In: *AIP Conf. Proc.* 610 (2002), pp. 218–230. DOI: 10.1063/1.1469931.

[29] J. C. Pati and A. Salam. "Lepton number as the fourth "color"". In: *Phys. Rev. D* 10 (1 July 1974), pp. 275–289. DOI: 10.1103/PhysRevD.10.275.

[30] R. N. Mohapatra and J. C. Pati. ""Natural" left-right symmetry". In: *Phys. Rev. D* 11 (9 May 1975), pp. 2558–2561. DOI: 10.1103/PhysRevD.11.2558.

[31] G. Senjanović and R. N. Mohapatra. "Exact left-right symmetry and spontaneous violation of parity". In: *Phys. Rev. D* 12 (5 Sept. 1975), pp. 1502–1505. DOI: 10.1103/PhysRevD.12.1502.

[32] G. Senjanović. "Spontaneous breakdown of parity in a class of gauge theories". In: *Nuclear Physics B* 153.Supplement C (1979), pp. 334–364. ISSN: 0550-3213. DOI: https://doi.org/10.1016/0550-3213(79)90604-7.

[33] G. Branco, L. Lavoura, and J. Silva. *CP violation*. Oxford University Press, 1999. ISBN: 9780198503996.

[34] M. Nemevsek, G. Senjanovic, and V. Tello. "Connecting Dirac and Majorana Neutrino Mass Matrices in the Minimal Left-Right Symmetric Model". In: *Phys. Rev. Lett.* 110.15 (2013), p. 151802. DOI: 10.1103/PhysRevLett.110.151802.

[35] *Standard Model Public Results*. atlas.web.cern.ch/Atlas/GROUPS/PHYSICS/CombinedSummaryPlots/SM/.

[36] ATLAS Collaboration. "Search for supersymmetry in final states with two same-sign or three leptons and jets using 36 fb^{-1} of $\sqrt{s} = 13$ TeV pp collision data with the ATLAS detector". In: *JHEP* 09 (2017), p. 084. DOI: 10.1007/JHEP09(2017)084.

[37] M. Perelstein. "Little Higgs models and their phenomenology". In: *Prog. Part. Nucl. Phys.* 58 (2007), pp. 247–291. DOI: 10.1016/j.ppnp.2006.04.001.

[38] A. G. Akeroyd, C.-W. Chiang, and N. Gaur. "Leptonic signatures of doubly charged Higgs boson production at the LHC". In: *JHEP* 11 (2010), p. 005. DOI: 10.1007/JHEP11(2010)005.

[39] J. Alwall, P. Schuster, and N. Toro. "Simplified Models for a First Characterization of New Physics at the LHC". In: *Phys. Rev.* D79 (2009), p. 075020. DOI: 10.1103/PhysRevD.79.075020.

[40] R. S. Chivukula et al. "Top Quark Seesaw Theory of Electroweak Symmetry Breaking". In: *Phys. Rev.* D59 (1999), p. 075003. DOI: 10.1103/PhysRevD.59.075003.

[41] A. Zee. "Quantum Numbers of Majorana Neutrino Masses". In: *Nucl. Phys.* B264 (1986), pp. 99–110. DOI: 10.1016/0550-3213(86)90475-X.

[42] K.S. Babu. "Model of "calculable" Majorana neutrino masses". In: *Physics Letters B* 203.1 (1988), pp. 132–136. ISSN: 0370-2693. DOI: https://doi.org/10.1016/0370-2693(88)91584-5.

[43] M. Kohda, H. Sugiyama, and K. Tsumura. "Lepton number violation at the LHC with leptoquark and diquark". In: *Phys. Lett.* B718 (2013), pp. 1436–1440. DOI: 10.1016/j.physletb.2012.12.048.

[44] ATLAS Collaboration. "Inclusive search for same-sign dilepton signatures in pp collisions at $\sqrt{s} = 7$ TeV with the ATLAS detector". In: *JHEP* 10 (2011), p. 107. DOI: 10.1007/JHEP10(2011)107.

[45] ATLAS Collaboration. "Search for anomalous production of prompt same-sign lepton pairs and pair-produced doubly charged Higgs bosons with $\sqrt{s} = 8$ TeV pp collisions using the ATLAS detector". In: *JHEP* 03 (2015), p. 041. DOI: 10.1007/JHEP03(2015)041.

[46] *$t\bar{t}H$ recommended cross sections, yellow report 4*. twiki.cern.ch/twiki/bin/view/LHCPhysics/CERNYellowReportPageAt13TeV.

[47] J R Andersen et al. "Handbook of LHC Higgs Cross Sections: 3. Higgs Properties". In: (2013). Ed. by S Heinemeyer et al. DOI: 10.5170/CERN-2013-004. arXiv: 1307.1347 [hep-ph].

[48] S. Catani et al. "Soft gluon resummation for Higgs boson production at hadron colliders". In: *JHEP* 07 (2003), p. 028. DOI: 10.1088/1126-6708/2003/07/028.

[49] M. Ciccolini, A. Denner, and S. Dittmaier. "Electroweak and QCD corrections to Higgs production via vector-boson fusion at the LHC". In: *Phys. Rev.* D77 (2008), p. 013002. DOI: 10.1103/PhysRevD.77.013002.

[50] O. Brein, A. Djouadi, and R. Harlander. "NNLO QCD corrections to the Higgs-strahlung processes at hadron colliders". In: *Phys. Lett.* B579 (2004), pp. 149–156. DOI: 10.1016/j.physletb.2003.10.112.

[51] F. Bezrukov and M. Shaposhnikov. "Why should we care about the top quark Yukawa coupling?" In: *J. Exp. Theor. Phys.* 120 (2015). [Zh. Eksp. Teor. Fiz.147,389(2015)], pp. 335–343. DOI: 10.1134/S1063776115030152.

[52] CDF Collaboration. "Search for the standard model Higgs boson produced in association with top quarks using the full CDF data set". In: *Phys. Rev. Lett.* 109 (2012), p. 181802. DOI: 10.1103/PhysRevLett.109.181802.

[53] The T.E.V.N.P.H. Working Group. "Combined CDF and DØ Upper Limits on Standard Model Higgs-Boson Production with up to 4.2 fb^{-1} of Data". In: *Proceedings, 44th Rencontres de Moriond on Electroweak Interactions and Unified Theories: La Thuile, Italy, March 7-14, 2009*. 2009. URL: https://inspirehep.net/record/816108/files/arXiv:0903.4001.pdf.

[54] ATLAS Collaboration. "Search for the associated production of the Higgs boson with a top quark pair in multilepton final states with the ATLAS detector". In: *Physics Letters B* 749.Supplement C (2015), pp. 519–541. ISSN: 0370-2693. DOI: https://doi.org/10.1016/j.physletb.2015.07.079.

[55] ATLAS Collaboration. "Search for $H \to \gamma\gamma$ produced in association with top quarks and constraints on the Yukawa coupling between the top quark and the Higgs boson using data taken at 7 TeV and 8 TeV with the ATLAS detector". In: *Physics Letters B* 740.Supplement C (2015), pp. 222–242. ISSN: 0370-2693. DOI: https://doi.org/10.1016/j.physletb.2014.11.049.

[56] ATLAS Collaboration. "Search for the Standard Model Higgs boson produced in association with top quarks and decaying into $b\bar{b}$ in pp collisions at $\sqrt{s} = 8$ TeV with the ATLAS detector". In: *The European Physical Journal C* 75.7 (July 2015), p. 349. ISSN: 1434-6052. DOI: 10.1140/epjc/s10052-015-3543-1.

[57] CMS Collaboration. "Search for the associated production of the Higgs boson with a top-quark pair". In: *JHEP* 09 (2014), p. 087. DOI: 10.1007/JHEP09(2014)087,10.1007/JHEP10(2014)106.

[58] K. Huitu et al. "Doubly charged Higgs at LHC". In: *Nucl. Phys.* B487 (1997), pp. 27–42. DOI: 10.1016/S0550-3213(97)87466-4.

[59] A. G. Akeroyd and M. Aoki. "Single and pair production of doubly charged Higgs bosons at hadron colliders". In: *Phys. Rev.* D72 (2005), p. 035011. DOI: 10.1103/PhysRevD.72.035011.

[60] V. Rentala, W. Shepherd, and S. Su. "A Simplified Model Approach to Same-sign Dilepton Resonances". In: *Phys. Rev.* D84 (2011), p. 035004. DOI: 10.1103/PhysRevD.84.035004.

[61] P. Fileviez Pérez et al. "Neutrino masses and the CERN LHC: Testing the type II seesaw mechanism". In: *Phys. Rev. D* 78 (1 July 2008), p. 015018. DOI: 10.1103/PhysRevD.78.015018.

[62] L3 Collaboration. "Search for doubly charged Higgs bosons at LEP". In: *Phys. Lett.* B576 (2003), pp. 18–28. DOI: 10.1016/j.physletb.2003.09.082.

[63] DØ Collaboration. "Search for doubly-charged Higgs boson pair production in $p\bar{p}$ collisions at $\sqrt{s} = 1.96$ TeV". In: *Phys. Rev. Lett.* 108 (2012), p. 021801. DOI: 10.1103/PhysRevLett.108.021801.

[64] CDF Collaboration. "Search for Doubly Charged Higgs Bosons with Lepton-Flavor-Violating Decays involving Tau Leptons". In: *Phys. Rev. Lett.* 101 (2008), p. 121801. DOI: 10.1103/PhysRevLett.101.121801.

[65] CMS Collaboration. "Search for a doubly-charged Higgs boson with $\sqrt{s} = 8$ TeV pp collisions at the CMS experiment". In: (2016).

[66] OPAL Collaboration. "Search for the single production of doubly charged Higgs bosons and constraints on their couplings from Bhabha scattering". In: *Phys. Lett.* B577 (2003), pp. 93–108. DOI: 10.1016/j.physletb.2003.10.034.

[67] Ho T.-H., Ching C.-R., and Tao Z.-J. "Production of right-handed gauge bosons and heavy Majorana neutrinos at the Superconducting Super Collider". In: *Phys. Rev. D* 42 (7 Oct. 1990), pp. 2265–2273. DOI: 10.1103/PhysRevD.42.2265.

[68] W.-Y. Keung and G. Senjanović. "Majorana Neutrinos and the Production of the Right-Handed Charged Gauge Boson". In: *Phys. Rev. Lett.* 50 (19 May 1983), pp. 1427–1430. DOI: 10.1103/PhysRevLett.50.1427.

[69] A. Datta, M. Guchait, and D. P. Roy. "Prospect of heavy right-handed neutrino search at energies reached at the Superconducting Super Collider and CERN Large Hadron Collider". In: *Phys. Rev. D* 47 (3 Feb. 1993), pp. 961–966. DOI: 10.1103/PhysRevD.47.961.

[70] ATLAS Collaboration. "Search for heavy neutrinos and right-handed W bosons in events with two leptons and jets in pp collisions at $\sqrt{s} = 7$ TeV with the ATLAS detector". In: *Eur. Phys. J.* C72 (2012), p. 2056. DOI: 10.1140/epjc/s10052-012-2056-4.

[71] CMS Collaboration. "Search for heavy neutrinos and W_R bosons with right-handed couplings in a left-right symmetric model in pp collisions at sqrt(s) = 7 TeV". In: *Phys. Rev. Lett.* 109 (2012), p. 261802. DOI: 10.1103/PhysRevLett.109.261802.

[72] ATLAS Collaboration. "Search for heavy Majorana neutrinos with the ATLAS detector in pp collisions at $\sqrt{s} = 8$ TeV". In: *JHEP* 07 (2015), p. 162. DOI: 10.1007/JHEP07(2015)162.

[73] CMS Collaboration. "Search for heavy neutrinos and W bosons with right-handed couplings in proton-proton collisions at $\sqrt{s} = 8$ TeV". In: *Eur. Phys. J.* C74.11 (2014), p. 3149. DOI: 10.1140/epjc/s10052-014-3149-z.

[74] O. S. Brüning et al. *LHC Design Report*. CERN Yellow Reports: Monographs. Geneva: CERN, 2004. URL: https://cds.cern.ch/record/782076.

[75] J. Wenninger. "Approaching the Nominal Performance at the LHC". In: *Proceedings, 8th International Particle Accelerator Conference (IPAC 2017): Copenhagen, Denmark, May 14-19, 2017*. 2017. DOI: 10.18429/JACoW-IPAC2017-MOYAA1.

[76] *Luminosity Public Results Run 2*. https://twiki.cern.ch/twiki/bin/view/AtlasPublic/LuminosityPublicResultsRun2.

[77] C. Lefèvre. "The CERN accelerator complex. Complexe des accélérateurs du CERN". Dec. 2008.

[78] R. Scrivens et al. "Overview of the status and developments on primary ion sources at CERN*". In: CERN-ATS-2011-172 (Sept. 2011), 4 p.

[79] Bruce R. et al. "LHC Run 2: Results and challenges." In: (2016). URL: https://hb2016.esss.se/prepress/papers/moam5p50.pdf.

[80] M. A. Furman. "Electron Cloud Effects in Accelerators". In: *Proceedings, 5th Workshop on Electron-Cloud Effects (ECLOUD'12): La Biodola, Isola d'Elba, Italy, June 5-9, 2012*. 2013. DOI: 10.5170/CERN-2013-002.1.

[81] ATLAS Collaboration. "The ATLAS Experiment at the CERN Large Hadron Collider". In: *JINST* 3 (2008). Also published by CERN Geneva in 2010, S08003. 437 p. URL: https://cds.cern.ch/record/1129811.

[82] ATLAS Collaboration. *ATLAS magnet system: Technical Design Report, 1*. Technical Design Report ATLAS. Geneva: CERN, 1997. URL: https://cds.cern.ch/record/338080.

[83] ATLAS Collaboration. *ATLAS inner detector: Technical Design Report, 1*. Technical Design Report ATLAS. Geneva: CERN, 1997. URL: https://cds.cern.ch/record/331063.

[84] F. Hugging. "The ATLAS Pixel Insertable B-Layer (IBL)". In: *Nucl. Instrum. Meth.* A650 (2011), pp. 45–49. DOI: 10.1016/j.nima.2010.12.113.

[85] N. Wermes and G. Hallewel. *ATLAS pixel detector: Technical Design Report*. Technical Design Report ATLAS. Geneva: CERN, 1998.

[86] ATLAS Collaboration. *The Silicon Microstrip Sensors of the ATLAS SemiConductor Tracker*. Tech. rep. ATL-INDET-PUB-2007-007. ATL-COM-INDET-2007-008. CERN-ATL-COM-INDET-2007-008. 1. Geneva: CERN, Mar. 2007.

[87] E. Hines. "Performance of Particle Identification with the ATLAS Transition Radiation Tracker". In: *Particles and fields. Proceedings, Meeting of the Division of the American Physical Society, DPF 2011, Providence, USA, August 9-13, 2011*. 2011. arXiv: 1109.5925.

[88] S. Gadomski. "Updated impact parameter resolutions of the ATLAS Inner Detector". In: (2000).

[89] *Inned Detector Public Performance in Run 2*. twiki.cern.ch/twiki/bin/view/AtlasPublic/InDetTrackingPerformanceApprovedPlots.

[90] C.W. Fabjan and F. Gianotti. "Calorimetry for Particle Physics". In: *Rev. Mod. Phys.* 75.CERN-EP-2003-075 (Oct. 2003), 1243–1286. 96 p.

[91] B Aubert et al. "Construction, assembly and tests of the ATLAS electromagnetic barrel calorimeter". In: *Nucl. Instrum. Methods Phys. Res., A* 558.CERN-PH-EP-2005-034 (July 2005), 388–418. 77 p. URL: https://cds.cern.ch/record/883909.

[92] F. Fiorini and ATLAS Tile Calorimeter. "ATLAS tile calorimeter data preparation for LHC first beam data taking and commissioning data". In: *Journal of Physics: Conference Series* 219.2 (2010), p. 022030.

[93] D. M. Gingrich. "Construction, assembly and testing of the ATLAS hadronic end-cap calorimeter". In: *Journal of Instrumentation* 2.05 (2007), P05005.

[94] R. S. Orr. "The ATLAS Forward Calorimeter". In: ATL-LARG-SLIDE-2011-592 (Sept. 2011).

[95] ATLAS Collaboration. *ATLAS muon spectrometer: Technical Design Report*. Technical Design Report ATLAS. Geneva: CERN, 1997.

[96] ATLAS Collaboration. *Technical Design Report for the Phase-I Upgrade of the ATLAS TDAQ System*. Tech. rep. CERN-LHCC-2013-018. ATLAS-TDR-023. Final version presented to December 2013 LHCC. Sept. 2013.

[97] ATLAS Collaboration. "Performance of the ATLAS Trigger System in 2015". In: *Eur. Phys. J.* C77.5 (2017), p. 317. DOI: 10.1140/epjc/s10052-017-4852-3.

[98] I. Riu. "The ATLAS Level-1 Topological Trigger performance in Run 2". In: *J. Phys. Conf. Ser.* 898.3 (2017), p. 032037. DOI: 10.1088/1742-6596/898/3/032037.

[99] Artz S. et al. *Upgrade of the ATLAS Central Trigger for LHC Run-2*. Tech. rep. ATL-DAQ-PROC-2014-042. 02. Geneva: CERN, Nov. 2014.

[100] A. Kazarov and ATLAS Collaboration. *The ATLAS Data Flow System for LHC Run II*. Tech. rep. ATL-DAQ-PROC-2015-064. Geneva: CERN, Dec. 2015.

[101] *Egamma Trigger Public Results*. twiki.cern.ch/twiki/pub/AtlasPublic/EgammaTriggerPublicResults/.

[102] *Muon Trigger Public Results*. twiki.cern.ch/twiki/pub/AtlasPublic/MuonTriggerPublicResults/.

[103] M. Bruschi. *Diffraction and Forward Physics in ATLAS: results and perspectives*. Tech. rep. ATL-PHYS-PROC-2014-278. Geneva: CERN, Dec. 2014.

[104] "ATLAS Forward Detector for Luminosity Measurements and Monitoring Letter of Intent". In: (2004).

[105] A. Sidoti. *Minimum Bias Trigger Scintillators in ATLAS Run II*. Tech. rep. ATL-DAQ-PROC-2014-010. 10. Geneva: CERN, June 2014.

[106] V. Cindro et al. "The ATLAS Beam Conditions Monitor". In: *Journal of Instrumentation* 3.02 (2008), P02004.

[107] *Roman pots for the LHC*. http://cerncourier.com/cws/article/cern/27975.

[108] ATLAS Collaboration. *Electron efficiency measurements with the ATLAS detector using the 2015 LHC proton-proton collision data*. Tech. rep. ATLAS-CONF-2016-024. Geneva: CERN, June 2016. URL: https://cds.cern.ch/record/2157687.

[109] W. Lampl et al. *Calorimeter Clustering Algorithms: Description and Performance*. Tech. rep. ATL-LARG-PUB-2008-002. ATL-COM-LARG-2008-003. Geneva: CERN, Apr. 2008.

[110] ATLAS Collaboration. "Electron and photon energy calibration with the ATLAS detector using LHC Run 1 data". In: *Eur. Phys. J.* C74.10 (2014), p. 3071. DOI: 10.1140/epjc/s10052-014-3071-4.

[111] ATLAS Collaboration. *Electron and photon energy calibration with the ATLAS detector using data collected in 2015 at* $\sqrt{s} = 13$ TeV. Tech. rep. ATL-PHYS-PUB-2016-015. Geneva: CERN, Aug. 2016.

[112] ATLAS Collaboration. "Muon reconstruction performance of the ATLAS detector in proton–proton collision data at $\sqrt{s}$ =13 TeV". In: *Eur. Phys. J.* C76.5 (2016), p. 292. DOI: 10.1140/epjc/s10052-016-4120-y.

[113] J. Illingworth and J. Kittler. "A survey of the hough transform". In: *Computer Vision, Graphics, and Image Processing* 44.1 (1988), pp. 87–116. ISSN: 0734-189X. DOI: https://doi.org/10.1016/S0734-189X(88)80033-1.

[114] ATLAS Collaboration. "Performance of the ATLAS Trigger System in 2015". In: *Eur. Phys. J. C* 77.CERN-EP-2016-241. 5 (Nov. 2016), 317. 76 p.

[115] ATLAS Collaboration. *Performance of missing transverse momentum reconstruction for the ATLAS detector in the first proton-proton collisions at at $\sqrt{s}$= 13 TeV*. Tech. rep. ATL-PHYS-PUB-2015-027. Geneva: CERN, July 2015.

[116] S. Catani et al. "Longitudinally invariant K_t clustering algorithms for hadron hadron collisions". In: *Nucl. Phys.* B406 (1993), pp. 187–224. DOI: 10.1016/0550-3213(93)90166-M.

[117] Yuri L. Dokshitzer et al. "Better jet clustering algorithms". In: *JHEP* 08 (1997), p. 001. DOI: 10.1088/1126-6708/1997/08/001.

[118] M. Cacciari, G. P. Salam, and G. Soyez. "The Anti-k_t jet clustering algorithm". In: *JHEP* 04 (2008), p. 063. DOI: 10.1088/1126-6708/2008/04/063.

[119] ATLAS Collaboration. "Performance of pile-up mitigation techniques for jets in pp collisions at $\sqrt{s}$ = 8 TeV using the ATLAS detector". In: *Eur. Phys. J.* C76.11 (2016), p. 581. DOI: 10.1140/epjc/s10052-016-4395-z. arXiv: 1510.03823 [hep-ex].

[120] ATLAS Collaboration. *Optimisation of the ATLAS b-tagging performance for the 2016 LHC Run*. Tech. rep. ATL-PHYS-PUB-2016-012. Geneva: CERN, June 2016.

[121] *Jet Performance Public Plots*. atlas.web.cern.ch/Atlas/GROUPS/PHYSICS/PLOTS/JETM-2016-010/.

[122] A. Schwartzman. "Jet energy calibration at the LHC". In: *Int. J. Mod. Phys. A* 30.arXiv:1509.05459 (Sept. 2015), 1546002. 25 p.

[123] ATLAS Collaboration. *Measurement of the tau lepton reconstruction and identification performance in the ATLAS experiment using pp collisions at $\sqrt{s}$=13 TeV*. Tech. rep. ATLAS-CONF-2017-029. Geneva: CERN, May 2017.

[124] D. et al. Adams. *Recommendations of the Physics Objects and Analysis Harmonisation Study Groups 2014*. Tech. rep. ATL-COM-PHYS-2014-451. Geneva: CERN, May 2014.

[125] S. Höche. "Introduction to parton-shower event generators". In: *Proceedings, Theoretical Advanced Study Institute in Elementary Particle Physics: Journeys Through the Precision Frontier: Amplitudes for Colliders (TASI 2014): Boulder, Colorado, June 2-27, 2014*. 2015, pp. 235–295. DOI: 10.1142/9789814678766_0005.

[126] H.-L. Lai et al. "New parton distributions for collider physics". In: *Phys. Rev. D* 82 (2010), p. 074024. DOI: 10.1103/PhysRevD.82.074024.

[127] J. Gao et al. "CT10 next-to-next-to-leading order global analysis of QCD". In: *Phys. Rev.* D89.3 (2014), p. 033009. DOI: 10.1103/PhysRevD.89.033009.

[128] J. Pumplin et al. "New generation of parton distributions with uncertainties from global QCD analysis". In: *JHEP* 07 (2002), p. 012. DOI: 10.1088/1126-6708/2002/07/012.

[129] R. D. Ball et al. "Parton distributions with LHC data". In: *Nucl. Phys. B* 867 (2013), pp. 244–289. DOI: 10.1016/j.nuclphysb.2012.10.003.

[130] R. D. Ball et al. "Parton distributions for the LHC Run II". In: *JHEP* 04 (2015), p. 040. DOI: 10.1007/JHEP04(2015)040.

[131] M. Bahr et al. "Herwig++ Physics and Manual". In: *Eur. Phys. J.* C58 (2008), pp. 639–707. DOI: 10.1140/epjc/s10052-008-0798-9.

[132] T. Gleisberg et al. "Event generation with SHERPA 1.1". In: *JHEP* 02 (2009), p. 007. DOI: 10.1088/1126-6708/2009/02/007.

[133] T. Sjöstrand, S. Mrenna, and Peter Z. Skands. "PYTHIA 6.4 physics and manual". In: *JHEP* 05 (2006), p. 026. DOI: 10.1088/1126-6708/2006/05/026.

[134] J. Alwall et al. "The automated computation of tree-level and next-to-leading order differential cross sections, and their matching to parton shower simulations". In: *JHEP* 07 (2014), p. 079. DOI: 10.1007/JHEP07(2014)079.

[135] S. Höche et al. "QCD matrix elements + parton showers: The NLO case". In: *JHEP* 04 (2013), p. 027. DOI: 10.1007/JHEP04(2013)027. arXiv: 1207.5030 [hep-ph].

[136] S. Alioli et al. "A general framework for implementing NLO calculations in shower Monte Carlo programs: the POWHEG BOX". In: *JHEP* 06 (2010), p. 043. DOI: 10.1007/JHEP06(2010)043.

[137] B. Andersson et al. “Parton Fragmentation and String Dynamics”. In: *Phys. Rept.* 97 (1983), pp. 31–145. DOI: 10.1016/0370-1573(83)90080-7.

[138] B. R. Webber. “A QCD Model for Jet Fragmentation Including Soft Gluon Interference”. In: *Nucl. Phys.* B238 (1984), pp. 492–528. DOI: 10.1016/0550-3213(84)90333-X.

[139] G. Marchesini and B. R. Webber. “Monte Carlo Simulation of General Hard Processes with Coherent QCD Radiation”. In: *Nucl. Phys.* B310 (1988), pp. 461–526. DOI: 10.1016/0550-3213(88)90089-2.

[140] ATLAS Collaboration. *ATLAS Run 1 Pythia8 tunes*. Tech. rep. ATL-PHYS-PUB-2014-021. Geneva: CERN, Nov. 2014. URL: https://cds.cern.ch/record/1966419.

[141] ATLAS Collaboration. “Measurement of the Z/γ^* boson transverse momentum distribution in pp collisions at $\sqrt{s} = 7$ TeV with the ATLAS detector”. In: *JHEP* 09 (2014), p. 145. DOI: 10.1007/JHEP09(2014)145.

[142] P.Z. Skands. “Tuning Monte Carlo generators: The Perugia tunes”. In: *Phys. Rev.* D82 (2010), p. 074018. DOI: 10.1103/PhysRevD.82.074018.

[143] ATLAS Collaboration. *Studies on top-quark Monte Carlo modelling for Top2016*. Tech. rep. ATL-PHYS-PUB-2016-020. Geneva: CERN, Sept. 2016.

[144] R. Frederix and S. Frixione. “Merging meets matching in MC@NLO”. In: *JHEP* 12 (2012), p. 061. DOI: 10.1007/JHEP12(2012)061.

[145] J. Catmore et al. *A New Petabyte-scale Data Derivation Framework for ATLAS*. Tech. rep. ATL-SOFT-PROC-2015-041. 7. Geneva: CERN, May 2015.

[146] ATLAS Collaboration. “ATLAS: Detector and physics performance technical design report. Volume 1”. In: CERN-LHCC-99-14, ATLAS-TDR-14 (1999).

[147] M. Baak et al. “HistFitter software framework for statistical data analysis”. In: *Eur. Phys. J.* C75 (2015), p. 153. DOI: 10.1140/epjc/s10052-015-3327-7.

[148] S. S. Wilks. “The Large-Sample Distribution of the Likelihood Ratio for Testing Composite Hypotheses”. In: *Ann. Math. Statist.* 9.1 (Mar. 1938), pp. 60–62. DOI: 10.1214/aoms/1177732360.

[149] P. Golonka and Z. Was. "PHOTOS Monte Carlo: a precision tool for QED corrections in Z and W decays". In: *Eur. Phys. J. C* 45.hep-ph/0506026. CERN-PH-TH-2005-091. IFJPAN-V-2005-01 (June 2005), pp. 97–107.

[150] G. Cowan et al. "Asymptotic formulae for likelihood-based tests of new physics". In: *The European Physical Journal C* 71.2 (Feb. 2011), p. 1554. ISSN: 1434-6052. DOI: 10.1140/epjc/s10052-011-1554-0.

[151] S. Frixione et al. "Electroweak and QCD corrections to top-pair hadroproduction in association with heavy bosons". In: *JHEP* 06 (Apr. 2015), 184. 27 p.

[152] A. D. Martin et al. "Parton distributions for the LHC". In: *Eur. Phys. J.* C63 (2009), pp. 189–285. DOI: 10.1140/epjc/s10052-009-1072-5.

[153] ATLAS Collaboration. "Measurement of the production of a W boson in association with a charm quark in pp collisions at $\sqrt{s} = 7$ TeV with the ATLAS detector". In: *JHEP* 05 (2014), p. 068. DOI: 10.1007/JHEP05(2014)068.

[154] *Statistical tool for $t\bar{t}H$ analysis*. https://twiki.cern.ch/twiki/bin/viewauth/AtlasProtected/TtHFitter.

[155] K. Cranmer et al. "HistFactory: A tool for creating statistical models for use with RooFit and RooStats". In: CERN-OPEN-2012-016 (2012).

[156] ATLAS Collaboration. "Evidence for the associated production of the Higgs boson and a top quark pair with the ATLAS detector". In: *Submitted to: Phys. Rev. D* (2017). eprint: 1712.08891.

[157] P.C. Bhat. "Multivariate Analysis Methods in Particle Physics". In: *Annual Review of Nuclear and Particle Science* 61.1 (2011), pp. 281–309. DOI: 10.1146/annurev.nucl.012809.104427.

[158] G. Ucchielli. *Multivariate analysis methods in the search for the Higgs boson produced in association with top pairs at the ATLAS experiment at LHC*. Tech. rep. University of Bologna, Nov. 2014. URL: http://amslaurea.unibo.it/7607/1/ucchielli_giulia_tesi.pdf.

[159] *ATLAS isolation and fake forum*. twiki.cern.ch/twiki/bin/view/AtlasProtected/IsolationFakeForum.

[160] ATLAS Collaboration. "Measurement of inclusive and differential cross sections in the $H \to ZZ^* \to 4\ell$ decay channel in pp collisions at $\sqrt{s}$ = 13 TeV with the ATLAS detector". In: (2017). arXiv: 1708.02810 [hep-ex].

[161] ATLAS Collaboration. "Search for doubly charged Higgs boson production in multi-lepton final states with the ATLAS detector using proton-proton collisions at $\sqrt{s} = 13$ TeV". In: (2017). arXiv: 1710.09748 [hep-ex].

[162] M. Muhlleitner and M. Spira. "A Note on doubly charged Higgs pair production at hadron colliders". In: *Phys. Rev.* D68 (2003), p. 117701. DOI: 10.1103/PhysRevD.68.117701.

[163] C. Anastasiou et al. "High precision QCD at hadron colliders: Electroweak gauge boson rapidity distributions at NNLO". In: *Phys. Rev.* D69 (2004), p. 094008. DOI: 10.1103/PhysRevD.69.094008.

[164] S. G. Bondarenko and A. A. Sapronov. "NLO EW and QCD proton-proton cross section calculations with mcsanc-v1.01". In: *Comput. Phys. Commun.* 184 (2013), pp. 2343–2350. DOI: 10.1016/j.cpc.2013.05.010.

[165] T. Gleisberg and S. Hoeche. "Comix, a new matrix element generator". In: *JHEP* 12 (2008), p. 039. DOI: 10.1088/1126-6708/2008/12/039.

[166] F. Cascioli, P. Maierhofer, and S. Pozzorini. "Scattering Amplitudes with Open Loops". In: *Phys. Rev. Lett.* 108 (2012), p. 111601. DOI: 10.1103/PhysRevLett.108.111601.

[167] P. Artoisenet et al. "Automatic spin-entangled decays of heavy resonances in Monte Carlo simulations". In: *Journal of High Energy Physics* 2013.3 (Mar. 2013). ISSN: 1029-8479. DOI: 10.1007/JHEP03(2013)015.

[168] M. Czakon and A. Mitov. "Top++: A program for the calculation of the top-pair cross-section at hadron colliders". In: *Computer Physics Communications* 185.11 (2014), pp. 2930–2938. ISSN: 0010-4655. DOI: https://doi.org/10.1016/j.cpc.2014.06.021.

[169] ATLAS Collaboration. "Search for high-mass new phenomena in the dilepton final state using proton-proton collisions at $\sqrt{s} = 13$ TeV with the ATLAS detector". In: *Phys. Lett.* B761 (2016), pp. 372–392. DOI: 10.1016/j.physletb.2016.08.055.

[170] J. Rojo et al. "The PDF4LHC report on PDFs and LHC data: Results from Run I and preparation for Run II". In: *J. Phys.* G42 (2015), p. 103103. DOI: 10.1088/0954-3899/42/10/103103.

[171] S. Dulat et al. "New parton distribution functions from a global analysis of quantum chromodynamics". In: *Phys. Rev.* D93.3 (2016), p. 033006. DOI: 10.1103/PhysRevD.93.033006.

[172] ATLAS Collaboration. *Multi-Boson Simulation for 13 TeV ATLAS Analyses*. Tech. rep. ATL-PHYS-PUB-2017-005. Geneva: CERN, May 2017.

[173] D. de Florian et al. "Handbook of LHC Higgs Cross Sections: 4. Deciphering the Nature of the Higgs Sector". In: (2016). DOI: 10.23731/CYRM-2017-002.

[174] A. Alloul et al. "FeynRules 2.0 - A complete toolbox for tree-level phenomenology". In: *Comput. Phys. Commun.* 185 (2014), pp. 2250–2300. DOI: 10.1016/j.cpc.2014.04.012.

[175] ATLAS Collaboration. "Improved luminosity determination in pp collisions at sqrt(s) = 7 TeV using the ATLAS detector at the LHC". In: *Eur. Phys. J.* C73.8 (2013), p. 2518. DOI: 10.1140/epjc/s10052-013-2518-3.

[176] G.L. Alberghi et al. "Choice and characterization of photomultipliers for the new ATLAS LUCID detector". In: *Journal of Instrumentation* 11.05 (2016), P05014.

[177] *Forward Detectors Public Results*. twiki.cern.ch/twiki/bin/view/AtlasPublic/ForwardDetPublicResults.